2016

Development of buckling-controlled braced frames for seismic design of steel buildings

Onur Seker
Iowa State University

Development of buckling-controlled braced frames for seismic design of steel buildings

by

Onur Seker

A dissertation submitted to the graduate faculty

in partial fulfillment of the requirements for the degree of

DOCTOR OF PHILOSOPHY

Major: Civil Engineering (Structural Engineering)

Program of Study Committee:
J. Jay Shen, Major Professor
Fouad S. Fanous
Jon M. Rouse
Alan M. Russell
Jeramy C. Ashlock

Iowa State University

Ames, Iowa

2016

DEDICATION

This work is dedicated to my sweet and supportive wife, Pinar Toru Seker, who kept me warm and working throughout the entire doctorate program.

I also dedicate this dissertation to my beloved mother, Yasemin Seker and my grandmother, Aysel Yel.

TABLE OF CONTENTS

NOMENCLATURE

AISC	American Institute of Steel Construction
ASTM	American Society for Testing and Materials
AWS	American Welding Society
BC	Buckling Controller
BCB	Buckling Controlled Brace
BCBF	Buckling Controlled Braced Frame
BR	Buckling Restrainer
BRB	Buckling-Restrained Brace
BRBF	Buckling-Restrained Braced Frame
CBF	Concentrically Braced Frames
CHS	Circular Hollow Section
CJP	Complete Joint Penetration
FC	Friction Coefficient
FE	Finite Element
FEM	Finite Element Method
FEMA	Federal Emergency Management Agency
HAZ	Heat Affected Zone
HSS	Hollow Structural Section
MF	Moment Frame
NSF	National Science Foundation
ODR	Overall Drift Ratio

PE	Probability of Exceedance
RHS	Rectangular Hollow Section
RT	Relative Thickness
SCBF	Special Concentrically Braced Frame
SDR	Story Drift Ratio
SFRS	Seismic Force Resisting System
SG	Strain Gauge
SHS	Square Hollow Section
SMRF	Special Moment Resisting Frame
SP-BRB	Sandwiched Plate Buckling Restrained Brace
TSXBF	Two-Story X-Braced Frame

ACKNOWLEDGMENTS

I would like to thank my adviser, Dr. Jay Shen, who provided me the opportunity to join his research team, for his patience with me and his persistence to educate me in terms of research and teaching.

Besides my adviser, I would like to thank my former adviser, Dr. Bulent Akbas, who opened new doors for me, for his constant guidance and support since the first day I met him.

Thanks must also go to good friends: Cem Kalkan, Bahtiyar Atam and Koray Tugay.

Special thanks to the distinguished faculty members who served on my committee: Dr. Fanous, Dr. Rouse, Dr. Ashlock and Dr. Russell.

This research is partially supported by American Institute of Steel Construction (AISC) and Iowa State University (ISU). Special thanks are due to Chicago Metal Fabricators (CMF) and Garbe Iron Works (GIW) for their advices throughout the project and help with fabrication of the test specimens. I also thank ISU Structural Lab coordinator, Doug Wood for his assistance with the experimental portion of the study.

The opinions expressed in this report are solely those of the author and do not necessarily reflect the views of AISC, ISU, or other agencies and individuals whose names appear in this document.

ABSTRACT

Concentrically braced frames (CBFs) have become one of the most commonly used lateral force resisting systems in seismic regions after the 1994 Northridge Earthquake due to the unexpected damages observed in moment frames. Diagonal bracing members in ductile CBFs are designed as primary seismic energy dissipating mechanisms so that structural damage can be limited with bracings. Thus, overall structural performance in ductile CBFs can be associated with plastic deformation capability of the bracing members. In this regard, local buckling-induced premature fracture and unsymmetrical hysteretic behavior of conventional buckling braces raise concerns about the seismic performance of CBFs. Buckling-restrained braces (BRBs), when properly designed, can be effective in terms of overcoming many potential issues caused by the nature of conventional bracings. Nevertheless, some aspects of the current BRBs limit wide-spread application of these braces. The vast majority of the BRB designs developed to date are costly, heavy and unnecessarily complicated. Further, the previous research on BRBs lacked discussing the performance goals and simplicity parallel to each other, which resulted in impractical designs for engineering applications in terms of constructability. The present study aims at developing steel brace models that are simple, practical and cost-effective by reducing the high labor and fabrication cost, avoiding the complicated cross-sections and connections, as well as enhancing fracture life of the braces without altering the current habits formed in the design practice so far. For this purpose, three innovative brace models for new design and enhancing the performance of existing structures are developed and examined by means of numerical and experimental studies. The results point out that the developed brace models

are promising and capable of exhibiting symmetrical and stable inelastic cyclic response along with mitigating the possibility of brace fracture substantially. Further, the findings presented in this study expand the previous work in the literature by providing a framework for future studies.

CHAPTER I

INTRODUCTION

1. Background

Unexpected damages observed after the 1994 Northridge, the 1995 Kobe and the 1995 Hyogoken-Nanbu earthquakes have marked the end of an era for steel structures in the United States and Japan. The cyclic behavior of the pre-Northridge moment connections was extensively studied during the late 1960s and early 1970s (Popov et al. 1968, Krawinkler et al. 1971, Popov et al. 1972, 1973a, 1973b, 1975) using either small-scale or full-scale subassemblage tests. In light of these studies, the economy and anticipated ductility of special moment resisting frames (SMRFs) with welded pre-Northridge moment connections gradually attracted the steel construction industry's attention since the early 1970s and thus SMRFs became dominant among the other seismic force resisting systems (SFRS) in the years prior to the 1994 Northridge earthquake. SMRFs are designed to resist seismic events through their extensive flexural plastic deformation capabilities at their beam ends or plastic shear deformation in the panel zones without significant strength or stiffness loss. In other words, it was presumed that the expected damage under a severe ground motion is limited solely to the inelastic deformation of the steel elements (FEMA 2000a, 2000b). However, the welded pre-Northridge beam-to-column moment connections experienced severe damages during the recent earthquakes. Even though SMRFs did not collapse during the 1994 Northridge earthquake, engineers and researchers were alarmed by the unanticipated brittle beam-to-column connection failures observed after the earthquake.

Subsequent to the earthquake of 1994, SAC joint venture initiated a research program funded by the Federal Emergency Management Agency (FEMA), the American Institute of Steel Construction (AISC) and the National Science Foundation (NSF) to unveil the issues associated with the brittle connection failures. After six years of experimental and model-based studies, seismic provisions were altered significantly, a variety of new moment-resisting connections were proposed (FEMA 2000a, AISC 2010a) and stringent design and detailing requirements were introduced to the seismic design of SMRFs. It was found that the unpredicted brittle failure modes observed in the SMRFs were mainly due to the large variation in the actual steel material properties, severe stress concentrations due to the connection details and on-site welding practice prior to the earthquake (FEMA 2000b, 2000c). In addition, nearly every beam-column connection was rigid in the early steel moment frames. Therefore, the beam and column sizes adopted for the tests during the 1960s and 1970s were much lighter and shallower than the common beam and column sizes used in the SMRFs that were subjected to the recent earthquakes. This high discrepancy between the tested and the actual beam and column sizes of the beam-to-column connections also played a vital role in the connection failures. Development of the SMRFs and the reasons for the wide-spread brittle connection failures are discussed thoroughly in the related FEMA reports and literature after the recent earthquakes (FEMA 2000a, 2000b, 2000c, Nakashima et al. 1998, 2000).

After the lessons learned from the 1994 Northridge earthquake, concentrically braced frames (CBFs) have grown in popularity in the regions with high seismicity. In fact, braced frames are among the oldest structural systems and have been widely used in various forms for many decades. However, practicing engineers leaned towards CBFs in the seismic-prone

regions as a consequence of the recently-developed stringent requirements for the structural members and their labor intensive connections in SMRFs. It is, therefore, important to emphasize that the structural system selection was predominantly affected by the economic aspects of the lateral force resisting system. Furthermore, controlling the lateral deflections in SMRFs has been an unchanging difficulty for design engineers for years. Due to the flexible nature of SMRFs, design of a SMRF is generally governed by the stiffness requirement (drift requirement) rather than strength requirement, which results in beam and column sections substantially deeper and heavier than those required for the strength requirement. CBFs, on the other hand, are advantageous to the steel construction industry owing to their efficiency in terms of cost effectiveness due to their relatively low labor cost, ease of construction and large initial lateral stiffness that limits the lateral deflections.

The attempt at reducing the overall structural cost had an effect on the preferences for the bracing configurations in CBFs as well. Bracing configuration in a CBF can, in fact, play a decisive role in the economy, as well as design and overall seismic performance of conventional CBFs (Shen et al. 2014, 2015). Structural engineers have often preferred V- and inverted V-type CBFs to the CBFs with X-type brace configurations for their fewer gusset plate connections. However, due to the large seismic demands on the brace-intersected girders of V- and inverted-V type CBFs, the design of V- and inverted V-type CBFs often results in deep and heavy girder sections. On account of the disadvantages of having deep and heavy girders, the industry has been recently inclined to utilize two-story X-braced frames (TSXBFs) in order to mitigate the effect of the unbalanced forces by using V-type and inverted V-type bracing configurations in alternating stories. Currently, V-type, inverted

V-type and mixed type brace configurations are the most common bracing arrangements in the existing CBFs in seismic areas.

Owing to the aforementioned economic reasons, ductile CBFs have received much attention in the last two decades, but nevertheless seismic performance of conventional CBFs is far from perfect. Unsymmetrical hysteretic behavior and local buckling-induced premature fracture of bracing members have been of concern to many engineers and researchers. One efficient way to overcome the common issues related to seismic performance of CBFs is to restrain global and local buckling of the braces, if possible. Buckling-restrained braces (BRBs) are hysteretic dampers that dissipate the seismic energy through yielding in tension and compression without buckling under reversed cyclic loading. Therefore, BRBs, in general, are capable of providing symmetrical axial load-deformation response, as well as elongating the fracture life of bracings by controlling local plastic deformations to be formed. Furthermore, BRBs provide high lateral stiffness identical to that of conventional braces in order to control lateral displacements on structures. In other words, BRBs aim to resolve the problems associated with both SMRFs and conventional CBFs by controlling lateral deflections and brace buckling, as well as exhibiting a symmetrical cyclic response.

Buckling-restrained braced frames (BRBFs) are CBFs that incorporate BRBs as a substitute for conventional braces. BRBFs have attracted widespread interest for seismic applications in Japan after the 1995 Kobe earthquake (Uang et al. 2004, Xie 2005) for their significant seismic performance, symmetrical hysteretic behavior and notable energy dissipation capacity. Statistics of high-rise steel buildings in Japan showed that BRBs were extensively used for the majority of the tall buildings (greater than 60 meters) built after the earthquake of 1995 (Clark et al. 1999, Xie 2005). In addition to the general interest in Japan,

the United States and many other countries located in seismically active regions of Asia showed their interest in BRBs. For example, BRBs were installed for numerous new buildings and retrofitting projects in Taiwan (Xie 2005) in order to enhance the seismic performance of new and existing buildings. The first application of BRBs in the United States was a few years after the 1994 Northridge earthquake (Clark et al. 1999) and BRBs have been steadily growing in popularity in seismic areas since the late 1990s. Today, BRBs covering different types and configurations have many possible uses in many countries either as BRBFs or dual systems for retrofitting existing steel moment frames (Di Sarno and Elnashai 2009), reinforced concrete (R/C) moment frames (Di Sarno and Manfredi 2010, Sutcu et al. 2014, Corte et al. 2014) and R/C bridge bents (El-Baheya and Bruneau 2011).

2. Motivation

Ductile CBFs, which are referred as special concentrically braced frames (SCBFs) are earthquake-resistant structural systems. As such, it is expected that SCBFs would undergo significant inelastic deformations in order to compensate for the seismic force reduction made when designing the lateral force resisting system. Therefore, braces in a conventional CBF buckle and yield when subjected to an earthquake ground motion. Owing to the difference between the inelastic tensile and compressive behaviors, the braces exhibit an unsymmetrical hysteretic behavior. The potential issues arising from the unsymmetrical hysteretic response due to post-buckling behavior can be summarized as follows:

(1) Strength loss due to post-buckling behavior substantially reduces the overall energy dissipation capacity of a CBF.

(2) Substantial difference between the tensile and compressive strengths would impose significant demands on the brace-intersected girders, columns and beam-to-column connections during a seismic event.

(3) Isolated stories in a conventional SCBF may be subjected to significant lateral stiffness and strength reduction due to the rapid stiffness and strength degradation of the brace in compression subsequent to global buckling. As a result of the irregular lateral stiffness and strength distribution along the building height, plastic deformations may accumulate in the relatively weak (or soft) story or stories as the demand increases.

In addition to the common issues of exhibiting an unsymmetrical hysteretic response, conventional buckling braces, especially cold-formed tubular bracings are susceptible to premature fracture. Past studies demonstrated that the localized strain demands eventually lead to premature fracture of conventional braces during the first or second reversed tension cycle following the severe local buckling of the braces. Once fracture of the braces occurred, the beam-column connections would experience substantial damage due to framing action (Uriz and Mahin 2008), which might lead to column fracture or even collapse of the seismic force resisting system as a whole.

Several studies have been performed to evaluate seismic drift demands in SCBFs (Uriz 2005, Sabelli et al. 2001, Sabelli et al. 2003, McCormick et al. 2007). Based on the recent non-linear dynamic analyses results, the median peak story drift demands would increase up to 5.7% and 4.4% for low-rise and mid-rise SCBFs, respectively, when conventional SCBFs are subjected to MCE-level ground motions (Uriz and Mahin 2008, Fell et al. 2009). Furthermore, it is reported (Sabelli et al. 2001, Sabelli et al. 2003) that mean peak interstory drift demands on concentrically braced steel frames may reach nearly 4%

even for the 10% probability of exceedance (PE) in 50 year events. Recent test results of conventional tubular bracings, on the other hand, provided compelling evidence that both square and circular cold-formed steel tubular bracings are not capable of developing sufficient ductility to meet the expected seismic demands (Uriz and Mahin 2008, Tremblay et al. 2008, Fell et al. 2009). Moreover, the recent studies on testing of large-scale hollow structural shapes (HSS) under reversed cyclic loading consistently showed that fracture initiation of square or round cold-formed steel tubular bracings are likely to take place at an equivalent story drift ratio of around 2.0% soon after local buckling. This high discrepancy between fracture life of conventional bracings and seismic drift demands on the structural system strongly resembles the presumptions about SMRFs prior to the earthquake of 1994, since it was believed that the typical pre-Northridge connection employed in steel moment-frame construction was capable of developing large plastic rotations, without significant strength degradation (FEMA 2000c). It is, therefore, important to develop a cost-effective method to improve seismic performance of the new and existing CBFs in seismic regions, such as California, in which the steel building market comprises a considerable number of high-rise SCBFs including office buildings and hospitals.

A general rule of thumb for capacity-based design is to control the location of the inelastic deformations so as to protect the critical zones or structural members that are not desired to experience plastic deformations. Owing to the increasing trend in utilizing SCBFs as a seismic force resisting system, seismic design codes have been altered substantially in view of capacity design philosophy in the last decade. In order to introduce a more rigorous design procedure for SCBFs, the current seismic design provisions (AISC 2010b) considers the inelastic dynamic response of SCBFs together with the capacity design approach. For this

purpose, the design code encourages engineers to assume an anticipated mechanism for seismic design of SCBFs based on limited research conducted on system response of SCBFs. Further, the current seismic codes, such as AISC 341 (2010), require that the protected structural members that are desired to remain elastic (e.g. girders) shall be designed based on the expected yielding and buckling (or post-buckling) capacity of the bracings. However, regardless of dynamic properties of the structure and complexity of potential deformation patterns in braced frames, the code considers only the first-mode loading pattern for seismic design of SCBFs with the assumption that all braces in all stories buckle or yield simultaneously. Furthermore, recent studies (Shen et al. 2014, 2015) addressed that the suggested structural analysis cases for several brace deformation scenarios and the assumptions about the potential mechanisms given in the seismic code are less likely to occur and would not reflect the actual inelastic dynamic response of SCBFs. In other words, the efforts to avoid the adverse effect of the unsymmetrical hysteretic behavior of conventional braces on the other structural members and the overall behavior might be ineffective.

As an alternative to conventional braces, BRBs can be effective in terms of overcoming many potential issues caused by the nature of conventional bracings. Nevertheless, some aspects of the current BRBs have raised economic concerns for wide-spread application of these braces in the US. For instance, the vast majority of the proposed BRBs to date are proprietary (Uang et al. 2004) and therefore application of both concrete-encased (unbonded) and all-steel BRBs are costly, especially for regular office buildings. In addition to the cost of being proprietary, concrete-encased BRBs are heavy and difficult to inspect, which restricts their application from being more common in the steel construction market.

Comparatively speaking, all-steel BRBs can be regarded as more convenient for the industry. Although concrete-encased BRBs and all-steel BRBs share the very same concept of providing continuous lateral support along the length, all-steel BRBs are lighter due to absence of encasing mortar, and there exist many possible arrangements that might offer simplicity and performance for all-steel BRBs at the same time. Unfortunately, the advantage of having numerous possibilities to enhance the performance resulted in unnecessarily complicated (Chou et al. 2010, Zhao et al. 2011, Ma et al. 2012, Dusicka and Tinker 2013) all-steel BRB designs, which often require closely spaced bolted or welded attachments (Eryasar and Topkaya 2010), as well as cross sections consisting a combination of plates and structural shapes (HSS, Channels, Tee etc.). Hence, the majority of all-steel BRB models developed to date traded one aspect for another and lacked consideration of performance goals and simplicity in parallel, which resulted in impractical designs for engineering applications in terms of constructability. Furthermore, potential stability issues of utilizing a polyethylene-based temporary coating and applicability of the unbonding material to an actual steel construction are still unclear for all-steel BRBs.

3. Objectives

The objectives of the present study are to:

- Develop a new buckling-controlled brace (BCB) concept that consolidates the common design practice for CBFs with the idea of controlling buckling in a simple and cost effective way.

- Enhance fracture life of the conventional braces in new and existing CBFs by utilizing a simple technique in order to improve overall seismic performance of steel braced frames in seismic prone regions.
- Develop an innovative three-segment steel brace for seismic design of steel braced frames.

Steel brace models included in this study are evaluated in terms of capacity in comparison with conventional bracings. Based on the summarized objectives of the study, the remaining chapters are organized as follows:

- Chapter II assesses the efficiency of the developed Tube-in-Tube BCBs in terms of hysteretic response and fracture life of bracings by means of testing and finite element (FE) simulations.
- Chapter III presents a simple technique that aims at mitigating the likelihood of premature brace fracture in CBFs. The developed method can be used for enhancing performance of new and existing steel braced frames. The FE simulation results of steel bracings are discussed in terms of the local strain demand, as well as inelastic cyclic response of the braces.
- Chapter IV presents an innovative three-segment steel brace with non-uniform cross-section. Analytical, numerical and experimental investigations of the three-segment steel brace are presented and discussed.
- Chapter V summarizes the present research and suggests proposals for the potential future studies.

4. Literature Review

A significant amount of experimental and numerical research has been carried out on SCBFs and BRBFs to date. A brief summary of the studies related to the present study is reviewed herein. Comprehensive literature surveys on the cyclic performance of conventional bracing members and development of BRBs can be found in the related reports and review papers (Uang et al. 2004, Xie 2005).

4.1. Literature on CBFs

Seismic performance of braced frames relies upon the ductile behavior of their structural components and connections. Therefore, the structural members and connections in ductile CBFs are expected to provide sufficient ductility when subjected to severe earthquake ground motions. As earthquake-resistant structural systems, it is desired that SCBFs dissipate the seismic input energy through yielding and buckling of their braces. Thus, it is essential to prevent brittle failure modes, premature fracture of the braces, and potential stability issues caused by inelastic deformation of the structural members other than braces, in order to ensure plastic deformation capability of the lateral force resisting system.

Gusset plate connections in CBFs are responsible for transferring the lateral loads from the braces to the beams and columns. Thus, it is critical for the gusset plates and their connections to be capable of transferring the internal forces without experiencing brittle failure states. Brittle failure modes such as weld or bolt fracture, block shear failure and net section fracture are considered to be the least desirable failure modes for gusset plate connections (Astaneh-Asl 1998). However, weld fracture, fracture of net section, and buckling of gusset plates have been reported in the aftermath of the past earthquakes, such as

the 1985 Mexico, the 1994 Northridge and the 1995 Kobe earthquakes (Astaneh-Asl et al. 1985, Astaneh-Asl et al. 1986a, 1994, 1995, 1998). Since ductile detailing of the connections is one of the keys to improve overall structural performance and to prevent significant strength and stiffness loss during an earthquake, design and detailing of the connections in ductile CBFs have been studied extensively, and rigorous detailing requirements were developed (Astaneh-Asl et al. 1998, Lehman et al. 2008, Yoo et al. 2008, Roeder et al. 2011). Even though different approaches were proposed for ductile connection detailing, the purpose of these studies was to allow more desirable ductile modes to govern, such as tensile yielding and global buckling of bracing members so as to tolerate large inelastic deformation demands imposed by severe ground motions. Hence, the current seismic design provisions (AISC 2010b) stipulates a design approach that considers the limit states based on the expected tensile and compressive capacities of the bracing members, as well as expected in-plane moments and out-of-plane rotational demands for the design of the gusset plates and their connections, in order to avoid brittle connection failures.

Inelastic dynamic response of CBFs is highly dependent on hysteretic behavior of the braces. During a ground shaking, brace members are subjected to tension and compression repeatedly. Typically, axially loaded steel members buckle when they reach the critical buckling load, which is usually less than their tension strength capacity. Owing to the induced second-order bending moment subsequent to global buckling, the compressive strength degrades substantially as the amplitude of excursion increases. Therefore, conventional steel bracing members exhibit an unsymmetrical inelastic cyclic response when a CBF is subjected to reversed-cyclic loading as in an earthquake ground motion. Typical axial force-deformation relationship of a tubular bracing is shown in Fig. 1.1.

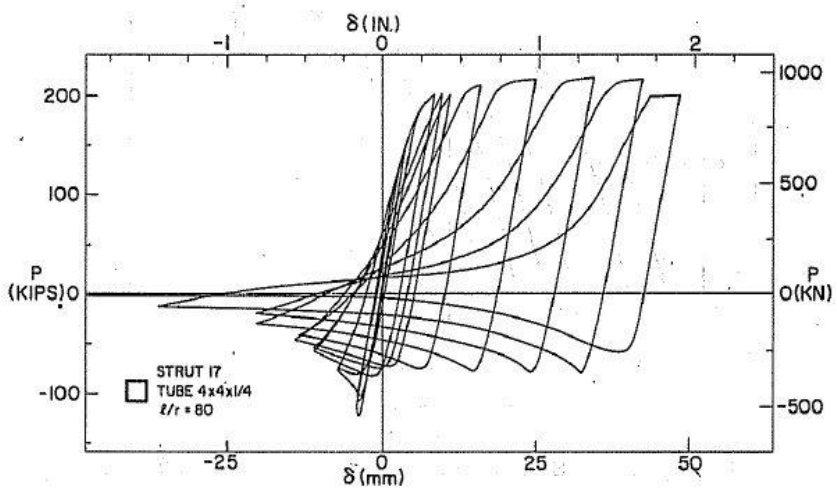

Figure 1.1. Typical hysteretic behavior of a tubular bracing (Popov and Black 1981)

Similar to beam-to-column connections in SMRFs, the ductility provided by steel bracing members in CBFs is the main source of seismic energy dissipation capability. Numerous studies have been conducted on the axially loaded steel members (column members) to reveal the inelastic cyclic behavior of bracings since the early 1970s up till today (Shibata et al 1973, Jain et al. 1978, Black et al. 1980, Popov and Black 1981, Astaneh-Asl et al. 1986b, Aslani et al. 1991, Walpole 1996, Tremblay 2002, Elchalakani et al. 2003, Shaback and Brown 2003, Broderick et al. 2005, Goggins et al. 2006, Han et al. 2007, Uriz and Mahin 2008, Tremblay et al. 2008, Fell et al. 2009). Several different structural shapes including I-shaped sections, pipes, double-angles, channels and hollow sections (circular or rectangular) have been tested with the purpose of assessing critical buckling load, ductility, boundary conditions, buckling shape, hysteretic and post-buckling behavior and fracture life of bracing members. Past studies indicated that the most influential parameter in determining the hysteretic behavior of bracings is the effective slenderness ratio (KL/r ratio) (Jain et al. 1978, Popov and Black 1981), even though there are other parameters that somehow affect the hysteresis loops such as section compactness (width-to-thickness

ratio) and cross-sectional shape. Note that inelastic cyclic behavior of a considerable number of different shapes has been experimentally investigated for decades, but today, the vast majority of the bracing members used in braced frame steel construction comprise cold-formed square or circular steel tubing mainly because of the significant advantages they offer to the industry in terms of labor and material cost. Therefore, considering their popularity, cold-formed tubular bracings require more attention than other structural shapes.

Past studies pointed out that initiation of fracture in a tubular bracing member is caused by the high strain concentration in the compression fibers of the cross-section at the mid-length, in which the plastic hinge formation occurs subsequent to global buckling. Influential parameters on fracture life of a bracing member have been examined by researchers (Gugerli 1982, Lee and Goel 1987, Tang and Goel 1988, Tremblay 2002, Fell et al. 2009) and empirical formulas, as well as FEM-based methods (Fell et al. 2006, Kanvinde and Deierlein 2007, Tirca and Chen 2014) were proposed for fracture prediction. Slenderness ratio, section compactness, cross-sectional shape, loading history were found to be the influential parameters on fracture life of steel bracings. Previous studies also indicated that regardless of the other key parameters, width-to-thickness (or diameter-to-thickness) ratio is the most influential parameter in determining the fracture life (Han et al. 2007, Tremblay et al 2008, Fell et al. 2009), since initiation of fracture in a tubular bracing is directly related to the local buckling-induced strain concentration at the plastic hinge location.

Besides the section compactness, fracture life of an axially-loaded steel member is substantially affected by the size of the bracing member tested (Tremblay et al. 2008), as well as the loading protocol used in the test program (Fell et al. 2009). Due to the limitation on test setups and stroke/loading capacity of actuators, the majority of the available test

results in the literature have been obtained from small-scale, small-size bracing members so far. In addition, the early studies on inelastic cyclic behavior of bracing members were often conducted using loading protocols consist of larger compression cycles (Aslani et al. 1991), which may result in overestimation of the fracture life. For instance, bracing members with the same size and slenderness ratio would withstand excursions with two times larger amplitudes when a compression-dominated loading protocols is adopted in lieu of a standard symmetrical loading protocols (Fell et al 2009). Hence, only a few recent, large-scale experimental studies on testing of conventional ductile CBFs and single cold-formed tubular bracing members are reviewed in detail herein.

4.1.1. The Full-Scale SCBF Tested at UCB (Uriz and Mahin, 2008)

Uriz and Mahin (2008) carried out an experimental study on two-story, one bay, chevron (inverted V-) type special concentrically braced frame in order to evaluate the inelastic behavior of a conventional ductile CBF. The significance of the study is that it is the first nearly full-scale SCBF test specimen with the brace, girder and column sizes close to those in actual CBFs. Most notably, similar to the impact of the 1994 Northridge earthquake, the unexpected failure modes observed in the test had a substantial impact on the industry, as well as the researchers.

The test specimen was designed and detailed in accordance with the design procedure and detailing requirements of AISC Seismic Design Provisions (AISC 1997). As shown in Fig. 1.2(a), the specimen was nearly full-scale with 9 ft tall story height and 20 ft span length. The braces were fabricated from cold-formed square hollow sections (HSS6x6x3/8), and wide flange sections were used for the columns and girders. The target drifts were

applied and monitored at the top floor loading beam (Fig. 1.2a). The roof displacement history adopted for the test consisted of six cycles at a roof drift corresponding to buckling deformation of the braces, four cycles at half the deformation corresponding to the design drift ratio, four cycles at the design drift, and two cycles at 1.5 times the design drift. The test results are given in Fig. 1.2(b) in terms of roof drift (%) and base shear force relationship. As shown in Fig. 1.3(b), the braces fractured during the first cycle at 1.35% overall drift ratio (ODR) when the lower story drift ratio (SDR) was around 2.80%. It is also reported that last two cycles at a roof drift ratio of around 2% were not completed due to fracture at the beam-column connections of the first story (Fig. 1.3c).

Based on the test results, observed deformation patterns and failure modes, the following can be discussed:

i. Local buckling-induced large strains at the filleted corners of the braces triggered the fracture initiation in the vicinity of the plastic hinge location when monitored roof drift and the first story drift ratios were 1.35% and 2.80%, respectively (Fig. 1.3a).
ii. Subsequent to global buckling of the first story braces, lateral stiffness of the first story deteriorated and beams and columns began to contribute lateral resistance significantly due to the frame action.
iii. Soon after fracture of the braces, substantial flexural demands were imposed to columns rapidly and led to fracture of the first story beam-column connection (Fig. 1.3c) as a results of having deep girders and shear tabs, as well as large gusset plate sizes at beam-column-gusset connections.
iv. Once global buckling of the braces occurred, the plastic deformations concentrated in the first story. Therefore, due to the formation of weak/soft story, the braces and

columns of the first story fracture while the damage in the second story was not substantial.

v. Overall performance of the tested SCBF was poor in comparison with the expected seismic demands in SCBFs (Uriz 2005, McCormick et al. 2007).

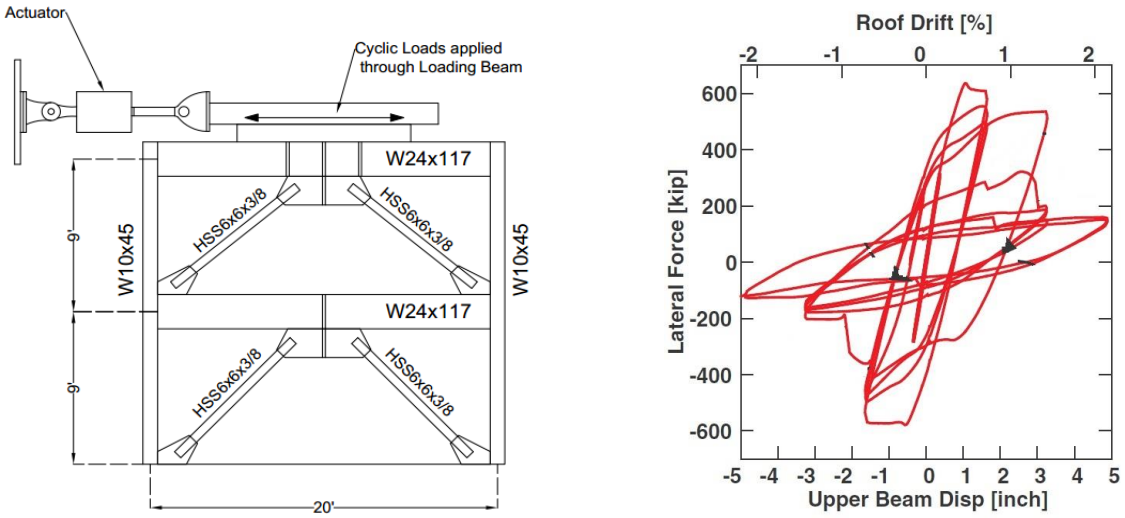

Figure 1.2. (a) Elevation view, and (b) Test results of the tested SCBF at UC Berkeley

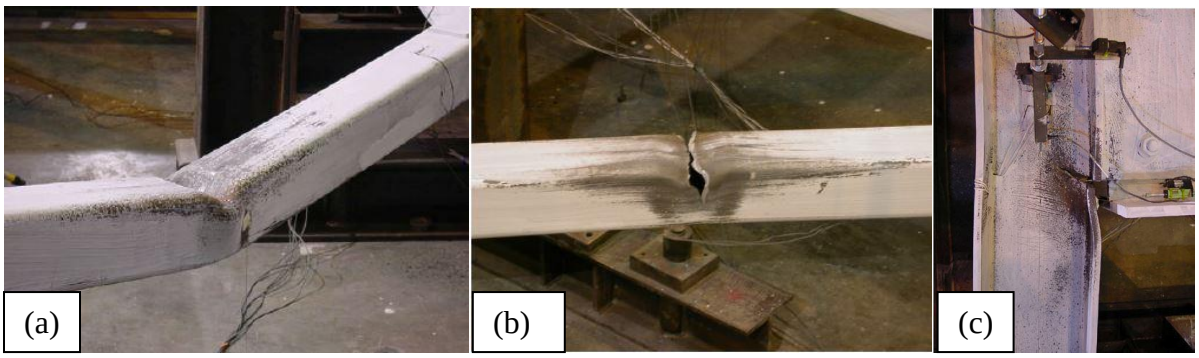

Figure 1.3. Deformations observed during the test (a) Local buckling of the brace (the 1st cycle at 2.80% SDR), (b) Fracture of the brace (the 1st cycle at 2.80% SDR), and (c) Fracture of the column (the 4st cycle at 2.80% SDR)

4.1.2. Inelastic Cyclic Testing of Large Size Steel Bracing Members (Tremblay et al. 2008)

Tremblay et al. (2008) conducted an extensive experimental program to examine the cyclic inelastic response of 34 large size single steel brace specimens including square

tubing, circular tubing, and W-shape bracing members. Unlike the past test programs, the length and size of the tested braces were very similar to the commonly used member sizes in braced steel frame construction. Furthermore, the boundary conditions of the steel brace specimens realistically reflected the actual boundary conditions of gusset plates in a CBF.

The total lengths of five cold-formed HSS specimens were adjusted to obtain slenderness ratios of around 40 and 60, which were within the range of common brace slenderness ratio in CBFs. The length of the specimens and the brace inclination with respect to the horizontal were adopted from the surveyed building applications. Test setup is equipped with a double acting actuator so as to represent the relative axial displacements of the braces in a mid-story of an actual CBF. The test specimens were subjected to cyclic quasi-static loading.

The preliminary results of the test program are presented in Fig. 1.4 in terms of story drift ratio (Δ/h_s) and normalized axial force (applied axial force divided by the yielding strength). It should be noted that the preliminary results included herein consist of three rectangular hollow sections (RHS) and two circular hollow sections (CHS). Each plot given in Fig. 1.4 indicates the tested brace section and the two influential parameters on fracture life and hysteretic response of bracings, which are slenderness ratio (KL/r) and width-to-thickness ratio (b/t or D/t). Based on the test results, the following observations can be made:

i. Neither square nor circular hollow sections were capable of resisting an axial deformation corresponding to an equivalent story drift ratio (Δ/h_s) of 2% without experiencing fracture.

ii. Regardless of slenderness ratio or cross-sectional shape, fracture life elongates as the width-to-thickness ratio decreases.

iii. With the same b/t ratio (or D/t), slender braces are likely to sustain longer than the relatively stockier braces.

iv. On the whole, the experimental study strongly indicated that the tested cold-formed hollow sections, either square or circular, are not capable of providing enough ductility capacity to CBFs to withstand subjection to severe ground motions.

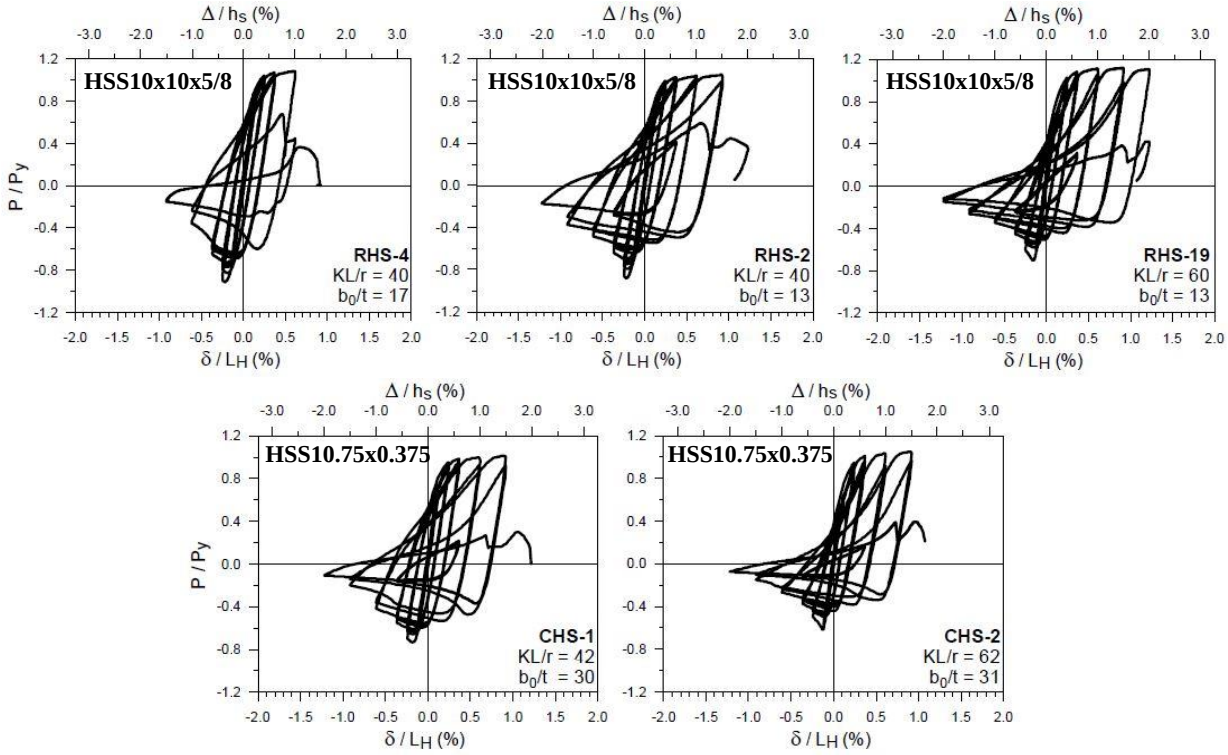

Figure 1.4. The preliminary test results on cold-formed tubular members

4.2. Literature on BRBs

The idea of restraining or controlling brace from buckling was first established with the simple concept of providing lateral support along the length of the axially-loaded members and remained the same since the early 1970s. Still, various details and configurations have been developed to improve BRB performance. Chronologically, BRB configurations can be divided into three major groups: (1) Panel BRBs, which are consist of a

steel plate encased with precast concrete panels with some unbonding material between them (Xie 2005); (2) Unbonded BRBs, which are composed of a steel core encased with mortar-infilled steel tube (Xie 2005); and (3) All-steel BRBs, which are conceptually the same with unbonded BRBs except that the buckling-restraining mechanisms in all-steel BRBs are made of steel components. Although panel BRBs are the first BRBs tested, currently, the industry and researchers turned their attention to unbonded and all-steel BRBs.

Conventional unbonded BRBs (hereafter called concrete-encased BRBs) was the first type of BRB that is introduced to the US for seismic applications (Clark et al. 1999, Uang et al. 2004). As shown in Fig. 1.5, typically, concrete-encased BRBs consist of:

i. A load-carrying system (yielding steel core) that is usually made of rectangular or cruciform shaped welded steel plates. Steel core yields in tension and compression under reversed cyclic loading to provide symmetrical axial load-deformation response, as illustrated in Fig. 1.5.

ii. An unbonding material. The function of the unbonding material between steel core and mortar is to minimize the shear force transfer due to the friction between the core and the encasing.

iii. A buckling restraining mechanism that is composed of a concrete or mortar-infilled steel tube. The buckling-restraining mechanism is responsible for preventing the steel core from buckling without contributing the load-bearing capacity.

Similar to concrete-encased BRBs, an all-steel BRB is composed of a yielding steel core as a load-bearing system coated with a low-friction material and a buckling restrainer. Buckling-restrainer in all-steel BRBs may consist of combination of several steel shapes, such as channels, Tee shapes, rectangular plates, square hollow sections, together with filler

plates and bolted or welded attachments. Fig. 1.6 illustrates the scheme of a common type of all-steel BRB configuration, which consists of a steel core plate with stoppers as load-bearing core sandwiched between two plates (or the alike) that are bolted or welded together along the length as buckling-restrainer, hereafter referred as Sandwiched Plate BRB (SP-BRB).

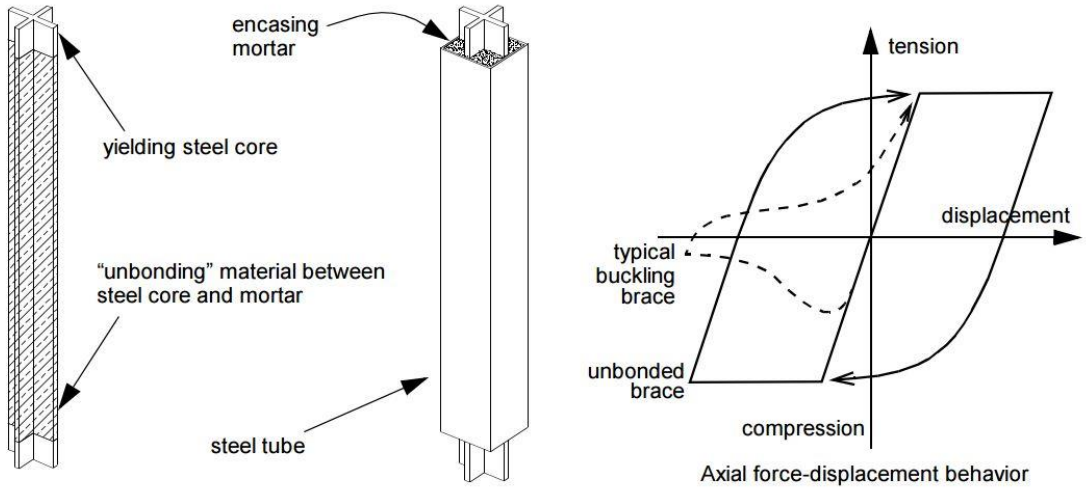

Figure 1.5. Scheme and hysteretic behavior of a typical concrete-encased BRB (Clark et al. 1999).

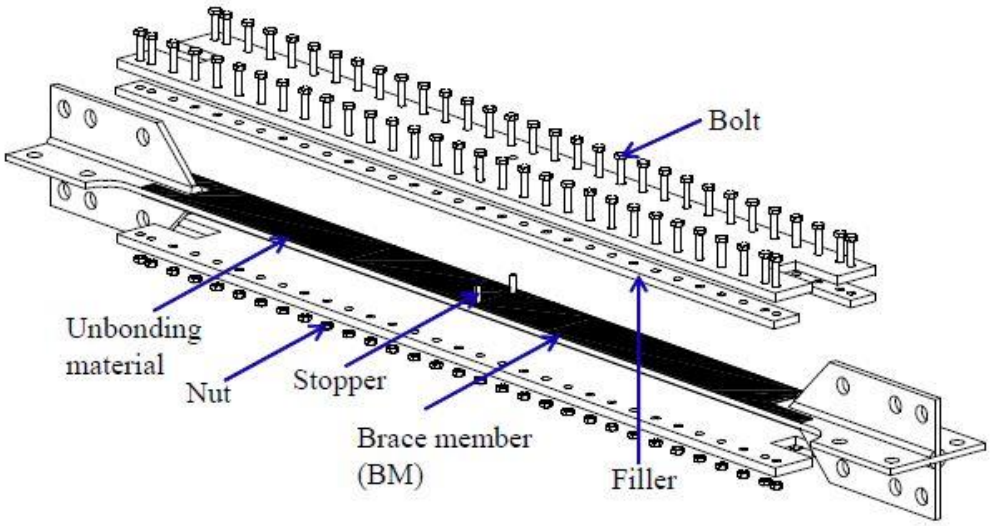

Figure 1.6. Scheme of a sandwiched plate all-steel buckling-restrained brace (Usami et al. 2011).

All-steel BRB configurations alternative to common SP-BRBs have generated considerable research interest. Thus, various all-steel BRB configurations have been recently developed with different attachments, buckling-restrainers and yielding core sections in order to investigate the optimum gap amplitude, adequacy of the stiffness of buckling-restrainer, the spacing of bolted or welded attachments and low-cycle fatigue behavior of the yielding core segment.

Due to the variety of the previously developed BRB models, the BRB studies summarized in the following sections are divided into groups based on their configurations and the objective of the studies.

4.2.1. Studies on Concrete-Encased BRBs

Despite their popularity among others, past tests on isolated concrete-encased BRBs and buckling-restrained braced frame (BRBF) specimens implied that, in most cases, the limit state is governed by connection failure due to out-of-plane deformation (Fig. 1.7) and weld cracking rather than core fracture (Uriz and Mahin 2008, Palmer et al. 2014). Moreover, even though isolated BRB specimens, when the failure state is controlled by core fracture, tend to attain large cumulative ductility (Black et al. 2002, Merritt et al. 2003), the peak drift demands reached by tested BRBF specimens have thus far been moderate at best (Uriz and Mahin 2008, Palmer et al. 2014, Khoo et al. 2016). Further, the inelastic cyclic response of isolated BRB specimens has been traditionally measured in terms of the strain demand on the load-bearing core based on the reduced core length, which can be as short as one quarter of the brace length (Tremblay et al. 2006), as opposed to the equivalent drift demand on structure. In other words, even when well-protected connections were employed to the test

setups, the inconsistency between the lengths to measure the strain and drift demands may lead to misinterpretation of the peak ductility obtained from testing of isolated BRB specimens.

Figure 1.7. Typical connection failure due to out-of-plane end rotation (Palmer et al. 2014)

Literature surveys on concrete-encased BRBs provided compelling evidence to the previously mentioned problem. One of the most recent studies on testing of large-scale BRBF specimens has been conducted by Palmer et al. (2014). Six BRB specimens with different connection types were included in the plane frame test program to overcome the undesired failure modes due to end rotations. It is, however, reported that all BRB specimens in the planar frame test failed at a drift angle of around 2.0% on account of the connection failures (either out-of-plane deformation of BRB or weld fracture in gusset plate) (Palmer et al. 2014). Their observations also pointed out that the significant demand on beams and columns imposed by the beam-column-gusset connections resulted in local flange buckling

and fracture in beams, as well as tearing of column webs through the flanges prior to BRB fracture (Palmer et al. 2014). Likewise, unexpected damages in beam-column-gusset connections have been commonly observed in a number of well-recognized test programs, in all of which the failure state is determined by out-of-plane deformation of the BRB connections. For instance, Uriz and Mahin (2008) carried out a total of three cyclic tests on near full-scale one-story one-bay BRBF specimens with two different bracing configurations. The experimental data showed that the frame with chevron type bracings attained 2.0% story drift angle while the other two specimens with diagonal bracings reached relatively larger drift demands, on the order of 2.6% (Uriz and Mahin 2008). Uriz and Mahin (2008) also observed cracking of welds at gusset and beam-to-column connections, column yielding and fracture initiation in the beam flange along with out-of-plane deformation of BRBs. Instead of adopting a standard quasi-static cyclic loading protocol, a full-scale two-story one-bay braced frame with diagonal bracing configuration that incorporates double-core concrete-encased BRBs tested by Khoo et al. (2016) under bi-directional pseudo-dynamic loading protocol. The peak drift demands on the stories varied from 1.0% to 3.0% during the test (Khoo et al. 2016), which were consistent with the results of the previous test programs. Besides the poor-to-moderate global performance of the frame, cracking in welded connections, local buckling and yielding of columns took place. In an effort to avoid the potential damages concentrated on beam-column-gusset connections, Palmer et al. (2016) proposed a highly labor-intensive enhancement strategy for the connections utilizing continuity and extended doubler plates, which was much alike to the stringent requirements introduced for the moment frames in the aftermath of the 1994 Northridge earthquake.

4.2.2. Studies on Testing and FEA of Sandwiched Plate BRBs (SP-BRBs)

Numerous investigations have been made on stiffness and strength of buckling restraining mechanisms since the late 1980s (Watanabe et al. 1988). One of the recent experimental studies on SP-BRBs were conducted on 12 small-scale all-steel BRB specimens in order to investigate effect of different welded or bolted attachments of buckling restraining mechanisms on the performance of core segments with various aspect ratios by Eryasar and Topkaya (2010). The core segment wrapped with a temporary low-friction greasy polyethylene film. Their test results showed that stable hysteretic behavior can be achieved with closely spaced attachments, which do not allow buckling restrainer (BR) to deform locally. It is important to note that as in many other studies alike neither the potential stability issues of utilizing a temporary coating nor the applicability of the unbonding material to an actual steel construction was discussed. Tremblay et al. (2006) carried out an experimental study on both concrete-encased BRBs with reduced core length and SP-BRBs using quasi-static and dynamic loading protocols to assess the performance of buckling-restrainer with emphasis on fracture life and strain demands on the core segment. Their conclusion on all-steel BRBs suggested that a higher performance can be obtained by keeping the gap between the core and the BR as small as possible, using stiff BR components and providing a low-friction contact between the core and the BR. It should, however, be noted that an unbonding material was not utilized for the test of SP-BRBs. The study confirmed that the local buckling tendency of the steel core plate is extremely sensitive to the gap amplitude, as well as the impact of friction between the core segment and the BR. The paper does not provide information on how to determine the size of the gap and BR stiffness. In other words, the interrelationship among the gap, BR stiffness and contact friction coefficient is not addressed

in order to achieve an optimal all-steel BRB performance. In addition, the effect of b/c ratio was not addressed and a b/t ratio of 10 was kept for all specimens.

Several FEM-based numerical studies were conducted to enhance the hysteretic behavior of the current SP-BRBs and to develop new BRB configurations. A recent FEM-based parametric study performed by Hoveidae and Rafezy (2012) to address that the gap amplitude would not affect hysteretic behavior significantly if the buckling restrainer has enough strength and rigidity. Also, the authors proposed an overall constraint ratio, which is the modified version of the one proposed by Watanabe et al. (1988) for concrete-encased BRBs. Furthermore, the steel plate with b/t equal to 10 was proven to be vulnerable to low-cycle fatigue induced fracture, but the numerical simulation cannot consider such fracture. Thus, it is unclear whether the conclusion remains valid if fracture life was included. Chou and Chen (2012) numerically and experimentally investigated the effect of BRB length and the cross-sectional area on buckling load variation in addition to the effect of restraining member size and number of bolts. They concluded that a small gap substituting unbonded material between the core plate and restraining members does not affect the cyclic behavior of the studied BRB. Note that a constant b/t ratio of 6.8 was used for all specimens. It is not clear whether the conclusion can be extended to a larger b/t ratio, such as b/t ratio of 10 as in the aforementioned references. Genna and Gelfi (2012) experimentally and numerically examined the parameters that effect the magnitude of the contact forces between the core and the bolted BR. Six specimens have been tested: in three of them the steel core has a 50x5 mm (b/t=10) cross section, and in the remaining three the core has a 50x7 mm (b/t≈7) cross section. For each core thickness, three different gap amplitudes considered: 0.5 mm, 1 mm and 2 mm. Their conclusion was that the tendency of the lateral thrust to increase for an

increasing gap, and to be higher for the smaller thickness, based on the results of the experimental and numerical studies. However, the overall length of the specimens were 900 mm (~35 in), which would affect the number of waves along the core length, and more importantly, the numerical results presented in the paper were based on the 2D FE models, which are not capable of representing three dimensional stress and strain effects.

Fatigue life problems and the effect of yield strength of core segments in SP-BRBs were also addressed by researchers. For instance, Usami et al. (2011) carried out an experimental study to assess fatigue life of SP-BRBs. A total of twelve tests conducted and the fatigue curves of the BRBs were evaluated. All the specimens had 1 mm gap in the through thickness while two different gap amplitudes, 2 mm and 6 mm, were adopted in the through width direction. Two different loading protocols with constant and increasing amplitudes were imposed. Their major conclusion was that any kind of heat-treatment of load-carrying system, such as conventional welded stoppers, would cause premature cracking of the core segment during the cycles. Moreover, the comparison of fatigue curves between the full-scale BRB tests and the material tests shows that the number of cycles to reach fatigue life (N_f) in BRB tests are consistently smaller than those in the material tests at the same strain range. The effect of low-yield strength of the core plate on SP-BRB performance was demonstrated in the study of Ma et al. (2012a). Even though the BR configuration used in the study was extremely complicated, the cumulative and maximum ductilities were much larger than the acceptance criteria stipulated in the AISC Recommended Provisions (AISC 2010b). Their results based on two test specimens indicated that the SP-BRBs with low-yield strength core plates exhibited a better energy dissipation capacity compared to the common steel types.

4.2.3. Studies on All-Steel BRBs Alternative to SP-BRBs

A considerable number of approaches alternative to the common SP-BRBs have generated significant research interest recently. Tabatabaei et al. (2014) studied an all-steel reduced length BRB model, which was lighter and replaceable. A polyethylene-based coating material together with a ceramic painting adopted for debonding mechanism. The focus on the experimental portion of the study was to compare the cyclic performance of two different BR configurations. In addition to the experimental study, a set of non-linear finite element simulations were carried out to investigate the impact of the different arrangements on the hysteretic behavior. Their results showed that the replaceable reduced length BRBs have a greater energy dissipation capacity compared to full-length BRBs.

Instead of using steel plates as load-bearing core in the Sandwiched Plate BRB (SP-BRB), Zhao et al. (2011) studied another type of BRB with cruciform-shaped four angles (back-to-back) as load-bearing core encased in a square tube made of two large-sized angles welded together as buckling restrainer. The gap between the core and buckling restrainer had to be large enough to avoid the friction between the core and buckling restrainer. The extended angle legs in the core behave as unstiffened elements. As a result, the steel core suffered local and global buckling, forcing the restrainer to bend. Furthermore, such restrained buckling imposed significant rotational demand on brace ends. It was concluded that increasing the stiffness ratio of the restrainer over the steel core might not be cost-effective to prevent global buckling, and smaller gap would alleviate the rotational demand on the brace ends. It was also reported that reducing the core width-to-thickness ratio is more effective than reducing the gap for ensuring core local stability and stable cyclic performance. The studies also concluded that the ratio between the buckling amplitude and

buckling half wave length is the key parameter governing the cyclic performance of this type of BRB. It is of significance for Zhao et al. (2011, 2012, 2014) to present the impact of gap amplitude on a BRB on a much larger scale than that demonstrated in SP-BRB. The major concern with those studies is that a systematic study of the relationship between gap, friction, and restrainer-core stiffness ratio does not exist. It was concluded that the smaller gap would be beneficial, but failed to discuss the possible range of the gap. It is apparent that the significant gaps used in the experiments caused global buckling, which makes one wonder whether the system can still be called buckling-restrained brace. If the gap becomes infinitely small, there will be friction force between the core and restrainer, which was not addressed in the studies. Furthermore, the system seems to be labor-extensive due to its unnecessarily complex design.

Ju et al. (2009) conducted a research on a new BRB model with unconstrained length and performed component tests of seven BRBs to evaluate effect of the thickness of the external tube and the length of the unrestrained part of the core by keeping the gap amplitude constant. Based on the test results, the authors have modified the formula known as Watanabe's criteria (Watanabe et al. 1988), which relates elastic critical buckling load of the buckling-restraining mechanism to yielding strength of the core segment. The authors also concluded that the specimen with the thickest external tube and 300 mm unconstrained length behaved stably. However, either a critical unconstrained length ratio in terms of a fraction of the total length or an optimal outer tube thickness relative to the brace member is not suggested. In addition, no information on the surface friction between the brace member and the outer tube is provided. Also, the high cost of the gusset connections with W-shape braces are not considered in the studied BRB model.

Two full-scale BRB specimens and one full-scale subassemblage were tested using cruciform shaped plates as core and square tubing as buckling-restrainer under uniaxial quasi-static cyclic loading by Ma et al. (2009). Similar to previous studies on fatigue life (Usami et al. 2011), the study concluded that there should be no additional weld on the yielding part of the core except the necessary connections between the plates; otherwise the low cycle fatigue property of the brace would decrease. Ma et al. (2012b) also numerically examined the influence of initial eccentricity, the ratio of the width to the thickness of the core and the ratio of the gap to the width of the core segment of BRB models that consist of a core plate and a square tube and a curve-fitted equation for the BR design of the BRB was recommended based on the simulation results.

CHAPTER II

DEVELOPMENT OF TUBE-IN-TUBE BUCKLING CONTROLLED BRACES FOR SEISMIC DESIGN OF STEEL BRACED FRAMES

1. Introduction

Concentrically braced frames (CBFs) have become one of the most commonly used lateral force resisting systems in seismic regions after the 1994 Northridge Earthquake due to the unexpected damages observed in moment frames (MFs). Braces, which are the major seismic energy dissipating components in a CBF, are prone to local buckling-induced premature fracture. As such, seismic performance of the bracing members, as well as ductile CBFs may be questionable in terms of energy dissipation capability. Furthermore, unstable and unsymmetrical cyclic behavior of conventional braces impose large demands on the brace-intersected girders and beam-to-column connections in CBFs. One key approach to overcome possibility of premature brace fracture, as well as to acquire stable cyclic response and significant energy absorption capability is to control global and local buckling of braces. In this chapter, a new buckling-controlled brace (BCB) concept that consolidates the common design practice for CBFs with the idea of controlling buckling in a simple and cost effective way is presented.

Initiation of fracture in a tubular bracing member is caused by the high strain concentration in the compression fibers of the cross-section at the mid-length, where the plastic hinge formation occurs subsequent to global buckling of a conventional brace. Recent studies on testing of large-scale hollow structural shapes (HSS) under reversed cyclic loading consistently showed that fracture initiation of square or round cold-formed steel tubular

bracings likely to take place at around design story drift level soon after local buckling (Elchalakani et al. 2003, Uriz and Mahin 2008, Tremblay et al. 2008, Fell et al. 2009). In other words, tubular bracing members, which offer significant advantages to the industry in terms of labor and material cost, may not be ductile enough to undergo as large deformations as anticipated by the seismic provisions (AISC 2010b).

A further concern that arises from the conventional bracing members incorporated in CBFs is that the unstable nature of their hysteretic behavior owing to the difference between yielding strength in tension and buckling/post-buckling strength in compression, which may impose notable unbalanced forces on the structural members that are designed to remain elastic when the structure subjected to a severe earthquake ground motion. Due to the large demands imposed by the unbalanced brace forces, the depth and the weight of the brace-intersected girders would increase substantially. Besides its economic and architectural flaws, such design with deep girders would amplify the demands on columns significantly even under minor rotational demands at beam-to-column connections and therefore may lead to fracture at column flanges (Uriz and Mahin 2008).

As seismic fuses, various types of buckling-restrained braces (BRBs) with different configurations have been developed and tested in the past few decades. Currently, the most common BRBs are concrete-encased BRBs, even though all-steel BRBs have been steadily growing in popularity. Despite their popularity, concrete-encased BRBs are often costly, heavy and difficult to inspect. All-steel type BRBs, on the other hand, are lighter and offer the advantage of developing different core and buckling-restrainer configurations. Unfortunately, in most cases, the idea of restraining column members from buckling, if possible, resulted in extremely complex BRB configurations, even though the concept of

BRBs is simple. Typically, all-steel BRBs consist of combination of steel plates, channels or square tubes and filler plates with bolted or welded attachments. Thus, there remains a need for simple, practical and cost-effective design for all-steel BRBs to attract the industry more. Such improvement can be achieved by:

(a) Reducing the higher labor and fabrication cost of the current BRBFs.

(b) Avoiding the unnecessarily complicated cross-sections and connections that are typically used in the current all-steel BRB configurations.

(c) Enhancing fracture life of the braces and overall seismic performance of steel braced frames without altering the current habits in the design practice.

In order to develop an effective substitute for conventional braces with little or no additional cost, the most commonly used structural shapes in the practice have been used in the present study. As shown in Figure 2.1, the Tube-in-Tube BCB consist of a main brace, which is responsible for lateral resistance to the seismic forces and an outer tube that controls the global and local buckling of the main brace by providing a continuous lateral support along its length. Note that the gap between the tubes is to allow the inside tube to slide freely so that the outer tube does not contribute to the axial load-carrying system. This system also enables HSS to be utilized, which are widely available in the market and help avoid labor-intensive connections.

The purpose of this study is to examine the efficiency of the Tube-in-Tube BCBs by means of testing and non-linear finite element simulations. Most notably, unlike past studies, our study aims to respond the following questions clearly and quantitatively:

(1) What are the most influential parameters for buckling control?

(2) How do the key parameters affect the cyclic behavior individually?

(3) How do the key parameters interact with each other?

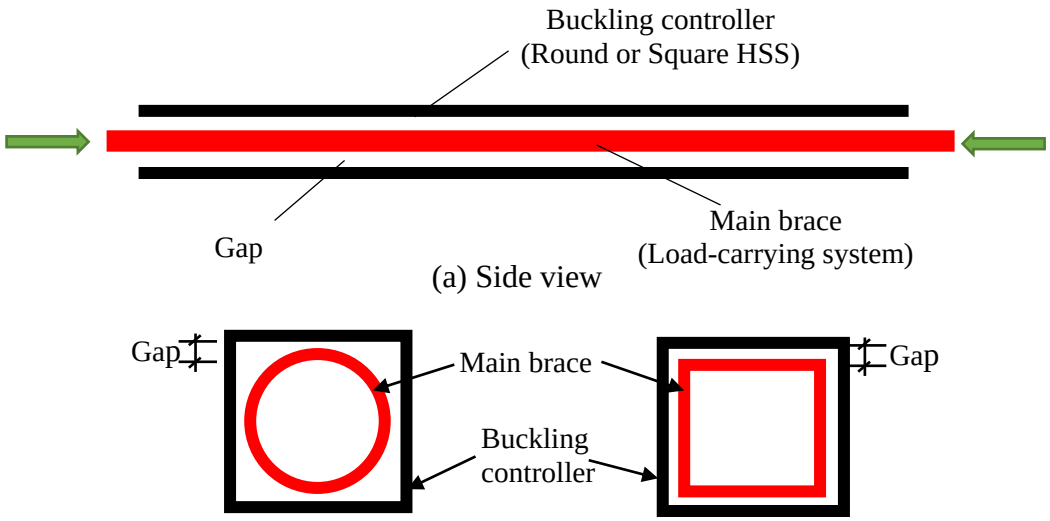

Figure 2.1. Scheme of Tube-in-Tube BCBs

2. Experimental Study

A set of small-scale Tube-in-Tube type all-steel BCB (TinT-BCB) specimens with different parameters have been tested at structural laboratory of Iowa State University under reversed cyclic loading to investigate hysteretic behavior of the developed BCBs. The primary objective of the experimental study is to evaluate the influential parameters that might have substantial impact on the hysteretic stability and the fracture life. In addition the key parameters and the interaction between them, significance of the connection design is also investigated through the experimental study.

Past studies showed that together with connection design there are essentially three critical parameters that affect the cyclic behavior of the BRBs (Tremblay et al. 2006, Zhao et al. 2011, Genna and Gelfi 2012, Hoveidae and Rafezy 2012). In addition to the uncertainties,

such as initial imperfection and the actual yield stress of the steel, the influential parameters can be summarized as follows:

(1) The initial gap between the main brace and the buckling controller (BC).

(2) The stiffness of the buckling controller.

(3) The friction between the main brace and the buckling controller surfaces.

(4) Connection design.

Table 2.1 summarizes the main brace and outer tube sections, the gap amplitude, the outer tube thickness and gusset plate design of the tested specimens. As can be seen from Table 2.1, in order to characterize the impact of the selected parameters, as well as the connection design, the same main brace size was employed for all specimens. The main brace section was selected considering the available loading capacity of the test equipment, as well as the slenderness ratio and D/t ratio (diameter to wall thickness ratio). It should be noted that experimental portion of the study does not cover the effect of the coefficient of friction between the two tubes. Even though utilizing an un-bonding low-friction coating has become conventional for both concrete-encased and all-steel BRBs, the stability of the commonly used coatings (e.g. grease or polyethylene-based coatings) and their applications in a real structure remains unclear. Thus, the impact of the coefficient of friction will be discussed thoroughly in the numerical portion of the study.

Table 2.1. Section properties of the specimens.

Test Name	Main Brace	Outer Tube	Gusset Plate Reinforcement	Gap* (in)	BC Thickness** (in)
TinT#1	HSS 1.900x0.125	HSS 2 ½ x2 ½ x 1/8	N	0.175	0.125
TinT#2		HSS 2 ½ x2 ½ x 1/8	Y	0.175	0.125
TinT#3		HSS 2 ½ x2 ½ x 1/4	Y	0.0625	0.250

* Based on nominal wall thickness, **Nominal wall thickness of the outer tube, N: NO, Y: YES.

Each specimen has its own characteristics to reveal how the design parameters would affect hysteretic response of the developed BCBs:

- Specimen TinT#1 is specifically designed to emphasize the significance of proper connection design and its potential effects on the overall cyclic response. For this purpose, the gusset plates has been designed in accordance with the requirements for conventional ductile braced frames. Besides, TinT#1 has a relatively large gap amplitude and moderate buckling-controller (BC) stiffness, which cannot be regarded as the ideal case, especially for controlling local buckling of the load-bearing tube. Thus, TinT#1 can be considered as a control group for the other two specimens.
- Specimen TinT#2 is designed to be identical with the first specimen in terms of the gap amplitude and the BC stiffness while the gusset plates are reinforced with vertical stiffener plates to minimize end rotations.
- Specimen TinT#3 is designed to represent virtually the ideal case (with small gap and stiff outer tube) in order to indicate the sensitivity of the controlling design parameters. Therefore, the thickness of the outer tube is increased compared to the first two specimens and the gap amplitude is adjusted to a small but practical value, which takes the required tolerances in an actual construction into consideration.

2.1. Design and Fabrication of the Tested TinT-BCB Specimens

TinT-BCB specimens were shop fabricated using round and square hollow sections with gusset assemblies at their ends. The total lengths of the specimens were determined based on the dimensions of the test setup. Side and section views of the first specimen (TinT#1) are shown in Fig. 2.2(a). The first test specimen consisted of a round

HSS1.900x0.125, eight 6”x1/2”x3/16” net section reinforcing plates, a square HSS2 ½ x 2 ½ x 1/8 section and two 3/8” thick gusset plates. The total length of the main brace, the outer tube and the entire assembly were 42”, 37.25” and 50”, respectively. The locations of the reinforcing plates were determined based on the geometry of the cross section. The nominal gap between the two tubes was 0.175” (Fig. 2.2a).

Design of TinT#2 and TinT#3 were identical to each other except for their outer tube sizes. Specimen TinT#2 was composed of a circular HSS1.900x0.125, eight 4½”x1/2”x1/8” net section reinforcing plates, a square HSS 2 ½ x2 ½ x 1/8 and two gusset assemblies. The main brace was encased with a square HSS 2 ½ x2 ½ x ¼ outer tube in Specimen TinT#3 while the design of the gusset assemblies and the main brace size of the specimen were identical to those of TinT#2. The total length of the main brace, the outer tube and the entire assembly were 42”, 37.25” and 51.50”, respectively, for both TinT#2 and TinT#3. Shop drawings of TinT#2 and TinT#3 are given in Fig. 2.2(b) and (c).

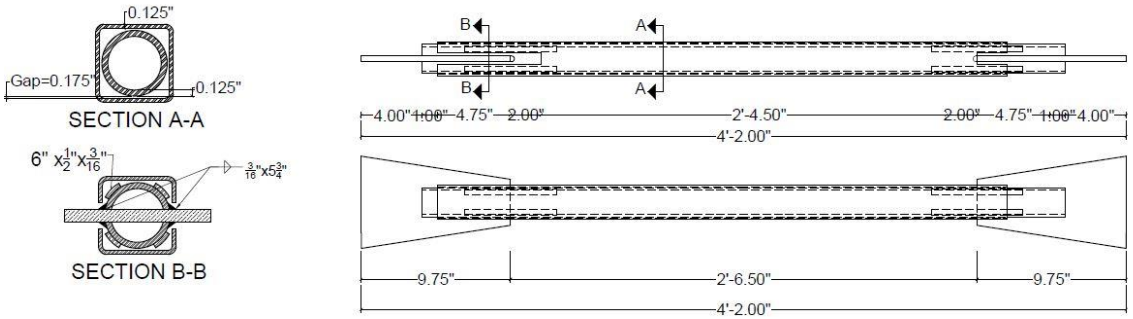

(a) TinT#1

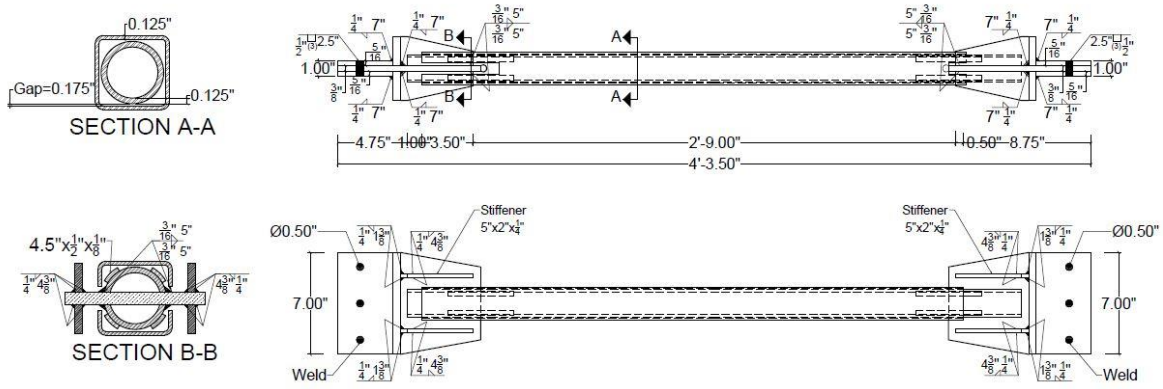

(b) TinT#2

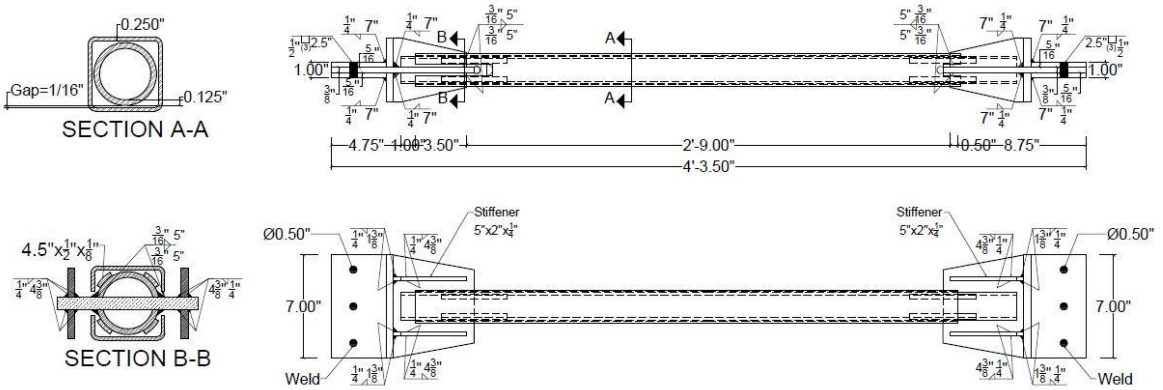

(c) TinT#3

Figure 2.2. Shop drawings of TinT-BCB specimens

Both ends of the main brace is slotted for welded gusset plate connections and two holes with a radius of 3/16" were drilled at the end of each slotted length. The slotted portion of the main brace (Fig. 2.2a and 2.2b) was fillet welded to the 3/8" thick gusset plates with 3/16" thick, 5" long welds. There was a 0.5" distance between the brace end and the vertical supporting plate. The 4.5" long net section reinforcing plates are connected to the main brace

with two 1/8” thick, 4.5” long fillet welds. Each gusset assembly consisted of a 3/8” thick gusset plate, four ¼” thick stiffeners, two horizontal supporting plates and two vertical supporting plates. Fig. 2.3(a) illustrates the details of the gusset assemblies. All the connections between the plates were either fillet or plug welded connections. Each gusset plate was connected to two horizontal supporting plates with three plug welds. Three holes with a radius of 1/4” were drilled from the 3/8” thick gusset plates, as well as the horizontal supporting plates (Fig. 2.3a). The three plug welds were 0.5” in diameter. 0.5” thick vertical supporting plates are fillet welded to the horizontal supporting plate from one side and fillet welded to the gusset plate on the other side. The welding details of the stiffeners are given in Fig. 2.3(a). Each stiffener is fillet welded to the vertical supporting plate, as well as the gusset plate. A right triangle with 3/8” side length are cut from the sharp edge of the ¼” thick stiffeners to allow continuous welding between the gusset plates and the vertical supporting plates. As shown in Fig. 2.3(a), a ¼” (i.e. the thickness of the fillet weld) distance between the end of the fillet welds and the edge of the triangle was left so as not to damage the edge of the stiffener plates (AISC, 2011).

Fig. 2.3(b) demonstrates the scheme of a typical chevron type TinT-BCB frame with stiffeners. In order to provide near-fixed end conditions, stiffeners are welded to the gusset plates and beam/column flanges. Stiffener sizes can be selected to provide the same rotational constraint against in-plane and out-of-plane end rotations. It is noteworthy that dimensions of gusset plates in BCBFs are reduced substantially due to absence of the clearance between the assumed fold line and brace end, since end rotations are virtually fixed. Therefore, the reduction in gusset plate cost would compensate for the additional cost

of employing stiffeners. Still, BCBF arrangements without gusset plate reinforcement might be an effective option in some cases, which is discussed in the latter sections of this chapter.

Gusset assemblies of TinT#2 and TinT#3 were designed and detailed to represent the actual boundary conditions of beam-column-gusset connection in a TinT-BCBF. Thus, vertical and horizontal supporting plates shown in Fig. 2.3(a), were incorporated to represent beam/column flanges in an actual BCBF. Furthermore, the horizontal supporting plates were utilized to increase the thickness of the gusset assembly that is attached to the grips of the test equipment with the purpose of minimizing the possibility of uneven stress distribution, as well as the relative movement around the gripped area.

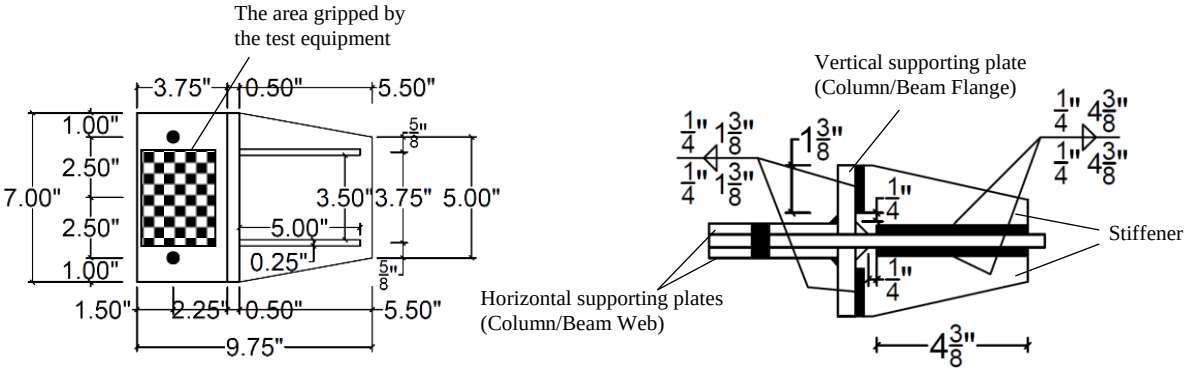

(a) Gusset assembly

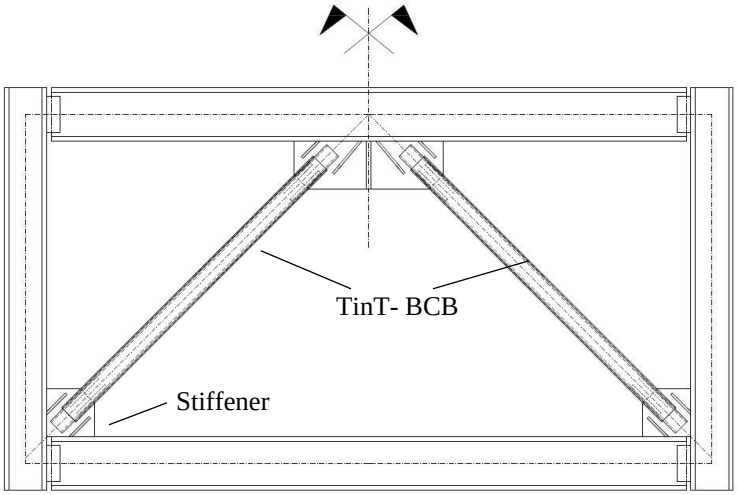

(b) Configuration of a TinT-BCB frame with stiffeners

Figure 2.3. Illustration of a TinT Frame and details of gusset assembly

The specified material properties for all specimens are given in Table 2.2. The main brace and the outer tube (BC) were made of ASTM A500 Gr.B type of steel with nominal yield stresses of 42 ksi and 46 ksi, respectively. Gusset plates, net section reinforcing plates and stiffeners to reinforce the gusset plates were cut from ASTM A36 type of steel plates.

Table 2.2. Specified Material Properties

Member	Type of Steel	F_y (ksi)	F_u (ksi)
Square HSS	ASTM A500 Gr. B	46	58
Round HSS	ASTM A500 Gr. B	42	58
Gusset Plate	ASTM A36	36	58
Stiffener	ASTM A36	36	58
Net Section Reinforcing Plate	ASTM A36	36	58

Coupon tests were carried out to determine the actual material properties of the main braces, which were expected experience plastic deformations. The dimensions of the coupon specimens and the loading rate adopted for testing were determined according to ASTM E8 (2015). The measured yield ($F_{y,meas}$), ultimate ($F_{u,meas}$) stresses and the strain value at the fracture obtained from the coupon test were around 55 ksi, 83 ksi and 29%, respectively, for the main brace of TinT#1 specimen. The main braces of TinT#2 of TinT#3 specimens were cut from the same piece. Therefore, the coupon test results were applicable to both TinT#2 and TinT#3 specimens. Two identical coupon specimens were cut from the main brace and tested. Based on 0.2% offset assumption, the measured yield ($F_{y,meas}$) stresses were found to be 56 ksi and 55 ksi for the first and second coupon specimens, respectively. The measured ultimate ($F_{u,meas}$) stresses were around 64.5 ksi and 63.5 ksi for the first and second coupon specimens, respectively. The average of the expected material strength factors, R_y and R_t

were 1.32 and 1.10, respectively. The strain values at the fracture were about 30% and 25.6%. The details of the coupon test results are given in Appendix.

2.2. Test Setup and Instrumentation

TinT-BCB specimens were subjected to displacement-control step-wise incremental cyclic loading. The tests have been performed using a MTS 647 Side-Loading Hydraulic Wedge Grips, which has the maximum loading capacity of 110 kips both in tension and compression. Lower end of the specimens were fixed. The displacement-type loading was applied from the top grip (Fig. 2.4). Instrumentation was installed for each test to measure strains, applied loads and displacements. As an attempt to measure the strain demands in the load-carrying system for the first time in the literature, a total of eighteen, six and four post-yield strain gauges have been mounted on TinT#1, TinT#2 and TinT#3 specimens, respectively, to monitor strains in axial and radial directions. The test setup and data acquisition system are given in Fig. 2.4.

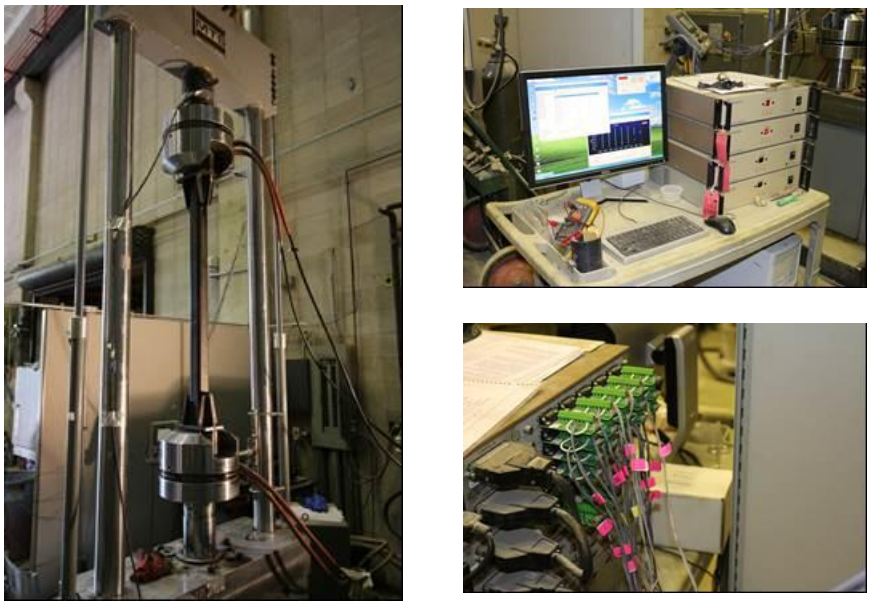

Figure 2.4. Test setup and data acquisition system

2.3. Loading protocol

A modified version of the loading protocol given in AISC Seismic Provisions (2010) was adopted for the tests. AISC defines a quasi-static cyclic loading protocol for qualification of BRB brace test specimens in terms of the deformation quantities corresponding to first significant yielding (Δ_{by}) and the design story drift (Δ_{bm}). The US loading protocol suggests two cycles at Δ_{by}, $0.5\Delta_{bm}$, Δ_{bm}, $1.5\Delta_{bm}$ and $2\Delta_{bm}$ deformation levels. Since BRBs are treated as hysteretic dampers, AISC requires a number of additional cycles for brace test specimens at $1.5\Delta_{bm}$ to ensure that cumulative inelastic deformation of the specimen is larger than 200 times the yield deformation. Note that according to AISC brace specimen testing protocol, the design story drift cannot be taken as less than 0.01 times story height.

In this study, the design story drift was assumed to be 2% of story height for all specimens. Axial displacements were converted to equivalent story drift ratios (interstory drift angle) by assuming a brace inclination of 45 degrees with respect to the centerline of the girder. Eq. 2.1 is derived based on the kinematic relationship given in Fig. 2.5. Even though the given relationship between the drift angle and the axial displacement is approximate and does not take the uncertainties into account, such as flexural deformation of girders, it was essential to provide a link between the global seismic demand on the braced frames and the brace capacities (Fell et al. 2009). Since story drift ratio (SDR) has been traditionally considered as the major index to measure seismic demands, the axial deformations were related to the overall response in terms of story drift ratio for the sake of the discussion.

$$\theta = \frac{\Delta}{h} = \frac{\delta / \cos\alpha}{L_b \sin\alpha} \qquad \text{(Eq. 2.1)}$$

Where;

θ: Interstory drift angle (Story drift ratio).

δ: Axial displacement corresponding to a drift angle.

L_b: Length of the main brace.

α: Angle between the centerlines of the brace and the girder.

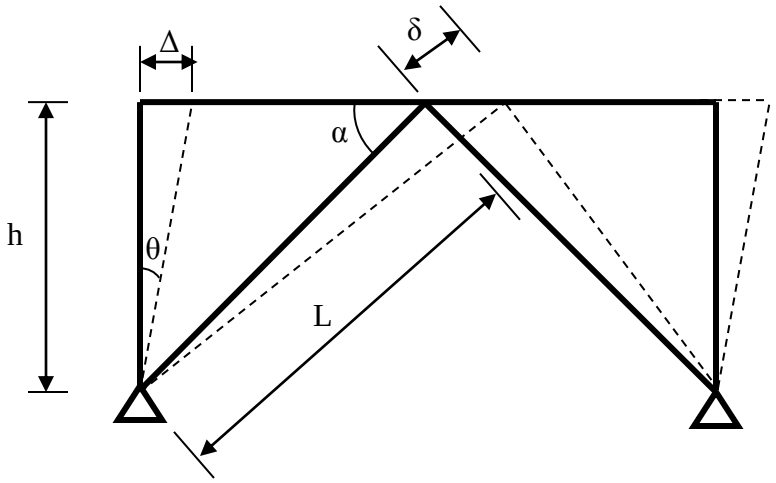

Figure 2.5. Illustration of kinematic relationship between drift angle and axial displacement

A slightly modified version of the loading protocol stipulated in AISC Seismic Provisions (2010) was adopted for the first test (TinT#1). The loading sequence used in the first test and the applied axial displacements at each cycle are given in Figure 2.6 and Table 2.3. Note that the displacements given in Fig. 2.6 were determined based on the minimum specified material properties. Two cycles were applied to produce 0.5 times the yield deformation ($0.5\Delta_{by}$), the yield deformation (Δ_{by}), 1.5 times the yield deformation ($1.5\Delta_{by}$) and brace deformations corresponding to 0.5 times the design story drift ($0.5\Delta_{bm}$) and the design story drift (Δ_{bm}). The test was terminated after the cycles at Δ_{bm}. Thus, the dashed lines in Fig. 2.6 represents the incomplete cycles due to fracture initiation.

Table 2.3. Loading sequence used in the testing of TinT#1.

Cycle	δ (in)	Story Drift Ratio (%)
2@ $0.5\Delta_{by}$	±0.0304	0.14
2@ Δ_{by}	±0.0608	0.28
2@ $1.5\Delta_{by}$	±0.0912	0.42
2@ $0.5\Delta_{bm}$	±0.2200	1.00
2@ $1.0\Delta_{bm}$	±0.4400	2.00
2@ $1.5\Delta_{bm}$	±0.6600	3.00
2@ $2.0\Delta_{bm}$	±0.8800	4.00

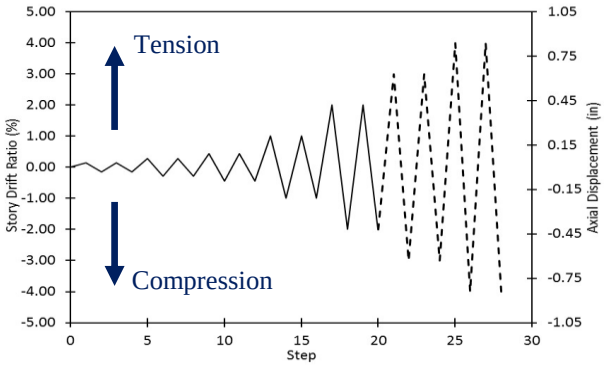

Figure 2.6. Loading protocol of TinT#1.

In the second and third tests (TinT#2 and TinT#3), a number of elastic and inelastic cycles added to the US protocol (AISC 2010b). Fig. 2.7(a) and Table 2.4 present number of cycles at each deformation level, applied axial displacements and the story drift ratios corresponding to each axial displacement. The axial displacements given in Table 2.4 were determined based on the coupon test results. First, two cycles were applied to produce 0.5 times the yield deformation ($0.5\Delta_{by}$), the yield deformation (Δ_{by}) and 1.5 times the yield deformation ($1.5\Delta_{by}$). Then, the amplitude of the applied axial displacements were increased gradually with a constant increment of 0.5% story drift ratio until reaching a story drift ratio of 4%.

Table 2.4. Loading sequence used in the testing of TinT#2 and TinT#3

Cycle	δ (in)	Story Drift Ratio (%)
2@ $0.5\Delta_{bv}$	±0.021	0.10
2@ Δ_{by}	±0.062	0.30
2@ $1.5\Delta_{by}$	±0.093	0.44
2@ $0.5\Delta_{bm}$	±0.210	1.00
2@ $0.75\Delta_{bm}$	±0.315	1.50
2@ $1.0\Delta_{bm}$	±0.420	2.00
2@ $1.25\Delta_{bm}$	±0.525	2.50
2@ $1.5\Delta_{bm}$	±0.630	3.00
1@ $1.75\Delta_{bm}$	±0.735	3.50
1@ $2.0\Delta_{bm}$	±0.840	4.00

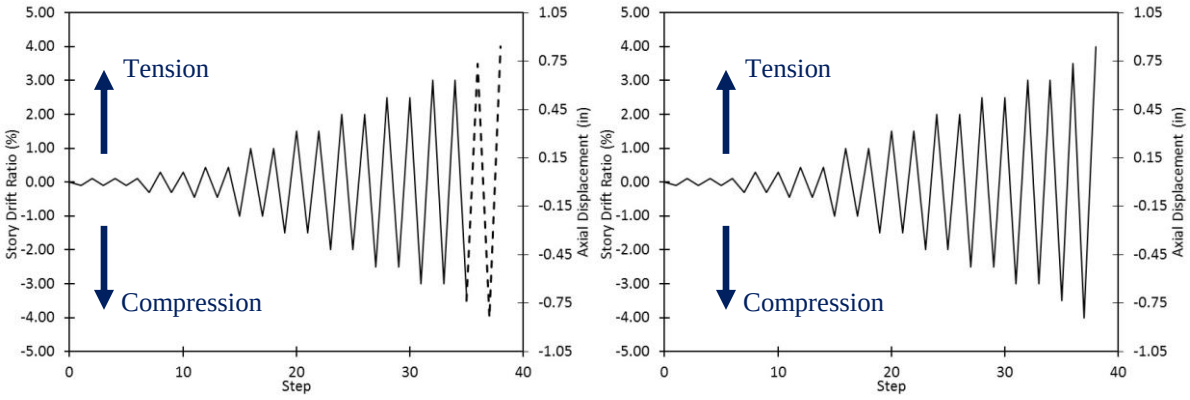

(a) TinT#2 (b) TinT#3

Figure 2.7. Loading protocol used in the testing of TinT#2 and TinT#3

2.4. Test results

2.4.1. TinT#1

The axial load-deformation response of the specimen is given in Figure 2.8. The specimen remained elastic during the first two cycles. It appears that hysteretic response was stable up to story drift ratio of 1% with virtually the same strength in tension and compression. Nevertheless, strength deteoration in compression strength became substantial during the 9th cycle shortly after 1% story drift ratio due to the flexural deformation of the gusset plate to the loading end. Fracture initiation was observed at the corner of the slotted upper end of the outer tube when the displacement in compression was corresponding to a story drift ratio of about 1.7% (Fig. 2.9). The top slotted portion of the outer tube experienced excessive flexural deformation imposed by the out-of-plane rotation of the gusset plate and therefore the fracture was triggered. As can be seen from Fig. 2.8, there was a loss in the compression strength following the fracture initiation. The test was terminated and unloaded during the 10th cycle at story drift ratio of 1%.

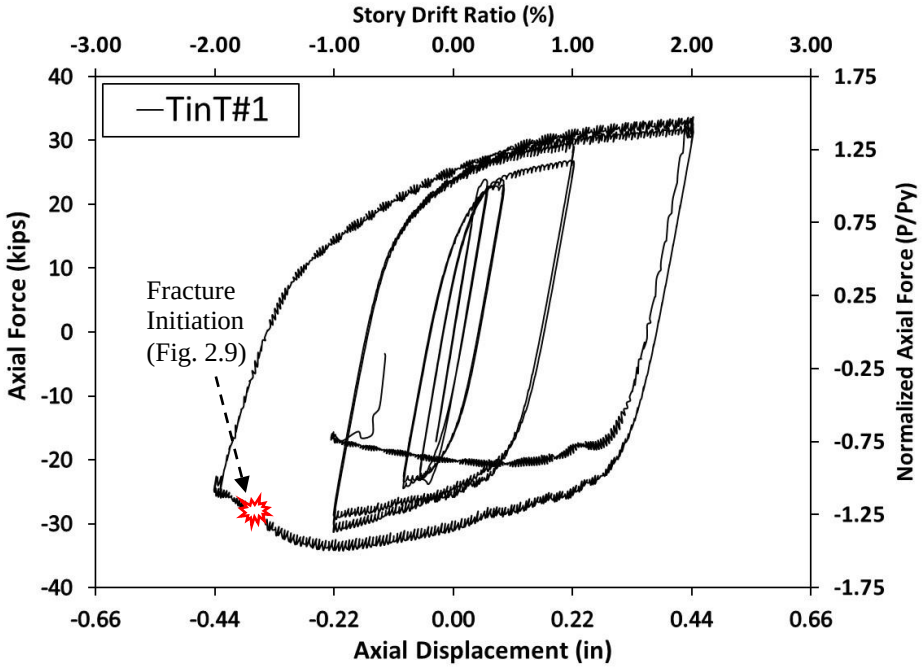

Figure 2.8. Test results of TinT#1

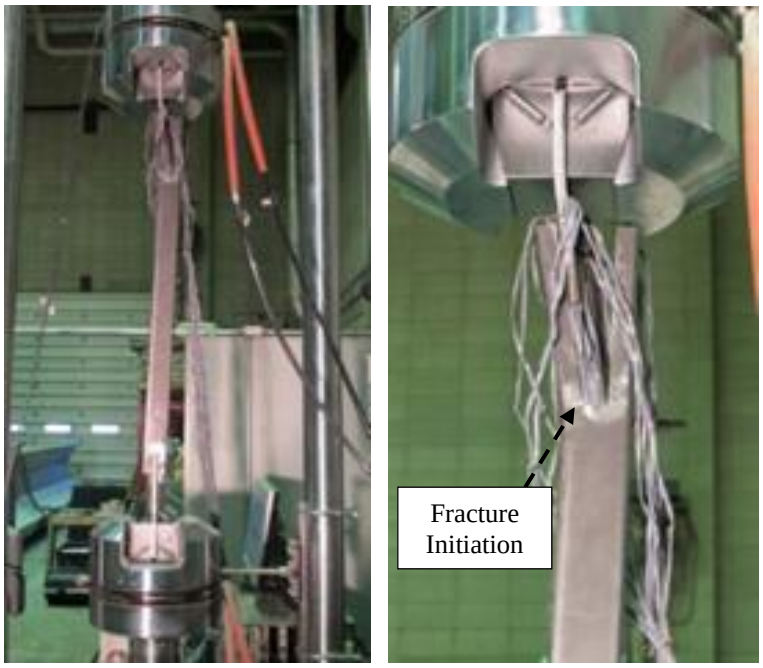

Figure 2.9. Fracture initiation at a story drift ratio of 1.7%

As mentioned earlier, the aim of testing Specimen TinT#1 was to provide a control group for the other two specimens. Therefore, as a deliberate attempt to perceive the impact

of the controlling design parameters, the observations on TinT#1 specimen divulged that the end rotations would affect the hysteretic behavior of TinT-BCBs substantially by imposing large demands on the outer tube (BC) when the gap was large and gusset plates were conventionally designed. It is apparent that the excessive rotational demand at brace ends is not practical for the seismic design practice. In order to improve the energy dissipation capability of the studied TinT-BCBs for the seismic design application, and to alleviate the possibility of fracture at the brace ends, it was crucial to enhance the connection design. The possible solutions to enhance the connection design are discussed through the finite element simulations in the following section.

2.4.1.1. FEM-based simulation of TinT#1

Finite element method (FEM) is a powerful tool that capable of predicting the actual behavior of the structural components. Thus, FE simulation is utilized to evaluate cyclic behavior of TinT#1 in detail, as well as to assess the alternatives for enhancing the connection design. In order to build a reliable FE model, the tested TinT#1 specimen has been simulated and the simulation results are compared with the test results. As soon as the FE model was calibrated based on the physical test results, the outer tube of the tested specimen was removed for the second phase of the numerical study with the intention of consolidating the evaluation of the braces with and without outer tube. Then, the calibrated FE model is utilized to compare the efficiency of the alternatives for an improved connection design.

The FE models were built in a general purpose finite element software ABAQUS 6.12.3 (Hibbit et al. 2012). Newton-Raphson method was adopted for the large displacement

non-linear static analyses. 3D modeling of the specimen was performed using 8-node linear brick elements with reduced integration points (C3D8R). The mesh adopted for the main brace consists of 11,040 elements divided into 2 and 38 elements in the through thickness and in the circumferential directions, respectively. The meshed parts of the FE model of the tested TinT#1 specimen is shown in Fig. 2.10. Non-linear material properties were determined to obtain a reasonable agreement with the test results. Combined hardening rule was adopted for the material definition. Contact elements were introduced for the simulation of TinT#l. Tangential and normal behavior definitions of the contact elements between the outer tube and the main brace were defined properly to simulate the interaction between the two tubes. A surface friction coefficient of 0.30 was assumed and specified for the tangential behavior. The initial deflection of the brace was assumed to be 0.1% of the total length (L/1,000) based on the first global elastic buckling mode for both the main brace and the outer tube.

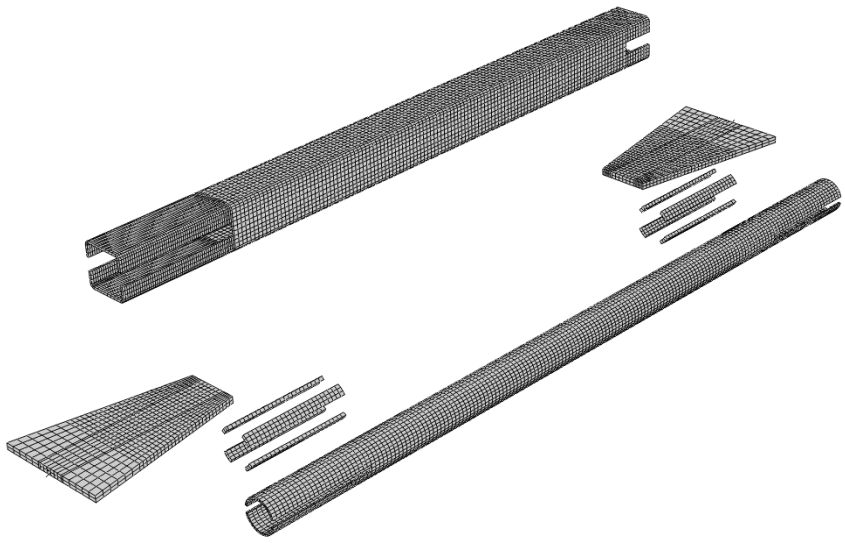

Figure 2.10. The parts of the assembly of TinT#1

Axial force – displacement and normalized axial force (Axial force divided by yield strength) – story drift ratio relation of the simulated and tested TinT#1 are compared in Fig. 2.11. The simulated hysteretic behavior of the main brace of TinT#1 (TinT#1 w/o the outer tube) is also plotted and compared in Fig. 2.11. It appears that the overall cyclic response of the simulated TinT#1 specimen is in satisfactory agreement with the physical test results. The outer tube of the calibrated FE model was removed to simulate the behavior of the main brace w/o the outer tube. The total energies dissipated by the two models with and without outer tube (TinT#1 and Conventional brace) can easily be compared in terms of hysteretic responses. As detailed in Fig. 2.11, it is apparent that the area enclosed by the hysteresis loops of the TinT#1 simulation was larger than that of the conventional buckling brace. It is also clear that the strength degradation became substantial subsequent to the global buckling of the conventional brace while the hysteresis loops of TinT#1 remained stable.

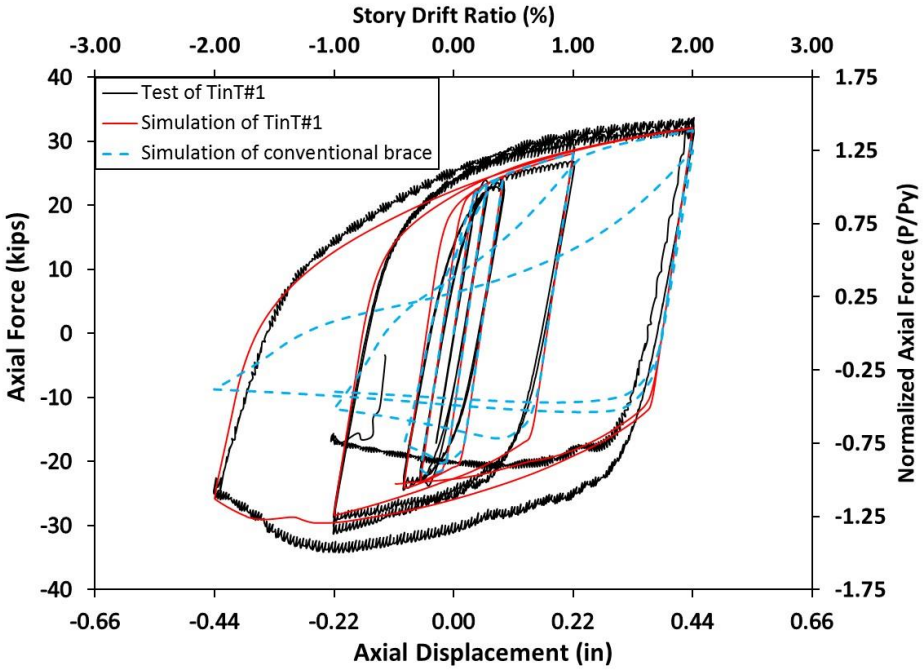

Figure 2.11. Cyclic behaviors of TinT-BCBs from the experiment and numerical simulation together with that of the conventional brace (TinT#1 w/o the outer tube).

Deformed shapes and Von Mises stress contours of the models with and without outer tube at a story drift ratio of 2% are represented in Fig. 2.12. The conventional brace experienced out-of-plane buckling at a story drift ratio of around 0.25%. Subsequent to global buckling, the plastic hinge formation occurred in the mid-length of the conventional brace, as shown in Fig. 2.12(c). On the other hand, the constraint provided by the outer tube avoided the global buckling, as well as the plastic hinge formation in the mid-length of the main brace of TinT#1. The location of the plastic hinge in TinT#1 specimen shifted from mid-length to a region closer the loading end. The deformed shapes of the tested (Fig. 2.9) and the simulated (Fig. 2.12a) specimens were fairly consistent with each other. As observed during the test, the slotted portion of the outer tube experienced very large flexural deformations during the cycles. Hence, the interaction between the main brace assembly and the outer tube is successfully emulated through the FE simulation.

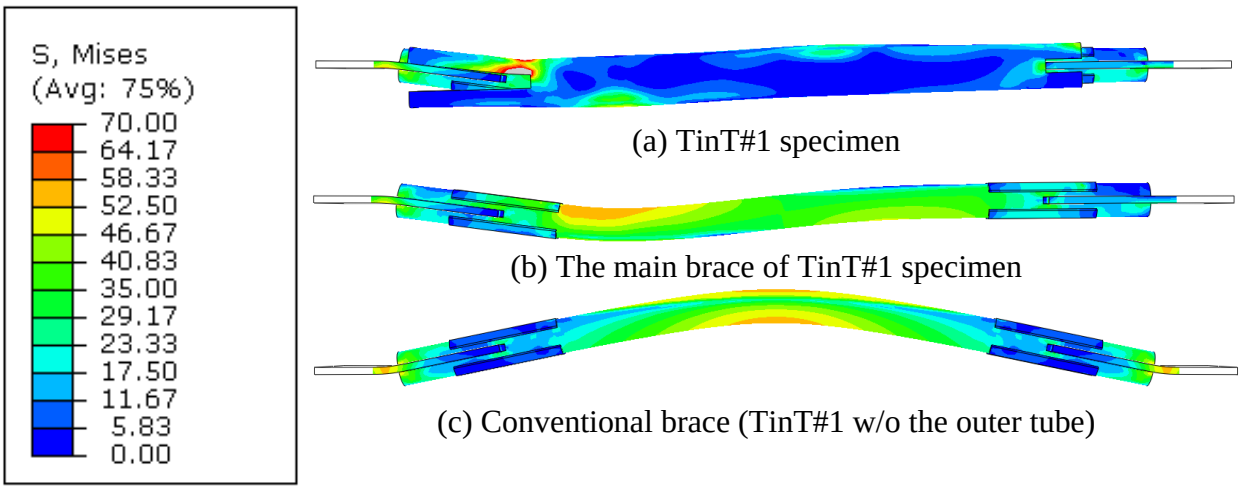

Figure 2.12. Von Mises contours (ksi) and deformed shapes at a story drift ratio of 2%

The inelastic cyclic responses of the tested and simulated TinT#1 specimens are presented together with the cyclic response of the conventional brace. The reliability of the

FE model is examined through the hysteretic response and deformed shapes. The key observations can be summarized as follows:

(1) The FE model was capable of simulating overall hysteretic response, as well as the critical deformation patterns of the tested TinT#1 specimen satisfactorily.

(2) The interaction between the main brace assembly and the outer tube is successfully emulated through the FE simulation.

(3) Utilizing an outer tube increases the energy dissipation capability of the main brace substantially.

(4) The strength degradation became substantial subsequent to the global buckling of the conventional brace while the hysteresis loops of TinT#1 remained stable.

2.4.1.2. Design of supports of the TinT-BCBs

The tested TinT-BCB with conventional gusset plates (TinT#1) helped establish a reliable FE model with challenging deformation patterns. As discussed previously, it is clear that the excessive rotational demand at brace ends is not practical for the seismic design practice. Efficiency of the two supports is examined through FE simulations. Support I consists of two 2.5”x0.5” plates welded to the conventional gusset plates (Fig. 2.13a). Each gusset plate reinforced with relatively small four stiffener plates (2”x3/8”) in the TinT-BCB with Support II (Fig. 2.13b). The size of the stiffeners was determined so that resulting supports provide the same rotational constraints for in-plane and out-of-plane bending moments. Meshing of the two FE models are given in Fig. 2.13.

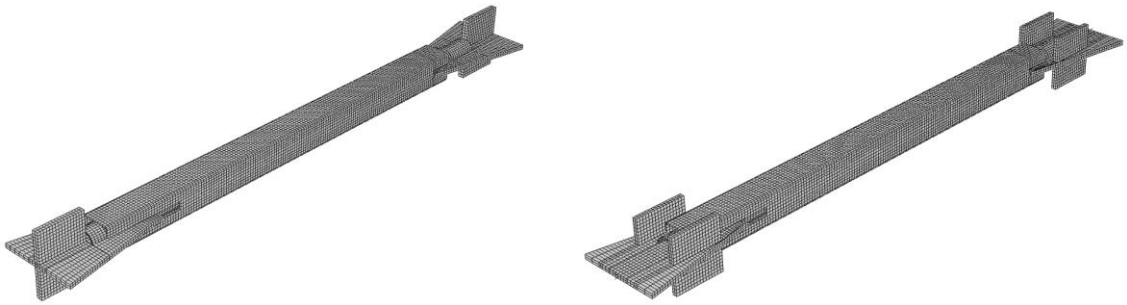

(a) Support I (2.5”x0.5” Stiffeners) (b) Support II (2”x3/8” Stiffeners)

Figure 2.13. The mesh adopted for the TinT-BCBs

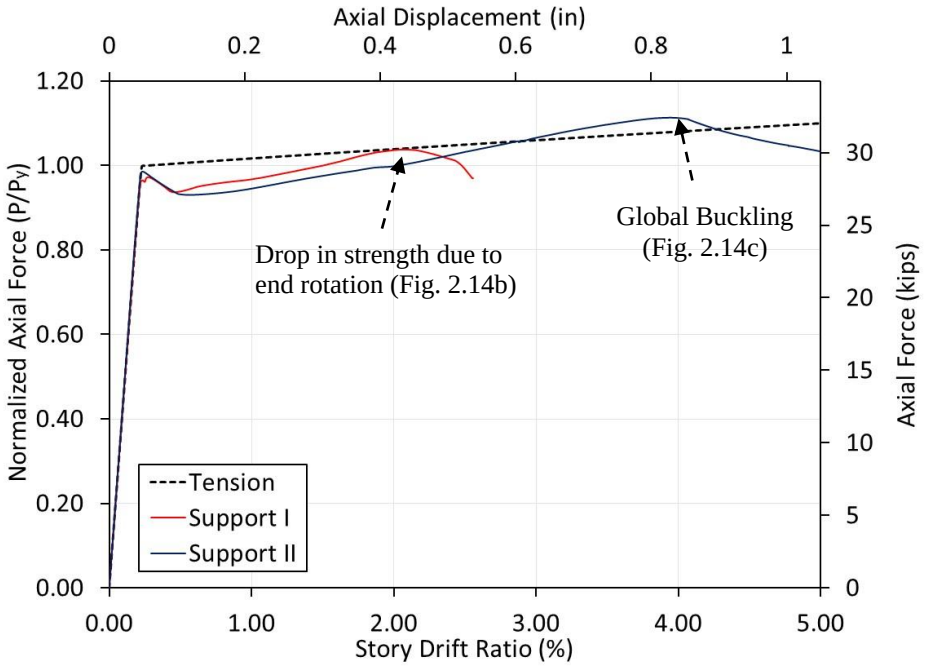

(a) Pushover results

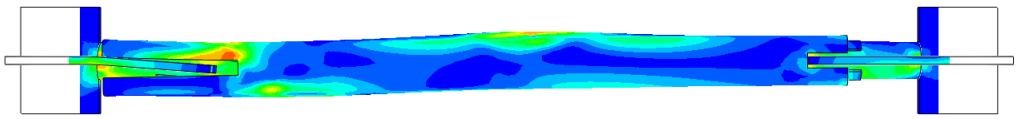

(b) Deformed shape of TinT-BCB with support I at 2% SDR

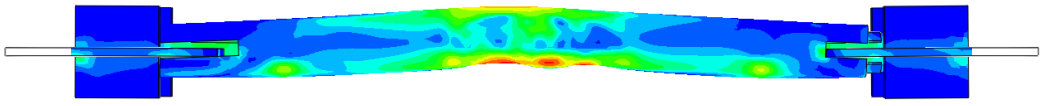

(c) Deformed shape of TinT-BCB with support II at 4% SDR

Figure 2.14. Comparison of the TinT-BCBs with different end supports

The results of the analyses are presented in Fig. 2.14(a) in terms of axial force-displacement and normalized axial force-story drift ratio. The TinT-BCB with support I experienced strength degradation soon after a story drift ratio of 2% due to out-of-plane rotation of its gusset plate. The TinT-BCB with support II, on the other hand, did not experience strength or stiffness loss until a story drift ratio of 4%. Global buckling of the entire assembly took place after 4% story drift ratio in the TinT-BCB with support II. Figs. 2.14(b) and (c) illustrate the deformed shapes of the models at different deformation levels. It is obvious that support II offers a simple and efficient way of alleviating rotational demands on the gusset plates by providing a near-fixed end condition for TinT-BCBs. Hence, support II is introduced for the following tests of TinT-BCBs as well as for the simulation cases of the FEM-based parametric study.

2.4.1.3. Key Observations on TinT#1

The first BCB specimen (TinT#1) has been tested and simulated. The test and simulation results were compared through hysteretic response and deformed shapes. Based on the results of the test and FEM-based numerical study conducted on TinT#1 Specimen, the key observations can be summarized as follows:

(1) Despite the large gap amplitude and conventional gusset plate design, encasing the main brace with an outer tube enhances the energy dissipation capability of the main brace substantially, and provides stable hysteresis loops.

(2) The end rotations affect the hysteretic behavior of TinT-BCBs substantially by imposing large demands on the outer tube (BC) when the gusset plates are designed as conventional gusset plates.

(3) An enhanced connection design to mitigate the rotational demands at brace ends can be achieved by providing near-fixed end condition for TinT-BCBs. The second end support option offers an efficient way of alleviating rotational demands on the gusset plates with little additional cost.

(4) The FE model is capable of simulating overall hysteretic response of the tested TinT#1 specimen and the interaction between the main brace assembly and the buckling-controller.

2.4.2. TinT#2 and TinT#3

Subsequent to testing of TinT#1 specimen, the gusset plates were redesigned and reinforced with the stiffeners for TinT#2 and TinT#3 specimens. Furthermore, horizontal and vertical supporting plates were also introduced to the gusset assembly of TinT#2 and TinT#3 so as to represent the beam/column flange with the intention of replicating the actual boundary conditions of a TinT-BCB in an actual BCBF (Fig. 2.3). As discussed earlier, the size of the main brace (HSS 1.900x0.125), the gap amplitude (0.175") and the relative stiffness of the buckling-controller (HSS2½x2½x1/8) were identical for TinT#1 and TinT#2. It is, therefore, important to observe the hysteretic behaviors of the two specimens with regard to the influence of the end rotations.

The hysteretic response of TinT#2 specimen is given in Fig. 2.15(a) in terms of axial load-deformation and normalized axial load-story drift ratio relationship. The hysteretic response of TinT#2 appears stable during the first 14 cycles. The first significant yielding observed at around 0.28% SDR in compression. Strength degradation took place during the first compression cycle at 3% story drift ratio. The strengths in compression were about 75% and 70% of the yielding strength at the end of the first and the second compression cycles at

3% story drift ratio, respectively. Strength loss in tension capacity was not observed during the first cycle at 3% story drift ratio. Pinching in tension became noticeable and the tension capacity was reduced to 65% of the yield strength after 2% story drift ratio during the second cycle at 3% story drift ratio. The last cycle prior to the fracture of the inside tube was at 3.5% story drift ratio.

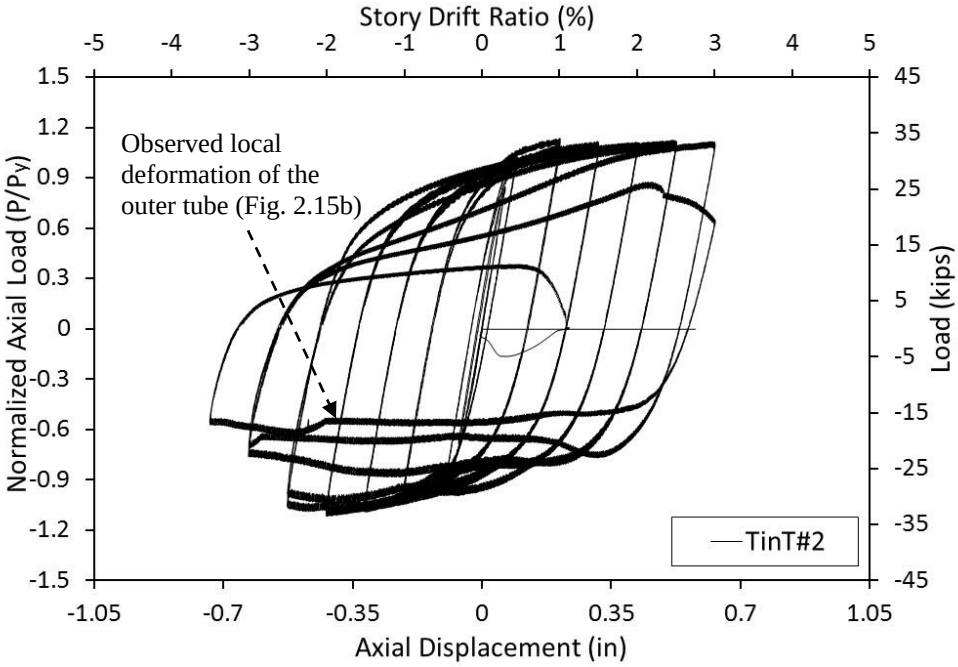

(a) Hysteretic response of the tested TinT#2 Specimen

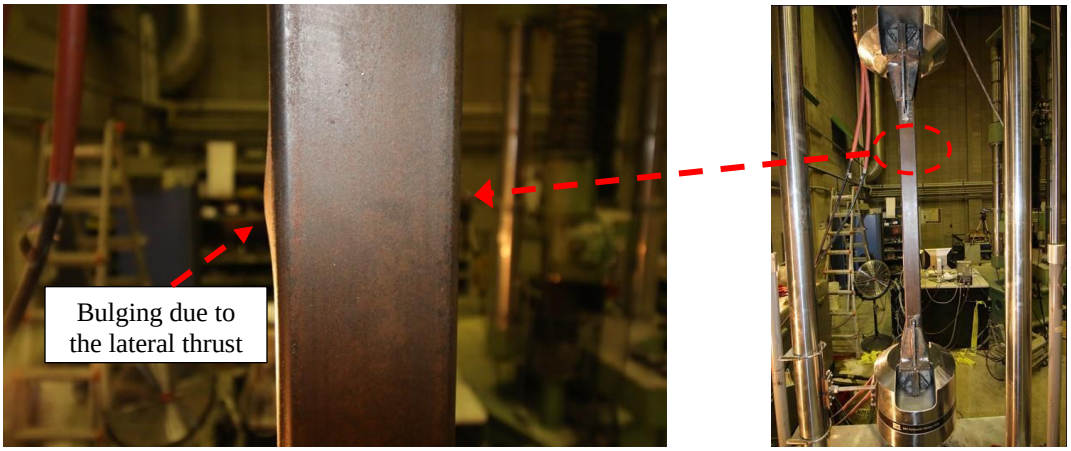

(b) Local deformation of the outer tube during the compression cycle at 3.5% SDR

Figure 2.15. Test Results of TinT#2 Specimen (Gap=0.175", t_{BC}=0.125")

Local deformation of the outer tube close to the loading end of the specimen was observed at 2% story drift ratio in compression during the first compression cycle at a story drift ratio of 3.5%, as demonstrated in Fig. 2.15(b). As seen in Fig. 2.15(a), the compression strength increased temporarily due to the friction force transfer between the tubes, but nevertheless the outer was not thick enough to locally resist the lateral thrust caused by possible local deformation of the inside tube. Therefore, the strength in compression dropped to 55% of the initial yield strength when the specimen was subjected to an axial deformation corresponding to 3.5% story drift ratio in compression. The fracture of the main brace occurred in a ductile manner at a story drift ratio of around 1.5% in tension during the reversed cycle to 3.5% story drift ratio. It is observed that the top and bottom gusset assemblies were able to provide near-fixed end condition, since the end rotations were not noticeable during the test.

TinT#3 had smaller gap amplitude (1/16”) and relatively thicker outer tube (HSS2½x2½x1/4) compared to the second specimen while its main brace size and gusset assembly were identical to those of TinT#2 specimen. The hysteretic response of TinT#3 specimen is given in Fig. 2.16(a). The specimen exhibited a stable cyclic response until a story drift ratio of 3.5%. Similar to the hysteresis of TinT#2, yielding of the main brace occurred at around 0.28% SDR in compression. The compression strength dropped linearly after a story drift ratio of 1.5% during the compression cycle to 3.5% story drift ratio and lost 20% of its initial yielding strength when the equivalent story drift ratio was 3.5%. The tension load bearing capacity of the specimen, on the other hand, did not drop during the reversed tension cycle to 3.5% story drift ratio. The last cycle prior to fracture initiation was at a story drift ratio of 4%. As seen in Fig. 2.16(a), a growth in compression strength was

observed during the last compression cycle, which would be attributable to the friction force between the two tubes. The specimen lost 40% of its initial yielding strength when the axial deformation was corresponding to an equivalent story drift ratio of 4%. The test was terminated during the 18th cycle at a story drift ratio of 4% due to possible cracking of the inside tube. The gusset assemblies prevented rotational demands at brace ends throughout the protocol.

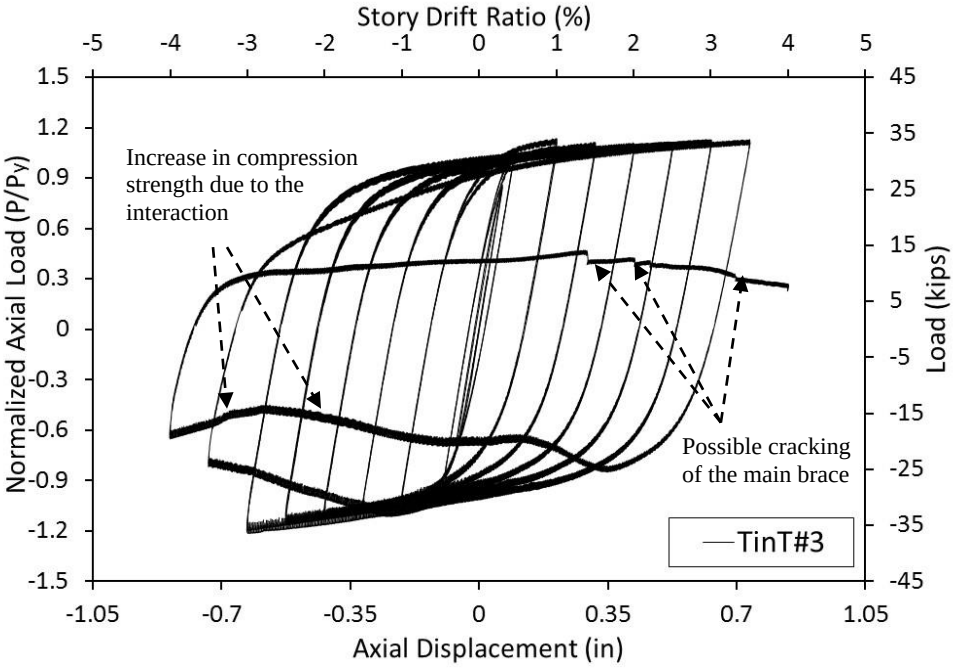

(a) Hysteretic response of the tested TinT#3 Specimen

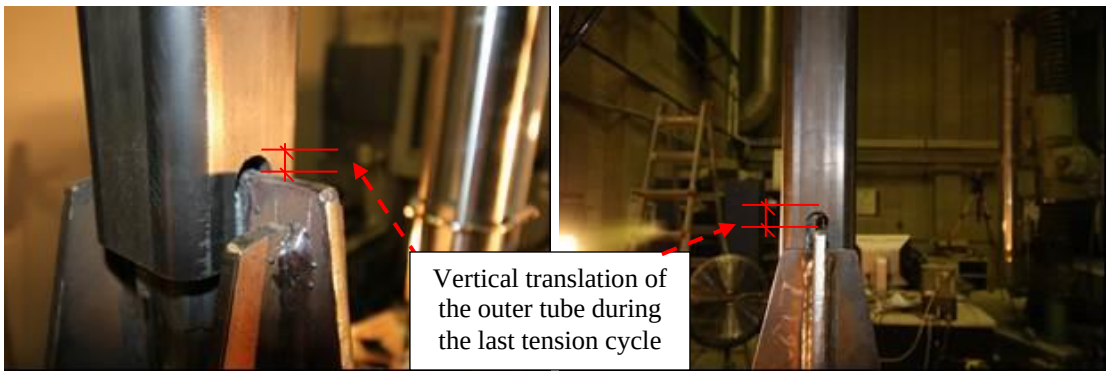

(b) Vertical translation of the outer tube during the last tension cycle to 4.0% SDR

Figure 2.16. Test Results of TinT#3 Specimen (Gap=1/16", t_{BC}=0.25")

In contrast to the observed in TinT#2 test, local deformation of the outer tube due to the lateral thrust was not observed during the third test, owing to the larger outer tube thickness. It is, however, evident from the rapid increase in the compression strength during the compression cycle to 4% SDR (Fig. 2.16a) that there was a substantial interaction between the two tubes, which transferred a significant amount of shear force from one tube to another due to the friction. The interaction between the tubes became obvious during the reversed tension cycle to 4% SDR, in which the vertical translation of the outer tube took place. As presented in Fig. 2.16(b), because of the potential lateral deformation of the inside tube, the outer tube was pulled together with the inside tube and translated vertically during the last tension cycle. Note that the outer tube was not welded either to the gusset plates or to the inside tube.

Compression strength adjustment factors (β), which account for compression overstrength with respect to tension strength (AISC 2010b), were also investigated. Table 2.5 summarizes the compression strength adjustment factors for each deformation quantity in terms of story drift ratio. Hysteretic response of TinT#2 specimen was stable with virtually the same strengths in tension and compression until the cycle at 3% story drift ratio while compression strength of TinT#3 was slightly larger than the tension strength until the cycle at a story drift ratio of 3.5%. The maximum compression strength adjustment factors were found to be 0.99 and 1.08 for TinT#2 and TinT#3, respectively.

Table 2.5. Compression strength adjustment factors (β)

Story Drift Ratio	TinT#2	TinT#3
1.50%	0.99	0.99
2.00%	0.98	1.03
2.50%	0.96	1.05
3.00%	0.70	1.08
3.50%	NA	0.74

The buckling-controller outer tube of TinT#2 specimen was removed after the test to observe the ultimate deformed shape of the main brace. Fig. 2.17 shows the deformed shape of the fractured main brace after the test. It appears that the fracture triggered by the strain concentration due to the local plastic deformation of the main brace. The main brace experienced higher order local buckling prior to the fracture initiation so that the local-buckling-induced fracture occurred in the vicinity of the net section reinforcing plates close to the loading end of the specimen, where the local deformation of the outer tube observed (Fig. 2.15a). It is critical to note that the local plastic deformations were concentrated close the loading end of the main brace, which might have been due to the difference between the boundary conditions at each end. The displacement-type loading is applied from the top grips of the test equipment while the bottom grips were fixed. In an actual braced frame, axial deformation of a brace member is due to the relative movement of both ends, except for the braces in the first story. Therefore, the ductility of the tested specimens might have been underestimated due to the limitation on the test equipment used in the experimental study. Note that the outer tube of the TinT#3 was also removed after the test. It is again observed that the fracture of the main brace took place in a section that is close to the net section reinforcing plates to the loading end. The strain concentration due to the local plastic deformations led the main brace to fracture.

Figure 2.17. Fractured main brace of TinT#2

2.4.3. Observations on test results

An ensemble of small-scale Tube-in-Tube type all-steel BCB (TinT-BCB) specimens with different design parameters has been tested and the hysteretic behaviors under reversed cyclic loading are presented. The key observations on the experimental study can be summarized as follows:

(1) It is obvious that TinT-BCBs were capable of exhibiting stable hysteretic response as well as dissipating greater amount of energy compared to the conventional braces even when the gap amplitude was large and the gusset plates were designed as conventional gusset plates. Furthermore, providing a length of two times the gusset plate thickness ($2t_g$) clearance between the brace end and the assumed fold line to allow out-of-plane rotations might have been manipulated the buckling plane. There is a strong possibility that absence of $2t_g$ clearance would create a tendency for the main brace to buckle about both in and out-of-planes simultaneously, which would reduce the impact of the end rotations. Nevertheless, the effect of absence of the free length between the brace end and the line of restraint on the cyclic behavior of TinT-BCBs remains unstudied.

(2) It seems that performance of BCB specimens tend to improve substantially when near-fixed end condition is provided. Comparing hysteretic responses of TinT#1 and TinT#2 specimens clearly showed that an enhanced connection design develops a notable increase in energy dissipation capability of BCBs even when the gap was large and the buckling-controller stiffness was moderate. Therefore, for an optimal performance, the gusset plates of TinT-BCBs should be designed to be strong enough to resist in-plane and out-of-plane rotational demands without experiencing excessive flexural deformation when a TinT-BCB undergo large axial deformations.

(3) The maximum and cumulative inelastic ductilities of TinT#3 specimen were 15% and 26% larger than those of TinT#2, respectively. In other words, TinT-BCB specimens would sustain larger inelastic deformations when the gap between the main brace and the BC is small enough to avoid excessive P-M interaction and the thickness of the outer tube is sufficient to resist the lateral thrust imposed by the global or local deformation of the inside tube. It appears likely that the gap amplitude and the buckling-controller stiffness are the most influential parameters on the fracture life of BCBs. However, their individual impact on the cyclic behavior of TinT-BCBs as well as the interrelation between the gap and the BC stiffness remain unclear. Further study needed to reveal how the cyclic response is affected by interaction of the two design parameters.

(4) The outer tubes of TinT#2 and TinT#3 were able to control global buckling of the TinT-BCBs. Inevitably, the main braces of both specimens experienced local plastic deformations due to the fact that steel material softens and cumulates more plastic deformation as the number of cycles and the amplitude of the excursion increases.

(5) It is observed that the buckling-controller of TinT#2 specimen experienced local deformation due to the lateral thrust caused by the local plastic deformation of the main brace inside. Local deformation of TinT#3 specimen, on the other hand, was not visible during the test. Since the outer tube thickness of TinT#3 was two times the thickness of the outer tube of TinT#2 specimen and the gap amplitude of TinT#2 was almost three times the gap amplitude of TinT#3, the buckling-controller of TinT#3 specimen was more effective in terms of alleviating as well as resisting the contact pressure locally.

(6) It is evident from the test results that utilizing a two times thick outer tube and smaller gap amplitude postponed the local strain concentrations that initiate fracture. Therefore,

TinT#2 specimen fractured earlier than TinT#3 specimen. However, the observed deformation patterns of both TinT#2 and TinT#3 specimens were such that the local plastic deformations were concentrated in a section that is close the loading end of the main brace, where the displacement-type loading is applied from. Owing to the consistency between the locations of the fractured sections, it seems likely that the difference between the boundary conditions provided at each end might have an impact on the uneven distribution of the plastic deformations along the brace length. Since in an actual braced frame, axial deformation of a brace member is due to the relative movement of the both ends, it is potential that providing identical boundary conditions to each end would improve the fracture life of TinT-BCBs.

(7) Compression adjustment factor is a general index to measure the cyclic stability quantitatively. Symmetrical cyclic behavior of buckling controlled braces is an ideal case to mitigate seismic demands in braced frames, since the unbalanced forces due to compression overstrength of braces might impose substantial flexural demands on the brace-intersected girders. However, past studies indicate that both concrete-encased and all-steel BRBs would exhibit unsymmetrical cyclic behavior after reaching a certain deformation level due to the increase in compression strength. Owing to extremely small or zero gap amplitudes provided for the current concrete-encased and all-steel BRBs, lateral expansion (Poisson's effect) of the load-bearing core segment might develop considerable friction forces when the brace is in compression. Our results, on the other hand, showed that the compression and tension strengths of the tested TinT-BCBs were virtually identical with the maximum compression adjustment factors of 0.99 and 1.08. Despite the absence of low-friction coating between the contact surfaces, the cyclic behavior of the specimens were fairly stable due to the moderate-

to-large gap amplitudes adopted for the specimens, which allowed lateral movement of the inside tube without developing significant friction forces.

3. Parametric Study on TinT-BCBs

3.1. General remarks

A FEM-based parametric study was conducted on the TinT-BCBs for having a further comprehension of how the key design parameters interact with each other and affect the cyclic response of the TinT-BCBs. As mentioned earlier, in addition to proper connection design, there are three major design parameters that essentially control the cyclic behavior and fracture life of any kind of buckling restrained/controlled brace. Since it is validated by the experimental and numerical studies that support II offers a simple and efficient way for the engineering practice, the parametric study focuses on the three design parameter and the interaction between them:

(1) The gap amplitude between the tubes.

(2) The relative stiffness of the outer tube.

(3) The friction between the tubes.

It is essential to evaluate each design parameter interactively, since the three parameters are highly dependent on each other. Unfortunately, past studies have focused mainly on the critical constraint ratio of the buckling restrainer/controller to prevent global buckling of the entire BRB assembly (Watanabe et al. 1988, Chou and Chen 2010, Ma et al. 2012b, Hoveidae and Rafezy 2012). A few researchers have addressed the effect of the gap amplitude and the friction coefficient, but nevertheless they examined the impact of each parameter individually. Furthermore, it appears that majority of the recently developed all-

steel BRB models have complicated cross sections so that the researchers focused predominantly on resolving the issues associated with the attachments of the buckling-restraining system in lieu of revealing how the fundamental parameters interact with each other (Tremblay et al. 2006, Eryasar and Topkaya 2009). The objective of the present parametric study is to perceive the significance of the interaction between the three parameters in order to provide a solid foundation for the design provisions to be established in the future.

A reliable FEM-based model is the key to a successful numerical study. In this work, the development of FEM modeling began with simulating a conventional steel brace tested by Fell et al. (2009) to ensure that the FE model is able to capture the buckling deformation as well as the overall cyclic response of the tested brace properly. Then, the calibrated FE model of the conventional brace is encased with an outer tube to predict the cyclic behavior of TinT-BCBs with various design parameters.

Further, initial out-of-plane straightness is one of the controlling parameters that has a significant impact on buckling load of a bracing member and therefore needs to be considered in the simulations. Even though there are other ways for considering initial imperfections to initiate buckling, such as introducing a static surface load prior to cyclic loading, in this study, initial out-of-plane imperfections were taken into account based on the deformed shape obtained from an independent elastic buckling analysis of the specimens. By employing the initial deflection using the data from a separate analysis, we were able to guarantee that the static analyses start from zero stress condition. It should be noted that only first global buckling mode was considered for initial imperfections of all simulation cases.

Material non-linearity was introduced to replicate inelastic material properties. The modulus of elasticity and the Poisson's ratio were assumed to be 29,000 ksi and 0.3, respectively. ABAQUS offers the combined hardening rule (mixed plasticity), which is capable of representing both isotropic (expansion of the yielding surface) and kinematic (translation of the center of the yield surface) hardening rules (Lemaitre and Chaboche, 1990) for the simulation of metals subjected to cyclic loading. Therefore, non-linear combined hardening rule, which is available only with the Von Mises yielding surface criterion was employed to the material definition of the bracing member. The isotropic component of the material model is defined by three parameters, which are the yield surface size at zero plastic strain (σ_o), the maximum change in yield surface (Q_b) and the rate factor (b). The kinematic component is defined by kinematic hardening modulus (C) and kinematic hardening rate factor (γ). For this purpose, the uniaxial tensile coupon test data along with the cyclic test results were used to calibrate the material parameters to obtain a satisfactory agreement with the test results.

3.2. FE simulation of a conventional brace

FE simulation of a 10 ft long square hollow section (HSS) tested by Fell et al. (2009) was performed under standard symmetrical cyclic loading protocol based on the dimensions and the loading protocol provided by the authors (Fell et al. 2009). Slenderness and b/t (flat width-to-wall thickness) ratio of the tested specimen were around 77 and 14.2, respectively.

The numerical model consist of a tubular bracing (HSS4x4x1/4), four ¼" thick plates for net section reinforcement and two ½" thick gusset plates. The bracing member and gusset plates were meshed using two elements across their thicknesses. The mesh size of elements

located at 16” long mid-length of the specimen, in which the plastic hinge formation occurs was reduced by half so as to enhance the capability to simulate local buckling. The element aspect ratios of all elements were adjusted to a changing value in between 1 and 3 in order not to diminish the accuracy of the analyses. As suggested by the AISC Manual (2011), internal and external radii of the filleted corners of the square hollow sections were assumed to be the wall thickness of the section (t_w) and two times the wall thickness of the section ($2t_w$), respectively, to eliminate the possibility of the artificial stress concentration around corners due to sharp edges. The mesh adopted for the filleted corners divided into 3 elements and 35,744 linear hexahedral elements of type C3D8R were used in total. The measured yield stress of the center coupon was 67 ksi (Fell et al. 2009). The mixed plasticity was introduced with the following parameters: σ_o= 62 ksi, C_1=290 ksi, C_2=1450 ksi, γ_1=50 and γ_2=100, and the rate factor was taken as b=1. Since there was no measured data provided by the authors regarding the initial deflection, a global initial imperfection of 1.20” (L/1,000) was adopted based on the first global buckling mode shape (Fig. 2.18).

Comparison of test and simulation results and cyclic loading protocol used in the study are given in Fig. 2.19. Global buckling of the brace took place at a story drift ratio of 0.3% in both experiment and simulation. According to the observations during the experiment (Fell et al. 2009), local buckling of the brace occurred at the mid-length, where the plastic hinge formed at a drift ratio of 1.9% during the second compression cycle to 1.9% (Fig. 2.20b). A similar deformation pattern was captured in the vicinity of the mid-length in the simulation of the brace at the same deformation quantity (i.e. 1.9% SDR), as illustrated in Figs. 2.20(c) and (d). The comparison between the simulation and test results indicates that

the model predicts the global and local behavior well. Hence, it is justified that the calibrated FE model can be used as the main brace for the parametric study of the TinT-BCBs.

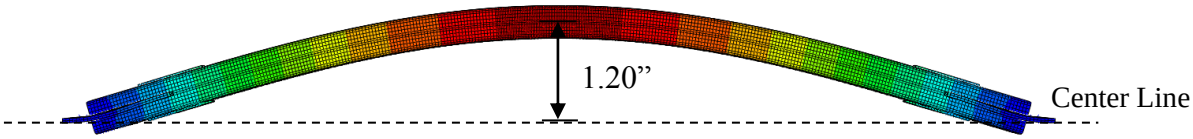

Figure 2.18. Initial imperfection based on first elastic global buckling mode (L/1,000)

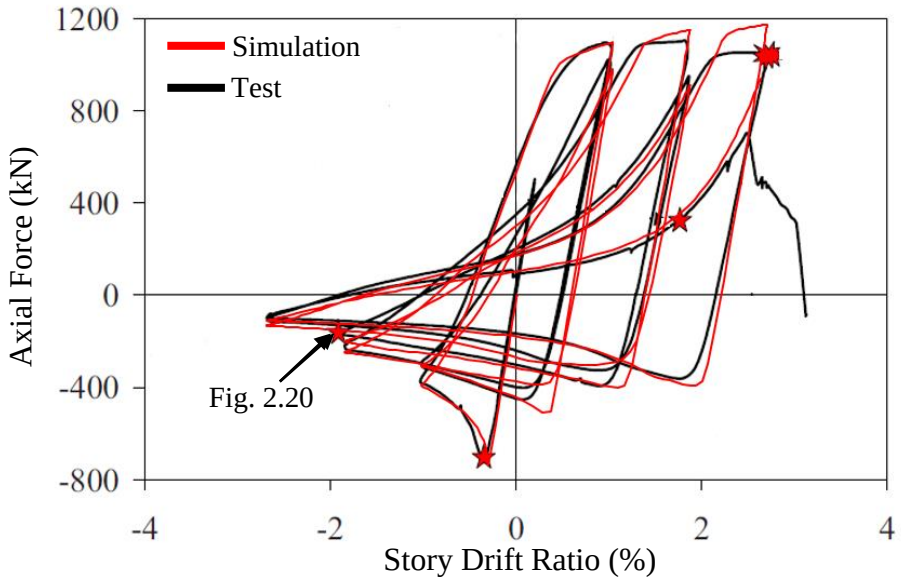

(a) Comparison of test and simulation results

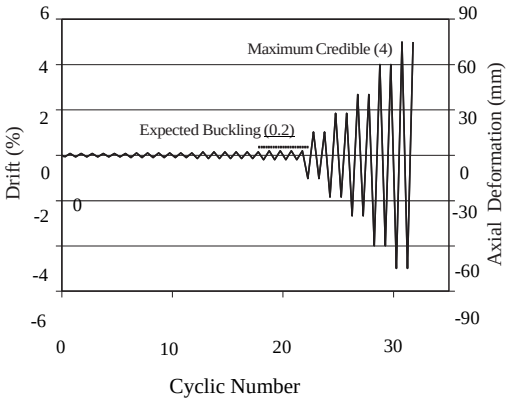

Standard Cyclic		
#cycles	**Δ_a (mm)**	**Drift (%)**
6	1.0	0.08
6	1.5	0.10
6	2.3	0.15
4	3.0	0.20 – B
2	15.5	1.03
2	27.9	1.85
2	40.4	2.68
2	59.9	4.00 - MCE
2+n	75.9	5.00

(b) Cyclic loading protocol

Figure 2.19. Test and FE simulation results of HSS4x4x1/4

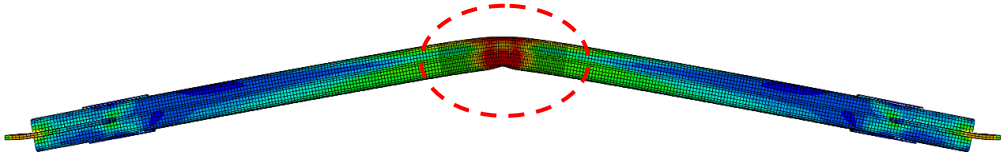

(a) Plastic hinge (Von Mises contours)

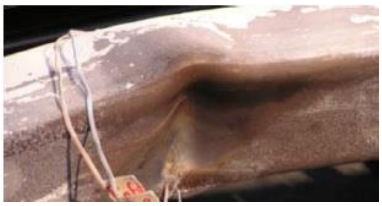

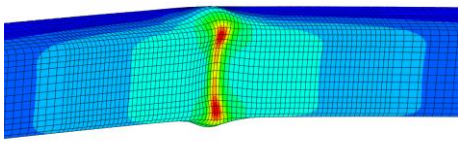

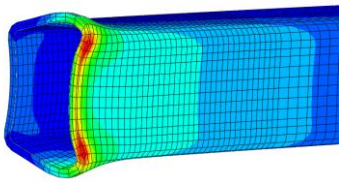

(b) The tested brace (c) Equivalent plastic strain (PEEQ) (d) Section view cut (PEEQ)

Figure 2.20. Local buckling of the brace at around a story drift ratio of 2%

3.3. Parametric study

A group of FE simulations were conducted on the TinT-BCBs under cyclic loading to examine the impact of the key parameters. As shown in Fig. 2.21, square hollow sections, which are the most commonly used structural shapes for bracings in CBFs were adopted for both the main brace and the buckling-controller of TinT-BCBs. The cross sections and the dimensions of the main brace, the net section reinforcing plates and the gusset plates were adopted from the previously calibrated FE model of the tested HSS4x4x1/4 specimen (Fell et al. 2009). Since the tested brace was designed to allow out-of-plane rotations, four stiffener plates with the dimensions of 10"x2"x1/8" were welded to each gusset plate in order to provide near-fixed end condition, as illustrated in Fig. 2.21. The axial displacements (δ) of the simplified cyclic loading protocol used in the study and the story drift ratios corresponding to the each deformation quantity are shown in Fig. 2.22 and Table 2.6. The axial displacements of each cycle were determined to develop story drift ratios of 1%, 2%, 3%, 4% and 5% in the BCBF is shown in Fig. 2.21(a).

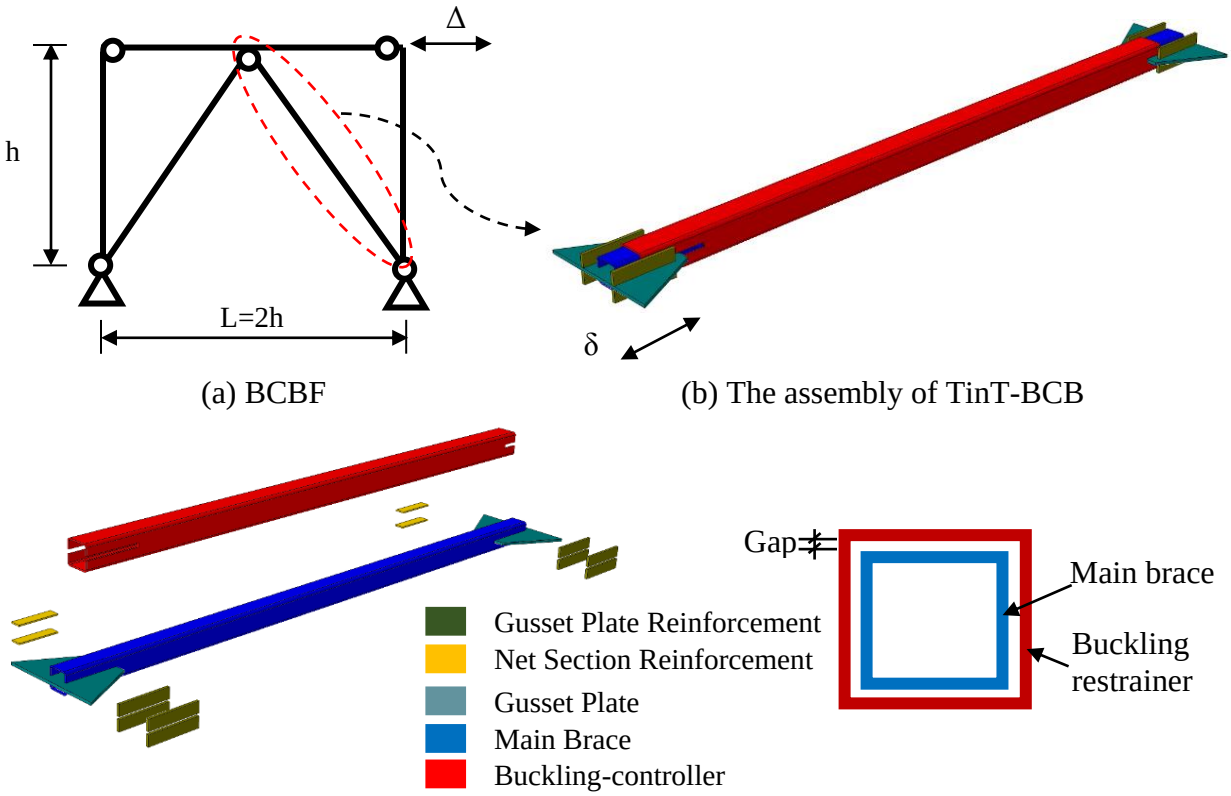

(a) BCBF (b) The assembly of TinT-BCB

(c) The parts of the assembly (d) Cross Section

Figure 2.21. Structural details of the TinT-BCB and its connections in a typical frame

Three different gap amplitudes and two different BC thicknesses were employed for the parametric study. Table 2.7 shows the simulation cases of the TinT-BCBs. The main brace section (HSS4x4x1/4) and the gusset assemblies were identical for all simulation cases. The outer tube thickness of each BCB model is given in terms of relative thickness, which is the ratio of outer tube thickness over inside tube thickness. TinT-BCBs with the gap amplitudes of 1/16”, 1/32” and 0.02” were compared in the parametric study. Across the groups, the gap and the thickness of the buckling controller are changed in such an order that any group can find its counterpart with only one of three factors being different.

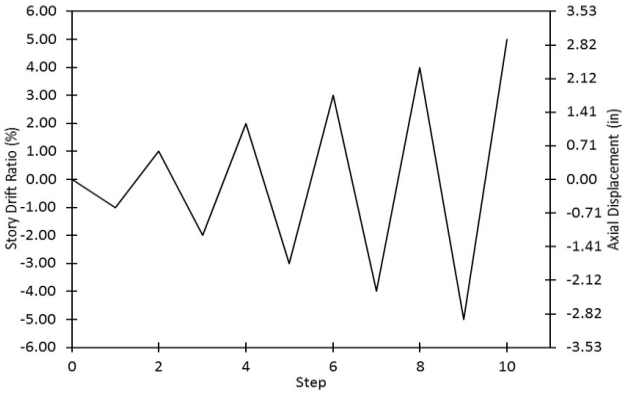

Figure 2.22. Simplified loading protocol used in the parametric study.

Table 2.6. Loading sequence used in the parametric study.

# of Cycle	δ (in)	Story Drift Ratio (%)*
1	±0.588	1.00
1	±1.176	2.00
1	±1.763	3.00
1	±2.352	4.00
1	±2.940	5.00

*Story Drift Ratio=$2\delta/L_b$

Each simulation set (e.g. SS1) includes three identical models with the friction coefficients of 0.30, 0.10 and 0.02, which account for the surface frictions of bare steel, a polyethylene-based low-friction coating and an extremely low-friction coating, respectively. The measured friction coefficient between the unlubricated steel surfaces (bare steel) might be less than 0.30 (Genna and Gelfi 2012). However, a friction coefficient of 0.30 is acceptable for numerical simulations of tested BRBs to gain a reasonable agreement with the test and simulation results (Korzekwa and Tremblay 2009). In an attempt to develop a uniform strain demand in the core segment, the core segments of the SP-BRBs were conventionally wrapped with a polyethylene-based film together with grease or ceramic painting as an unbonding mechanism between the surfaces so as to reduce surface friction (Chou and Chen 2010, Hoveidae and Rafezy 2012, Tabatabaei et al. 2014). As pointed out by the recent numerical studies on all-steel BRBs, adopting a friction coefficient of 0.10 to simulate a polyethylene-based unbonding mechanism provides reasonable results (Chou and Chen 2010, Hoveidae and Rafezy 2012). The friction coefficient of 0.02 was incorporated to assess the case of utilizing an extremely low-friction coating material.

Table 2.7. Simulation cases used in the study

Simulation Case	Main Brace	t_{BC}* (Relative Thickness)	FC** (μ)	Gap (in)
SS-1A	HSS4x4x1/4	0.25" (RT=1.0)***	0.30	1/16
SS-1B			0.10	
SS-1C			0.02	
SS-2A		0.50" (RT=2.0)	0.30	1/16
SS-2B			0.10	
SS-2C			0.02	
SS-3A		0.25" (RT=1.0)	0.30	1/32
SS-3B			0.10	
SS-3C			0.02	
SS-4A		0.50" (RT=2.0)	0.30	1/32
SS-4B			0.10	
SS-4C			0.02	
SS-5A		0.25" (RT=1.0)	0.30	0.02
SS-5B			0.10	
SS-5C			0.02	
SS-6A		0.50" (RT=2.0)	0.30	0.02
SS-6B			0.10	
SS-6C			0.02	

*Wall thickness of the outer tube (Buckling-controller) ; ** FC: Friction coefficient;
***RT: Relative thickness ($RT=t_{BC}/t_{MB}$ where t_{BC}=Thickness of outer tube, t_{MB}=Thickness of main brace).

3.3.1. Effect of relative stiffness

TinT-BCBs with the two relative thickness (RT) ratios (i.e. the outer tube thickness over the inner tube thickness) of 1.0 and 2.0 were included in the parametric study. Hysteretic responses, deformed shapes and relative stress distributions of all TinT-BCB models are summarized in Figure 2.23 through 2.28. Deformed shapes and stress contours are plotted at 2% story drift ratio. The ordinate and abscissa of the plots represent the normalized axial force and story drift ratio (%), respectively. The observations on the effect of the relative stiffness is presented as follows with an emphasis on its interrelations with the gap and the coefficient of friction:

(1) Relative thickness (RT) of 1.0 was sufficient to prevent global buckling for all BCBs while it is capability to control local buckling varied and was sensitive to the gap amplitude and friction coefficient (FC).

(2) Comparing the hysteretic responses of SS1 and SS2 groups given in Figs. 2.23 and 2.24 show that energy dissipation capacities of the TinT-BCB specimens with the moderate gap amplitude (1/16") were improved dramatically in any case, when relative thickness ratio was changed from 1.0 to 2.0.

(3) As shown in Fig. 2.23(a), similar to the deformation observed during the testing of TinT#2 specimen (Fig. 2.15), with the moderate gap amplitude (1/16") and friction coefficient of 0.30, the lateral thrust due to the local plastic deformation of the inside tube led the outer tube of SS1A to experience severe local deformation close to the loading end. The outer tube of SS2A, on the other hand, was able to resist the lateral thrust, as indicated in Fig. 2.24(a), despite the gap amplitude and the coefficient of friction.

(4) It seems that the influence of the gap amplitude on the hysteretic response became more noticeable when relative thickness was 1.0. Comparing the hysteretic response of simulation sets SS1 and SS3 reveals that reducing the gap amplitude by half:

- Improved the hysteretic stability of the BCBs with FC=0.30 (Figs. 2.23a and 2.25a) and;
- Prevented strength degradation in compression due to local buckling and pinching in tension for the BCBs with FC=0.10 and FC=0.02 (Figs. 2.23b, 2.23c and 2.25b, 2.25c).

(5) The impact of the friction coefficient on the stress distribution of the outer tube was substantial for SS1 and SS3 groups. As shown in Figs. 2.23 and 2.25, the outer tube stress became more uniform and less substantial as friction coefficient decreased.

(6) In general, regardless of the gap and friction between the tubes, hysteretic response of all specimens with the relative thickness of 2.0 (SS2, SS4 and SS6) remained substantially stable without significant strength and stiffness degradation up to a story drift ratio of 4% while the hysteretic response of the specimens with relative thickness of 1.0 (SS1, SS3 and SS5) were stable only up to a story drift ratio of 2%. It appears likely that the peak and cumulative inelastic ductilities of the TinT-BCBs are primarily governed by the relative stiffness of the outer tube when the gap amplitude is 1/16" or less.

3.3.2. Effect of gap amplitude

TinT-BCBs with 1/16", 1/32" and 0.02" gap amplitudes were compared in the parametric study. The effect of the gap amplitude on cyclic behavior appears to be influenced by the relative thickness of outer tubes and coefficient of friction. The observations on the effect of gap can be summarized as follows:

(1) The gap amplitude was the most influential parameter on controlling local buckling of the main brace. Comparing deformed shapes and hysteretic behaviors of the models with the same relative outer tube thickness and friction coefficient showed that the models with larger gaps experienced local buckling earlier. As shown in Fig. 2.23(a), the model with the moderate gap (1/16"), the relative outer tube thickness of 1.0 (RT=1.0) and 30% friction coefficient experienced local buckling in a cross-section close to the loading end at around 2% story drift ratio (SDR). On the other hand, formation of local plastic deformations is

postponed as the gap amplitude is reduced and thus local deformations became substantial at a story drift ratio of around 3% for SS3A and SS5A specimens, as interpreted from Figs. 2.25 and 2.27.

(2) The gap between the tubes provides a clearance for the main brace to deform laterally. Therefore, possibility of localized plastic deformations increases as the gap amplitude become larger. Furthermore, this effect can be either amplified or reduced based on the lateral resistance provided by the outer tube. Stress distributions of SS1, SS3 and SS5 are given in Figs. 2.23, 2.25 and 2.27, respectively. Comparing the main brace stress distribution of SS1 group (gap=1/16”) with that of SS3 (gap=1/32”) and SS5 (gap=0.02) groups, indicates that stress distribution becomes more uniform as the gap decreases, which provides a larger plastic zone and more energy dissipation capacity, consequently.

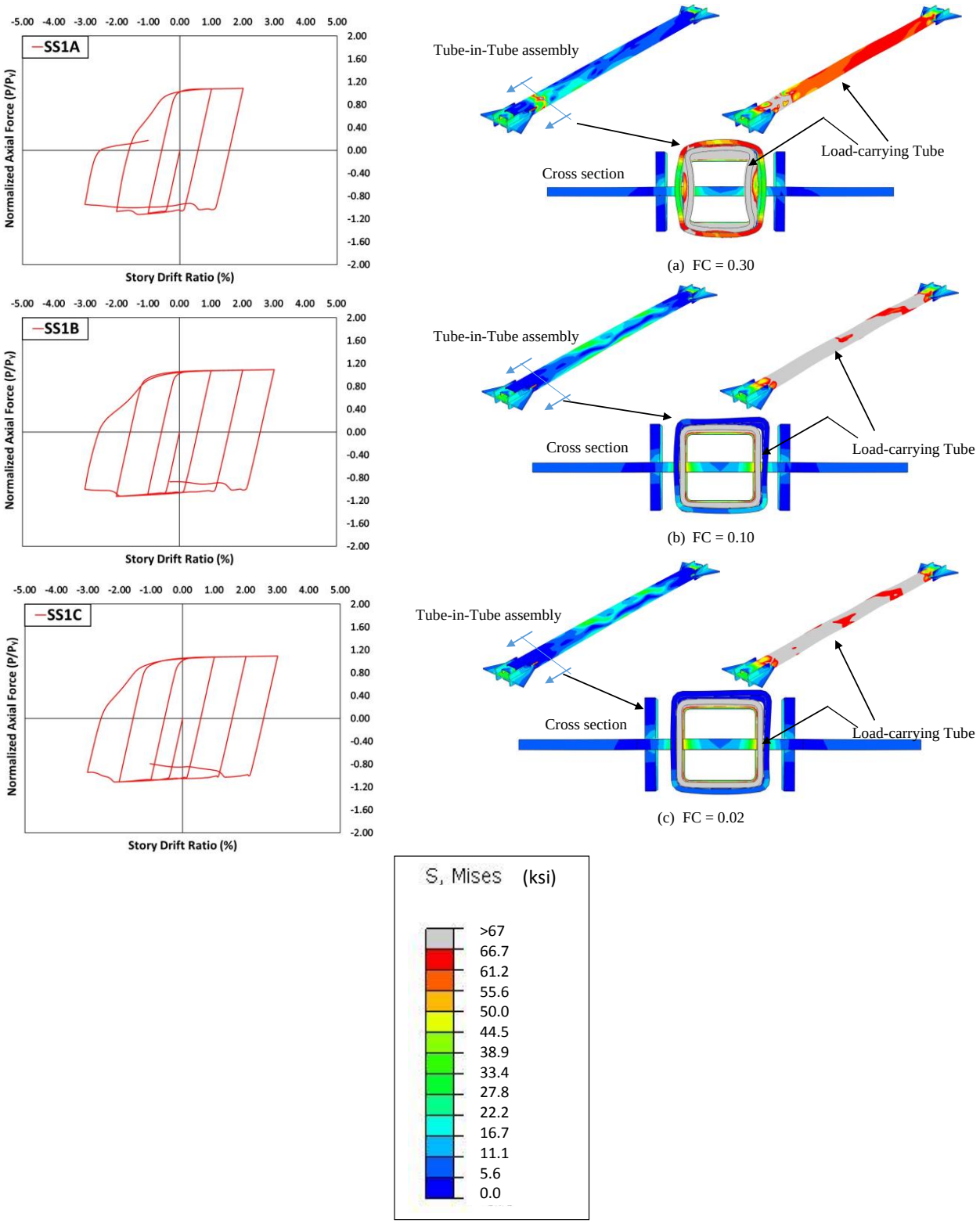

Figure 2.23. Response of SS1 group with gap = 1/16" and t_{BC} = 0.25". Left column: hysteresis; Right column: deformation and relative stress distribution at 2% SDR in compression

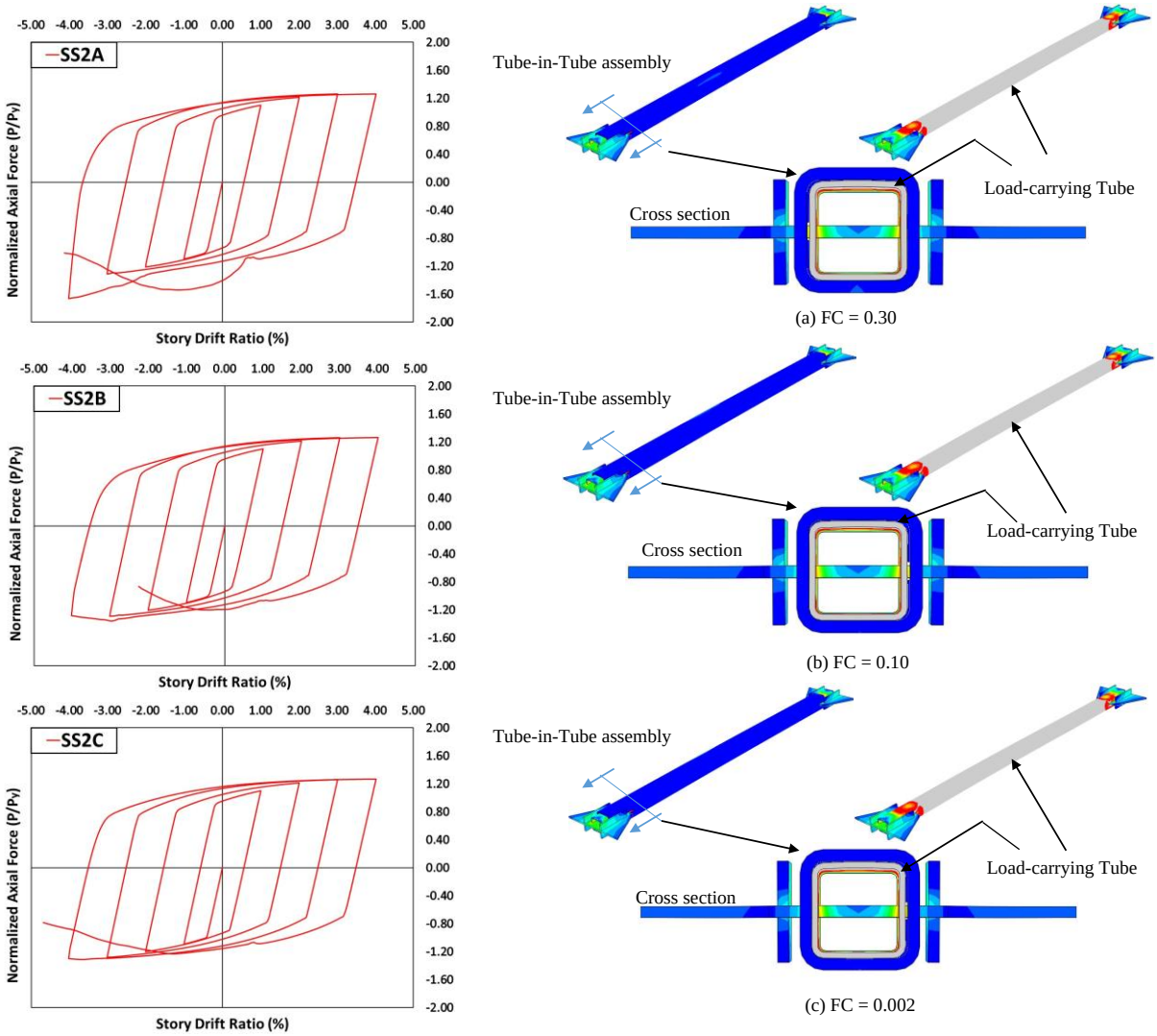

Figure 2.24. Response of SS2 group with gap = 1/16" and t_{BC} = 0.50". Left column: hysteresis; Right column: deformation and relative stress distribution at 2% SDR in compression

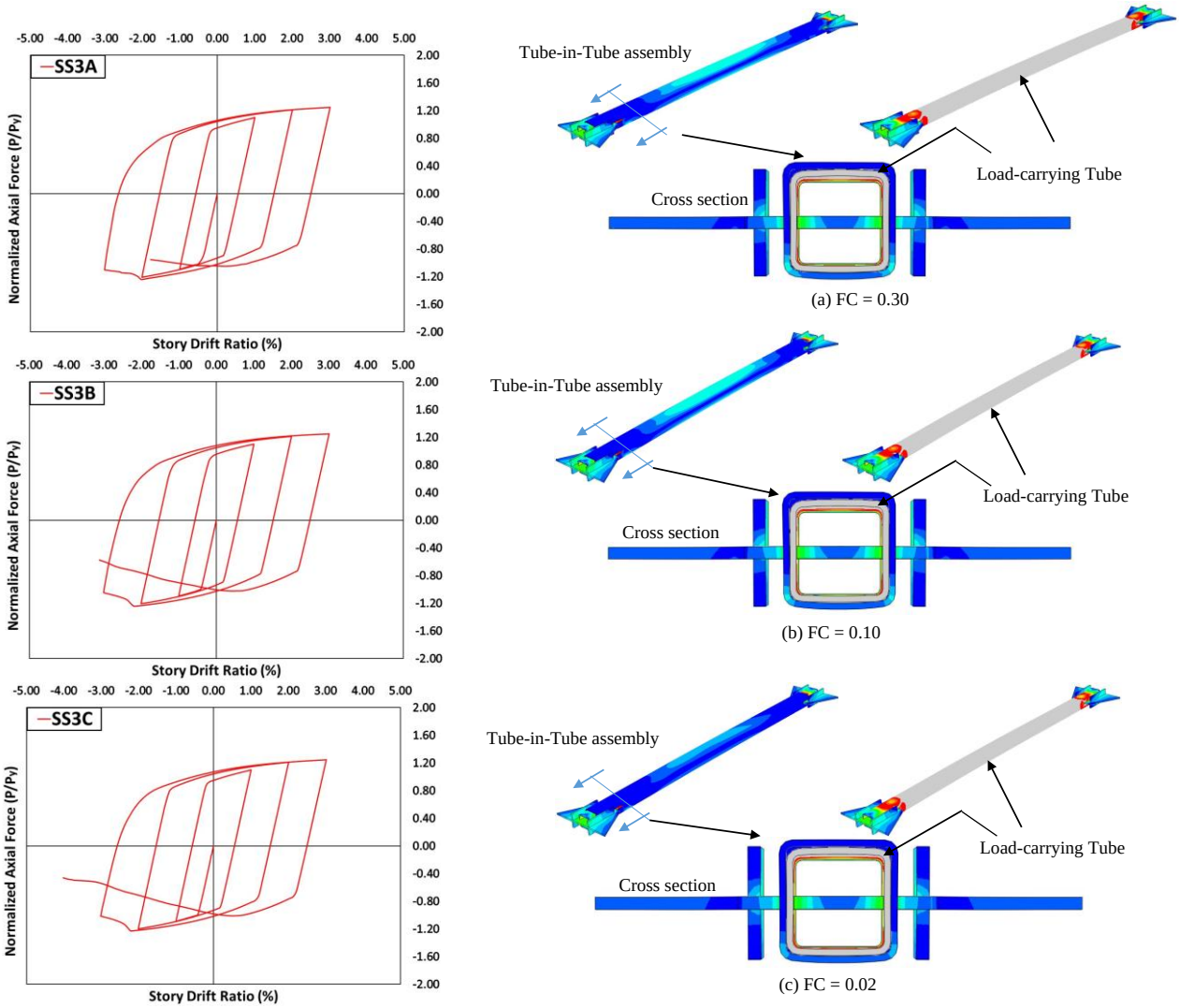

Figure 2.25. Response of SS3 group with gap = 1/32" and t_{BC} = 0.25". Left column: hysteresis; Right column: deformation and relative stress distribution at 2% SDR in compression

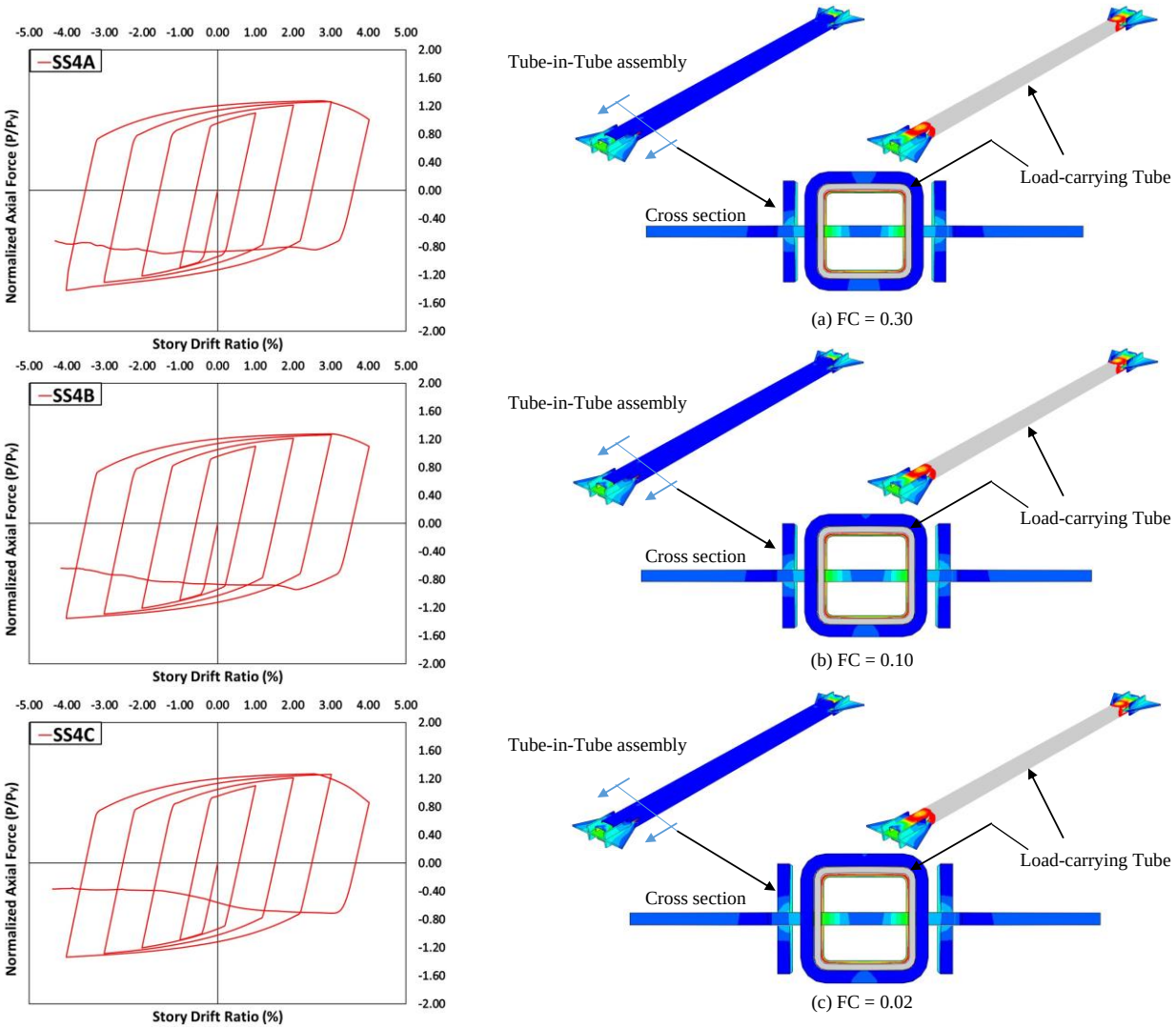

Figure 2.26. Response of SS4 group with gap = 1/32" and t_{BC} = 0.50". Left column: hysteresis; Right column: deformation and relative stress distribution at 2% SDR in compression

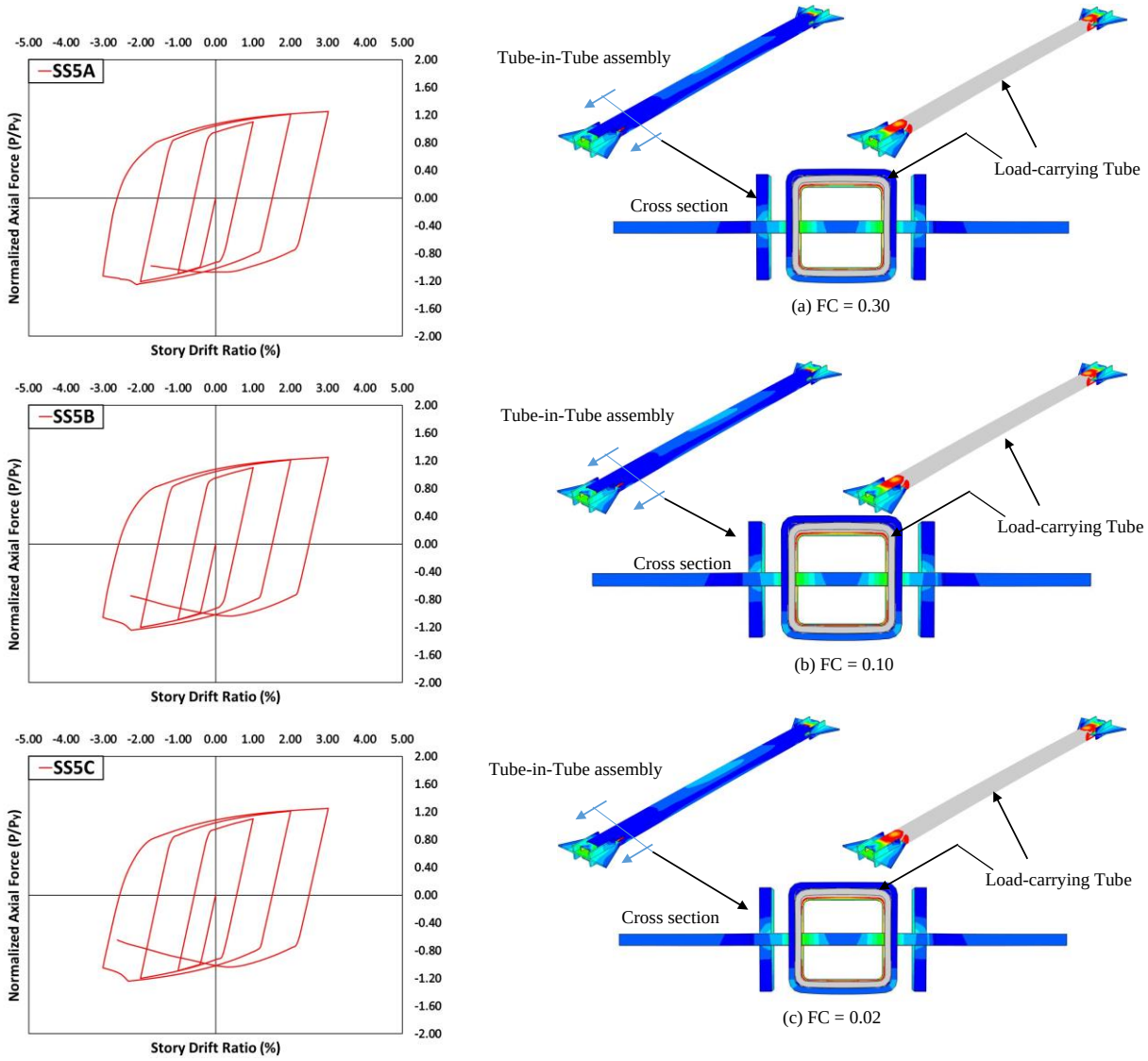

Figure 2.27. Response of SS5 group with gap = 0.02" and t_{BC} = 0.25". Left column: hysteresis; Right column: deformation and relative stress distribution at 2% SDR in compression

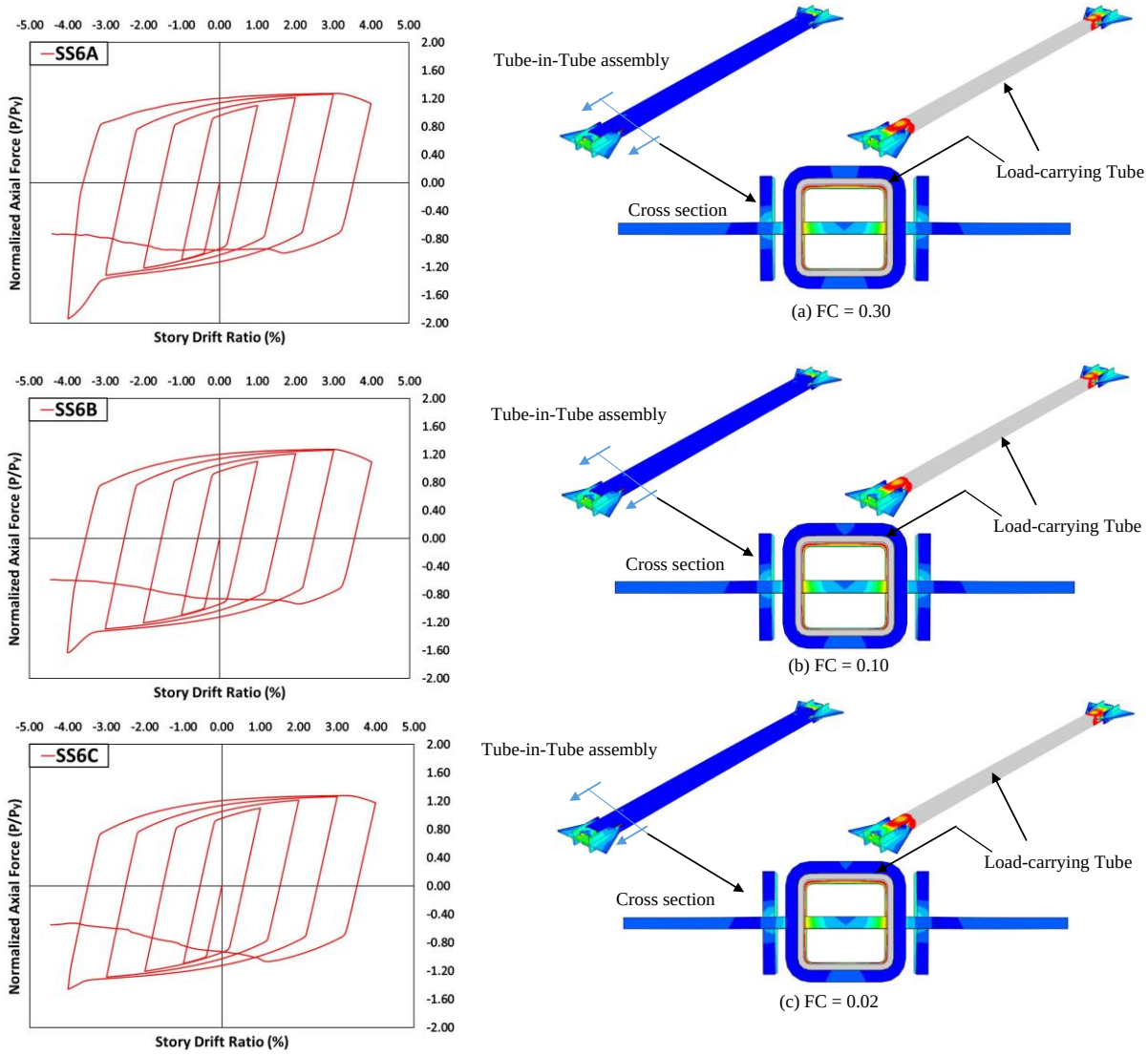

Figure 2.28. Response of SS6 group with gap = 0.02" and t_{BC} = 0.50". Left column: hysteresis; Right column: deformation and relative stress distribution at 2% SDR in compression

3.3.3. Effect of the coefficient of friction

Characteristics and significance of the impact of friction coefficient appear to be altered by the gap amplitude and the relative stiffness. Thus, the case-dependent effect of the friction is discussed considering the following two cases:

i. When the gap amplitude was the largest (1/16") and RT=1.0 (SS1 group), the ductility tended to be enhanced as the friction coefficient reduced (Fig. 2.23).

ii. When the gap was the smallest (0.02”) and RT=2.0 (e.g. SS6 group), the influence of the friction coefficient on the compression overstrength was significant (Fig. 2.28).

Fig. 2.29 compares the variation of compression overstrength (compression strength divided by tension strength at each deformation quantity) over the simulation cases of SS6 group. It seems that cyclic behavior of the three BCBs with 0.02, 0.10 and 0.30 friction coefficients were quite symmetrical with virtually the same strengths in tension and compression until 3% SDR. However, compression overstrength of the BCBs with 0.30 and 0.10 friction coefficients exceeded the limit specified by AISC Seismic Provisions (2010) at 4% SDR while the compression overstrength of the BCB with 0.02 friction coefficient was about 20%.

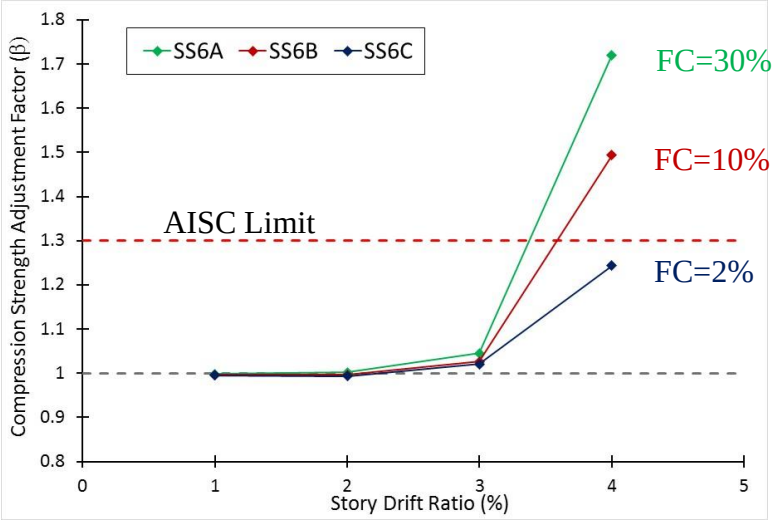

Figure 2.29. Compression adjustment factors of SS6 Group (Gap=0.02”, RT=2.0)

It is evident from the cyclic results of SS6 group that the friction coefficient is the key parameter to obtain symmetrical cyclic response when the gap is small and the outer tube is stiffer than the inside tube. Therefore, close attention paid to SS6 group to evaluate the impact of the friction coefficient. In order to quantify the involvement of the friction forces in

the compression strength without difficulty, in addition to the cyclic loading, a set of analyses were conducted on specimen SS6 under monotonic compression and tension loadings up to a story drift ratio of 5%. Fig. 2.30 demonstrates the comparison between the total compression strengths and the surface friction forces of the three models. It seems that the compression and tension strengths remained the same up to 3.20% SDR for the three models. However, the compression strength increased substantially between 3% and 5%. It can be interpreted from the results that the substantial increase in compression strength was due to the surface friction force transferred to the main brace. It is also noticed that the rapid increase in the friction force takes place soon after local plastic deformation of the main brace occurs. Hence, it is safe to claim that predominantly the bulging of the cross section developed an excessive interaction as well as a growth in compression strength.

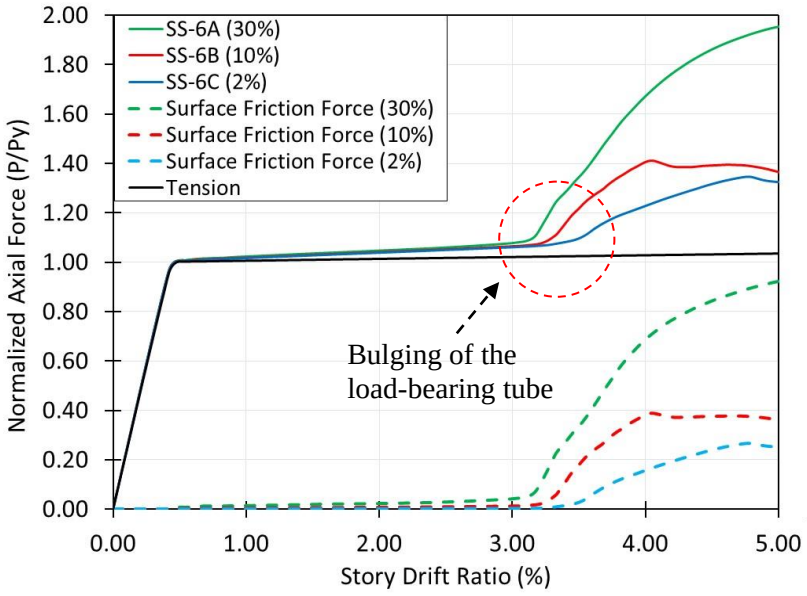

Figure 2.30. Pushover results of group SS6

3.3.4. Effect of gap distribution along the brace length

A buckling-controller (outer tube) can be applied to an actual buckling-controlled braced frame construction either by connecting one side of the outer tube to the gusset plate or without any connection between the outside tube and frame. Fig. 2.31 demonstrates the scheme of a typical chevron type TinT-BCB frame with possible applications of the buckling-controllers. The first option can be put into practice by welding the lower end of the outer tubes to the gusset plates at each corner (Fig. 2.31), which may result in almost evenly distributed initial gap amplitude along the brace length.

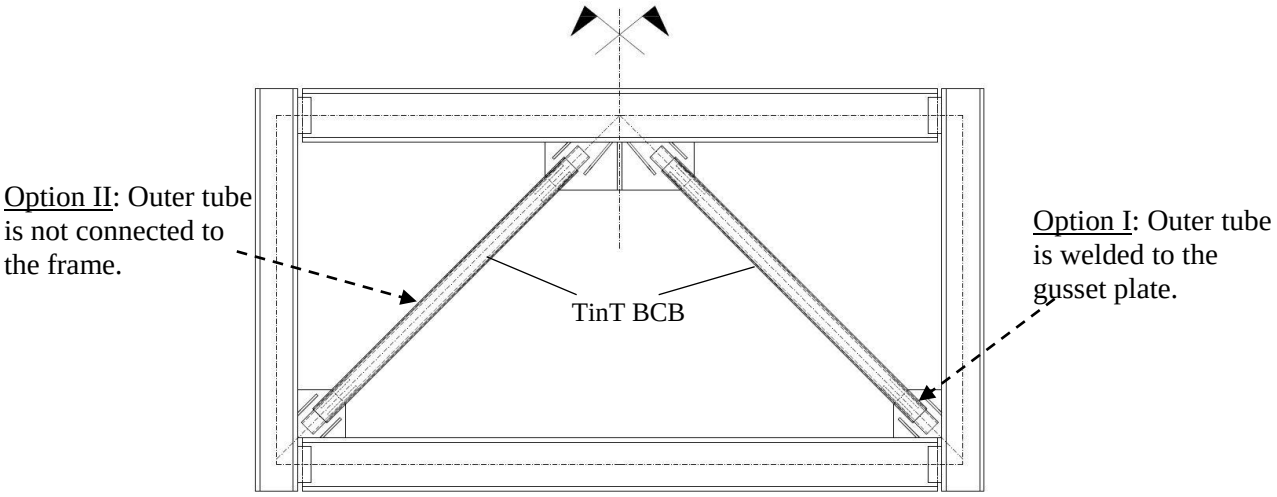

Figure 2.31. TinT-BCB frame with possible applications of buckling-controllers

Since the second option does not require any connection between the outer tube and the gusset plate, the gap is rarely uniform at any given cross section. An extreme case of having zero gap on one side and two times the initial gap amplitude on the other side has been considered for the comparison. Fig. 2.32 shows the cross-sections of the cases that were adopted for the comparison. Note that the initial gap amplitudes can be arbitrarily distributed in each direction of the cross-section as well as along the brace length when the outer tube is

not connected to the frame. In order to quantify the possible impact of uneven gap distribution, two models with the even gap amplitudes of 1/16" and 1/32" have been altered and compared with the original models. Table 2.8 shows the details of the models.

(a) Even Gap (b) Uneven Gap

Figure 2.32. Gap distributions

Table 2.8. Simulation cases used in the study

Simulation Case	Main Brace	t_{BR} (in)	Friction Coeff.	Tolerance (in)	Out-of-Plane Gap (in)	In-plane Gap (in)
SS2A Even Gap SS2A Uneven Gap	HSS 4x4x1/4	0.50	0.30	1/8	1/16 0 - 1/8	1/16
SS4A Even Gap SS4A Uneven Gap	HSS 4x4x1/4	0.50	0.30	1/16	1/32 0 - 1/16	1/32

Fig. 2.33 presents the results of the pushover analysis in terms of axial force and displacement. As shown in Fig. 2.33, initial gap distribution did not affect the overall pushover results of SS2A and SS4A braces substantially. Furthermore, the results of the SS4A models with even and uneven gap distributions were virtually the same (Figs. 2.33b). Comparing Figs. 2.33(a) and (b) illustrates that the impact of uneven gap distribution may increase as the tolerance between the tubes increases. However, the difference between the SS2A models with even and uneven initial gap distributions was less than 2% at its peak. It is, therefore, apperant that initial gap distribution had little effect on the overall inelastic behavior.

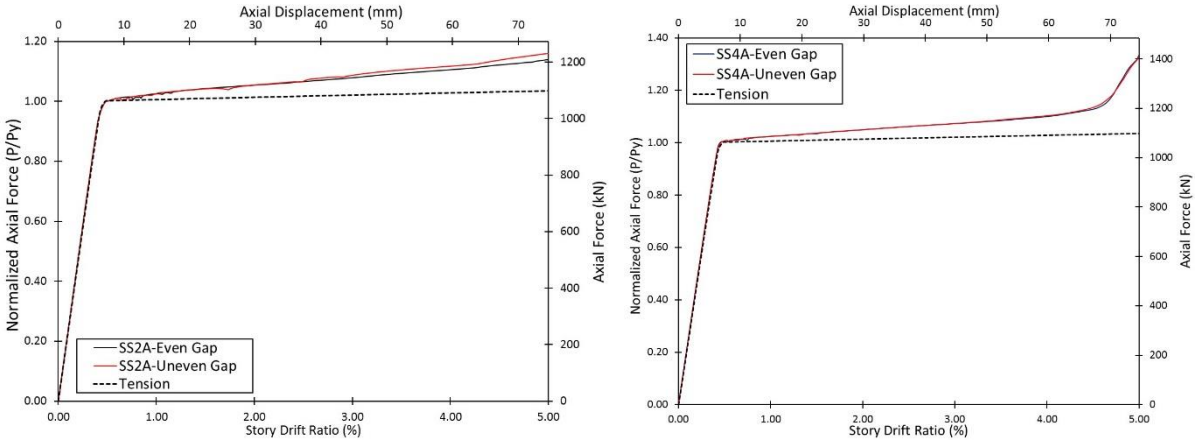

(a) SS2A (b) SS4A

Figure 2.33. Effect of gap distribution on TinT-BCB behavior

3.3.5. Conclusions on the parametric study

The FEM-based parametric study is carried out on TinT-BCBs to evaluate the impact of the key parameters, interactively. Performance of a TinT-BCB is mainly affected by three parameters: (a) The gap between the main brace and the buckling controller, (b) The friction coefficient, (c) Relative stiffness of the buckling controller. The model-based numerical simulations focused on the three factors, and quantified the impact of these parameters on cyclic behavior of the buckling-controlled braces. The conclusions can be drawn as follows:

(1) The thickness ratio of the buckling-controller over the load-bearing tube decides the effectiveness of buckling control. In general, the thickness ratio of 1.0 is sufficient to control global buckling, but a larger than 1.0 ratio is needed to control both local and global buckling.

(2) The gap between the two tubes is a sensitive parameter influencing local buckling, as well as global buckling. The smaller the gap, the less likely the local and global buckling will occur, but the more participation of the buckling controller in compression load bearing is observed due to an adverse interaction between the two tubes.

(3) The friction between the two tubes is a very delicate factor because its impact on the cyclic behavior of BCB varies heavily depending on other two primary factors. The impact of the friction becomes more prevailing when the gap is near zero and the buckling controller is heavier than the inner tube.

(4) Since each parameter is strongly influenced by the other two, the interaction among the three key parameters plays a decisive role on the overall cyclic response and the fracture life of TinT-BCBs. It seems that a higher cyclic performance can be achieved by combination of having a small gap (near-zero) amplitude, a buckling controller thicker than the main brace and utilizing a low-friction coating. As shown in Fig. 2.34, the cyclic response of TinT-BCB was substantially improved compared to that of a conventional bracing with the same size when the optimum parameters are adopted.

(5) Some less optimal but lower costly design combinations might consist of a noticeable gap and various sizes of the buckling controller so that the buckling of braces might be possible but controlled under targeted story drift limit.

(6) Although the impact of uneven gap distribution may increase as the tolerance between the tubes increases, the initial gap distribution along the brace length had little effect on the inelastic behavior of TinT-BCBs.

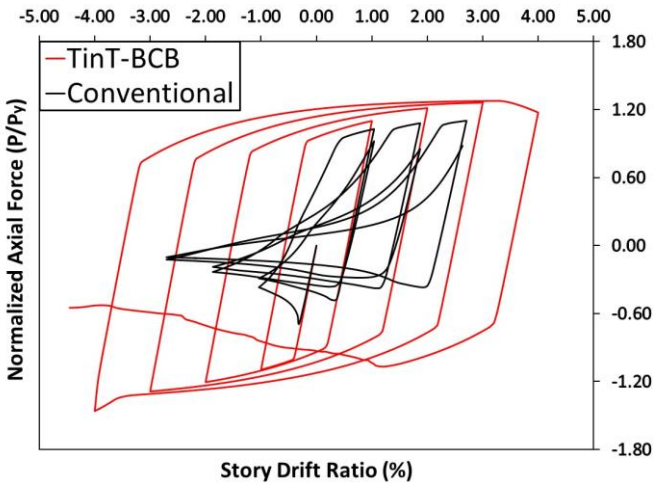

Figure 2.34. Comparison between a TinT-BCB with optimal design parameters and a conventional brace.

4. Application Example

This simple buckling-controlled brace system presented in the previous sections was used to modify a full-scale special concentrically braced frame (SCBF) tested by Uriz and Mahin (2008). The details of the loading protocol used in the study and cyclic behavior of the tested SCBF can be found in the introduction. The tested frame, shown in Fig. 2.35(a), was designed with an assumption that it would have around 2.0% overall drift ratio (ODR) without any fracture. However, the first-story brace completely fractured at 1.35% ODR (roof displacement divided by the total height) after local buckling due to out-of-plane buckling (Uriz and Mahin 2008). The simulation was able to predict the cyclic behavior as well as global and local buckling of the braces observed from the test, as shown in Fig. 2.35(b), (c) and (d).

The existing square HSS6x6x3/8 braces encased with square HSS7x7x1/2 buckling-controllers (outside tube) in both stories with all other members the same as original SCBF (Fig. 2.36b). The relative thickness of the outer tube was 1.33 times the inside tube and the gap amplitude between the tubes was 1/32”. Since the gap amplitude employed for the

modified frame was optimal, the gusset plates was not fastened with reinforcing stiffeners, as shown in Fig. 2.36(b). The loading protocol used in the simulation was identical to that is adopted for the experiment (Uriz and Mahin 2008).

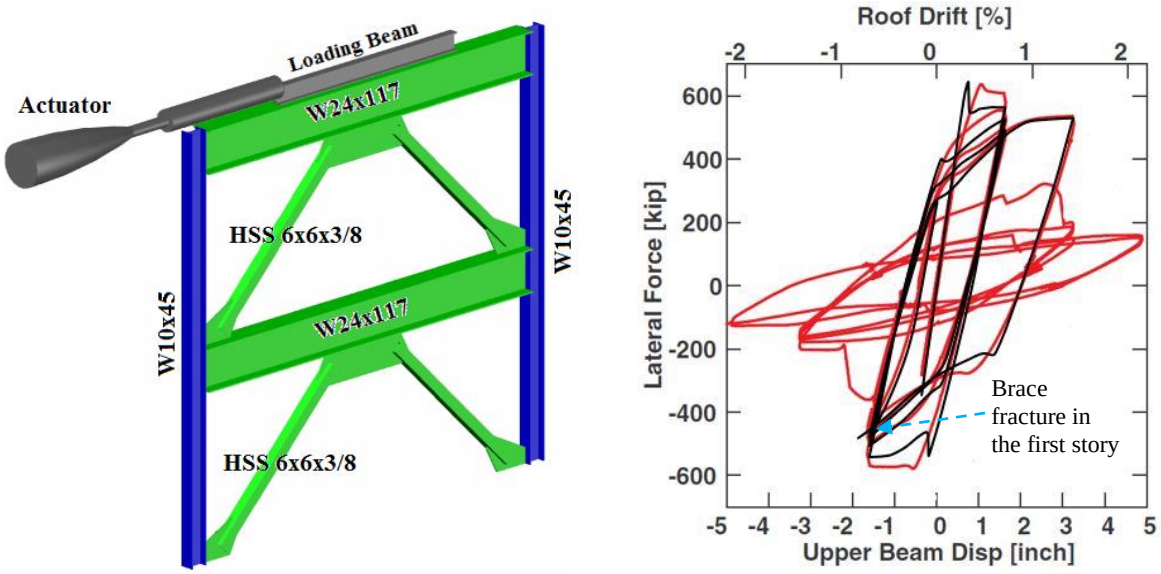

(a) Tested SCBF (Uriz and Mahin 2008) (b) Cyclic response of test and simulation

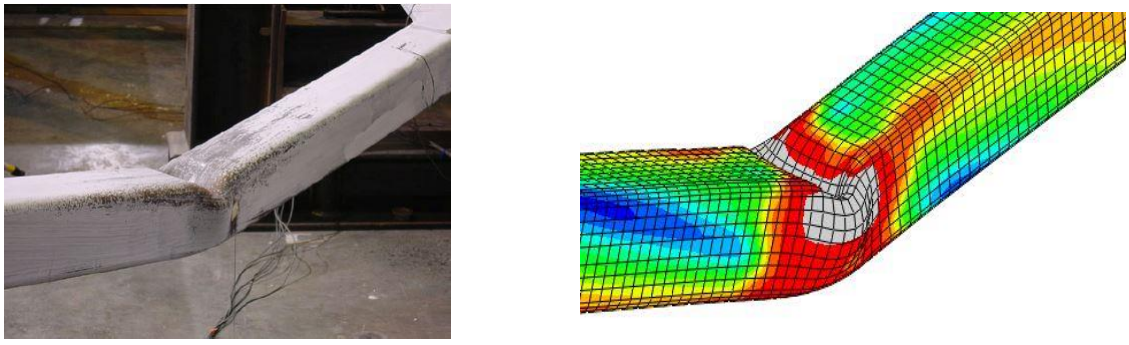

(c) Local buckling of the tested brace (d) Local buckling of the simulated brace

Figure 2.35. The tested and simulated full-scale SCBFs

The overall cyclic responses of the conventional and the modified frames are presented in Fig. 2.36(a) in terms of roof displacement and base shear. The hysteresis of the modified frame remained substantially stable throughout the loading protocol. As seen in Fig. 2.36(a), significant energy dissipation and higher lateral strength was attained with the

incorporated buckling-controllers. The enhanced frame did not experience global or local buckling throughout the simulation, while the panel zones suffered heavy stress, as shown in Fig. 2.36(c). Owing to the small gap amplitude employed, the conventional gusset plates did not develop significant end rotations, as anticipated. As indicated in Fig. 2.36(c), the hysteretic behavior of the TinT-BCBs was quite stable without significant strength and stiffness loss. As can be interpreted from the hysteresis of TinT-BCBs given in Fig. 2.36(c), the lower story reached a drift ratio of 3% while the maximum the second story drift was 2%. Unlike the tested SCBF, the distribution of lateral displacements along the frame height was relatively uniform in the enhanced frame and therefore plastic deformations did not concentrate in the lower story. It is also noteworthy that the cyclic response of the braces located at each story level exhibited a very similar hysteretic behavior, which mitigates the unbalanced vertical forces on the brace-intersected girders substantially. The relatively large stress distribution in the middle portions of the girders was caused by local stresses, which were concentrated along the length of the loading beam on the roof and the mid-gusset plate length in the first story. Note that the structural members and gusset plates of the tested SCBF were not altered when modifying the original SCBF. The frame was modified only by encasing the conventional braces with the outer tubes to control the buckling of the braces. As previously mentioned, gusset plate dimensions in a newly designed TinT-BCBF do not require large gusset plates sizes as in conventional CBFs, which would substantially reduce the local stress concentrations as well as flexural demands in columns.

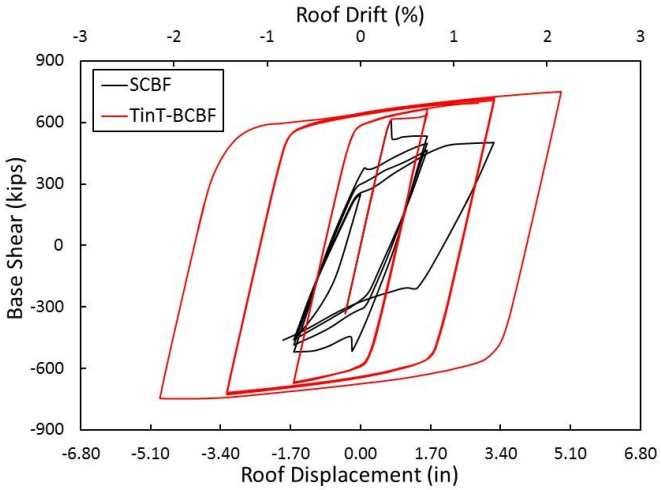

(a) Comparison of overall responses

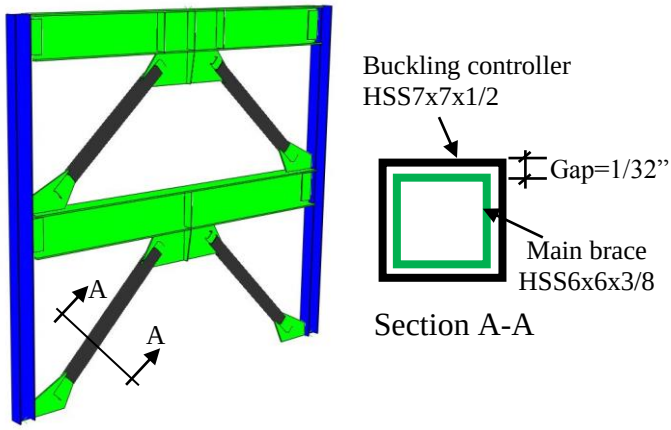

(b) The enhanced CBF with TinT-BCBs

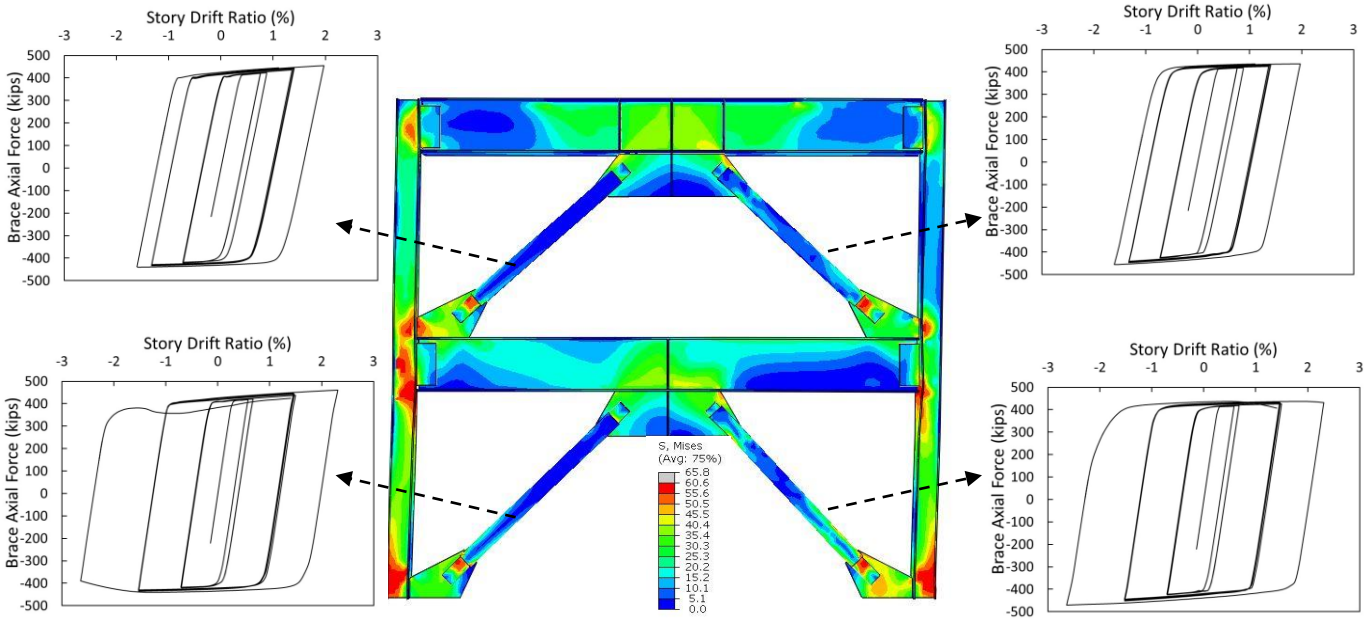

(c) Deformed shape of BCBF and hysteretic response of TinT-BCBs at last stage

Figure 2.36. Comparison of a full-scale conventional SCBF and the enhanced CBF with TinT-BCBs.

Overall, the enhanced frame showed a satisfactory cyclic performance in terms of hysteretic stability and uniform distribution of lateral deflections. Thus, BCBF applications without gusset plate reinforcement can be a cost-effective alternative for the seismic force resisting systems with high ductility demand when optimal design parameters are utilized.

5. Summary and Conclusions

A new and simple buckling-controlled brace, which has a high potential in terms of cost efficiency, constructability and performance, has been described and discussed through the combination of experimental and numerical studies. Experimental study consisted of testing of a set of small-scale BCB specimens under cyclic loading. The experimental portion of the study achieved the intended goals of identifying the impact of the controlling parameters as well as the significance of the connection design when optimal design parameters were not utilized. The aim of the second phase of the study was to investigate the impact of the previously identified parameters on the cyclic response and to discover the interrelationship among the key parameters. The FEM-based parametric study clearly achieved its objective of divulging the interaction among the parameters and identifying the optimal and practical range for the parameters so as to successfully attain the targeted performance level. Further, the example application has demonstrated its potential to significantly improve seismic performance of conventional steel braced frames in an economic way.

The findings presented in this study expand the previous work in the literature and develop an effective substitute for conventional braces, not only because of its promising cyclic behavior but also owing to the simplicity that is offered for the engineering practice. Furthermore, our study allows the future studies to elaborate on the all-steel type BRBs by providing a framework for the researchers. The key conclusions reached from the experimental and numerical results can briefly be summarized as follows:

(1) The experimental results are encouraging that the idea of encasing a tubular bracing with another to form a tube-in-tube cross-section offers an efficient way of enhancing fracture life and energy dissipation capability of the load-bearing tube.

(2) The gap amplitude between the tubes, the coefficient of friction between the contact surfaces and the relative stiffness of buckling-controller (the outer tube) are found to be the most influential parameters on the cyclic stability and fracture life.

(3) The interaction among the parameters is not straightforward, since there is a case-dependent interrelationship between the identified parameters. Thus, the impact of the key parameters cannot be evaluated individually without considering the conditions of the other parameters:

- The peak and cumulative inelastic ductilities are primarily governed by the relative stiffness of the outer tube when small to moderate gap amplitudes are employed.
- Formation of localized plastic deformations in the main brace (the inside tube) is mainly controlled by the amplitude of the gap. This impact can be amplified or condensed by the relative stiffness of the buckling-controller.
- Symmetry of hysteretic behavior is governed by the friction coefficient when the gap amplitude is near-zero and the outer tube is heavier than the inside tube.

(4) An optimal performance can be achieved by combination of having a small gap (near-zero) amplitude, a buckling controller thicker than the main brace and utilizing a low-friction coating.

(5) Gusset plate reinforcement is a necessity to succeed in securing a significant plastic deformation capability when the gap amplitude was large, but in spite of that the test results

(TinT#1) indicated that gusset plates without stiffeners can provide sufficient ductility and be an economical solution for the structural systems with less ductility demand.

(6) It is evident from the FE simulation of the modified SCBF, BCBF applications without gusset plate reinforcement can be a cost-effective alternative for the seismic force resisting systems with high ductility demand when optimal design parameters are utilized.

(7) The clearance of two times the gusset plate thickness ($2t_g$) between the brace end and the assumed fold line recommended for conventional brace connections in SCBFs, which results in tapered shaped large-size gusset plates, is not necessary for the gusset plates of TinT-BCBFs. Therefore, the economy in gusset plate design of BCBFs would reduce the overall cost of BCBFs substantially. In other words, a greater energy dissipation capacity can be achieved with little or no additional cost by employing BCBs as a substitute for conventional braces.

(8) Buckling control would play an important role on the brace-intersected beam response. Symmetrical hysteretic behavior of the BCBs might significantly reduce the seismic demand on the brace-intersected girders imposed by the unbalanced forces.

CHAPTER III

ELONGATION OF FRACTURE LIFE OF COLD-FORMED TUBULAR BRACINGS

1. Introduction

Concentrically braced frames (CBFs) are advantageous to the steel construction industry owing to their efficiency in terms of labor cost, ease of construction and large initial lateral stiffness that limits the lateral deflections, but nevertheless seismic performance of conventional CBFs is far from perfect. Diagonal bracing members in ductile (special) CBFs are designed as primary seismic energy dissipating mechanisms so that structural damage can be limited with bracings. Thus, overall structural performance in ductile CBFs can be associated with plastic deformation capability of the bracing members. In this regard, two major drawbacks raise concerns about incorporating conventional buckling braces, which would substantially affect the overall seismic response as well as performance of ductile CBFs: (1) Local buckling-induced premature fracture and, (2) Unsymmetrical hysteretic behavior of bracing members.

Early experimental data on testing of conventional buckling braces indicated that the majority of the tested conventional braces were composed of double-angles, double-channels, WT- and W-shapes (Jain et al. 1978, Black et al. 1980, Astaneh-Asl et al. 1982, Leowardi and Walpole 1996), which generally possess longer fracture life, on the order of 50% (Tremblay et al. 2008) to 85% (Fell et al. 2009), compared to tubular braces. However, braces in braced frame steel construction today are often comprised of cold-formed tubular steel bracings (circular or rectangular) for their economy with regard to low material cost and less labor-intensive connections. Hence, it might not be the most rational way to justify the

anticipated ductility of special CBFs based on the tested brace specimens predominantly made of double-angles (Astaneh-Asl et al. 1982) and W-shapes (Black et al. 1980, Leowardi and Walpole 1996) and to establish a design procedure accordingly.

Recent studies on testing of conventional tubular brace specimens consistently addressed that the localized strain demands lead to premature fracture of conventional braces during the first or second reversed tension cycle following the severe local buckling of the braces (Tremblay et al. 2008, Fell et al. 2009, Shaback and Brown 2003, Goggins et al. 2006, Han et al. 2007, Uriz and Mahin 2008). In order to quantify the energy dissipation capability of conventional tubular bracings, the experimental data reported by Shaback and Brown (2003), Han et al. (2007), Tremblay et al. (2008) and Fell et al. (2009) has been collected and summarized in Table 3.1. Note that the data included herein selected exclusively for hollow sections that are, more or less, close to the commonly used sections in practice. Likewise, test specimens with unrealistic effective slenderness (KL/r) and width-to-thickness (b/t or D/t) ratios were also excluded. Despite the fact that increasing the effective slenderness ratio (Tremblay 2008) or reducing width-to-thickness ratio (Tremblay et al. 2008, Fell et al. 2009) of any type of bracing most likely to improve the capability to withstand inelastic deformations, it is not realistic to enhance the ductility of braces in an actual braced frame by altering the KL/r and b/t ratios, due to the necessity to satisfy the strength requirements with a very limited number of available large-size hollow structural sections (HSS) that meet the section ductility requirement stipulated in the Seismic Provisions (AISC 2010b). Therefore, the recent test results presented in Table 3.1 call attention to the peak ductility ratios (μ) of large-size braces (e.g. HSS254x254x15), which are frequently utilized in the ductile CBF constructions in the seismic-prone zones and typically possess lower KL/r and larger b/t (or

D/t) ratios (Tremblay et al. 2008) compared to the small-size brace specimens that have been extensively detailed in the literature to date (Jain et al. 1978, Goggins et al. 2006, Zayas et al. 1980, Archambault et al. 1995, Nip et al. 2000).

Table 3.1. Peak brace ductilities of the recently tested tubular bracings

Item	Test ID	Brace Member (mm x mm x mm)	b/t or D/t	KL/r	Peak Brace Ductility (μ)*	Reference
1	S85-14	HSS100x100x6	13.7	85	10.00	Han et al. (2007)
2	HSS1-1	HSS102x102x6.4	14.2	77	8.90	Fell et al. (2009)
3	3B	HSS127x127x8.0	15.0	65	6.00	Shaback and Brown (2003)
4	2B	HSS152x152x9.5	12.1	52	7.00	
5	RHS19	HSS254x254x15	14.2	60	8.00	Tremblay et al. (2008)
6	RHS2	HSS254x254x15	14.2	40	6.00	
7	CHS2	HSS273x9.5	30.8	62	10.00	
8	CHS1	HSS273x9.5	30.8	42	8.50	

*The given ductility ratios are estimated from the published plots.

Further, a recent test program on full-size bracings made of HSS undertaken by Tremblay et al. (2008) emphasized that fracture initiation in square or round cold-formed HSS bracings likely to take place at around an equivalent story drift ratio of 2% soon after local buckling, while several studies on inelastic dynamic behavior of ductile CBFs (Uriz 2005, Sabelli et al. 2001, Sabelli et al. 2003, McCormick, 2007) addressed that the seismic drift demands on ductile CBFs can exceed 4.00%. It is, therefore, questionable if steel braced frames that incorporate conventional buckling braces fabricated from cold-formed hollow sections are capable of bearing seismic demands on the structure without failing. This high discrepancy between the fracture-prone nature of conventional tubular bracings and the severity of the expected seismic drift demands on the seismic force resisting system strongly recalls the presumptions about the typical pre-Northridge connections in special moment-resisting frames (SMRFs) prior to the earthquake of 1994 (FEMA 2000b).

Efficiency of the developed tube-in-tube buckling-controlled braces (TinT-BCBs) is discussed thoroughly in the previous chapter, but in spite of their substantial cyclic performance, due to their closed cross-sectional form, TinT-BCBs can only be employed to new CBFs. Considering popularity of the conventional CBFs in seismic areas and potential problems associated with their seismic performance, it was critical to develop a simple and effective performance-enhancing technique for existing CBFs. For this purpose, existing square or round hollow sections are encased with two channels that are attached to each other with fillet welded stitches, as shown in Fig. 3.1. It should, however, be noted that this brace configuration, which shares a similar concept with TinT-BCBs, can be employed to both new and existing CBFs. Furthermore, utilizing two channels as a buckling controller provides the design flexibility of adjusting the gap amplitude between the existing brace and buckling-controller freely.

Since optimal design parameters, such as small gap, stiff buckling controller and low contact friction, for stable hysteretic response are already examined, this chapter aims at investigating the efficiency of the developed BCBs with a special emphasis on the difficult task of evaluating the strain demands on the load-carrying system of BCBs, utilizing the strain data obtained from both the strain gauges and FE simulations. Note that the published literature on brace tests to date showed that the difficulties of introducing measured strain data to the discussion has not yet been challenged expect for a few studies (Han et al. 2007, Martinez-Saucedo et al. 2009, Haddad 2015), which were conducted to exclusively reveal the behavior of the connections. With the purpose of exploring the strain demands on the load-bearing system in BCBs, the strain readings obtained from testing and simulation of TinT#1 specimen are compared. Then, recently tested large-scale isolated tubular brace specimens

(Tremblay et al. 2008) and a tested full-scale ductile CBF specimen (Uriz and Mahin 2008) have been simulated and enhanced with buckling controllers to quantify the efficiency of the developed BCBs by means of the axial strain demands on the load-bearing system.

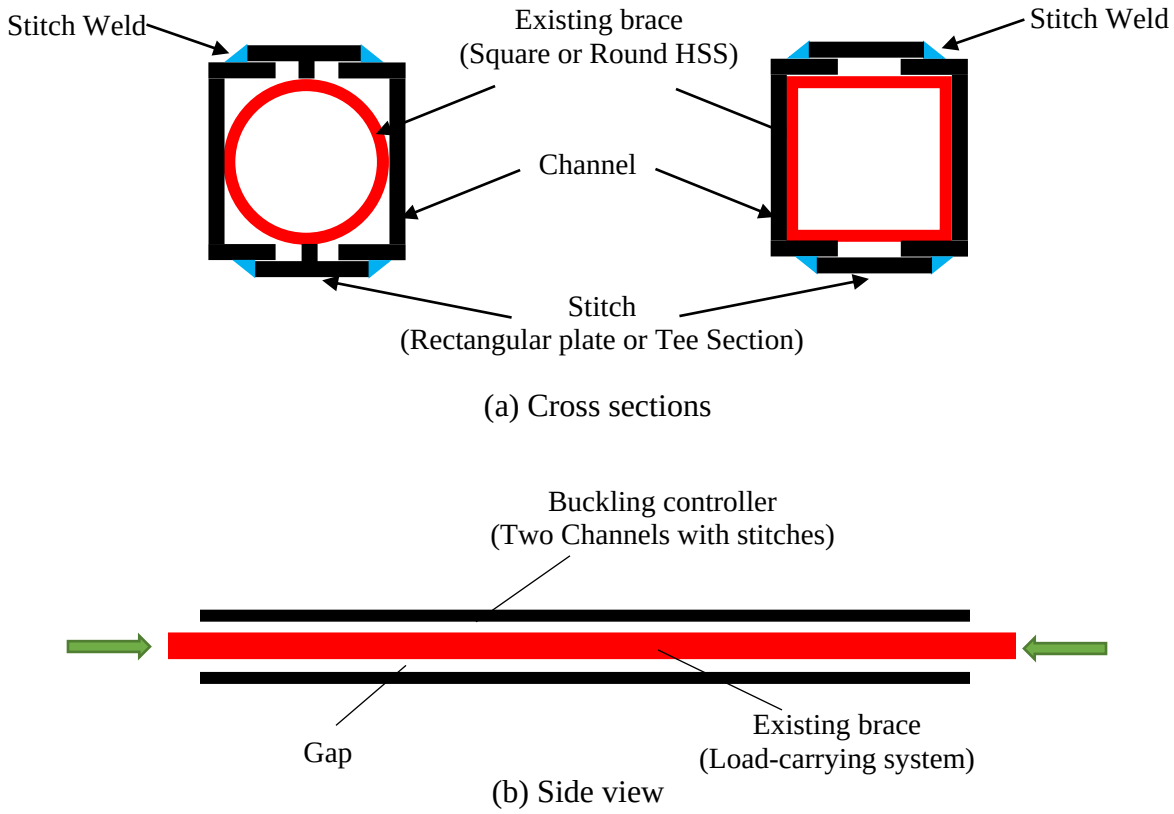

Figure 3.1. Scheme of the developed channel-encased BCBs

2. Effect of Stitch Spacing on Local Plastic Deformations

The first phase of the present study is to examine the developed channel-encased BCBs in terms of capability to alleviate local plastic deformations. For this purpose, two different BCB configurations with rectangular steel plates and Tee-shaped connectors (stitches) have been investigated through non-linear FE simulations. In order to reduce the computational cost due to cyclic loading, the specimens were subjected to monotonic compression and tension, respectively. Similar to the parametric study on TinT-BCBs, the

square HSS4x4x1/4 specimen tested by Fell et al. (2009) is adopted for the existing brace of all simulation cases of the first phase. Additionally, coefficient of friction is assumed and specified as 0.30 (bare steel surface) for all simulation cases. Since validation of the FE model with test results is presented in the previous chapter, the details of FE modeling is not included in this chapter.

2.1. Stitches made of rectangular plates

An ensemble of FE simulations was carried out on SHS-Ch-Pl group, which consist of a square hollow section (SHS) as existing brace, two channels (Ch) as buckling controller, and rectangular steel plates (Pl) as stitches. Fig. 3.2 shows the cross-section of the SHS-Ch-Pl models. Rectangular plates were fillet welded to the two channels to form a closed section for buckling-controller. Note that steel plates were utilized as stitches for their advantage of having wide variety of sizes.

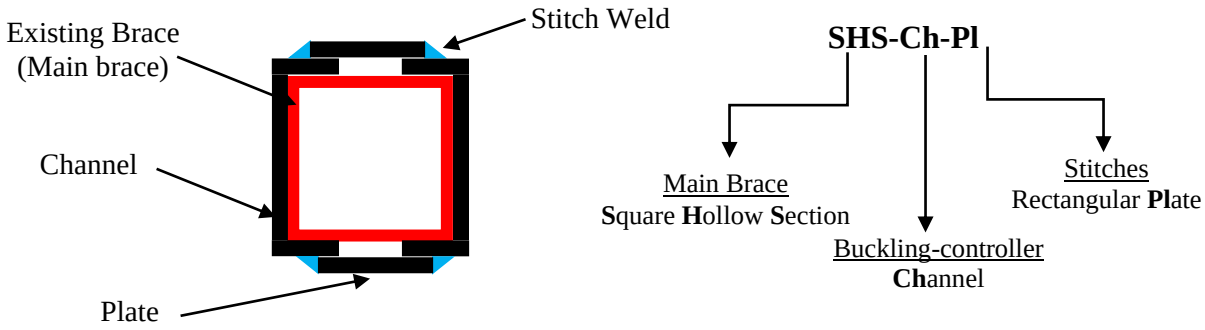

Figure 3.2. Scheme of SHS-Ch-Pl group

Table 3.2 presents the parameters of analysis cases for SHS-Ch-Pl configuration. The length and size of the existing brace, buckling controller section, in-plane and out-of-plane gaps were kept constant for all analysis cases while the stitch size and spacing between the stitches were altered. Buckling-controllers comprised of two C5x9 for all cases while three

different stitching methods were employed with constant and variable plate sizes. It should be noted that the difference between the in-plane and out-of-plane gaps is caused by the slope of approximately 16% on the inner flange surface of C-shapes. Therefore, the gap in the out-of-plane direction varied from 0.16” to 0.34”.

Table 3.2. Simulation cases for SHS-Ch-Pl simulation group

Model Name	Existing Brace	BC* Section	In-Plane Gap (in)	Out-of-Plane Gap (in)**	Stitch Size	Stitch Spacing	$\frac{\sum L_{stitch}}{\sum L_{BC}}$
SHS-Ch-Pl 01	HSS4x4x1/4	2C5x9	1/32”	0.34”	Pl. 4.5”x3.0”x1/4”	17”	17%
SHS-Ch-Pl 02						12”	23%
SHS-Ch-Pl 03						7.5”	30%
SHS-Ch-Pl 04					Pl. 4.5”x3.0”x1/4” Pl. 24”x4.5”x1/4”	7.5”	60%
SHS-Ch-Pl 05					NA	NA	100%

*BC: Buckling controller; **The largest gap amplitude in the out-of-plane direction; NA: Not Applicable.

Fig. 3.3 illustrates the stitch arrangements employed for SHS-Ch-Pl group and meshing of the parts (Fig. 3.3d). As shown in Fig. 3.3(a), first, with the same plate size, uniformly distributed stitch spacing (from stitch end to stitch end) was reduced from 17” to 7.5” gradually to solely observe the effect of stitch spacing (SHS-Ch-Pl 01 through SHS-Ch-Pl 03). Then, SHS-Ch-Pl 04 was developed to reduce local plastic deformations concentrated close to brace ends. The connector plates of SHS-Ch-Pl 05 case were continuously welded to the channels. Therefore, the last simulation case (SHS-Ch-Pl 05) was designed to be an extreme case, in which the plates were parts of the buckling-controller cross-section rather than acting as stitches.

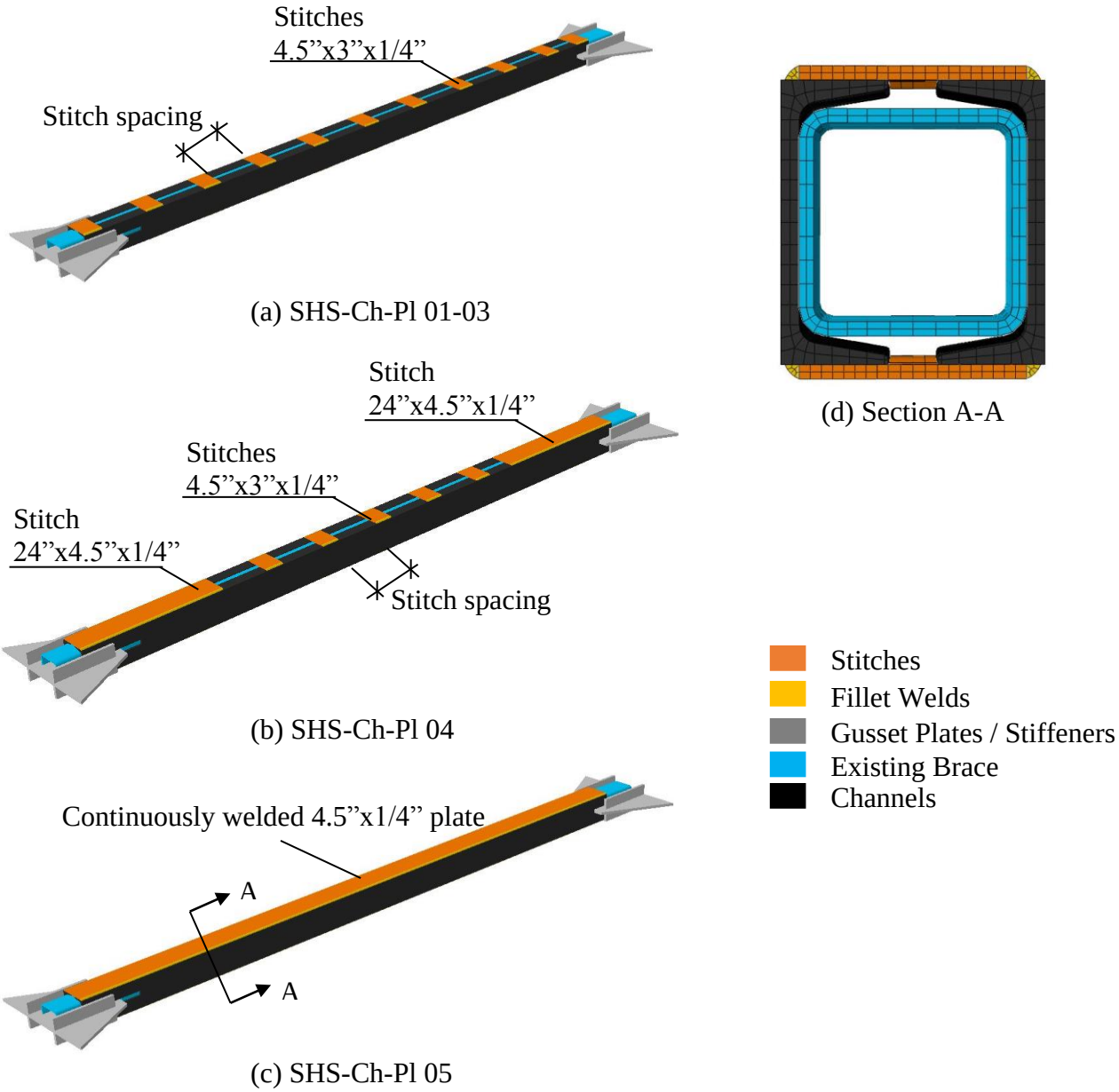

Figure 3.3. Stitch configuration of SHS-Ch-Pl group

Analyses results are given in Fig. 3.4 in terms of normalized axial force and equivalent story drift ratio (%). Note that equivalent story drift ratio is determined based on a brace inclination of 45 degree with respect to the horizontal. It seems that the buckling-controller with any stitch arrangements were successful in terms of controlling global

buckling. As a result, the brace behavior was not very sensitive to stitch spacing or arrangement until a story drift ratio of 2%. However, all specimens experienced a rapid change in stiffness and strength soon after 2% story drift ratio due to local plastic deformation of the existing brace in the vicinity of the loading end, as shown in Fig 3.5. It can be seen from the analyses results (Fig. 3.4) that a substantial increase in axial force took place for each specimen subsequent to formation of local plastic deformations, which was caused by the contribution of the buckling controller due to contact friction. The stress distributions given in Fig. 3.5 also indicate that the stress level of the buckling-controller due to local deformation of the existing brace was increased when closely-spaced stitches were employed.

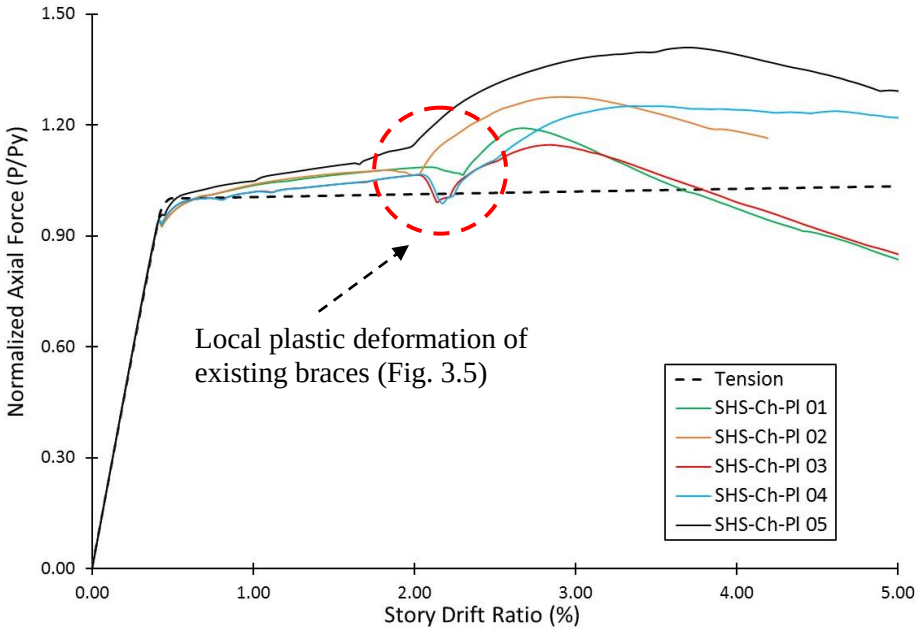

Figure 3.4. Pushover results of SHS-CH-Pl group

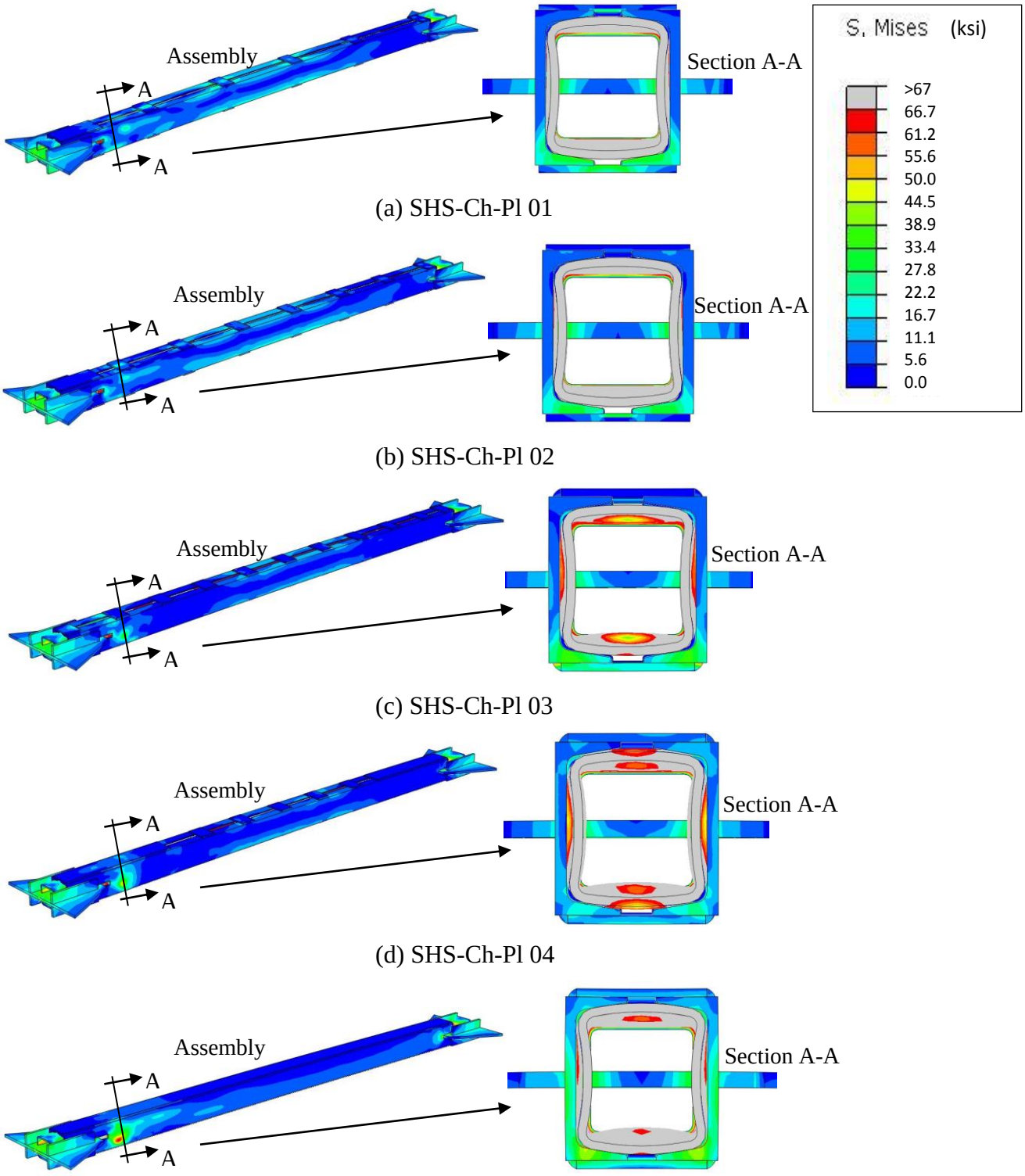

(a) SHS-Ch-Pl 01

(b) SHS-Ch-Pl 02

(c) SHS-Ch-Pl 03

(d) SHS-Ch-Pl 04

(e) SHS-Ch-Pl 05

Figure 3.5. Deformed shape and stress distribution at a story drift ratio of around 2%

On the whole, the simulation cases confirmed that formation of local plastic deformations in the existing brace is very sensitive to the gap amplitude. Owing to the slope of the inner flange surface of C-shapes, a large out-of-plane gap of 0.34" is employed. Therefore, either stitch spacing or stitch size did not influence local behavior of the existing braces significantly (Table 3.3). Development of local deformations on the buckling-controller, on the other hand, was significantly affected by the ratio of total stitch length over total buckling-controller length ($\sum L_{stitch}/\sum L_{BC}$), as given in Table 3.3. Plastic deformations imposed on the buckling-controller as well as stitch welds were more severe when the total stitch length ratio was smaller.

Further, Table 3.3 indicates that excessive local bending deformation of the buckling-controller began earlier as the stitch length ratio ($\sum L_{stitch}/\sum L_{BC}$) decreases. It is noteworthy that the configuration with variable plate size (SHS-Ch-Pl 04) exhibited a similar performance with the continuously welded plate case (SHS-Ch-Pl 05) in terms of formation of local plastic deformation on the buckling-controller. Thus, it can be concluded that the effect of the confinement provided at brace ends is more substantial than that of in the middle portion of the brace. In other words, a cost-effective application of the developed technique with a satisfactory performance can be achieved when the channels were connected with longer stitches (e.g. one fifth of the total length) at brace ends.

Table 3.3. Deformation status of SHS-Ch-Pl simulation group

Model Name	$\sum L_{stich}/\sum L_{BC}$	Local plastic deformation of existing brace	Severe BC deformation
SHS-Ch-Pl 01	17%	2.20% SDR	2.65% SDR
SHS-Ch-Pl 02	23%	2.05% SDR	2.80% SDR
SHS-Ch-Pl 03	30%	2.10% SDR	2.80% SDR
SHS-Ch-Pl 04	60%	2.10% SDR	3.50% SDR
SHS-Ch-Pl 05	100%	2.05% SDR	3.60% SDR

2.2. Stitches made of tee shapes

The analyses conducted in the previous section clearly demonstrated that independent from the size or spacing of the connectors, the large gap amplitude adopted for out-of-plane direction resulted in formation of severe local plastic deformations prematurely. Still, the analysis cases for SHS-Ch-Pl group helped establish concepts for economical stitch arrangements. As shown in Fig. 3.6, in order to reduce the gap amplitude, in lieu of using rectangular plates, wide flange tee (WT) shapes were implemented as stitches. With this buckling-controller configuration, it was possible to adjust both in-plane and out-of-plane gaps. This provides the ability of covering wide-variety of existing braces with different shapes and sizes in steel braced frames as well as determining the design parameters of the BCB without difficulty.

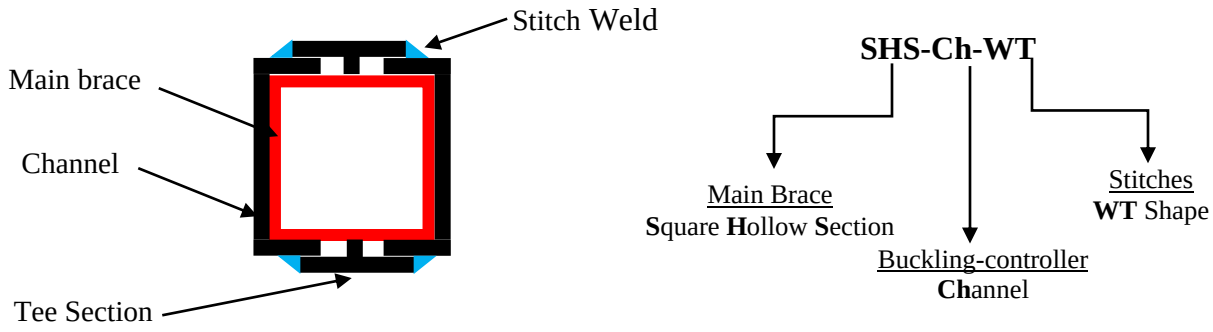

Figure 3.6. Scheme of SHS-Ch-WT group

Table 3.4. Simulation cases for SHS-Ch-WT group

Model Name	Existing Brace	BC Section	In-Plane Gap (in)	Out-of-Plane Gap (in)	Stitch	$\frac{\sum L_{stitch}}{\sum L_{BC}}$	$\frac{\sum L_{weld}}{\sum L_{BC}}$
SHS-Ch-WT 01	HSS4x4x1/4	2C5x9	1/32”	~0	WT4x6.5	60%	60%
SHS-Ch-WT 02						100%	60%
SHS-Ch-WT 03						100%	100%

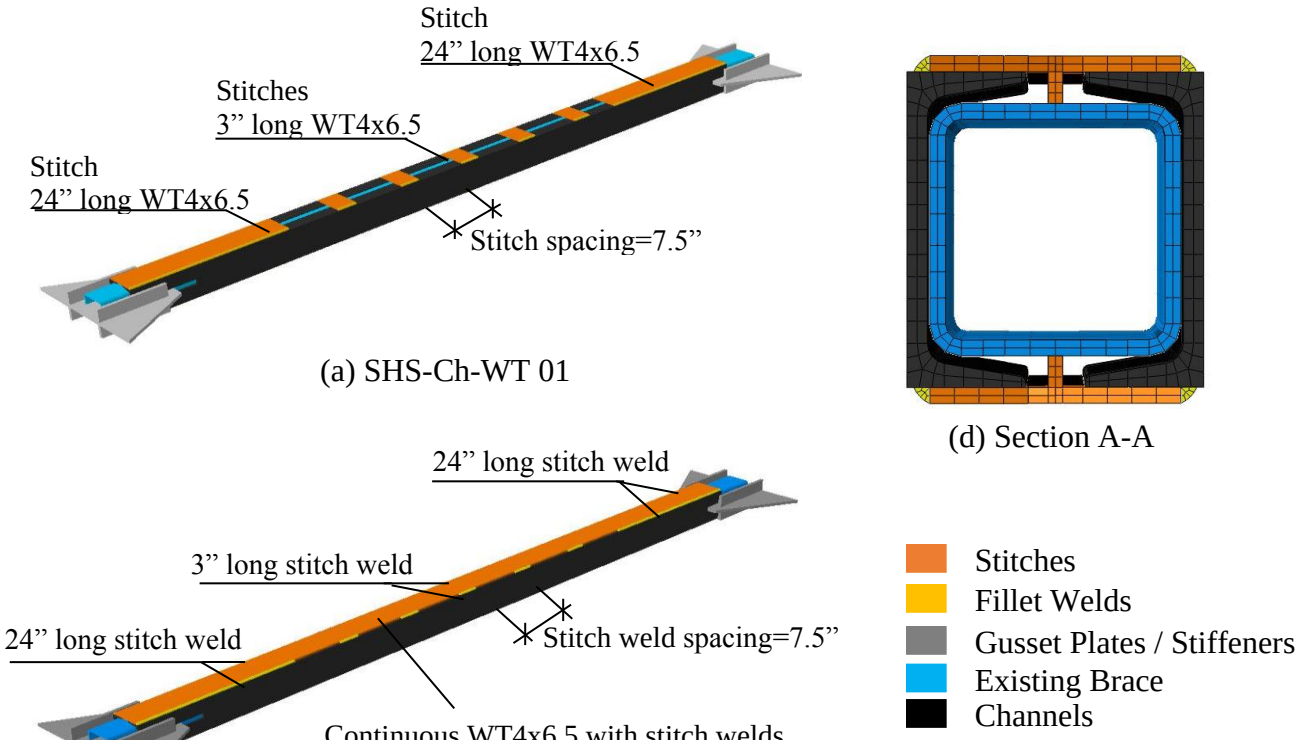

Figure 3.7. Configuration of SHS-Ch-WT group

Simulation cases for SHS-Ch-WT group are given in Table 3.4. Size of the existing brace and buckling-controller as well as the gap amplitudes were kept constant for the sake of the comparison. Out-of-plane gap was near zero for all cases while in-plane gap was adjusted to 1/32” with the purpose of accommodating lateral deformation of the existing brace as well as to alleviate the contribution of the buckling-controller to the load-bearing

system. Stitches of SHS-Ch-WT 01 consisted of a 24” long WT4x6.5 at each end and 3” long WT4x6.5 shapes in the middle portion with 7.5” spacing (Fig. 3.7a). The design was intended to provide a stiffer lateral support at the loading ends, since it was expected that plastic deformations concentrated at the loading ends rather than mid-length of the existing brace. SHS-Ch-WT 02 was designed to create a configuration with continuous WT section along the length connected with intermittent fillet welds with 7.5” spacing, as shown in Fig. 3.7(b). Note that the connector spacing of SHS-Ch-WT01 and the stitch weld spacing of SHS-Ch-WT02 were identical. The WT sections were continuously welded to the channels along the brace length and therefore acted as parts of the buckling-controller in SHS-Ch-WT 03 (Fig. 3.7c).

Pushover results of SHS-Ch-WT group and deformed shapes of the specimens at 4% story drift ratio are given in Figs. 3.8 and 3.9, respectively. Based on the pushover results and the relative stress distributions, the following can be discussed:

(1) It seems that regardless of stitch size and spacing, reducing the gap in out-of-plane direction improved the performance substantially. Existing brace and the buckling-controller of all specimens did not experience severe local deformations at a SDR of 4% (Fig. 3.9).

(2) Plastic deformations accumulated at the loading end. Therefore, either shape or arrangement of the stitches did not play a significant role on the location of the local plastic deformations.

(3) As seen in Fig. 3.8, no strength or stiffness degradation has been observed in any case. The stress distribution (Fig. 3.9) and load-deformation response (Fig. 3.8) of each SHS-Ch-WT case were virtually identical. Since the cost of welding is the same for SHS-Ch-WT 01 and SHS-Ch-WT 02, the two arrangements give designers the flexibility to compare the

material cost of having a continuous WT section along the BC length and the labor cost of cutting small pieces from the WT section.

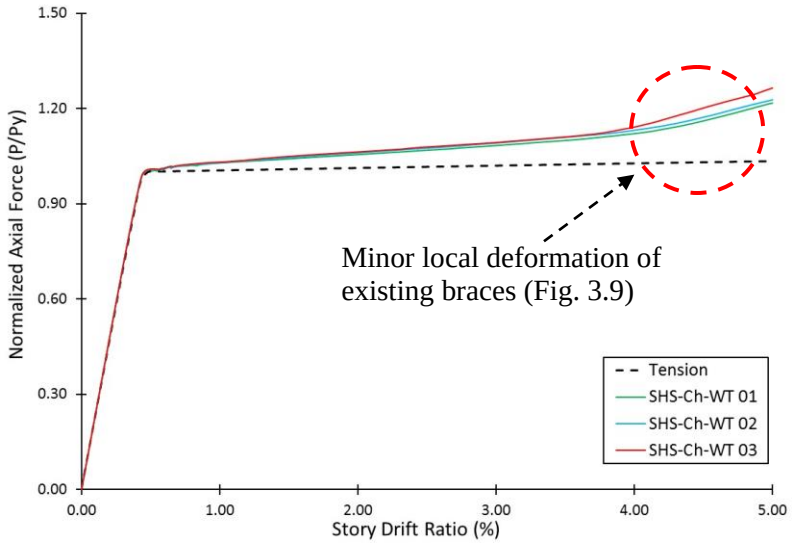

Figure 3.8. Pushover results of SHS-Ch-WT group

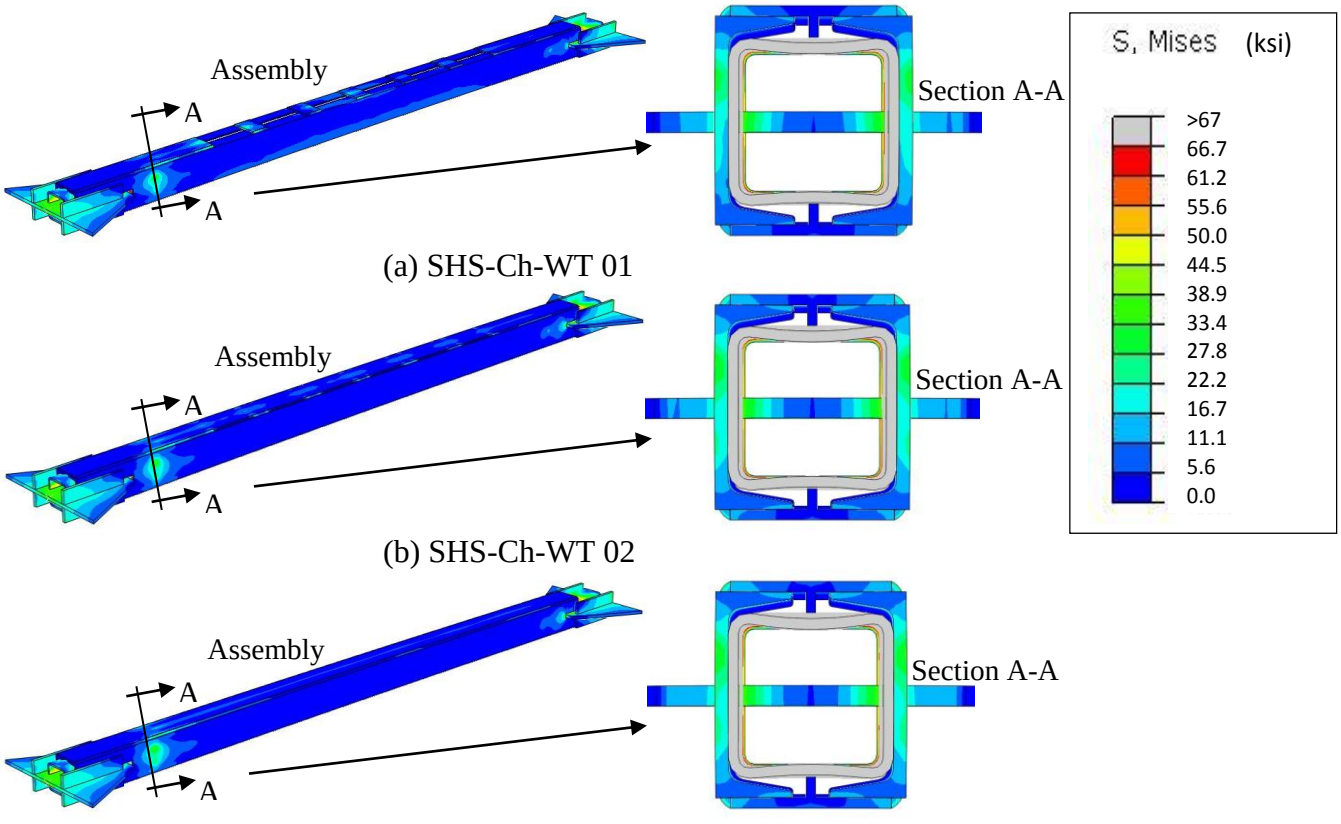

(a) SHS-Ch-WT 01

(b) SHS-Ch-WT 02

(c) SHS-Ch-WT 03

Figure 3.9. Deformed shape and stress distribution at a story drift ratio of around 4%

2.3. Key observations on channel-encased BCBs

Efficiency of two different connectors made of rectangular plates and Tee shapes were investigated through non-linear FE simulations. The key findings can be summarized as follows:

(1) The two simulation sets strongly confirmed that formation of local plastic deformations in the existing brace is very sensitive to the gap amplitude. Therefore, either stitch spacing or stitch size did not influence local behavior of the existing braces significantly when the gap amplitude was large.

(2) Employing near-zero and 1/32” gaps in out-of-plane and in-plane directions, respectively, did not develop large increase in compression strength. Thus, the gap sizes adopted for SHS-Ch-WT simulation group may be the optimum gap amplitudes to obtain symmetrical and stable cyclic response.

(3) Although channel-encased BCBs with rectangular plate connectors (SHS-Ch-Pl) are vulnerable to local plastic deformations after reaching a SDR of around 2% due to the large out-of-plane gap amplitude, they can be utilized for the structural systems that are expected to experience minor to moderate seismic demands.

(4) Overall, channel encased buckling-controlled braces are promising in terms of controlling global or local buckling of the existing braces. Most notably, the developed BCBs offer simplicity in regard to adjusting the design parameters based on the targeted cost and performance aspects.

3. Effect of Mesh Size on Strain Amplitude

The primary goal of the present model-based study is to evaluate likelihood of fracture in steel brace members. The first phase of the study focused on assessing the efficiency of the developed channel-encased BCBs in terms of mitigating local plastic deformations, which induce cracking and leads to complete fracture of bracing members. In the second phase, the goal is to reveal how the FE modeling parameters affect the simulation results such as deformed shapes, forces, displacements, deflections and strains. For this purpose, first, a full-scale SCBF tested by Uriz and Mahin (2008) is simulated and the results of the test and FE simulation are compared. Then, effect of mesh size is evaluated with regard to overall response of the CBF, as well as strain and out-of-plane deflection response of the bracings.

3.1. FE simulation of the SCBF tested at UCB

Uriz and Mahin (2008) performed an experimental study to evaluate the inelastic behavior of a conventional ductile CBF specimen, shown in Fig. 3.10(a). The specimen was nearly full-scale with 9 ft tall story height and 20 ft span length. Details of the loading protocol used in the study are given in Fig. 3.10(b). The frame designed and detailed in accordance with the design procedure and detailing requirements of AISC Seismic Design Provisions (1997). The details of the test setup and loading protocol can be found in the introduction.

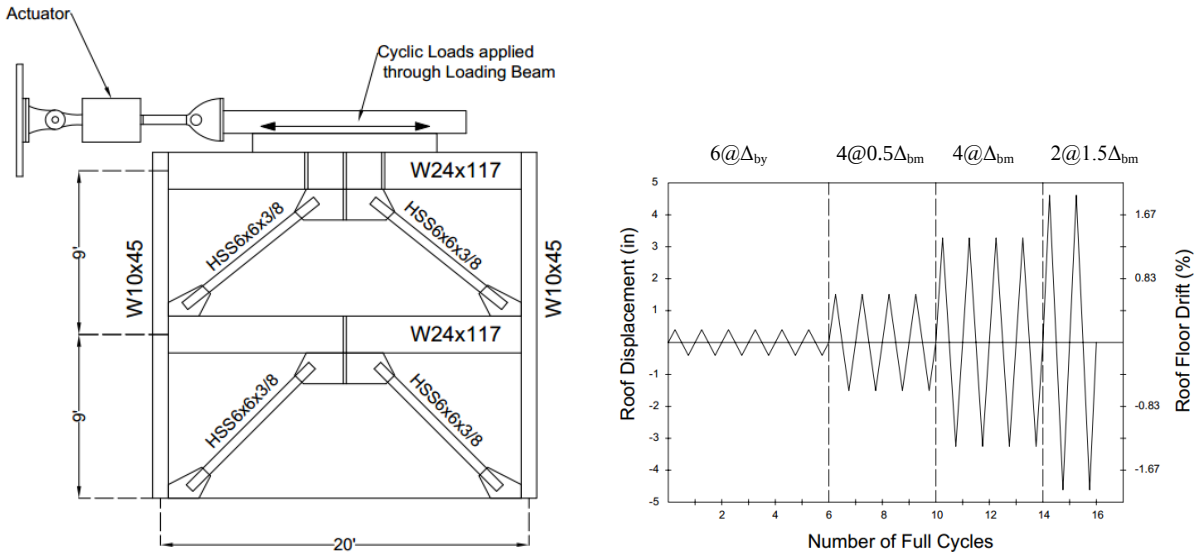

(a) Tested SCBF (b) Loading protocol

Figure 3.10. Full-scale SCBF tested at UCB (Uriz and Mahin 2008)

The FE models were built in a general purpose finite element software ABAQUS 6.12.3 (Hibbit et al. 2012). Newton-Raphson algorithm was employed to the non-linear static analyses. The FE model consisted of two W24x117 girders with a shear tab at each end, two W10x45 columns and four bracing members (HSS6x6x3/8) with a pair of 12”x4”x3/8” thick plates for net section reinforcement and a 7/8” thick gusset plates at their ends. The mesh adopted for each member is shown in Fig. 3.11(a). The mesh sizes were determined based on the observed deformation patterns during the test. Therefore, the mesh size of each member varied from location to location. The bracing members were meshed using two and seven elements across their thickness and width, respectively. The filleted corners of the square hollow sections were divided into three elements along their lengths. The mesh size of the first and second story braces along the axial direction was set to 0.8” and 2.4”, respectively, with the purpose of reducing the computational time. Since plastic deformations were concentrated on the first story braces and beam-to-column connections, the mesh size

adopted for the second story braces was coarser compared to that of the first story braces. The FE model is composed of 68,862 nodes and 40,780 linear hexahedral solid elements of type C3D8R in total.

Care was taken to simulate the testing conditions properly. Lateral supports were provided at three locations, as illustrated in Fig. 3.11(b). The nodes of the lower end of the columns and the base gusset plates were fixed. Displacement-controlled loading was applied to a surface at the top flange of second story girder, in which the loading beam connected to the girder (Fig. 3.10a).

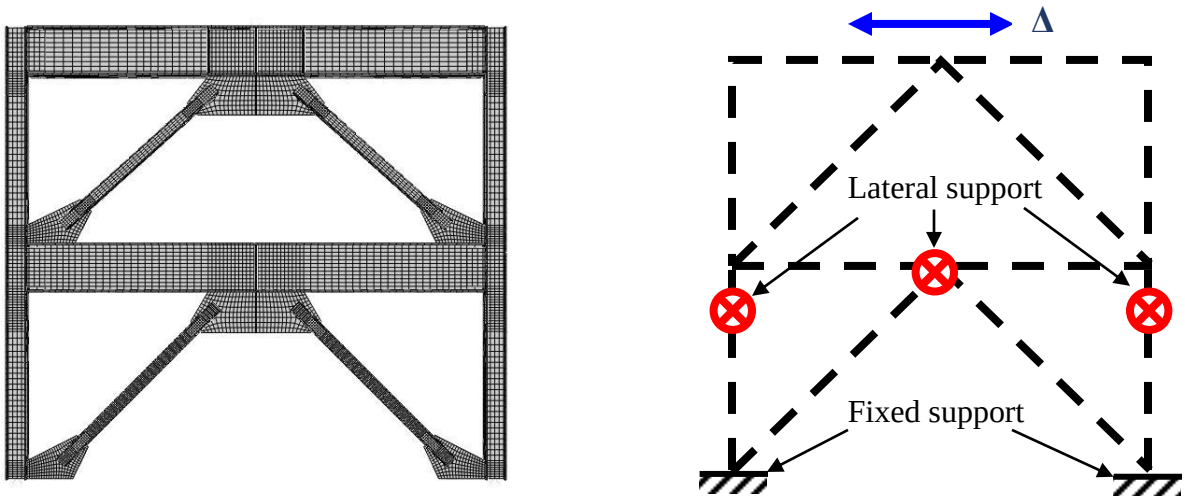

(a) Meshing of FE model (b) Restraints

Figure 3.11. Mesh and boundary conditions adopted for FE model

Material non-linearity was introduced based on the coupon test results provided by the authors (Uriz and Mahin 2008) to emulate inelastic material properties. Modulus of elasticity and Poisson's ratio were assumed to be 29,000 ksi and 0.3, respectively. Kinematic hardening rule was employed for the structural members other than braces. The mixed plasticity was introduced for braces with the following parameters: σ_o= 55 ksi, C_1=147 ksi, γ_1=25, and the rate factor was taken as b=1.

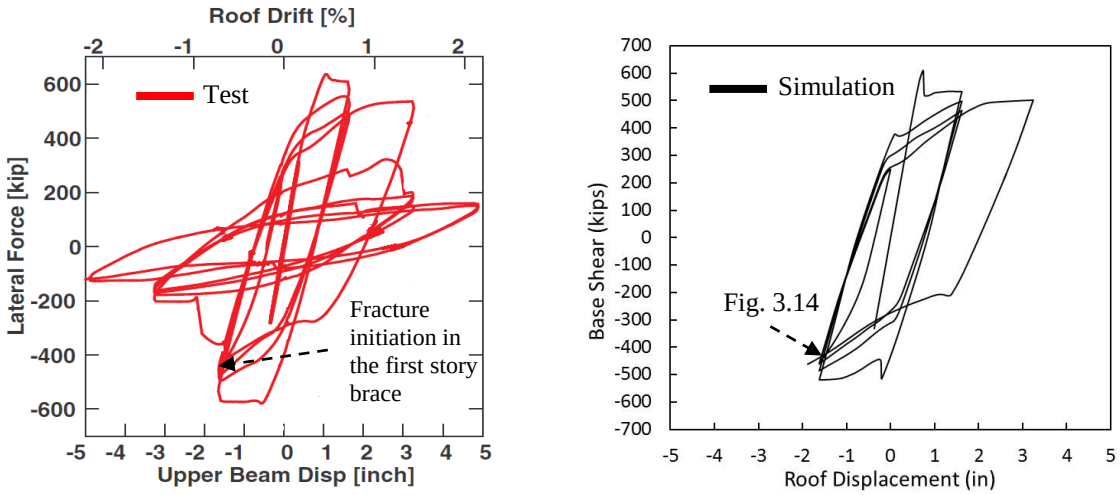

(a) Experimental results (Uriz and Mahin, 2008) (b) FE simulation results

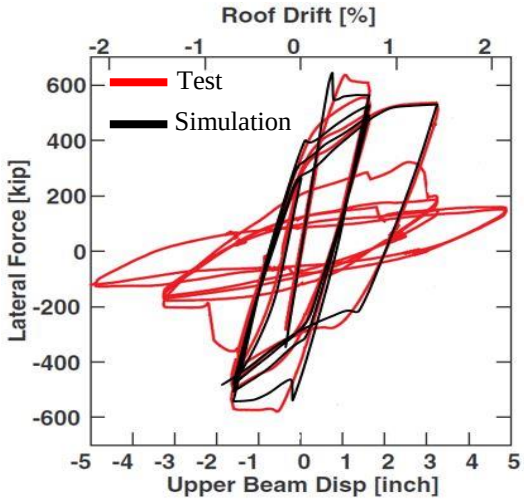

(c) Comparison of tested and simulated results

Figure 3.12. Load-displacement results of test and simulation of SCBF

First, force-displacement results and then critical deformed shapes of the tested and simulated frames are compared. Load-displacement relations of the tested and simulated frames were compared in Fig. 3.12 in terms of base shear and roof displacement. As seen in Fig. 3.12(c), the overall force-displacement relationship was satisfactorily predicted by the FE model until fracture initiation in the first story brace (Fig. 3.12a). In order to summarize the development of the damage in structural members of the tested frame, Table 3.5 and Fig.

3.13 present an overview based on the observations during the test (Uriz and Mahin, 2008). It should be noted that Fig. 3.13(a) shows the deformed shape of the frame during the last cycle at 2.8% first SDR while the deformed shapes of the beam-column connections and braces given in Figs. 3.13(b), (c) and (d) were obtained from different cycles and deformation levels with the purpose of presenting the development of structural damages in a compact way.

Table 3.5. Overview of observed deformations during the test (Uriz and Mahin, 2008)

Observed Deformation	Overall Drift Ratio*	Approximate First Story Drift Ratio**	Figure#
Severe Local Buckling of First Story Braces	1st cycle @$1.0\Delta_{bm}$ when (ODR=1.35%)	1st cycle @$1.0\Delta_{bm}$ (SDR≈2.8%)	3.13(b)
Fracture of First Story Braces	1st cycle @$1.0\Delta_{bm}$ (ODR=1.35%)	1st cycle @$1.0\Delta_{bm}$ (SDR≈2.8%)	3.13(c)
Fracture of the Column to the Right	4th cycle @$1.0\Delta_{bm}$ (ODR=1.35%)	4th cycle @$1.0\Delta_{bm}$ (SDR≈2.8%)	3.13(d)

*ODR: Lateral roof displacement divided by total height. **SDR: Story displacement divided by first story height.

The intended goal of testing was to reach an overall drift ratio of around 2% without experiencing brace fracture and plastic deformations in the members other than braces. However, the braces completely ruptured (Fig. 3.13a) from their mid-length during the first cycle at $1.0\Delta_{bm}$ (at 1.35% overall and 2.8% first story drift ratio) subsequent to severe local buckling of the braces (Fig. 3.13b). Furthermore, it was observed that the column fractured (Figs. 3.13d and e) due to the crack initiation in column flange along the fillet welds that connecting the shear tab to the column flange (Uriz et al. 2008). As presented in Fig. 3.13(a), the SCBF experienced a severe damage and gradually lost almost 65% of its lateral load capacity (Fig. 3.12a) during the first reversed cycle at 2.8% first story drift ratio. Soon after the complete fracture of the braces, large flexural deformations imposed by the beam-column connections led to crack initiation of column flange in early stages of the excursion (Fig.

3.13d). During the last cycle at 2.8% SDR, both braces completely and one of the columns partially fractured, as given in Fig. 3.13(a).

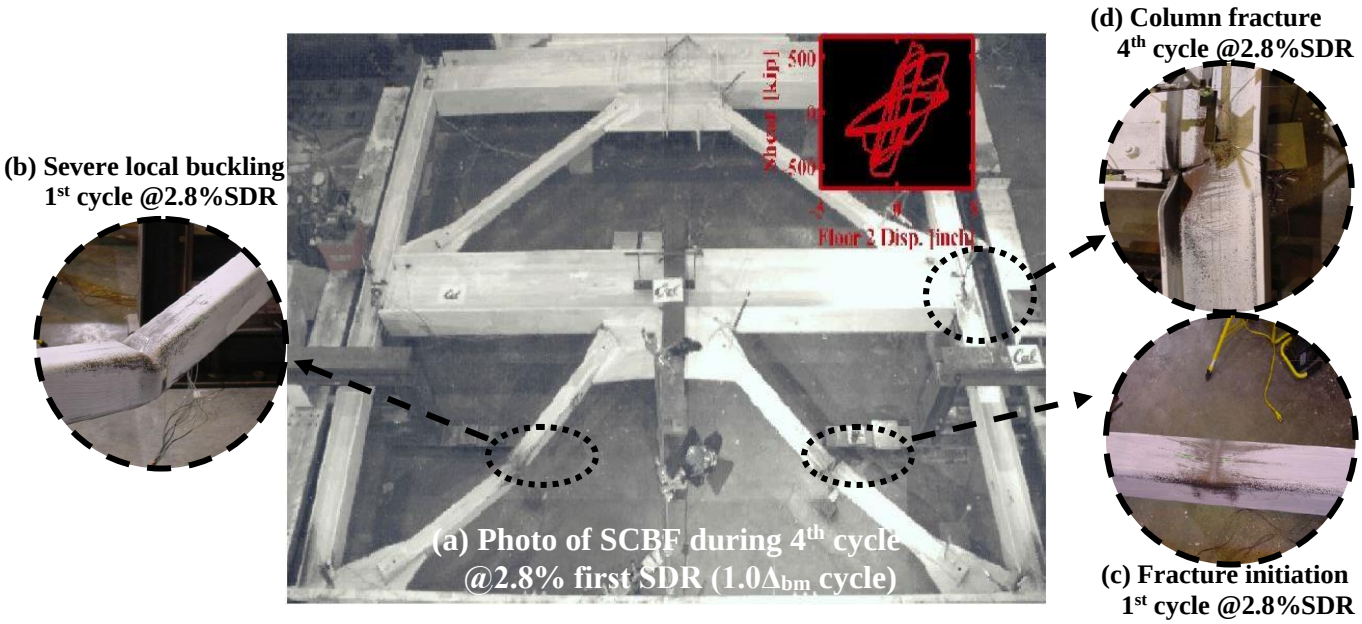

Figure 3.13. Deformed shape of the tested SCBF (Uriz and Mahin, 2008)

The deformed shapes and relative stress distributions of the simulated SCBF during the first reversed cycle to 2.8% story drift ratio ($1.0\Delta_{bm}$) are shown in Fig. 3.14. Since the goal is to develop a well-established numerical model that predicts strain amplitudes accurately, it was important to capture both overall structural response and the critical deformed shapes that induce strain concentrations, such as global and local buckling of the braces. Out-of-plane buckling of first story braces took place at a first story drift ratio of around 0.4% while the second story braces did not experience global buckling during the test and simulation. It is, in fact, observed that due to the accidental in-plane eccentricity, the first story braces experienced out-of-plane and in-plane buckling simultaneously, even though out-of-plane buckling was dominant. The FE model was also able to satisfactorily replicate local buckling behavior of the braces (Figs. 3.14b and f).

Moreover, the stress and strain concentrations at the filleted corners, in which the initial tearing began, were also captured very well, as shown in Figs. 3.14(c) and (g). Note that instead of equivalent stress, equivalent plastic strain contours were plotted in Figs. 3.14(f) and (g) so as to emphasize the local buckling-induced strain concentrations at the corners of the braces prior to fracture initiation. It was also observed that large stresses of the column flange accumulated in the vicinity lower flange of the beam (Figs. 3.14d and e). Comparing Fig. 3.13(d) and 3.14(d), indicates that local deformation of the column flange was also captured, even though fracture criterion was not introduced to the numerical model.

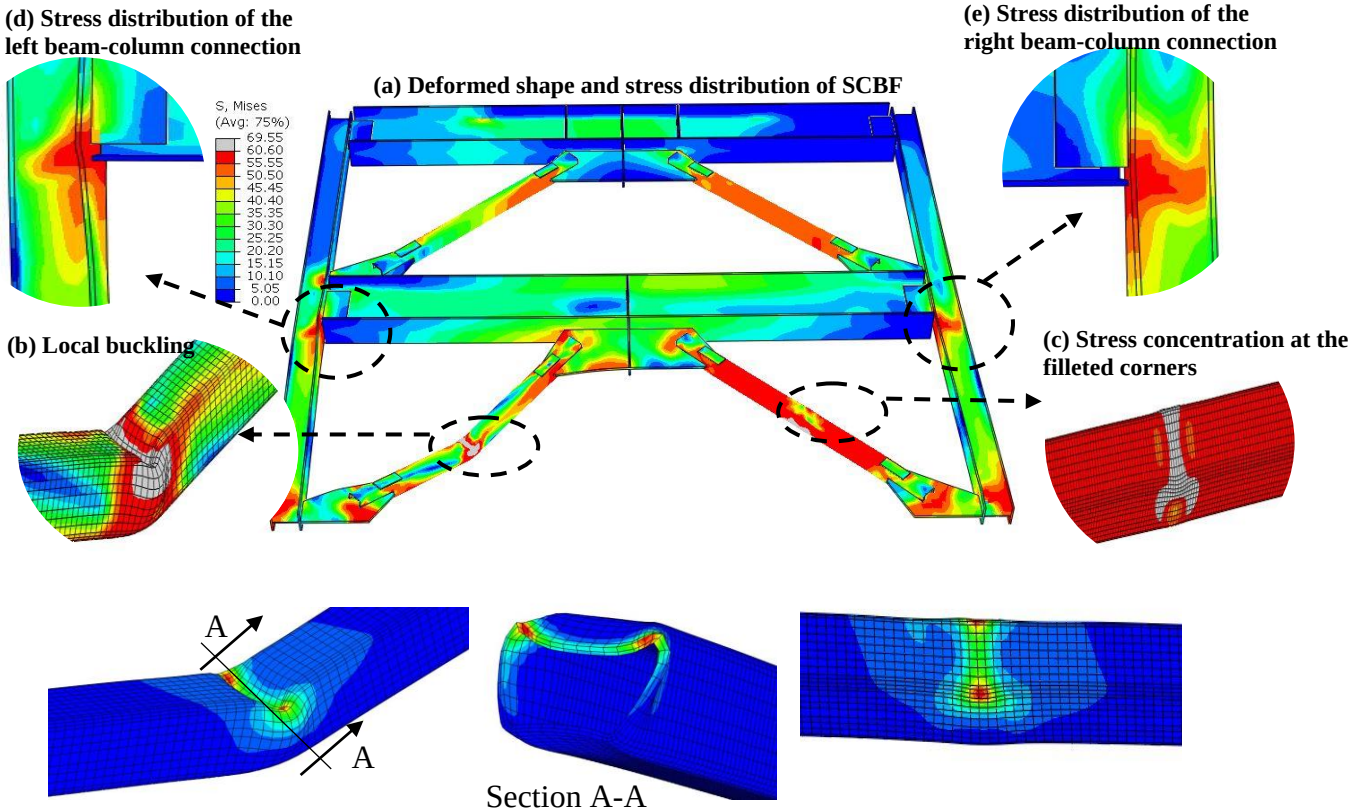

Figure 3.14. Deformed shape and stress distribution of the simulated SCBF during the first cycle at $1.0\Delta_{bm}$.

3.2. Effect of mesh size along the width and longitudinal directions

The numerical model emulated the overall force-displacement relationship, as well as the essential deformation patterns and stress concentrations observed during the physical test. Nevertheless, a mesh sensitivity analysis was carried out in order to discover the optimal mesh size for the braces along the width/depth and longitudinal directions considering the strain amplitudes, out-of-plane displacements, deformed shapes (e.g. local buckling) and computational time. Fig. 3.15 illustrates the mesh adopted for the first story braces in the simulated SCBF. As mentioned previously, the bracing members were meshed using two and seven elements across their thickness and width, respectively. The filleted corners of the square hollow sections were divided into three elements. For the sake of the comparison, only the mesh sizes along the length and flat width/depth directions were altered, respectively, for the mesh sensitivity analysis while the number of elements in the filleted corners and in the through the wall thickness (t_w) were remained constant. It was essential to consider the mesh size in each direction as a fraction of the brace dimension of concern. Therefore, with the intention of proposing a general range for the optimal mesh size of axially-loaded members, the simulation cases were established based on the normalized mesh size.

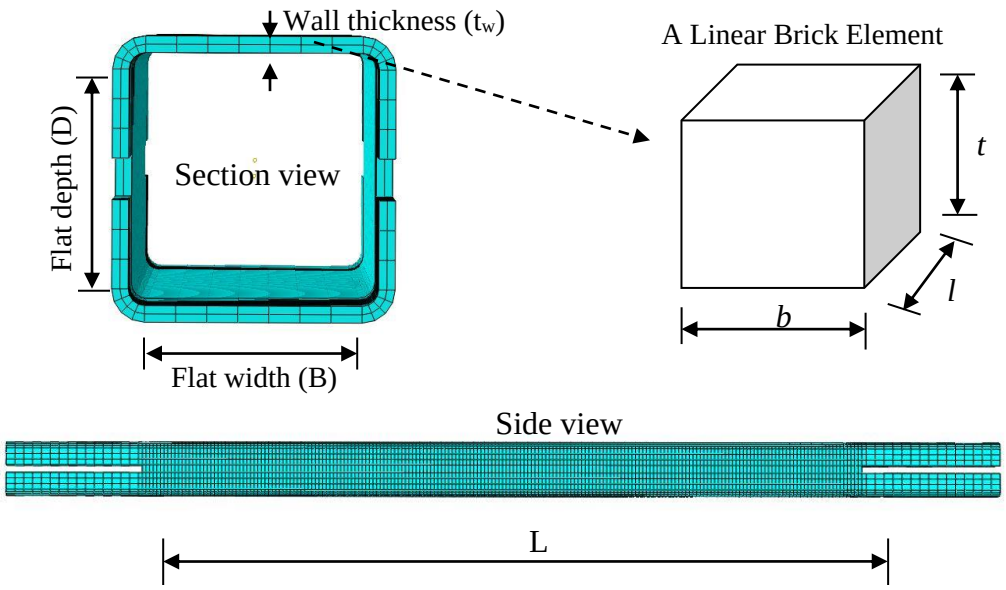

Figure 3.15. Meshing of the square hollow bracing in the simulated SCBF

Two sets of simulations were created as follows:

(a) The uniform longitudinal mesh size was adjusted in terms of the actual mesh size (l) divided by the distance from slotted end to slotted end (L). Table 3.6 presents the simulation cases with changing l/L values from 0.15% to 1.25%.

Table 3.6. Parametric study on the longitudinal mesh size

Model Name	Element size*				Normalized element size		
	t (in)	***b (in)***	***l (in)***	***Max. Aspect Ratio*****	***t/t_w***	***B/b***	***l/L***
***l/L*=1.25%**	0.175	0.658	1.00	**5.71**	0.500	7.00	**1.25%**
***l/L*=1.00%**			0.80	**4.57**			**1.00%**
***l/L*=0.50%**			0.40	**3.76**			**0.50%**
***l/L*=0.20%**			0.16	**4.11**			**0.20%**
***l/L*=0.15%**			0.12	**5.48**			**0.15%**

*D=B=4.604”; t_w=0.349”; L≈80”. **The maximum of the ratio of any two dimensions of the element.

(b) The aim of the second simulation group was to reveal how the mesh size in the flat width/depth direction affects the results. For this purpose, the ratio of flat section width (B)

over element width (b) were altered by dividing the flat width of the section into different number of elements while the other two element dimensions (t and l) were held constant, as given in Table 3.7. Note that the number of elements used in the flat width and flat depth directions was identical for each simulation case.

Table 3.7. Parametric study on the mesh size through flat width/depth

Model Name	Element size				Normalized element size		
	t (in)	*b (in)*	*l (in)*	*Max. Aspect Ratio*	t/t_w	*B/b*	*l/L*
B/b=7	0.175	**0.658**	0.80	4.57	0.500	**7.00**	1.00%
B/b=8		**0.576**				**8.00**	
B/b=10		**0.512**				**9.00**	
B/b=12		**0.384**				**12.00**	

*D=B=4.604”; t_w=0.349”; L≈80”

The simulation results were compared by means of the local buckling deformation and peak axial plastic strain at the plastic hinge location, load-displacement response of the frame and out-of-plane displacement of the braces. Fig. 3.16 illustrates the extraction process of the peak axial strain values for each simulation case. As shown in Fig. 3.16(a), (b) and (c), the maximum axial strain was obtained from the mid-section of the first story brace in compression. The peak axial strain readings of all cases were acquired from a node close to the filleted corners, in which the initial cracking of the tested brace occurred (Fig. 3.16d). Note that the red dot given in Fig. 3.16(d) represents the element node with the maximum plastic strain amplitude. However, the peak axial plastic strain values given in Figs. 3.17 and 3.18 were extracted from the integration point of an element that shares the red dotted node.

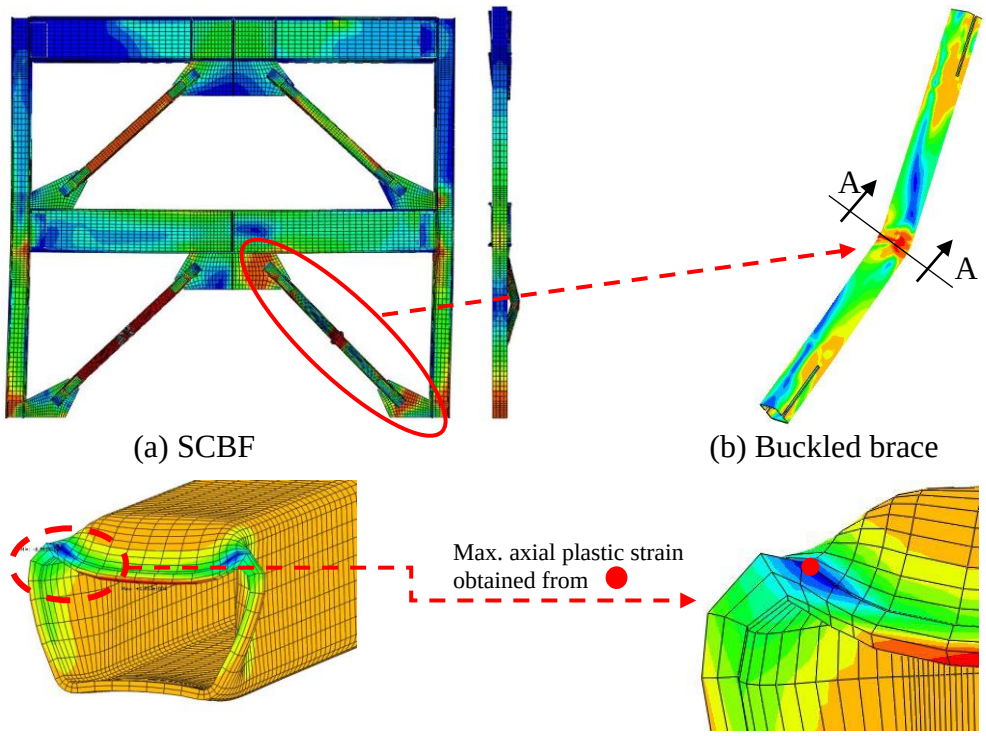

(a) SCBF (b) Buckled brace

(c) Section A-A (d) Peak axial plastic strain location

Figure 3.16. Illustration of plastic strain data processing

Fig. 3.17 presents the cyclic response of the frame, normalized peak axial plastic strain (axial strain divided by the maximum axial strain obtained from the simulation group) and out-of-plane displacement of the braces. Based on the results of the first simulation group, the following can be discussed:

(1) The global response of the simulated frame with a normalized longitudinal mesh size of 1.25% was slightly different than that of the other four cases. Still, the variation in the mesh size in axial direction of the braces did not play an important role in overall cyclic response of the SCBF (Fig. 3.17a).

(2) The peak out-of-plane displacement increased linearly as the mesh size decreased. Despite the increase, the peak out-of-plane displacements of the frames did not substantially

differ from each other. The maximum difference between the cases with the largest and smallest mesh sizes was about 7% (Fig. 3.17b).

(3) As seen in Fig. 3.17(c), the peak axial strain followed a trilinear path as the mesh size refined. First, the normalized peak strain amplitude showed a rapid increase from 30.1% to 69.5% when the normalized mesh size reduced from 1.25% to 1.00%. Then, the strain amplitude linearly increased from 69.5% and reached its peak value (100.0%) and dropped to 90.4% when the mesh size further decreased to 0.15% of the length. In other words, the axial strain amplitude and local deformations at the plastic hinge location were strongly influenced by the changes in the longitudinal mesh size.

The results of the second simulation set are compared in Fig. 3.18. It appears that the cyclic response of the frames were virtually identical (Fig. 3.18a). Furthermore, similar to the first simulation group, the maximum difference between the peak out-of-plane displacements of the bracings was on the order of 2% (Fig. 3.18b). Most notably, as can be interpreted from Fig. 3.18(c), the variation in the mesh size in the width direction did not affect the local buckling shape of the mid-section significantly. Even though there exist slight changes in the peak out-of-plane displacement and axial plastic strain amplitudes, it seems that the improvement in the observed local and global responses with a finer mesh size was quite negligible compared to its computational cost.

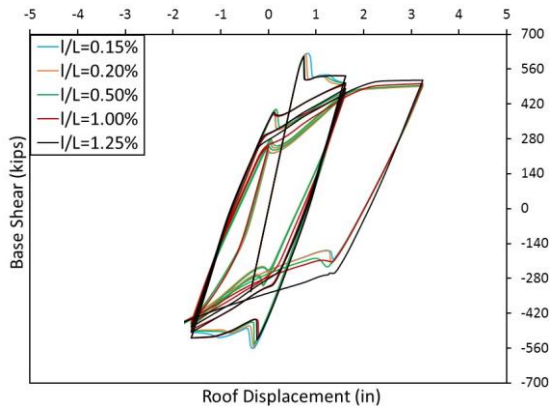

(a) Base shear vs. roof displacement

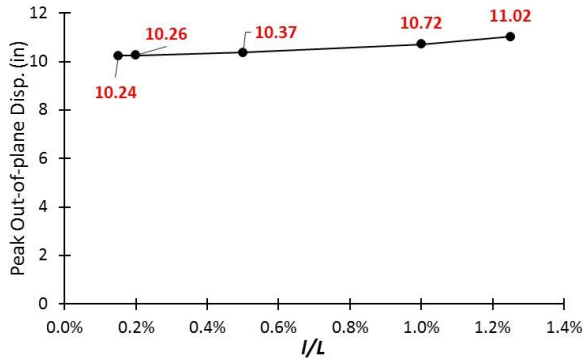

(b) Peak out-of-plane displacement of braces

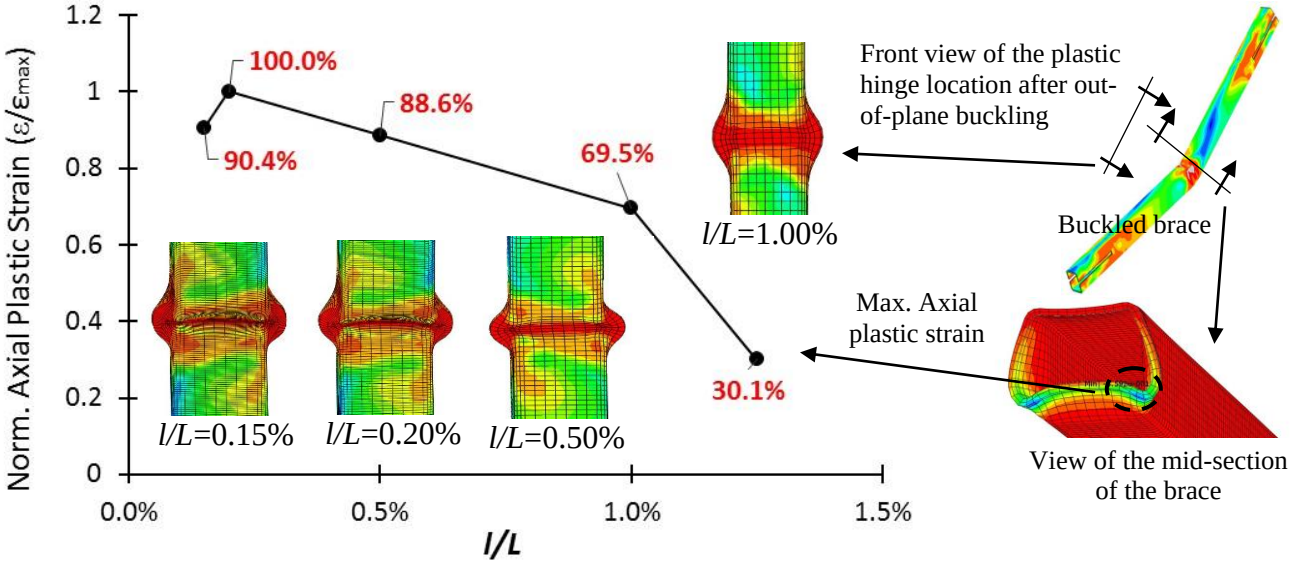

(c) Peak axial plastic strain and local buckling shapes of braces

Figure 3.17. Comparison of local and global responses of the frames with various longitudinal mesh sizes.

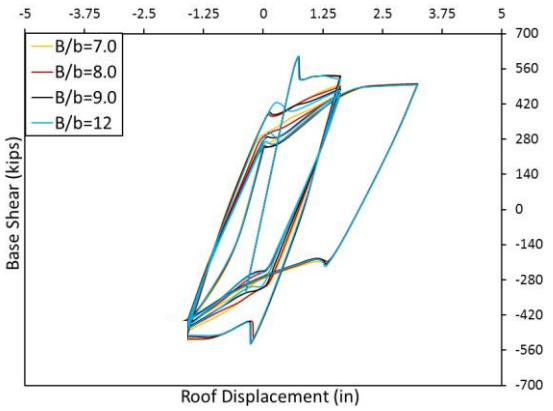

(a) Base shear vs. roof displacement

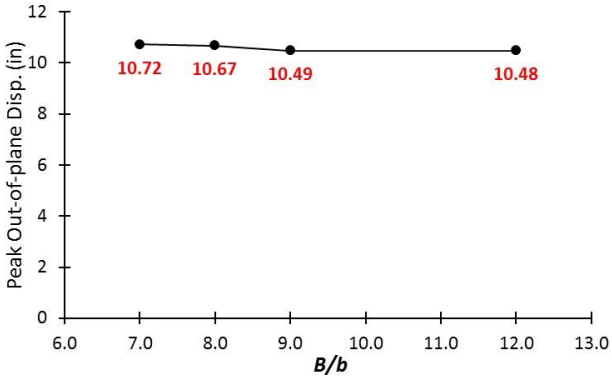

(b) Peak out-of-plane displacement of braces

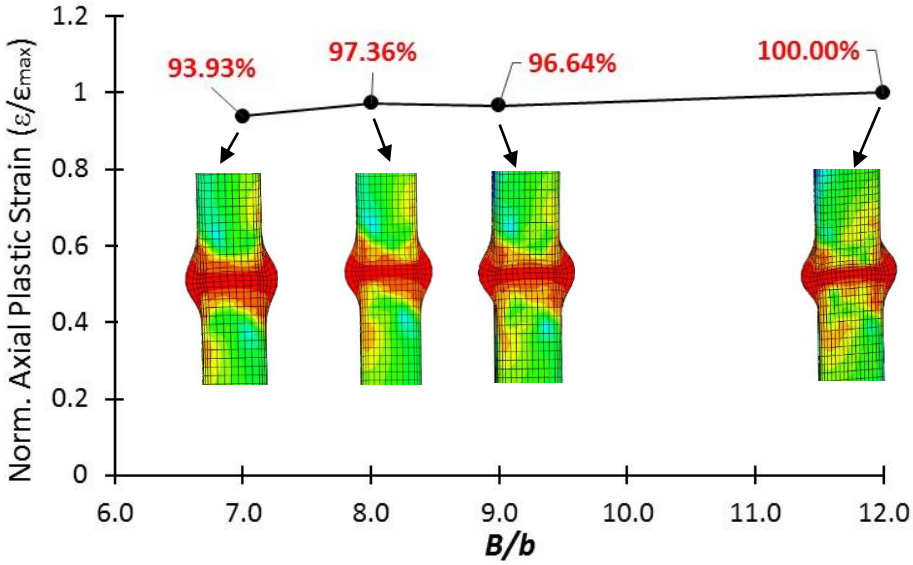

(c) Peak axial plastic strain and local buckling shapes of braces

Figure 3.18. Comparison of local and global responses of the frames with various mesh sizes in width/depth direction.

3.3. Key observations on mesh sensitivity analysis

FE simulation of a full-scale SCBF is presented and compared with the tested SCBF in terms of deformed shapes and overall cyclic response. Additionally, a thorough mesh sensitivity analysis was carried out using the calibrated FE model of the tested frame. In light of the numerical study, the following conclusions can be drawn:

(1) FE simulation successfully replicated the cyclic response of the frame, global and local buckling of the braces and stress concentrations until fracture of the braces.

(2) It appears that displacements are not very sensitive to the changes in the mesh size in any direction. However, local deformations, as well as stress and strain distributions are excessively affected by the mesh size.

(3) Our results strongly indicated that the longitudinal mesh size has a more substantial impact than that of the mesh size in the width direction on the local deformations and the strain demands. When the longitudinal mesh size is sufficiently small, the flat section width/depth and the filleted corners can be divided into at least 8 and 3 brick (solid) elements, respectively, to accurately simulate local stress concentrations in the rectangular hollow sections.

(4) The braces with a mesh size substantially less than 0.5% of the length (e.g. 0.15% and 0.20%) tended to overestimate the local deformations. On the other hand, a normalized mesh size of 1.25% was not able to capture local buckling of the braces. Thus, an optimal mesh size that satisfactorily predicts the strain concentrations and amplitudes can be composed of a relative longitudinal mesh size on the order of 0.5% to 1.0% of the length.

4. Numerical Evaluation of Local Strain Demands on Tubular Steel Bracings

Bracings are subjected to cyclic loading during an earthquake excitation with a number of severe cycles that develop large plastic deformations. A compressed column member (Fig. 3.19a), in general, buckles globally when it reaches its critical load and begins to deform laterally (Fig. 3.19b). This lateral deformation induces second-order bending moments and leads the plastic hinge formation at the mid-length of the brace. As presented in

Fig. 3.19(c), hollow-shaped bracings suffer from the high strain concentration in the compression fibers of the cross-section at the mid-length, in which the plastic hinge formation occurs subsequent to global buckling. It is apparent from the recent experimental studies that cracking of cold-formed hollow sections is triggered by local buckling-induced strain concentrations on concave side of the cross-section (Tremblay et al. 2008, Fell et al. 2009, Shaback and Brown 2003, Han et al. 2007, Uriz and Mahin 2008).

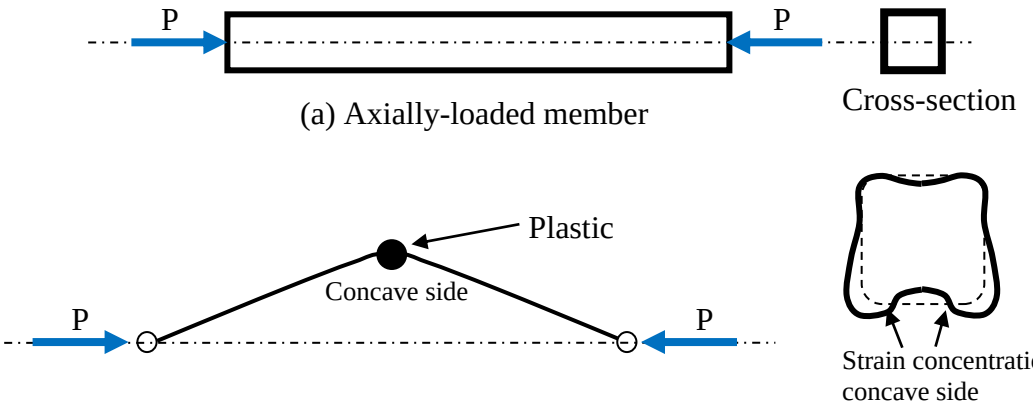

Figure 3.19. Illustration of global and local buckling of an axially-loaded member

In spite of the fact that this study does not intend to predict fracture, in order to alleviate likelihood of fracture in tubular bracings effectively, it is essential to perceive the mechanism behind the fracture initiation. Park et al. (2004) carried out an experimental study on steel members to determine the parameters that influence ultra-low-cycle fatigue behavior of thin-walled steel members (Park et al. 2004). Park et al. (2004) pointed out that the failure state is highly correlated with the peak axial strain amplitude. Moreover, in most cases, visible cracking initiated on the concave side at the extreme fiber of the cross-section when

the specimens subjected to tension (Park et al. 2004), which is consistent with cracking patterns observed during the inelastic cyclic testing of cold-formed tubular sections. Hence, in this study, the magnitude of axial plastic strain is selected as a measure to compare the possibility of fracture in tubular bracings with and without buckling-controllers.

4.1. Strain Demands on TinT#1 Specimen

Prior to the investigation into the strain demands, the simulated cyclic response of TinT#1 specimen is compared with the test results. Axial force – displacement and normalized axial force (Axial force divided by yield strength) – story drift ratio relationships of the simulated and tested TinT#1 are presented in Fig. 3.20 until fracture initiation. It appears that the overall cyclic response of the tested TinT#1 specimen was well-predicted by FE model. Note that critical deformed shapes of the simulated and tested specimen are compared in the previous chapter.

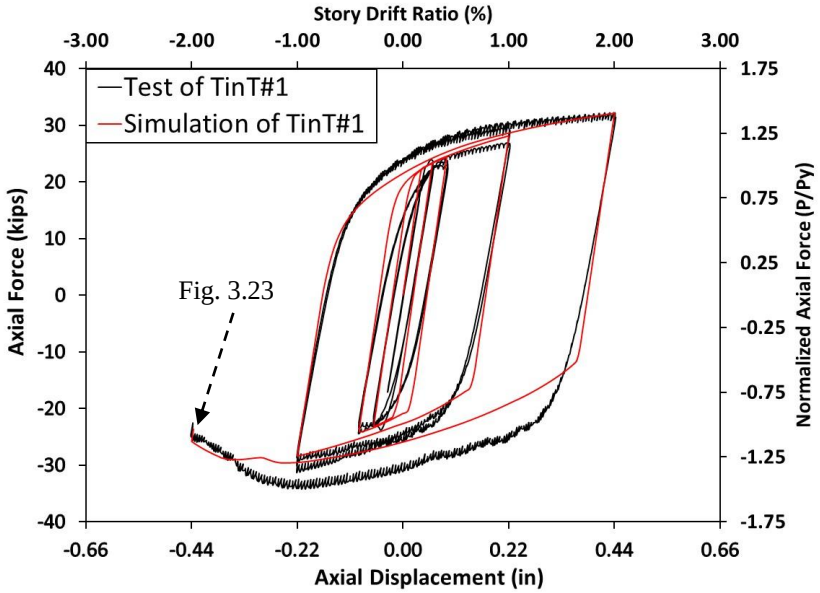

Figure 3.20. Cyclic behavior of TinT-BCB from the experiment and numerical simulation

Although the overall cyclic response and the critical deformation patterns are satisfactorily captured through the FE simulation, it was vital to examine the dissipated energy components of the analysis in order to ensure the reliability of the simulation conducted. Contributions of the plastic deformation, the elastic deformation, the stabilization (the artificial energy inserted to minimize the potential convergence problems) and the friction energies to the total energy dissipation are shown in Fig. 3.21(a). The results indicated that, in average, 94% of the total energy dissipated by the plastic energy component. On the other hand, the peak ratio of stabilization and friction energies to the total energy during the analysis were 2.3% and 0.6%, respectively. It is essential to note that the maximum ratio of stabilization energy to total strain energy was limited to 5% for the sake of the accuracy.

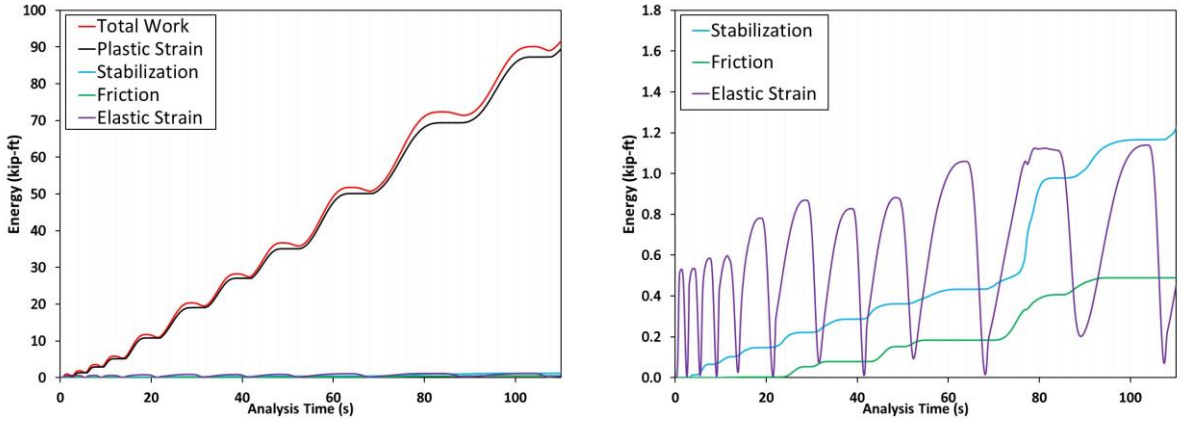

(a) Energy components (b) Stabilization, friction and elastic strain energies

Figure 3.21. Time history of the energy components dissipated by TinT#1

The peaks of the elastic strain energy stand for the deformations in compression (Fig. 3.21b). Therefore, each peak of the elastic strain energy corresponds to an increase in the friction energy, as well as in the stabilization energy due to the resistance of the outer tube. It

should, however, be noted that the friction energy increased only for the first cycle of each deformation quantity (e.g. story drift ratio of 1%) and remained virtually constant during the second cycle of each deformation level, which is consistent with the accumulation of the local deformations on the outer tube.

After reproducing the observed deformed shapes and hysteretic response successfully, the strain readings obtained from the strain gauges were compared with the strain data obtained from the FE simulation. A total of six strain gauges were mounted on the main brace of the TinT#1 in axial direction, as given in Fig. 3.22. Locations of the strain gauges in longitudinal direction are given in Fig. 3.22(a). As indicated in Fig. 3.22(b), the strain gauges were placed to each cross section along the brace length with an inclination of 45 degrees with respect to the horizontal axis of the cross-section. By doing that we were able to protect the strain gauges from the possible damages caused by the contact between the two tubes during the test.

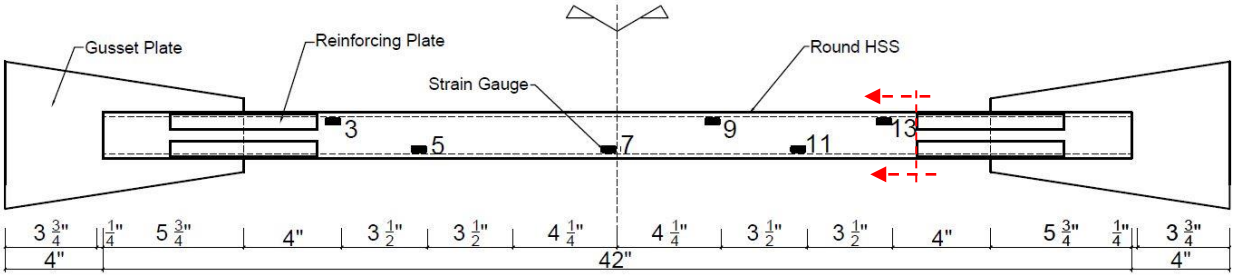

(a) Side view

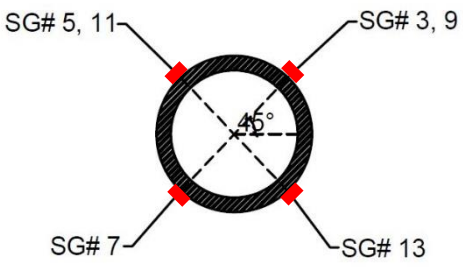

(b) Section view

Figure 3.22. Locations of the axial strain gauges mounted on the main brace of TinT#1

For the sake of the discussion, the strain gauges were divided into two groups based on the obtained strain readings:

(1) SG Group I consisted of the SGs (SG#3 and SG#5) installed on the sections that the axial compressive stresses are dominant;

(2) SG Group II was composed of the SGs (SG#7, 9, 11, 13) with tension-dominated cycles. The locations of the strain gauges along the brace length and the distribution of the SGs into groups are indicated in Fig. 3.23 utilizing the deformed shape and axial stress contours of the main brace of TinT#1 at 2% SDR.

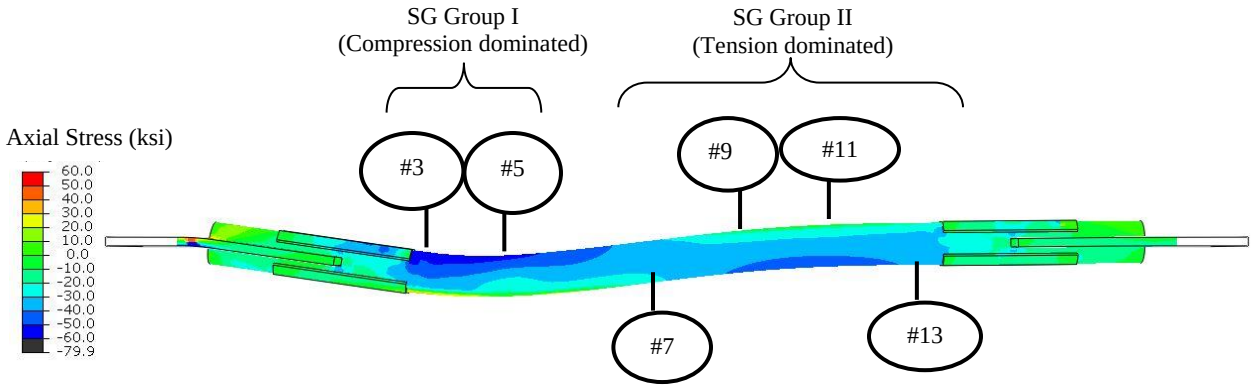

Figure 3.23. Axial stress contours of the main brace (TinT#1) and SG groups

Fig. 3.24(a) compares the strain readings of SG Group I (SG#3 and SG#5) extracted from the test and the FE simulation. It seems that the strain data obtained from the test and the FE simulation are in good agreement prior to the cycles at 1% story drift ratio. It is, nevertheless, the amplitude of the axial compressive strains obtained from the simulation increased up to 0.05 due to the bending deformation of the main brace shortly after a story drift ratio of around 1%, while the maximum compressive strain obtained from the test was around 0.01. Moreover, in contrast to the strain data measured from the test specimen, the strain readings of the simulated specimen exhibited a compression-dominated behavior

during the last few cycles, which was consistent with the deformed shape of the specimen (Fig. 3.23). It should be noted that SG#3 and SG#5 were placed on the compression side of the section and the double-curvature bending of the main brace took place (Fig. 3.23) soon after a story drift ratio of 1%. SG#3 and SG#5 did not fail during the test. It is, however, questionable whether or not the strain readings obtained from SG Group I reflected the actual behavior observed during the test.

The strain readings obtained from SG Group II are given in Fig. 3.24(b). The FE model replicated the trend in the measured data quite well. As seen in Fig. 3.24(b), the peak amplitudes of the strain readings from the FE simulation and the test were closer when the strain gauge locations were away from the loading end of the specimen, in which the compressive strains due to the flexural deformation were dominant (Fig. 3.23).

Comparison between the tested and simulated TinT#1 specimen is presented. The reliability of the FE model is examined through the hysteretic response, energy components and the strain readings. The following can be highlighted:

(1) The FE model was capable of simulating overall hysteretic response satisfactorily. Moreover, the interaction between the two tubes as well as the critical deformation patterns are successfully emulated through the FE simulation.

(2) The presented strain readings from the FE simulation followed a similar trend with the test data. A better agreement can be achieved by performing cyclic coupon tests in lieu of monotonic ones for calibration of the material parameters (Martinez-Saucedo et al. 2009).

(3) Comparing the strain readings of SG Group I and II indicated that the agreement between the test and simulation results was more satisfactory when the strain gauges were away from the sections, in which the flexural deformation was dominant. In addition, the strain readings

obtained from SG Group I might not have precisely indicated the actual behavior observed during the test, while the FE readings were consistent with each other, as well as compatible with the deformed shape of the tested specimen. Thus, it is likely that strain gauges would have malfunctioned when compressive strains due to flexural deformation were dominant.

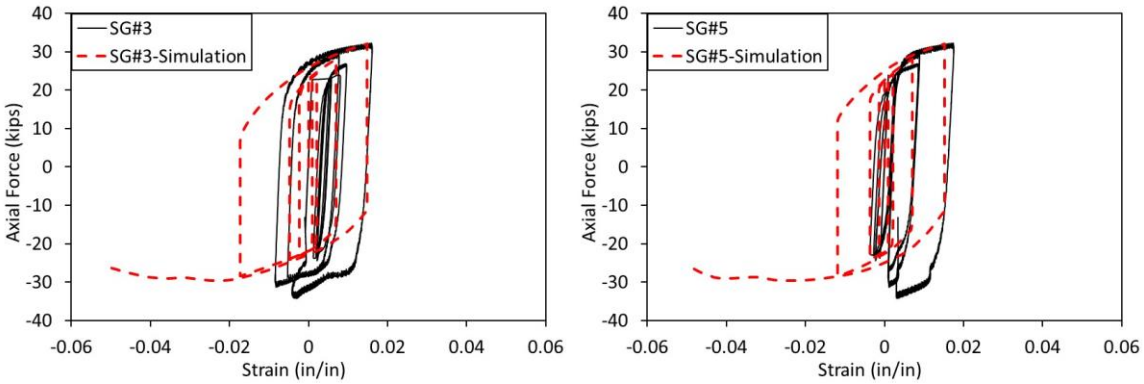

(a) SG Group I (SG#3 and SG#5)

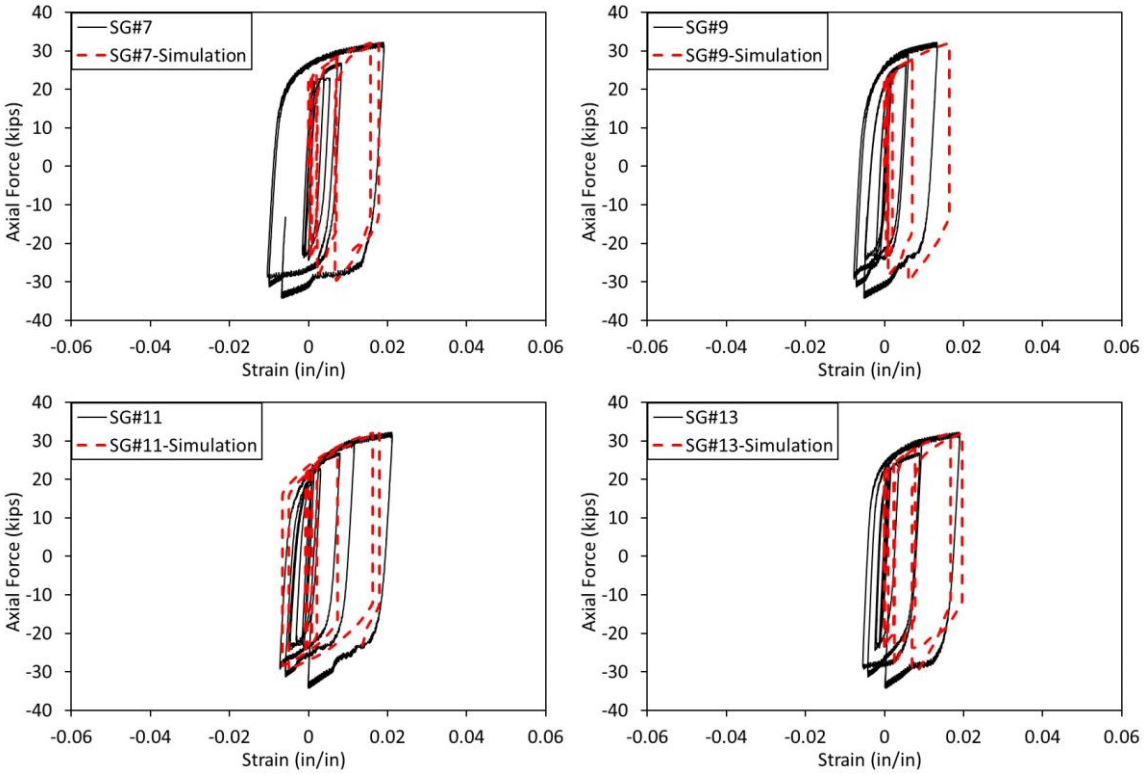

(b) SG Group II (SGs#7, 9, 11 and 13)

Figure 3.24. Axial load-axial strain readings obtained from test and simulation

4.2. Mitigation of Likelihood of Brace Fracture

In this section, influence of buckling control on the fracture life is discussed by means of axial plastic strain amplitudes. For this purpose, the axial plastic strain amplitudes of two large-size brace specimens made of circular hollow sections are compared with and without channel encasing using the optimal design parameters. Then, effect of stitch spacing on strain demand is discussed through isolated brace simulations. Lastly, the application example presented in the previous chapter is assessed in terms of reduction in strain demands.

4.2.1. Axial strain demand on isolated brace specimens w/ and w/o buckling controllers

Recently tested (Tremblay et al. 2008) two full-scale isolated brace specimens made of circular hollow sections (CHS) were selected for investigating the strain demands. As presented in Table 3.8, the size, slenderness and width-to-thickness (D/t) ratios of the tested braces were similar to the commonly used member sizes in braced steel frame construction (Tremblay et al. 2008).

Table 3.8. Properties of the tested circular braces (Tremblay et al. 2008)

Specimen	Section (in x in)	L_H (in)*	D/t	KL/r
CHS-1	HSS10.750x0.375	152	30.8	42
CHS-2	HSS10.750x0.375	228	30.8	62

*The distance from brace end to brace end.

Figs. 3.25(a) and (b) present the meshing of the specimen. The mesh densities were determined based on the expected deformation patterns and the mesh sensitivity analysis presented in section 3 of the present chapter. The longitudinal mesh size in the vicinity of the plastic hinge location was adjusted to a normalized mesh size of around 0.60% of the brace length (Fig. 3.25a). Three and fifty six elements were used in the through wall thickness and

circumferential directions, respectively (Fig. 3.25b). Test setup was equipped with a double acting actuator so as to represent the relative axial displacements of the braces in a mid-story of an actual CBF (Tremblay et al. 2008). The boundary conditions and the loading sequence (Fig. 3.25c) adopted for the simulation were identical to those used in the test. The step-wise displacement controlled loading applied from both ends, as shown in Fig. 3.25(a).

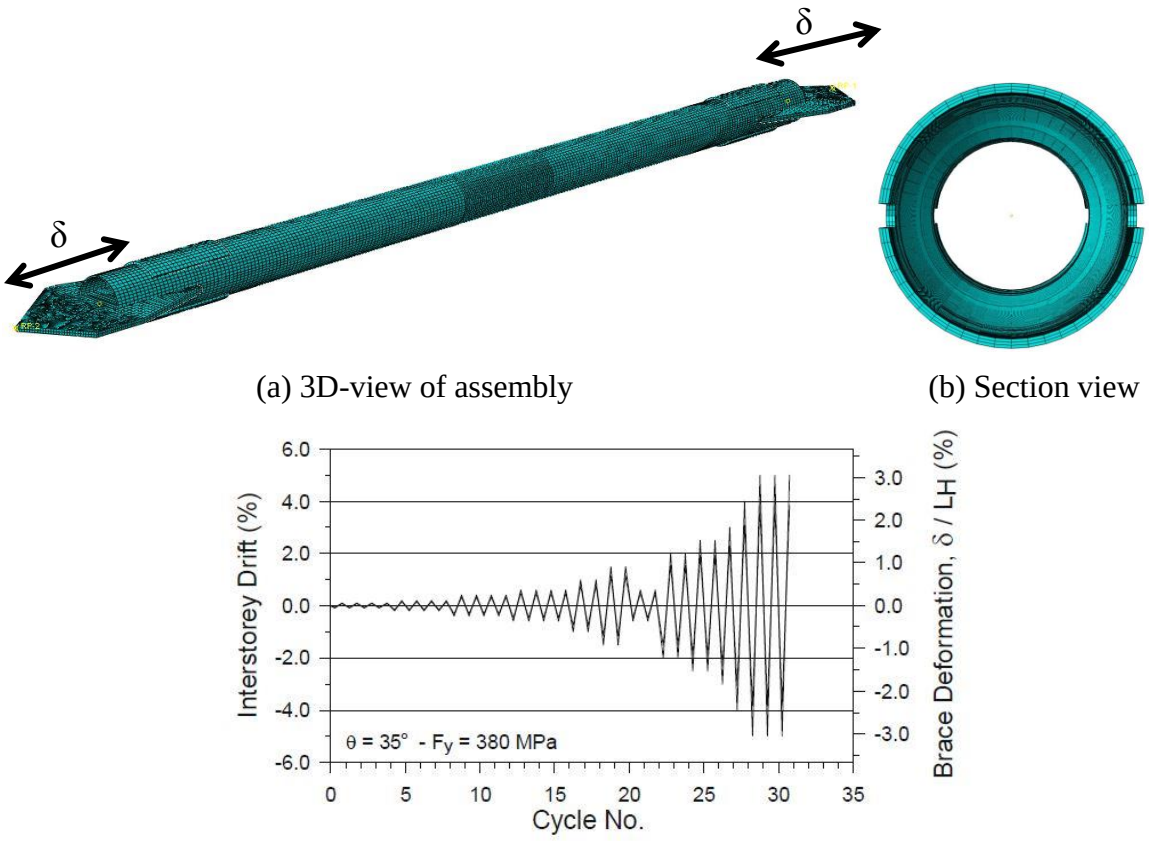

(a) 3D-view of assembly (b) Section view

(c) Loading protocol used in the test (Tremblay et al. 2008)

Figure 3.25. Mesh, loading protocol and boundary conditions adopted for single brace simulations.

The results of the test and simulation are presented in Fig. 3.26(a) and (b) in terms of story drift ratio (Δ/h_s) and normalized axial force (applied axial force divided by yielding strength). It is apparent that the cyclic responses of the tested and simulated circular braces

were in good agreement (Figs. 3.26a and b). The deformed shapes of the plastic hinge locations were also compared in Fig. 3.26(c) to justify that the mesh size adopted for the mid-length of the brace was adequate to simulate local buckling of the circular brace specimens.

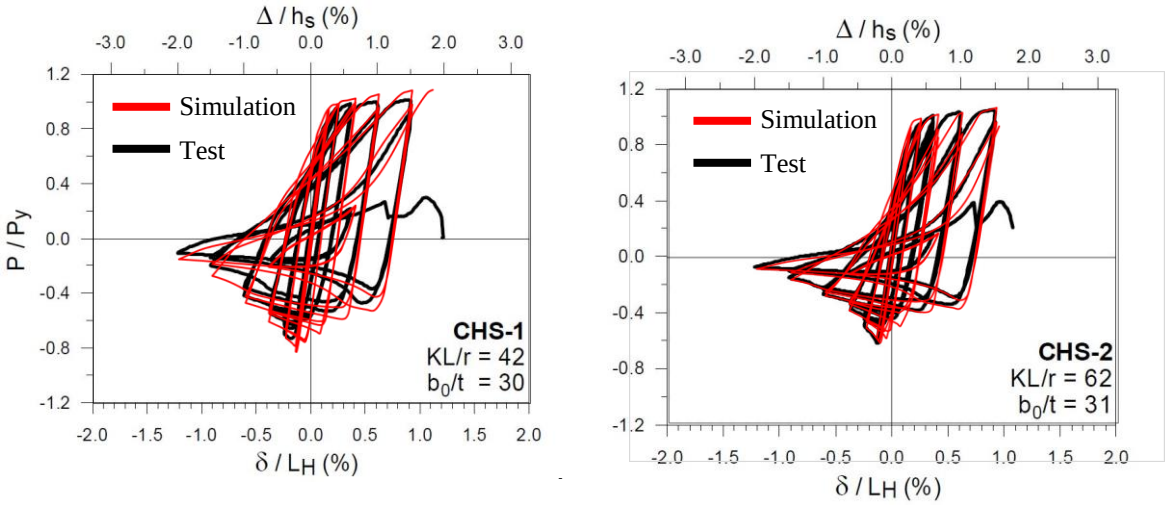

(a) Comparison of CHS-1 (b) Comparison of CHS-2

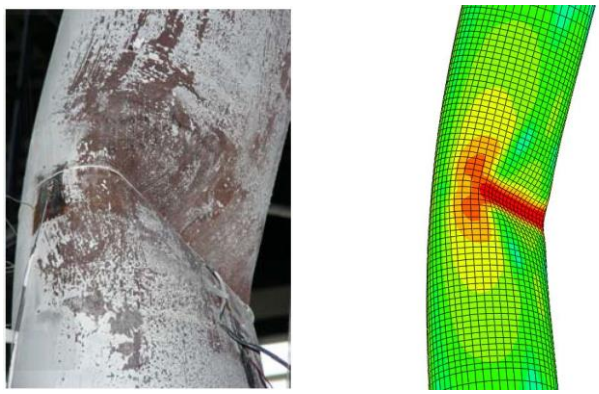

(c) Local buckling of a CHS specimen at plastic hinge location

Figure 3.26. Simulation of circular hollow sections tested by Tremblay et al. (2008)

Subsequent to the calibration of the FE models of the tested specimens, CHS-1 and CHS-2, were encased with two MC13x50 sections as buckling-controller and WT7x41 sections were used as stitches. Based on the results presented in section 2, the gaps in in-plane and out-of-plane directions were adjusted to be 1/32" and near-zero, respectively. Comparison between the results of the braces with and without channel encasing is drawn in

terms of hysteretic and peak axial plastic strain responses. Note that the peak axial strain values presented herein were obtained from different locations for the conventional (tested specimen) and the enhanced braces (channel-encased BCBs). As shown in Fig. 3.27(a), the peak strains were extracted from the mid-section, in which the fracture initiated during the test and a section close to the loading-end of the conventional and enhanced braces, respectively. It should also be noted that the given strain histories are normalized with the maximum strain values onset of the observed cracking in the tested braces for the sake of the discussion.

Hysteretic stability of the CHS-1 specimen appears to be improved substantially with virtually the same strengths in tension and compression after employing the buckling-controller (Fig. 3.27b). It is obvious that the buckling-controller had the ability to significantly enhance energy dissipation capability of the conventional brace. As indicated in Figs. 3.27(c), the axial plastic strain readings obtained from the conventional buckling brace (CHS-1) reached its maximum amplitude when the applied axial displacement was corresponding to an equivalent story drift ratio of 2.0% in compression. The enhanced brace, on the other hand, exhibited a strain response compatible with the applied loading history because of its uniform strain distribution along the length (Fig. 3.27a). The maximum axial plastic strain obtained from the enhanced brace was on the order of 14% of the peak axial strain obtained from the conventional brace, as given in Fig. 3.27(b).

The cyclic responses of the conventional brace (CHS-2) and the enhanced brace are shown in Fig. 3.28. Similar to enhanced CHS-1 specimen, either global or local buckling of the existing brace was not observed during the cyclic simulation of the enhanced brace. Thus, the cyclic response of the enhanced brace was stable without strength and stiffness

degradation (Fig. 3.28a). The maximum normalized strain obtained from the enhanced brace was found to be 12.3%, as presented in Fig. 3.28(b). It is also noticed that the strain history of the enhanced brace gradually increased and followed a path similar to the engineering strain (relative axial displacement divided by the brace length).

On the whole, our results indicated that besides their symmetrical and stable hysteresis, the developed channel-encased BCBs, regardless of the slenderness ratio of the main brace, were capable of mitigating the strain demands substantially on the order of 7 to 8 times the strain demands on the conventional braces.

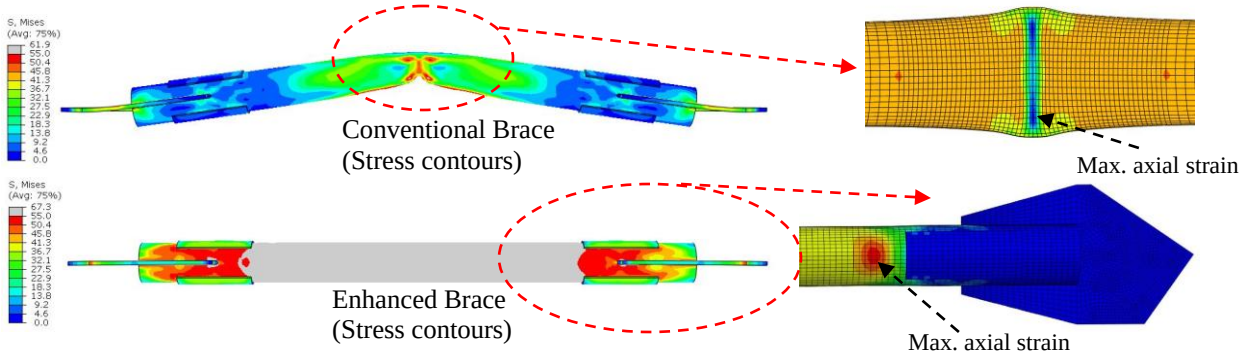

(a) Location of maximum axial plastic strains

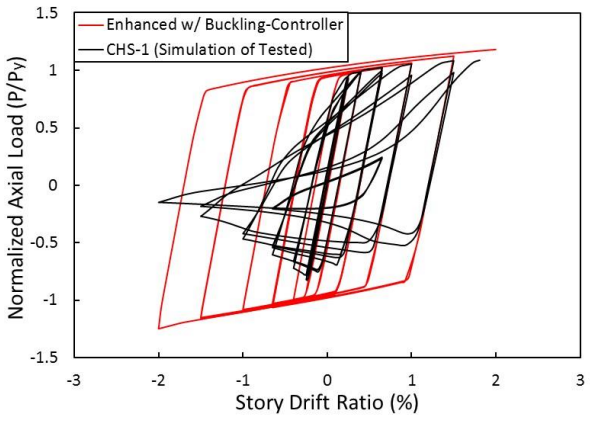

(b) Hysteretic response

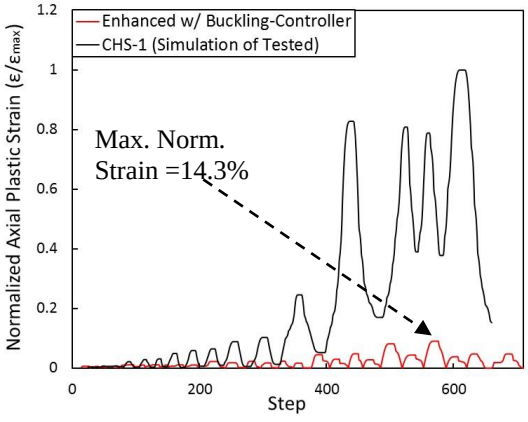

(c) Normalized axial plastic strain history

Figure 3.27. Response of CHS-1 w/ and w/o buckling-controller

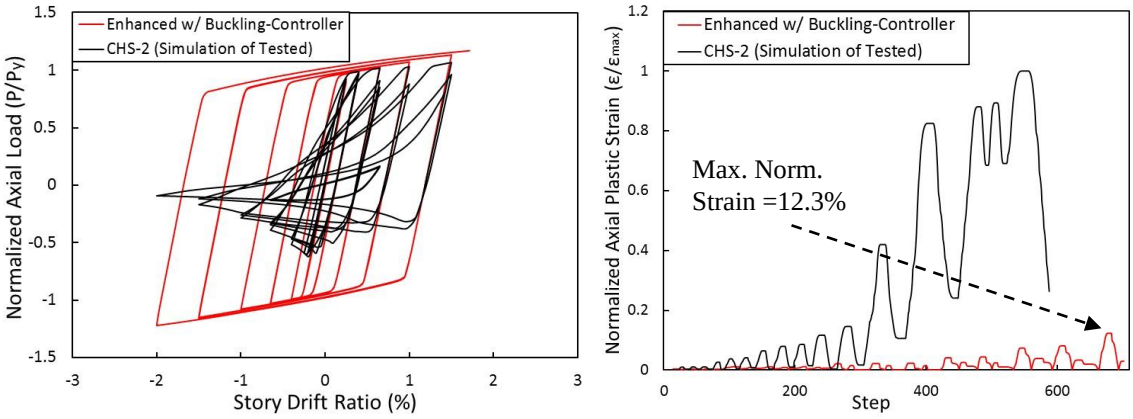

(a) Hysteretic response (b) Normalized axial plastic strain history

Figure 3.28. Response of CHS02 w/ and w/o buckling-controller

4.2.2. Effect of stitch spacing on axial strain demand

In the previous sections, it is justified that channel-encased buckling-controlled braces are promising in terms of controlling global or local buckling of the existing braces. In addition, mitigation of likelihood of brace fracture is evaluated through an ensemble of FE simulations. However, the effect of stitch spacing on the peak axial strain amplitude has not been discussed yet. In this section, several channel-encased brace models with different stitch spacing are compared with each other by means of axial plastic strain demands.

As illustrated in Fig. 3.29, one of the first story bracings was separated from the frame considering its assumed fold lines at each end and subjected to axial displacements from its upper end in order to reduce the computational cost of simulating the entire CBF with channel-encased braces. The applied axial displacements (δ_{axial}) were converted from the lateral displacement history of the first story (Δ_{story}) obtained from FE simulation of the SCBF (Fig. 3.29c). Note that the given loading history includes the cycles until the observed fracture initiation during the physical test.

Adequacy of the equivalent single brace is examined in Fig. 3.29(d) with reference to the estimated brace force-elongation results provided by Uriz and Mahin (2008). It appears that the results of the equivalent single brace model and test are in reasonable agreement, even though the FE model tends to slightly underestimate the lower story drift ratio compared to the test results. It should, however, be noted that the hysteretic response obtained from testing was approximate. Thus, based on the current findings from the testing and FE simulation, the equivalent single brace assumption can be considered to be effective and sufficiently accurate for the present study.

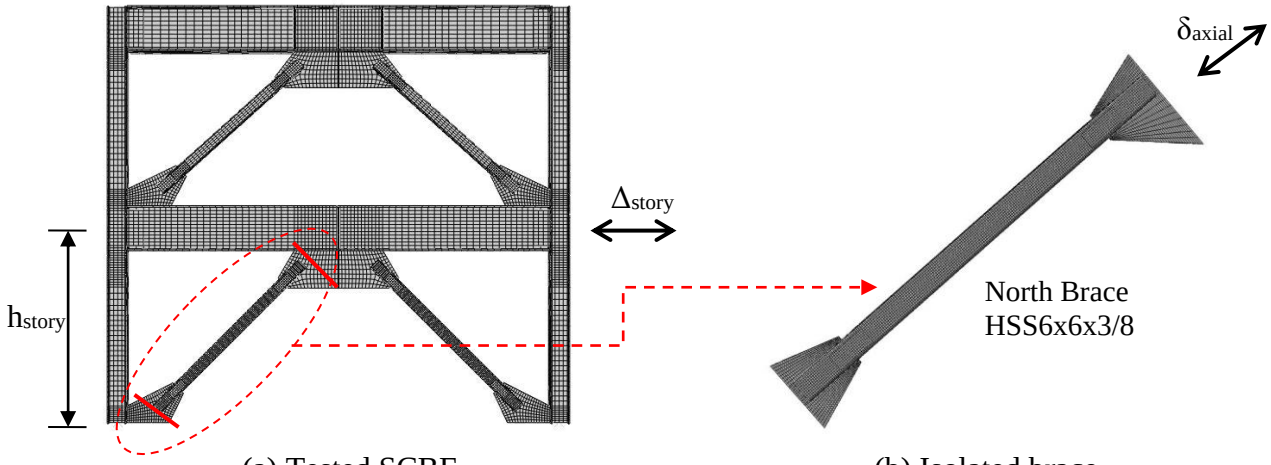

(a) Tested SCBF (b) Isolated brace

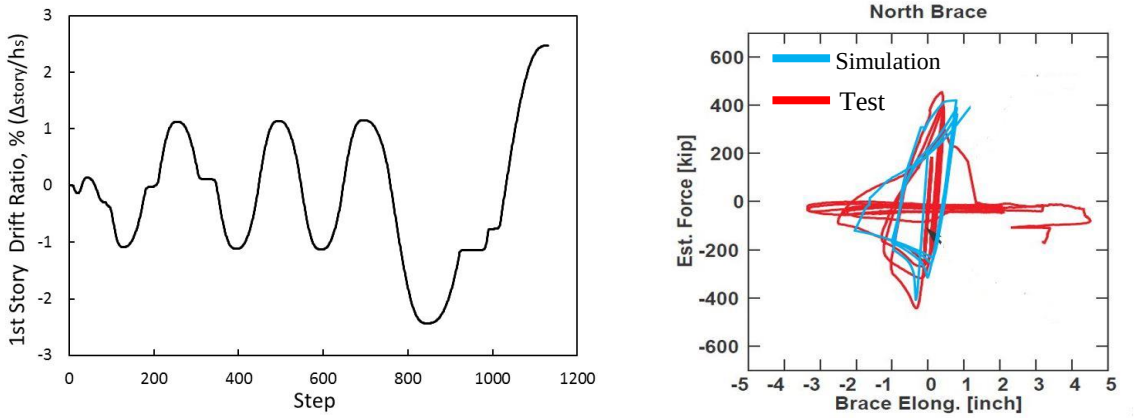

(c) Lower story drift history (d) Hysteretic response of the brace

Figure 3.29. Equivalent isolated brace model

The previously conducted mesh sensitivity analysis is used as a basis for meshing of the brace specimens. Square HSS6x6x3/8 brace specimen was meshed using two layers through the wall thickness. The flat width/depth and filleted corners were divided into seven and three elements, respectively. The uniformly distributed longitudinal mesh size was adjusted to a normalized mesh size of around 0.625% of the length in order to obtain satisfactory results.

Table 3.9 summarizes the simulation cases in terms of the existing brace, buckling-controller and stitch sections, and the details of intermittent fillet welds that attach the connectors made of WT sections to the channels. Since simulation of SHS-Ch-WT group presented in section 2.2 of this chapter drew attention to $\sum L_{weld}/\sum L_{BC}$ ratio as the most influential parameter in determining the stress distributions and load-deformation responses of the models, the simulation set given in Table 3.9 focuses on $\sum L_{weld}/\sum L_{BC}$ individually by keeping the other parameters constant for the investigated channel-encased BCBs.

Table 3.9. Simulation cases for the channel-encased braces

Model #	Existing Brace	BC Section	Stitch	$\frac{\sum L_{weld}}{\sum L_{BC}}$	Weld Length / Spacing
M00	Conventional Buckling Brace				
M 01	HSS6x6x3/8	2C8x18.75	WT4x9	43%	5” / 7.5”
M 02				65%	10” / 6.5”
M 03				100%	NA

*Out-of-plane gap≈0; In-plane gap=1/32”

The conventional brace and the three channel-encased braces were subjected to a displacement history based on the lower story drift ratio obtained from the frame simulation

(Fig. 3.29c). The findings were compared in Fig. 3.30 in terms of hysteretic and peak axial plastic strain responses. The following conclusions can be drawn:

(1) As seen in Fig. 3.30(a), notwithstanding the intermittent weld spacing, the hysteretic responses of the channel-encased braces were stable with symmetrical loops. Besides, the cyclic responses were virtually identical for the channel-encased specimens (M01, M02, and M03).

(2) The axial strains obtained from the enhanced braces were substantially smaller than those obtained from the conventional brace. The peak axial strain demands on the existing braces were reduced on the order of 14 to 28 times subsequent to the encasing (Fig. 3.30b).

(3) As indicated in Fig. 3.30(c), the peak plastic strain readings obtained from M01, M02 and M03 were 4.05%, 2.03% and 2.02%, respectively. Even though all channel-encased braces successfully alleviated the strain demands, the peak axial strains were influenced by the stitch weld spacing. It seems that the strain amplitudes decrease to a certain degree as the $\sum L_{weld}/\sum L_{BC}$ ratio increases, as shown in Fig. 3.30(c).

(4) It is also noteworthy that the peak strain amplitudes of the two cases with 65% and 100% $\sum L_{weld}/\sum L_{BC}$ ratios (M02 and M03) were virtually identical and around 2.00%, which is slightly larger than the engineering strain (relative displacement divided by the brace length). In other words, the lateral support provided by the developed channel-encased buckling-controller was close to the ideal case for controlling local plastic deformations when $\sum L_{weld}/\sum L_{BC}$ ratio was larger than 60%.

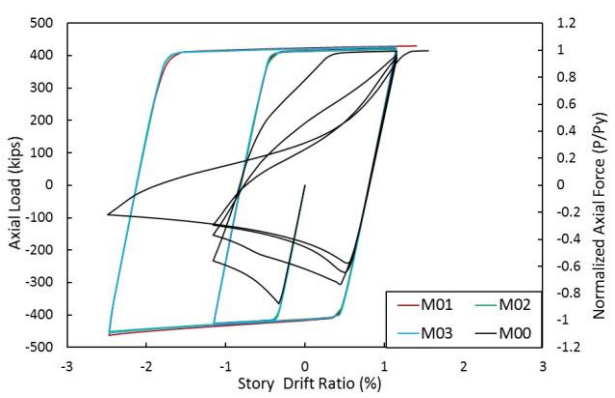

(a) Hysteretic response

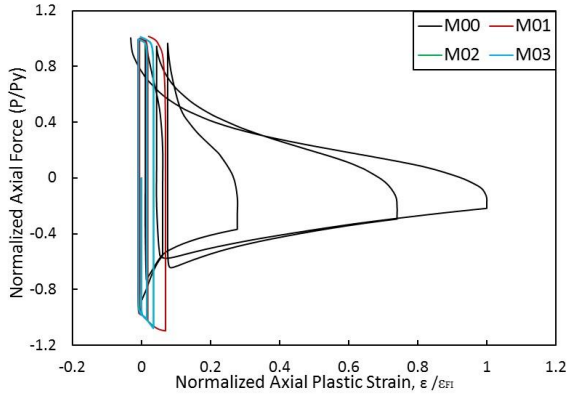

(b) Conventional and enhanced braces

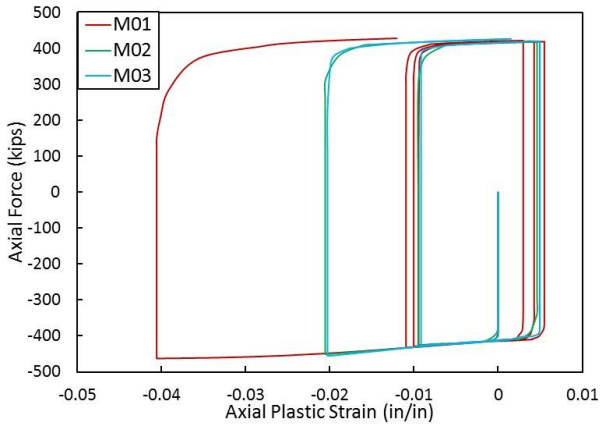

(c) Channel-encased braces

Figure 3.30. Hysteretic response and axial plastic strain results obtained from the braces

4.2.3. Ductile CBF specimen

Fig. 3.31 compares conventional SCBF and the enhanced CBF simulations in terms of inelastic cyclic response and maximum normalized axial plastic strain obtained from the brace that the fracture first initiated. Since inelastic cyclic behavior of the CBF modified with TinT-BCB is discussed and compared with the conventional CBF (Fig. 3.31a), this section focuses solely on the local strain demand on the braces. As indicated in Fig. 3.31(b), the buckling-controller efficiently mitigated the peak axial strain demand on the main brace. The reduction in the maximum axial plastic strain obtained from the enhanced braces was about 85% (Fig. 3.31b), which was consistent with the level of strain reduction attained by the

previously presented enhanced isolated brace specimens. This indicates that, regardless of the test setup, the developed buckling-controllers would considerably elongate the fracture life of conventional tubular bracings, not to mention ability to improve hysteretic stability and plastic energy dissipation capability.

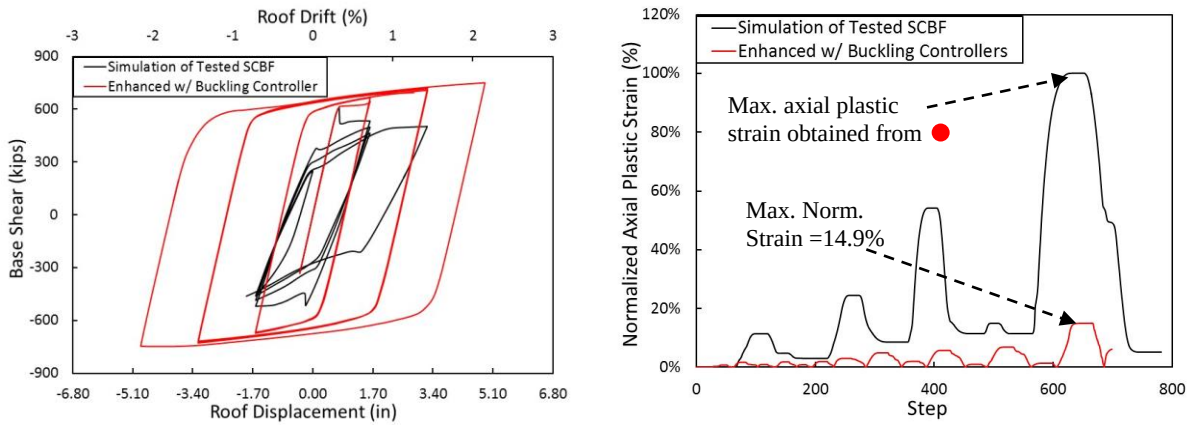

Figure 3.31. (a) Comparison of overall responses of conventional SCBF and the enhanced CBF and; (b) Normalized axial plastic strain history of the brace until cracking.

5. Summary and Conclusions

The comparative efficiency of the developed BCBs is evaluated numerically. The present numerical study on channel-encased buckling-controlled braces provides a conceptual foundation for simple and efficient way of enhancing seismic performance of existing CBFs located in seismic regions, as well as designing new buckling-controlled braced frames with the flexibility of adjusting the essential design parameters with ease. Brace specimens with several sizes and shapes were simulated with and without channel encasing and the findings were compared by means of hysteretic response, local plastic deformations and strain demands. The assessment of the developed channel-encased buckling-controlled brace model is composed of three steps. First, the effectiveness of two

different configurations is investigated in terms of alleviation of local plastic deformations. In the second phase, our goal was to reveal how the FE modeling parameters affect the simulation results. For this purpose, the effect of mesh size is evaluated with regard to the overall response of a tested CBF, and strain and deflection response of the bracings. A practical and efficient normalized mesh size range, which considers both computational cost and accuracy is emanated from the mesh sensitivity analysis. In an effort to evaluate likelihood of brace fracture, the strain demands on tested buckling-controlled brace are compared by means of FE simulations, as well as strain readings obtained from experiment. Then, the peak axial plastic strain amplitudes of several large-size brace specimens made of square and circular hollow sections are compared with and without channel encasing. The major conclusions are highlighted below:

(1) On the whole, channel-encased buckling-controlled braces are promising in terms of controlling global or local buckling as well as mitigating possibility of premature fracture of the braces in new and existing CBFs. Furthermore, the developed channel-encased BCBs offer simplicity in regard to employing the optimal design parameters.

(2) Either stitch spacing or stich size did not play an important role on local behavior of the existing braces when the gap amplitude was larger than the optimal gap range. Thus, employing the optimum gap amplitudes such as near-zero and 1/32” gaps in out-of-plane and in-plane directions, respectively, is the key to obtain symmetrical and stable cyclic response.

(3) Well-established FE models are capable of emulating the force-displacement response, global and local buckling behavior and stress concentrations of structural steel members. It is noticed that local deformations, stress and strain distributions in axially-loaded steel members are more sensitive to mesh size than force and displacement outputs. Moreover, it

was found that the longitudinal mesh size has a more substantial impact than that of the mesh size in the width direction on the local deformations and strains.

(4) Comparing the strain readings obtained from experiment and FE simulation indicated that the agreement between the test and simulation results was more satisfactory when the strain gauges were away from the flexural deformation. It is, however, questionable whether or not the strain readings obtained from the strain gauges mounted on the sections, in which the compressive strains due to bending were dominant, reflects the actual behavior observed during the test.

(5) Regardless of test setup (i.e. isolated brace or full-scale CBF specimen), connector design and effective slenderness ratio of the main brace, channel-encased braces successfully alleviated the strain demands on the existing braces by imposing uniform strain distribution along the brace length. Based on the shape and size of the existing brace, the peak axial strains were reduced on the order of 7 to 28 times subsequent to application of the encasing. This indicates that the developed technique would considerably elongate the fracture life of the tubular bracings.

(6) Peak axial strain amplitude decreases when stitch welds are closely-spaced. An optimal and cost-effective application of the developed technique with a satisfactory performance can be achieved when the channels were connected with longer stitches (e.g. one fifth of the total length) at brace ends with the ratio of the total intermittent weld length over the total buckling-controller length larger than 0.60.

CHAPTER IV

A THREE-SEGMENT STEEL BRACE FOR SEISMIC DESIGN OF CONCENTRICALLY BRACED FRAMES

1. Introduction

The inelastic cyclic behavior of braced frames is complicated because of the hysteretic behavior of their braces, which includes buckling and post-buckling phenomena. A compressed column member buckles globally when it reaches its critical load and begins to deform laterally. This lateral deformation induces second-order bending moments, which leads to plastic hinge formation at the mid-length of the brace while the rest of the member remains elastic. Therefore, employing a uniform cross-section (prismatic) along the length of an axially-loaded member is not the most efficient way to resist compressive loads (Timoshenko and Gere, 1961). An investigation of a buckled simple column is given in Fig. 4.1. As indicated in Fig. 4.1(c), the bending moment diagram for a buckled brace is not uniform, and thus the buckling load, as well as the hysteretic stability of a column member can be improved by reducing the cross-sectional area from each end of the brace (Timoshenko and Gere, 1961).

Ideally, such improvement can be achieved by utilizing a cross-section that is dependent to the bending-moment diagram, as shown in Fig. 4.2(a). However, a bar of parabolic non-prismatic cross-section is not practical for steel construction. As an alternative to the ideal case given in Fig. 4.2(a), a more practical steel brace model with sudden changes in cross-section can be used. Fig. 4.2(b) illustrates a three-segment brace model with hinged ends, which consists of two identical smaller edge segments and a larger section connected to

the two edge segments as a center segment. The concept is to develop a brace member with conventional structural steel shapes that provides significant inelastic deformation capacity primarily through its yielding in tension and compression. It is expected that the edge segments yield in tension and compression with the same strength while the center segment remains elastic.

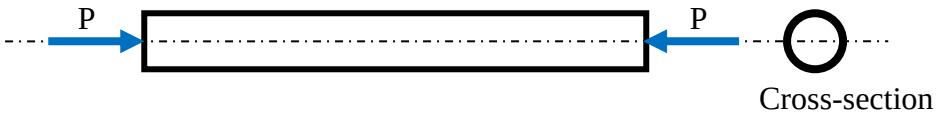

(a) Axially-loaded member with uniform cross-section

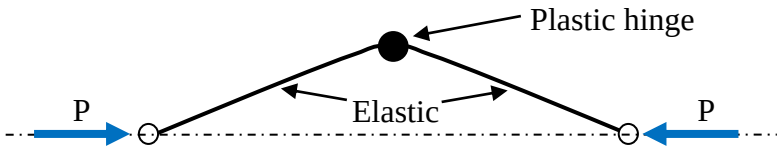

(b) Deformed shape and plastic hinge formation after global buckling

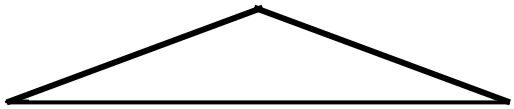

(c) Bending moment diagram after global buckling

Figure 4.1. Illustration of buckling of an axially-loaded member with uniform cross-section

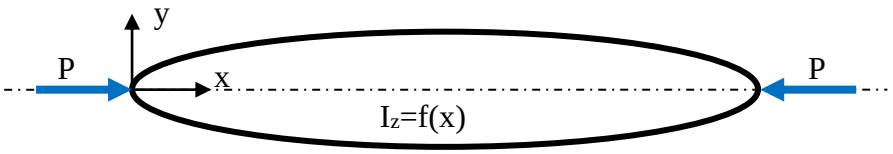

(a) Ideal column member to carry compressive loads

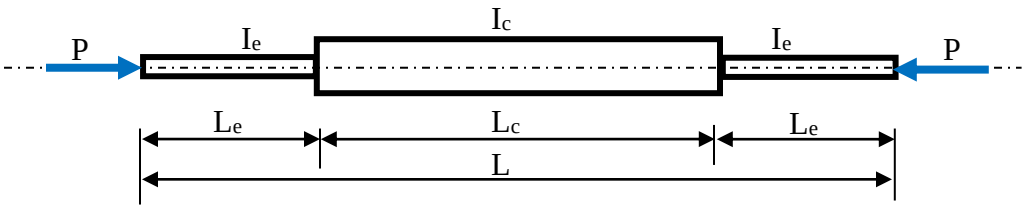

(b) A practicable column member with changes in cross-section

Figure 4.2. Column members with non-uniform cross-sections

In steel structures such members can easily be fabricated in a workshop by bolting or welding connector plates between the three segments. Several structural shapes with the different combinations can be used interchangeably as edge or center segments in order to increase ductility capacity of the brace. Figure 4.3 shows possible design options for the developed three-segment steel braces, employing square and round hollow structural sections (HSS). Considering the cost and ease of construction, either welded or bolted connection can be utilized to attach the edge segments to the center segments.

A sample design with bolted attachment is given in Fig. 4.3(a). First, two identical edge segments made of round or square HSS are pre-welded to gusset plates in a workshop. Then, a larger HSS is connected to the two end segments following the erection of the beams and columns. With this attachment, the developed three-segment brace model has a high potential to significantly speed up the construction process by assembling beam-gusset-brace assemblages in a workshop. In fact, construction of a CBF that incorporates the developed braces with bolted connectors might even be easier and faster than constructing a CBF with conventional braces owing to the shop-made brace-to-gusset connections in a three-segment CBF.

The second connector design option is similar to steel braced frame construction that incorporates conventional braces. Edge and center segments of the three-segment brace are welded together in a workshop (Fig. 4.3b). The end segments are to be fillet welded to the gusset plates after erection of the columns and girders. Even though the second option is not as advantageous as the bolted connection option in terms of construction speed, it takes the construction tolerances into consideration, which may seriously interrupt the construction process, if not met. In the numerical and experimental portions of this study, the second

option is employed. Configuration of a chevron type CBF that incorporates the proposed three-segment braces is shown in Fig. 4.3(c).

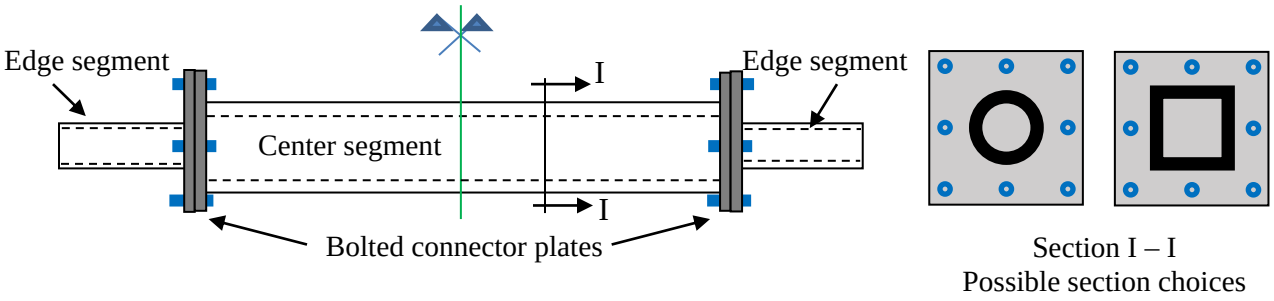

(a) Three-segment brace with bolted connector plates

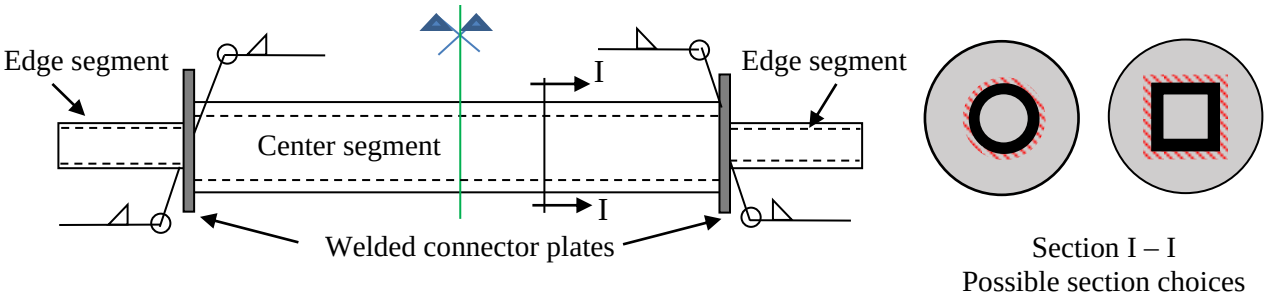

(b) Three-segment brace with welded connector plates

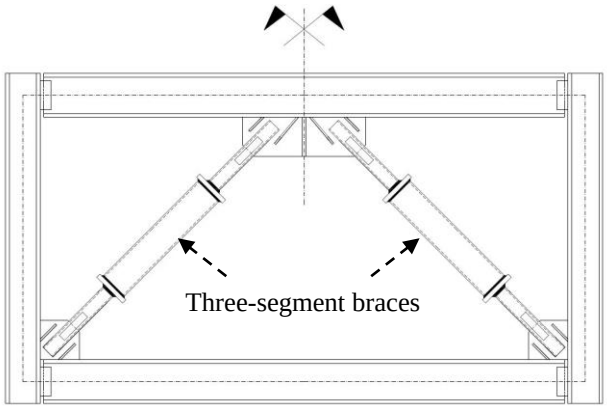

(c) Configuration of a CBF with three-segment braces

Figure 4.3. Connection options for the three-segment brace

The purpose of this chapter is to identify the critical design parameters and to assess cyclic behavior of the three-segment braces through testing and non-linear finite element simulations. The remaining sections of this chapter are organized as follows:

4.2. Identification of the essential design parameters

4.3. Cyclic behavior of three-segment braces

4.4. Experimental study

4.5. Summary and Conclusions

2. Identification of the Essential Design Parameters

The essential design parameters have been identified and investigated through analytical and numerical studies prior to the experimental program. The determination of the design parameters began with the analytical solution to a simple case of a three-segment column given in Fig. 4.4.

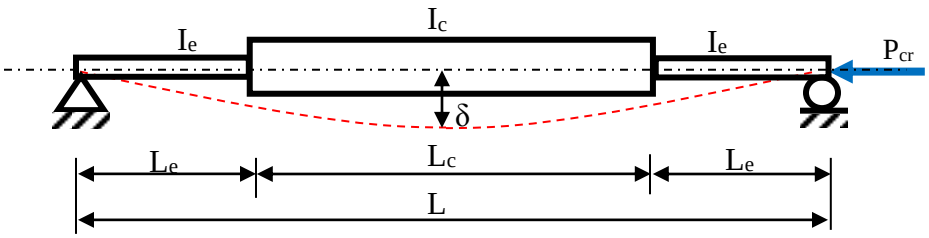

Figure 4.4. A column with changes in cross-section

Even though the intended goal of the study is to examine the inelastic cyclic behavior of the developed three-segment braces, it was important to provide a foundation for determining the design parameters. Thus, the determination of the design parameters embarked upon the

elastic solution to the eigenvalue problem prior to non-linear FEM simulations and testing. The elastic critical buckling load of the three-segment brace (P_{cr}) has been previously derived by Timoshenko and Gere (1961) from a differential equation based on the deflection curve, as represented in the following formula;

$$P_{cr} = \frac{mEI_c}{L^2} = \frac{\pi^2 EI_c}{L^2}\left[\frac{1}{\frac{L_c}{L} + \frac{2L_e}{L}\frac{I_c}{I_e} - \frac{1}{\pi}\left(\frac{I_c}{I_e} - 1\right)\sin\left(\frac{\pi L_c}{L}\right)}\right] \quad \text{(Eq. 4.1)}$$

in which, m is a factor depending on the length (L_e/L or L_c/L) and moment of inertia (I_c/I_e) ratios of the edge and center segments. L_e and L_c stands for the length of edge and center segments, respectively, and I_e and I_c are the moment of inertia of edge and center segments, respectively. It seems that the ratio of moment of inertia (I_c/I_e) along with the ratio of edge segment length over the total brace length (L_e/L) have a substantial impact on the buckling load.

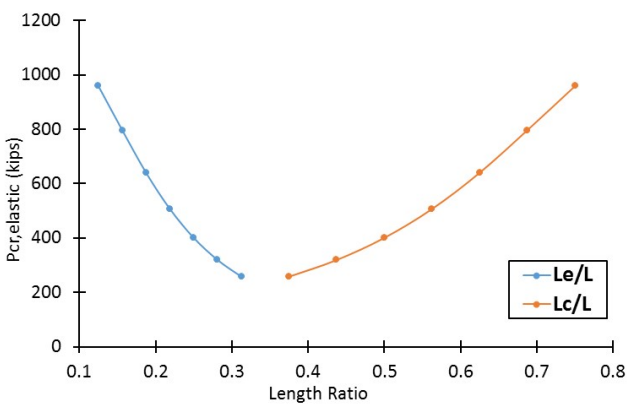

(a) Length ratio

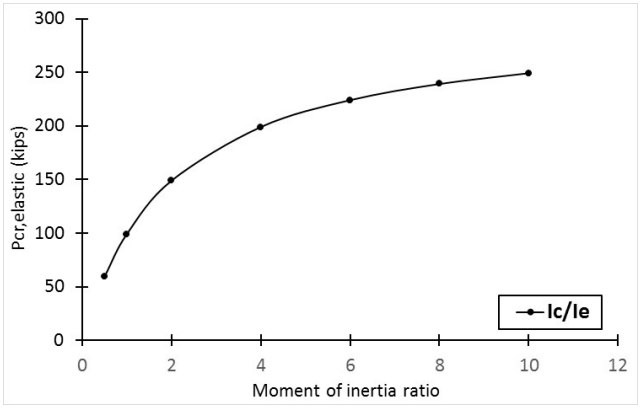

(b) Moment of inertia ratio

Figure 4.5. Variation of the elastic critical buckling load with respect to the length and moment of inertia ratios of center and edge segments.

According to the analytical solution to the buckling problem, variation of the elastic critical buckling load with several length and moment of inertia ratio values has been illustrated in Fig. 4.5. The critical load appears to increase as the edge length decreases and the I_c/I_e ratio increases, as indicated in Figs. 4.5(a) and (b).

Subsequent to identification of the two initial design parameters, a set of FEM simulations have been carried out with a variety of parameters. Fig. 4.6 demonstrates the configuration of the three-segment brace used in the parametric study. The brace model is composed of an elastic center segment and two yielding segments at each end, in which the major portion of the plastic deformations concentrated. The plastic zone length (L_p) starts from the end of the net section reinforcing plates to the face of the circular connector plate. The gusset assembly was designed based on the expected tension capacity of the edge segment ($R_yF_yA_e$). Therefore, the total length of the brace assembly was altered for each simulation case, while the distance from gusset plate to gusset plate (L) was adjusted to a constant length of 220".

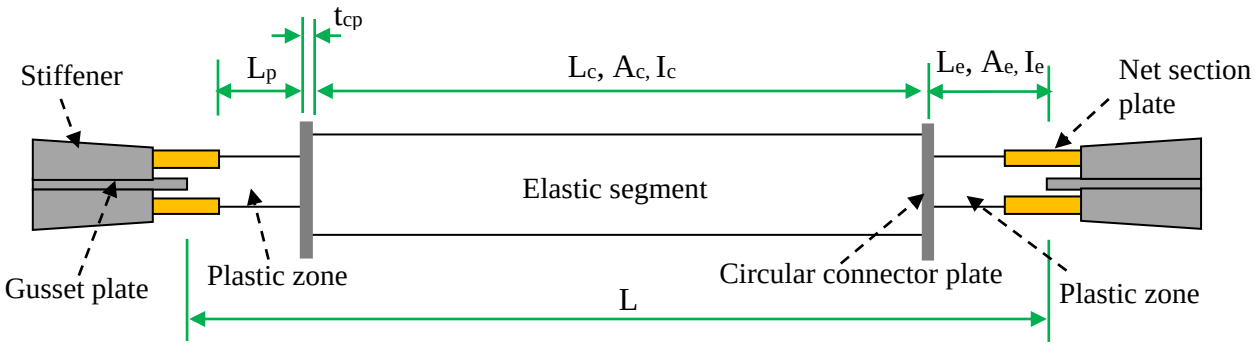

Figure 4.6. Configuration of the three-segment braces used in the parametric study

Definition of each variable used in the parametric study is given below:

L_c : The length of the elastic center segment.

L_e : The distance from the centerline of the connector plate to the end of the gusset plate.

L_p : The distance from the end of the net section reinforcing plate to the face of the connector plate. The length of the yielding segment (Plastic zone).

A_c : Gross area of the center tube.

A_e : Gross area of the edge tube.

I_c : Moment of inertia of the center tube.

I_e : Moment of inertia of the edge tube.

The simulation groups are given in Table 4.1. The analysis cases were divided into three groups as follows;

(1) Length ratio: The center (L_c) and edge (L_e) lengths are adjusted to different values while the area (A_c/A_e) and moment of inertia (I_c/I_e) ratios were constant.

(2) Moment of inertia ratio: The length ratios remained constant and the area and moment of inertia ratios were increased gradually. Note that the moment of inertia values are dependent to the cross-sectional area but the area ratios were intentionally adjusted to a value of equal to or larger than 1.70 for the second set, which allows the center segment to remain elastic.

(3) Edge length ratio: The last group is established to reveal the effect of yielding zone length (L_p) by altering solely the edge length (L_e) while the plastic zone length (L_p) and the other parameters were adjusted to a constant. Note that plastic zone length and the edge length were altered simultaneously in the length ratio simulation group.

Table 4.1. Simulation cases for determining the effect of the critical design parameters

	Model Name	Segment	D (in)	t (in)	L (in)	L_e/L	L_p/L	I_c/I_e	A_c/A_e
Length Ratio	L_1	Edge	6.5	0.500	27.5	0.125	9.10%	8.73	1.70
		Center	14	0.375	165				
	L_2	Edge	6.5	0.500	22.9	0.104	7.00%		
		Center	14	0.375	174.2				
	L_3	Edge	6.5	0.500	20.7	0.094	6.00%		
		Center	14	0.375	178.6				
	L_4	Edge	6.5	0.500	18.5	0.084	5.00%		
		Center	14	0.375	183				
Moment of Inertia Ratio	I_1	Edge	6.5	0.500	27.5	0.125	9.10%	8.73	1.70
		Center	14	0.375	165				
	I_2	Edge	6.5	0.500	27.5			16.09	3.31
		Center	14	0.75	165				
	I_3	Edge	6.5	0.500	27.5			25.74	5.79
		Center	14	1.375	165				
Edge Length Ratio	L_{e1}	Edge	6.5	0.500	27.5	0.125	9.10%	8.73	1.70
		Center	14	0.375	165				
	L_{e2}	Edge	6.5	0.500	26	0.118			
		Center	14	0.375	168				
	L_{e3}	Edge	6.5	0.500	25	0.113			
		Center	14	0.375	170				

The cross-sections of the center and edge segments of each simulation case were built-up with the intention of comparing the design parameters with ease. The three-segment brace models were subjected to displacement-controlled monotonic compressive load until reaching an equivalent story drift ratio of 4%. Note that yielding strength of the braces differed from each other based on the cross-sectional properties. Therefore, the simulation results of each group (Fig. 4.7) are presented in terms of normalized compressive axial force (applied axial force divided by the nominal yield strength of the edge segment) and equivalent story drift ratio. It should also be noted that the D/t (diameter-to-wall thickness) ratios of the edge segments in all cases were constant so that the local plastic deformation of

the edge segment would not affect the results. The major findings can be summarized as follows:

(1) The ductility as well as compression overstrength of the specimens are sensitive to the changes in the length ratio (L_e/L and L_p/L). As indicated in Fig. 4.7(a), the plastic deformation capability of the brace specimens tended to increase when the edge length and the plastic zone length were reduced simultaneously.

(2) It appears that the moment of inertia ratio (I_c/I_e) affects the critical buckling load. However, as shown in Fig. 4.7(b), the moment of inertia ratio did not play an important role on the inelastic deformation capability of the brace specimens. Note that the slight difference between the pushover curves given in Fig. 4.7(b) was caused by the variation of the initial stiffness of the specimens.

(3) It is evident from the analysis results given in Fig. 4.7(c) that variations in the edge length ratio (L_e/L) did not affect the results when the length of the yielding zone (L_p) was constant. It seems that the pushover results, as well as the deformed shapes and relative stress distributions of the specimens in L_e group were identical (Fig. 4.7c).

(4) Overall, the findings of the parametric study strongly indicated that the length ratio of the plastic zone over the total length (L_p/L) is the most influential parameter in determining the inelastic deformation capacity of the three-segment braces.

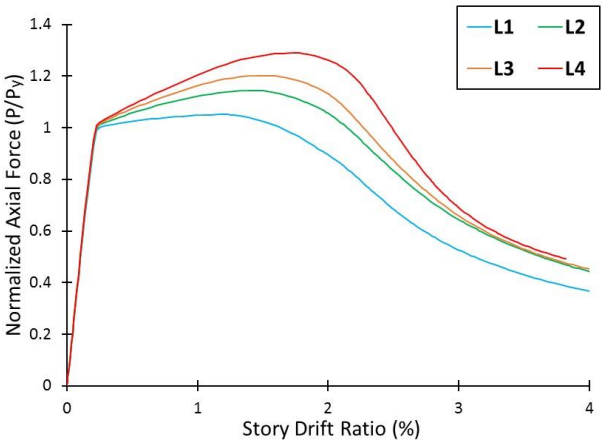

(a) Length ratio group (Group L)

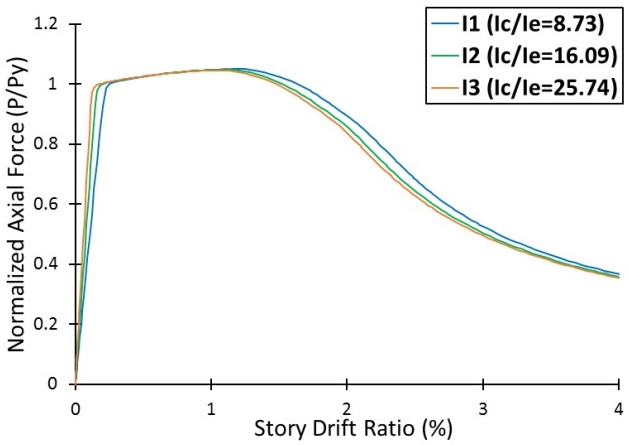

(b) Moment of inertia group (Group I)

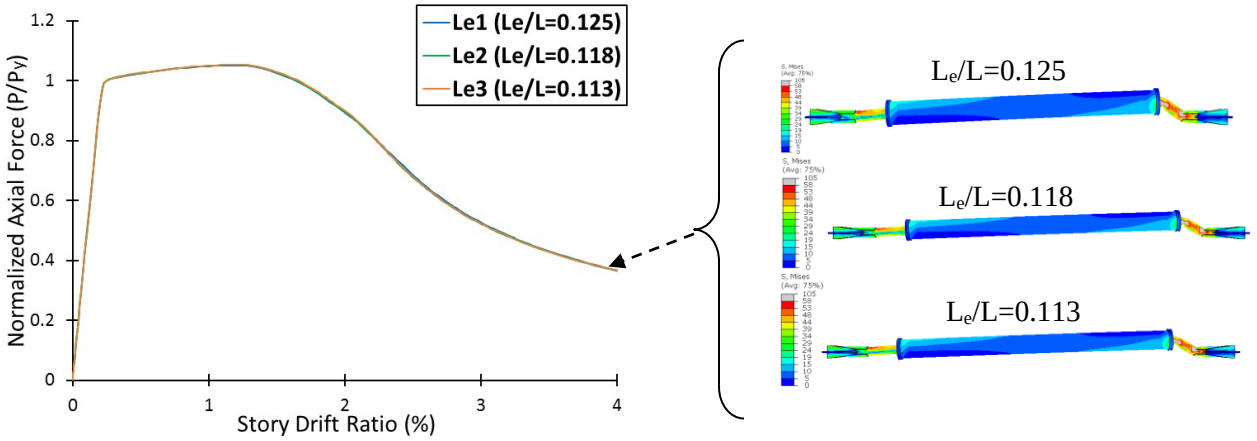

(c) Pushover results, deformed shapes and stress distributions of L_e group

Figure 4.7. Comparison of the simulation groups.

3. Cyclic Behavior of Three-segment Braces

Inelastic cyclic behavior of the three-segment braces is evaluated by means of a set of FE simulations in order to design the test specimens for the experimental study attentively. Table 4.2 presents the specimen options and the parameters related to their cyclic behavior. The design of each specimen and selection of the edge and center tube sections were based on the available loading capacity of the test equipment and the previously presented

parametric study for determination of the key design parameters. Additionally, the impact of the section compactness of the tubes on the cyclic behavior was also examined in this simulation group. As shown in Table 4.2, the outer diameter-to-wall thickness ratio (D/t) of each section is normalized with the limiting slenderness parameter for highly ductile compression elements (AISC, 2010b). Since the plastic deformations are expected to accumulate in the edge tubes, the normalized D/t ratios of the edge tubes in all cases were selected to be smaller than the limiting value stipulated in AISC Seismic Provisions (2010). The center tube section, on the other hand, had a wide variety of normalized D/t ratios on the order of 0.52 to 1.32. The length of the yielding segment (L_p) was limited to about one seventh of the total length in all cases. The distance from brace end to brace end was 42" while the total length (from gusset end to gusset end) was 51.5" for all specimens. The gross area of the center tubes were at least 60% larger than those of the edge tubes in all cases except for specimen#3, which was intentionally generated to assess the hysteretic response of the three-segment braces when the center and edge tubes have similar cross-sectional areas.

Table 4.2. Simulation cases for cyclic response evaluation.

Specimen	Edge Tube	Center Tube	λ_e/λ_{hd}*	λ_c/λ_{hd}**	I_c/I_e	A_c/A_e	L_p/L
#1	HSS1.9x0.188	HSS4x0.220	0.42	0.74	12.4	2.59	0.133
#2	HSS2.5x0.125	HSS4x0.125	0.82	1.32	4.31	1.63	0.131
#3	HSS2.5x0.188	HSS4x0.125	0.55	1.32	3.09	1.12	0.137
#4	HSS2.5x0.188	HSS4x0.250	0.55	0.66	5.68	2.17	0.137
#5	HSS2.5x0.188	HSS4x0.250	0.55	0.66	5.68	2.17	0.105
#6	HSS2.375x0.218	HSS4x0.313	0.45	0.52	7.12	2.44	0.129

*The ratio of $(D/t)_{Edge}$ over the limiting slenderness parameter for highly ductile compression elements (λ_{hd}).
** The ratio of $(D/t)_{Center}$ over the limiting slenderness parameter for highly ductile compression elements (λ_{hd}).

The FE models were built in a general purpose finite element software ABAQUS 6.12.3 (Hibbit et al. 2012). Newton-Raphson method was employed to the non-linear static

analyses. All parts of the specimens were modeled using 8-node linear brick elements with reduced integration points (C3D8R). Since actual material properties were not available before experiment, kinematic hardening rule was adopted with nominal material properties for the non-linear material definition. A simplified version of the loading protocol given in AISC Seismic Provisions (2010) was adopted for the cyclic simulations. The loading sequence used in the simulations and the applied axial displacements at each cycle are given in Figure 4.8 and Table 4.3, respectively.

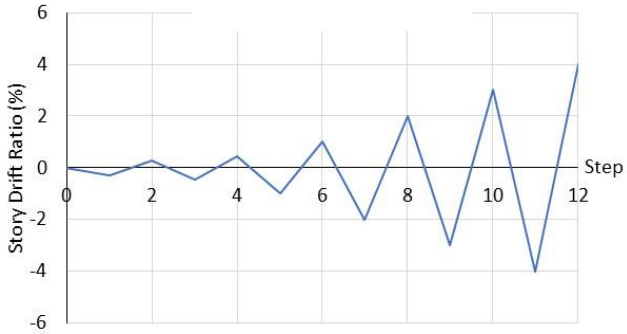

Figure 4.8. Cyclic loading protocol used in the study.

Table 4.3. Loading sequence used in the study.

Cycle	Δ_a (in)	Story Drift Ratio (%)*
1@ Δ_{by}	±0.063	0.28
1@ $1.5\Delta_{by}$	±0.095	0.42
1@ $0.5\Delta_{bm}$	±0.210	1.00
1@ $1.0\Delta_{bm}$	±0.420	2.00
1@ $1.5\Delta_{bm}$	±0.630	3.00
1@ $2.0\Delta_{bm}$	±0.840	4.00

*Story Drift Ratio=$2\Delta_a/L_b$ where
Δ_a: Axial displacement L_b: The brace length

The simulation results are discussed through the hysteretic response and deformed shape of the specimens. Table 4.4 summarizes the limit states and the observed deformation patterns for each limit state. The hysteretic stability of the specimens appears to be significantly affected by the section compactness (D/t ratio). Specimen#2, for example, was the model that possesses the largest normalized D/t ratio. As indicated in Table 4.4, it is observed that Specimen#2 was experienced local plastic deformations at around 1.00% SDR during the cycle to 2.00% SDR (Fig. 4.9b) while the other specimens with similar parameters but smaller D/t ratios, such as Specimen#4 (Fig. 4.10a) and Specimen#5 (Fig. 4.11a)

exhibited more stable hysteretic response, and experienced local plastic deformations in latter cycles. Necking of the edge tube of Specimen#2 began during the cycle at a story drift ratio of 2% while the necking due to compressive deformation began during the cycle at 3.00% SDR for Specimen#4 and Specimen#5. In other words, regardless of the impact of the other parameters, occurrence of the local plastic deformations was consistently postponed as normalized D/t ratio decreases, as in conventional buckling braces. Eventually, the necking of the edge tubes led specimens# 2, 4 and 5 to higher order local deformations, as shown in Figs. 4.9b, 4.10b and 4.11b.

Table 4.4. Observed deformation patterns

Specimen	λ_e/λ_{hd}*	λ_c/λ_{hd}**	A_c/A_e	L_p/L	Deformation Pattern	Cycle / Deformation	Critical Segment
#1	0.42	0.74	2.59	0.133	Local plastic deformation	During the 6th cycle @3.00% SDR	Edge Tube
#2	0.82	1.32	1.63	0.131	Local plastic deformation	During the 4th cycle @1.00% SDR	Edge Tube
#3	0.55	1.32	1.12	0.137	Global buckling	During the 4th cycle @1.41% SDR	Center Tube
#4	0.55	0.66	2.17	0.137	Local plastic deformation	During the 6th cycle @1.00% SDR	Edge Tube
#5	0.55	0.66	2.17	0.105	Local plastic deformation	During the 6th cycle @1.00% SDR	Edge Tube
#6	0.45	0.52	2.44	0.129	Local plastic deformation	During the 6th cycle @3.00% SDR	Edge Tube

*SDR: Story drift ratio.

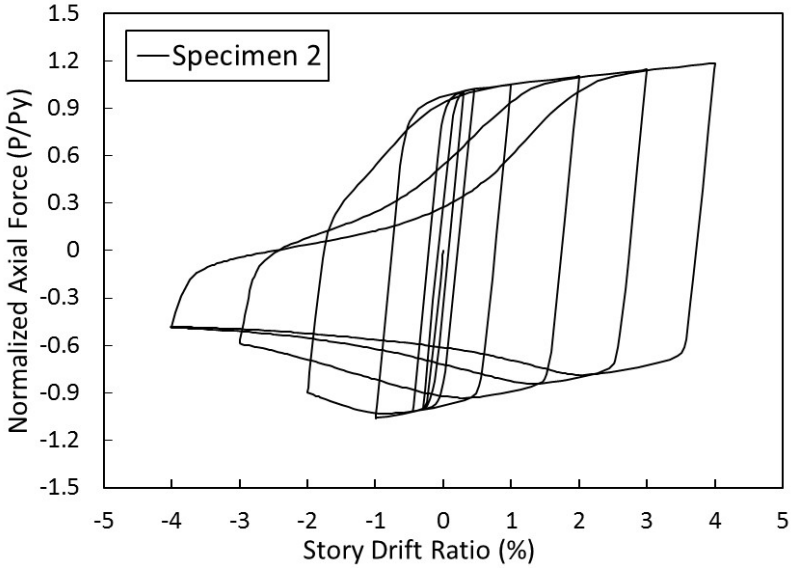

(a) Hysteresis

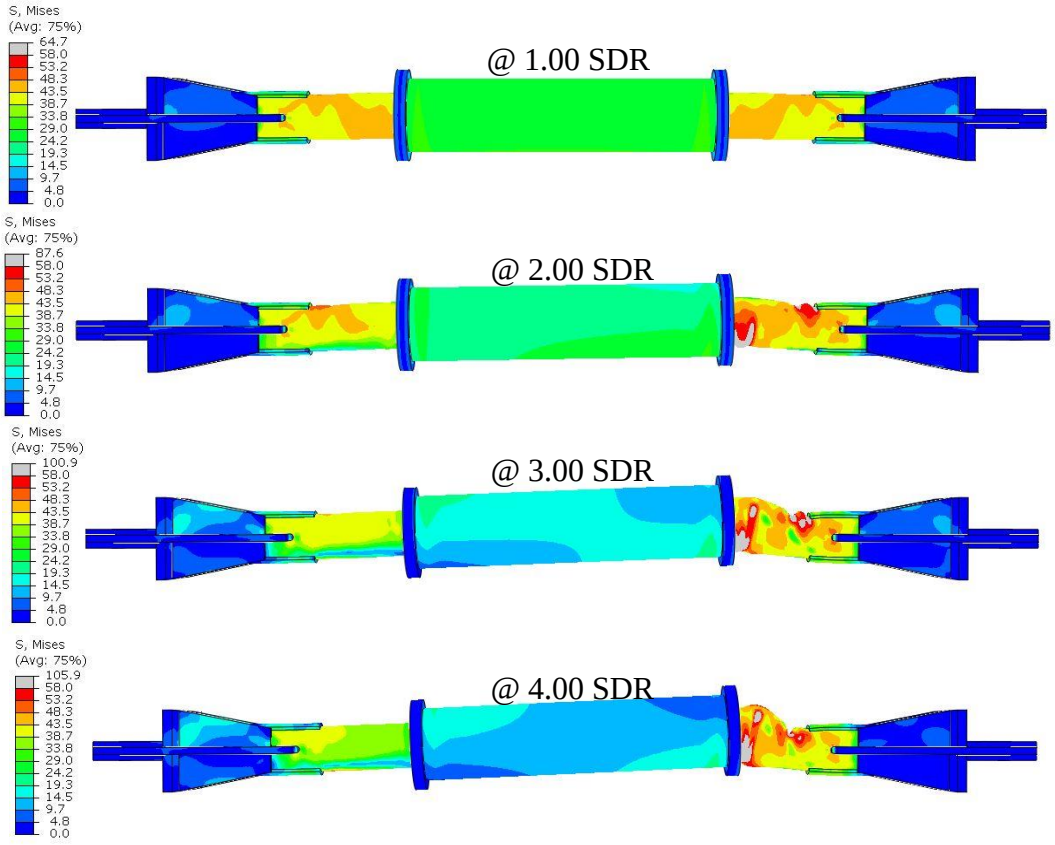

(b) Deformed shape and stress distribution (ksi)

Figure 4.9. Hysteretic response, deformed shape and stress distribution (ksi) of Specimen#2.

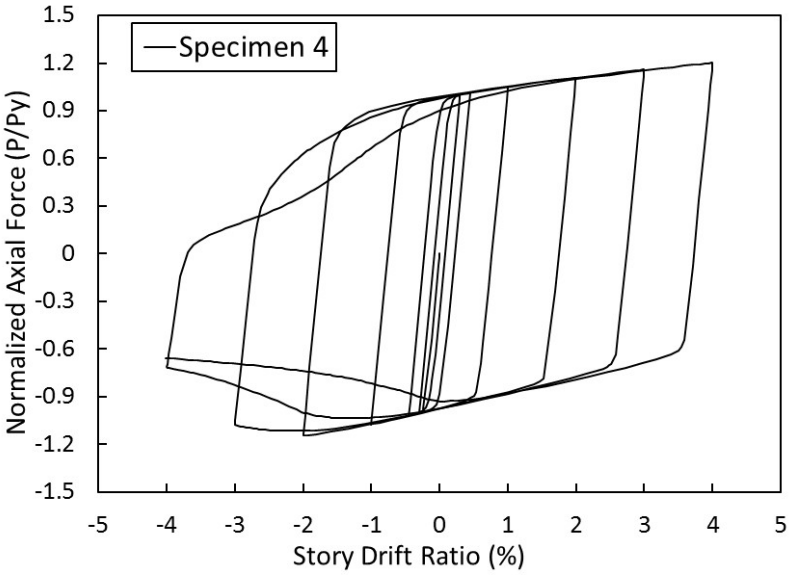

(a) Hysteresis

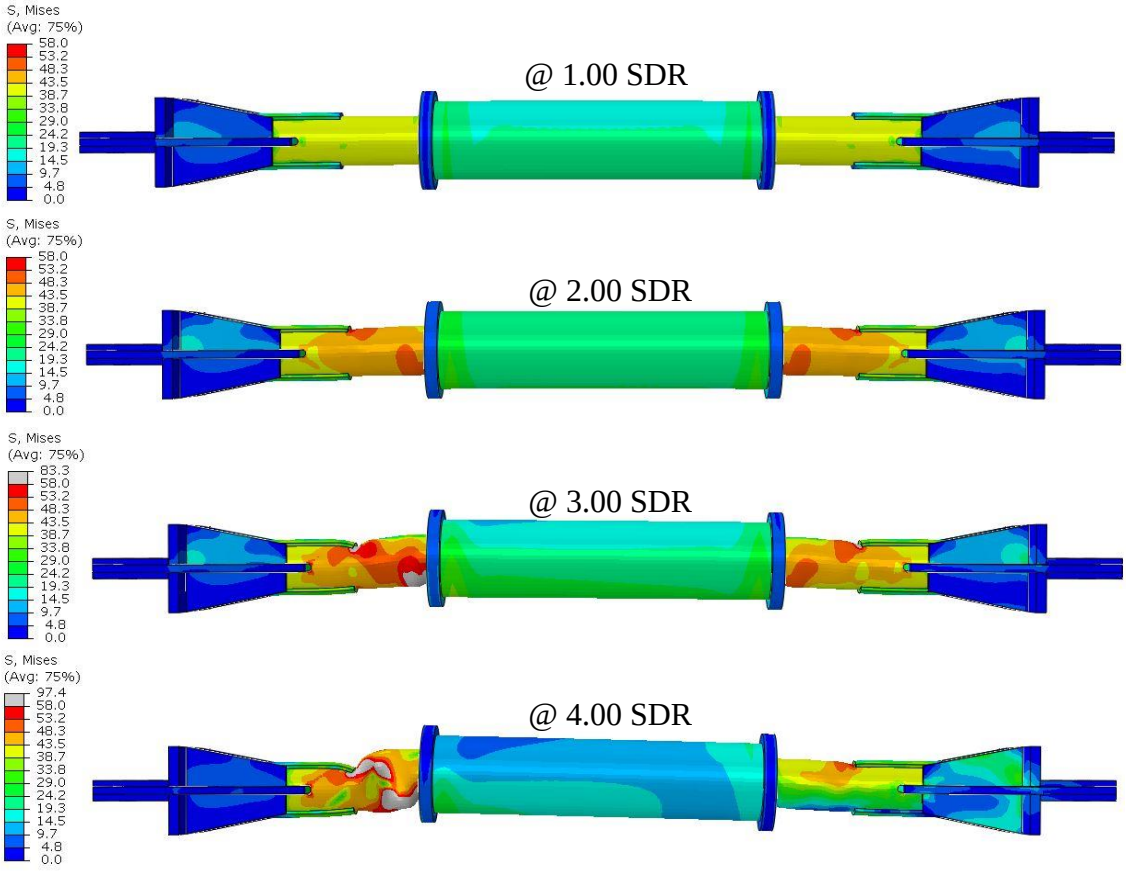

(b) Deformed shape and stress distribution (ksi)

Figure 4.10. Hysteretic response, deformed shape and stress distribution (ksi) of Specimen#4.

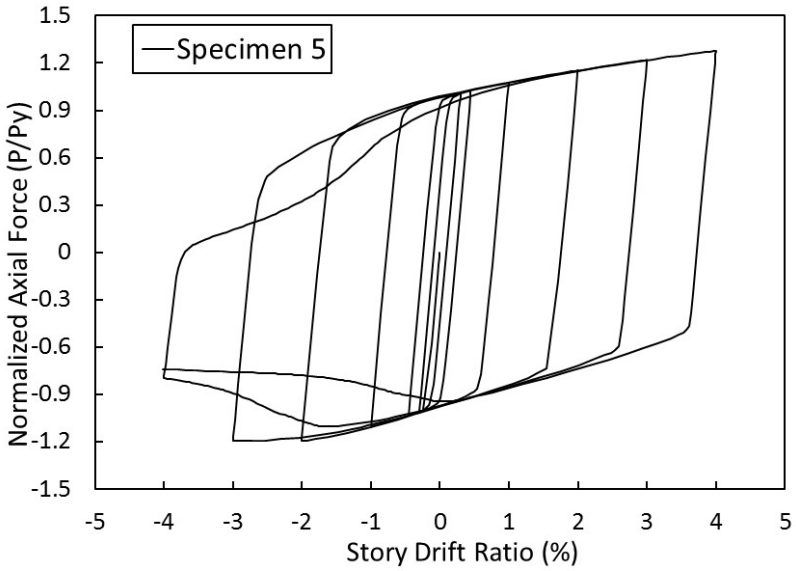

(a) Hysteresis

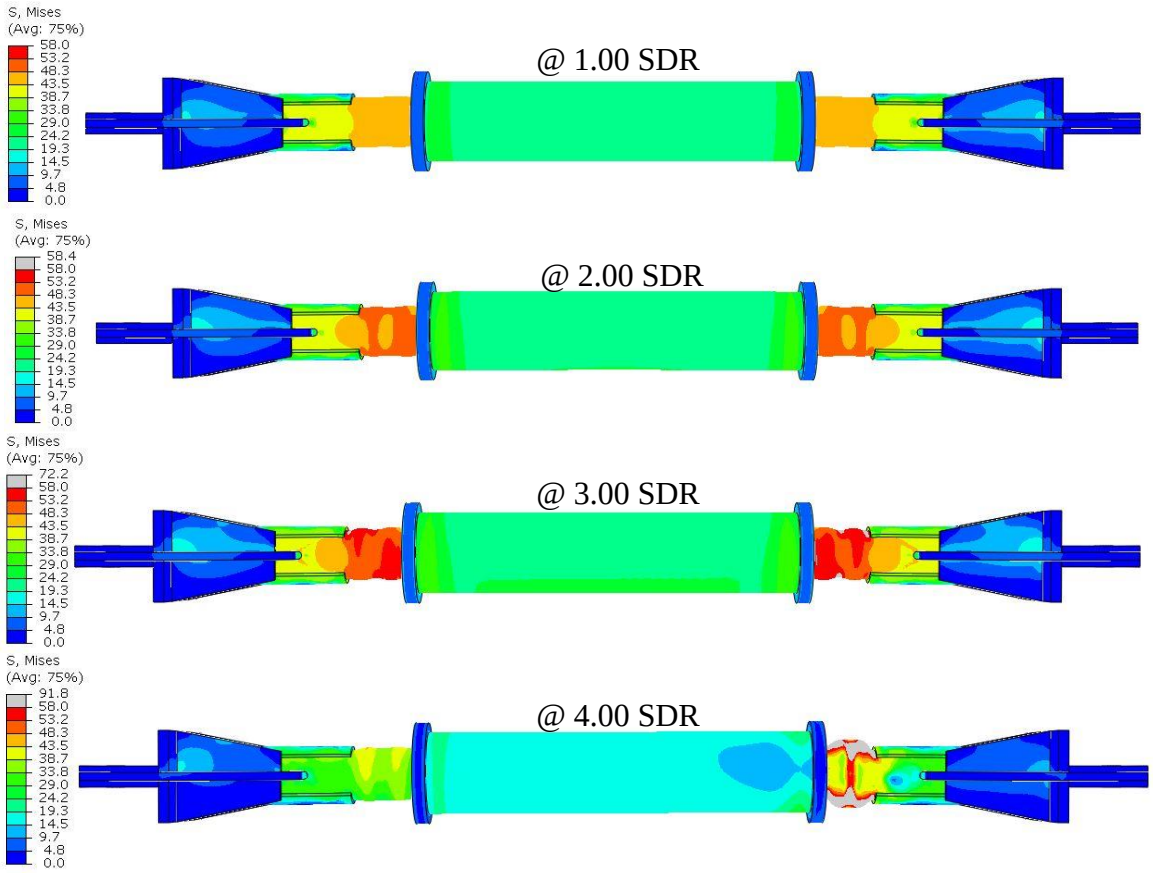

(b) Deformed shape and stress distribution (ksi)

Figure 4.11. Hysteretic response, deformed shape and stress distribution (ksi) of Specimen#5.

Hysteretic response of Specimen#3 was fairly stable until a story drift ratio of 3% (Fig. 4.12a). The center segment of Specimen#3 did not remain elastic, as anticipated. Since the gross area of the center tube of Specimen#3 was slightly larger than that of the edge tube, global buckling of the entire assembly took place during the cyclic simulation of Specimen#3 (Fig. 4.12b). Three plastic hinge formed during the simulation and the specimen kept almost 70% of its yielding strength at a story drift ratio of 4% in compression.

As indicated in Fig. 4.12(b), neither local nor global buckling took place during the cycle at 1% story drift ratio. As presented in Table 4.4 and Fig. 4.12(b), global buckling initiated at 1.41% SDR during the compression cycle to 2.00% SDR and plastic hinge formed in the mid-length of the center segment of Specimen#3 at 3% story drift ratio. Due to plastic deformation of the mid-length of the center tube, local buckling of the center tube became substantial at a story drift ratio of 4% (4.12b). Therefore, unlike the other simulation cases, inelastic cyclic behavior of Specimen#3 was not solely determined based on the limit states of the edge tube.

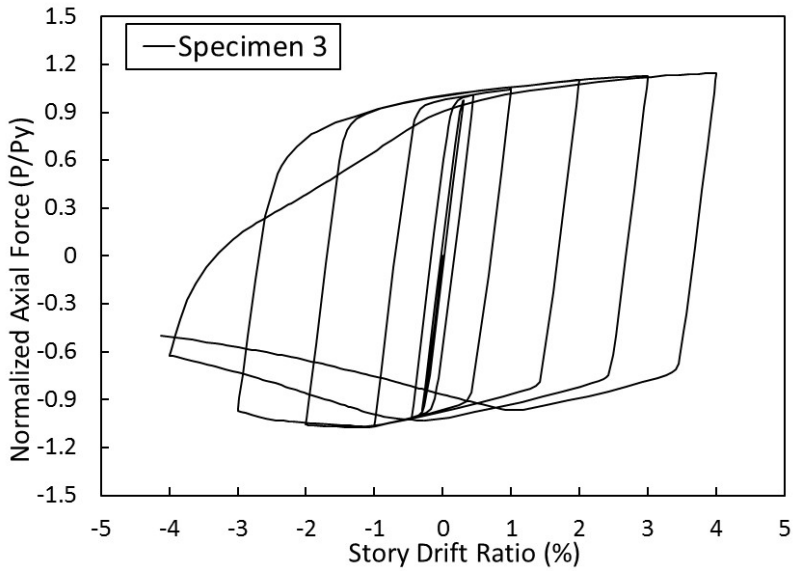

(a) Hysteresis

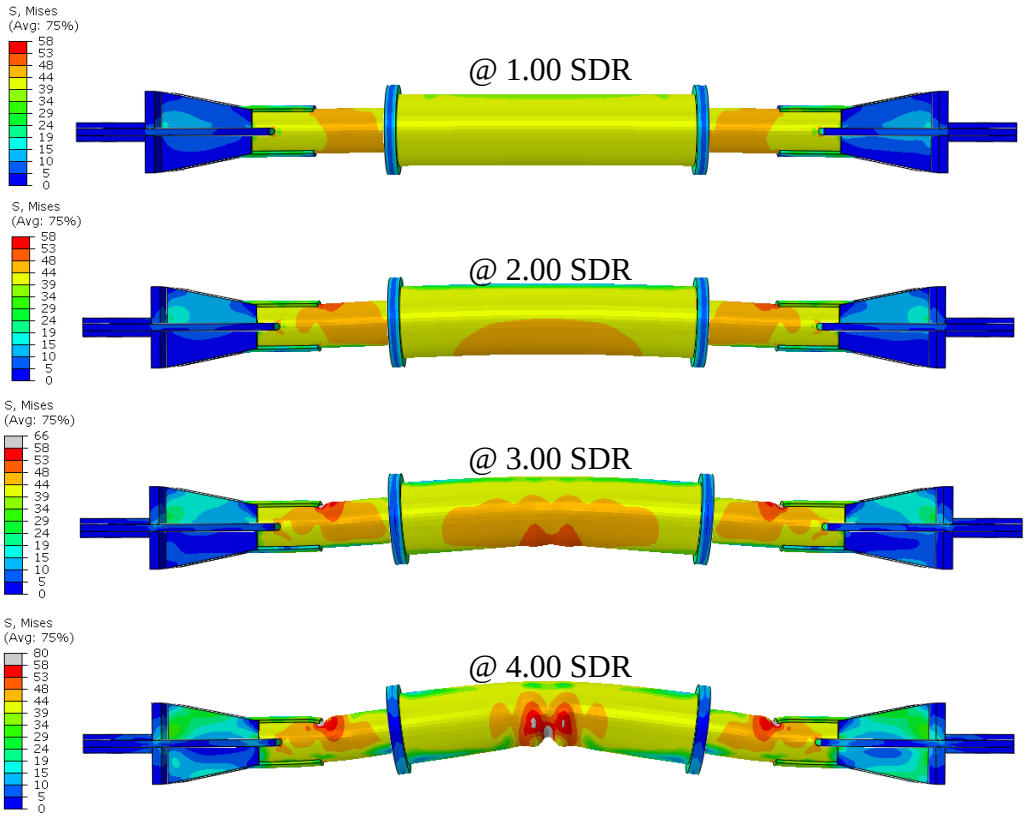

(b) Deformed shape and stress distribution (ksi)

Figure 4.12. Hysteretic response, deformed shape and stress distribution (ksi) of Specimen#3

Hysteretic responses and relative stress distributions of Specimen#1 and Specimen#6 are summarized in Fig. 4.13 and Fig. 4.14, respectively. Inelastic cyclic response of Specimen#1 and Specimen#6 were quite similar. It appears that the cyclic response of both specimens remained substantially stable up to a 3% story drift ratio (Figs. 4.13a and 4.14a) both in tension and compression, since the plastic zone and the connector plates did not experience local plastic deformations during the first five cycles (Figs. 4.13b and 4.14b). It is noticed that there was a slight drop in compression strength due to the necking of the edge segment subsequent to the compression cycle at 3% story drift ratio.

The compression overstrength with respect to the tension strength was less than 5% at any deformation level in the simulations both Specimen#1 and 6. Note that the gross area of the center segments of Specimen#1 and Specimen#6 were almost 2.5 times the cross-sectional area of the edge segments. Therefore, the center segments remained elastic during the cycles. Figs 4.13(b) and 4.14(b) shows the deformed shape of the specimens at each compression cycle. Necking of the edge tube due to compressive yielding occurred around a story drift ratios of 2% during the 4th cycle. Global buckling of Specimen#1 and 6 was initiated during the 5th cycle. As shown in Figs. 4.13(b) and 4.14(b), severe local plastic deformation of the edge tubes took place during the compression cycle at a story drift ratio of 3% during the sixth cycle (Table 4.4). Local deformations of the edge segments of Specimen#1 and 6 occurred in a region slightly close to the end of the net section reinforcing plates as well as in the vicinity of the welded connections between the connector plate and the edge tube. It is also noteworthy that the normalized D/t ratio of the center tube was not a controlling parameter when the gross area of the center tube was large enough to remain elastic.

On the whole, our simulation results indicated that Specimen#1 and Specimen#6 are promising in terms of energy dissipation capability, peak ductility as well as hysteretic stability. Thus, Specimen#1 and Specimen#6 of FEM-based numerical study were selected as the test specimens of the experimental program.

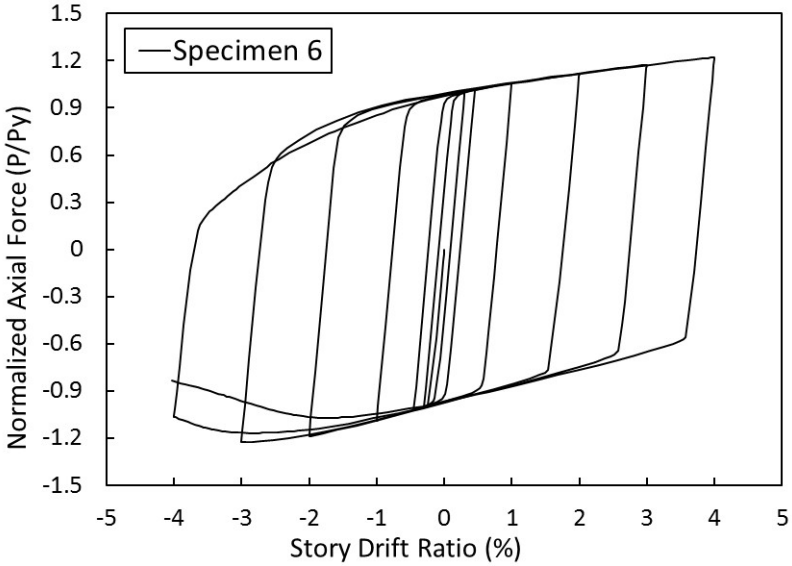

(a) Hysteresis

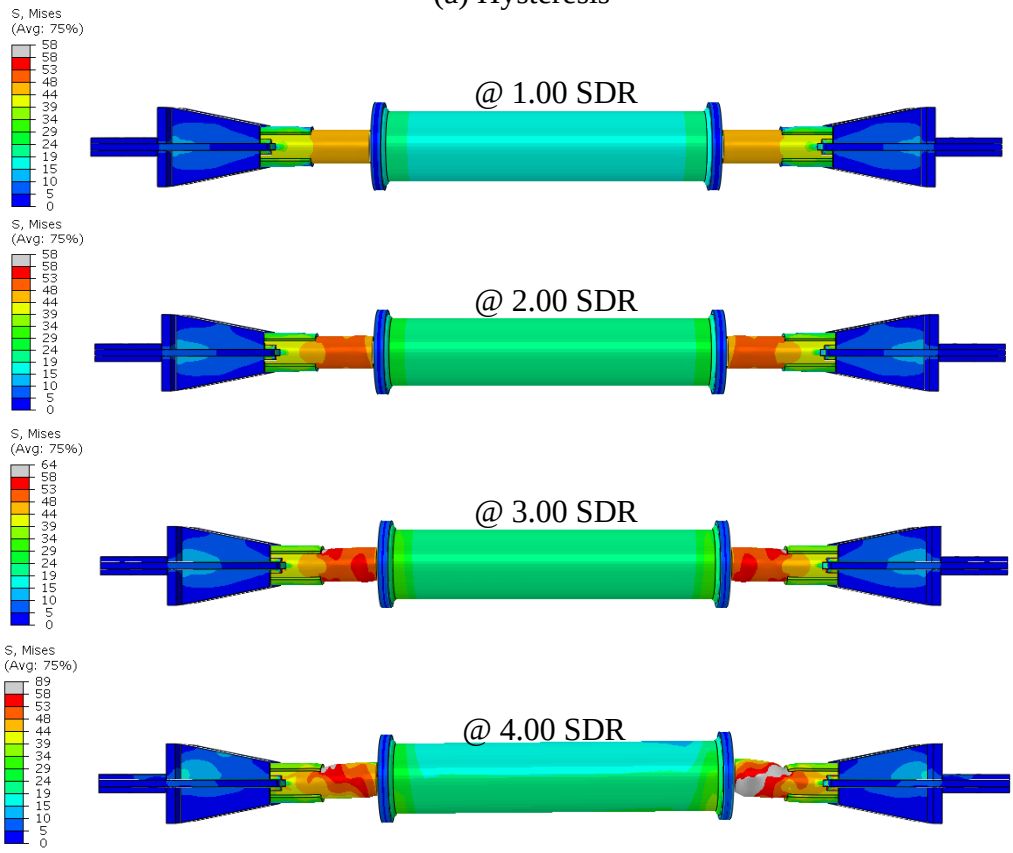

(b) Deformed shape and stress distribution (ksi)

Figure 4.13. Hysteretic response, deformed shape and stress distribution (ksi) of Specimen#1

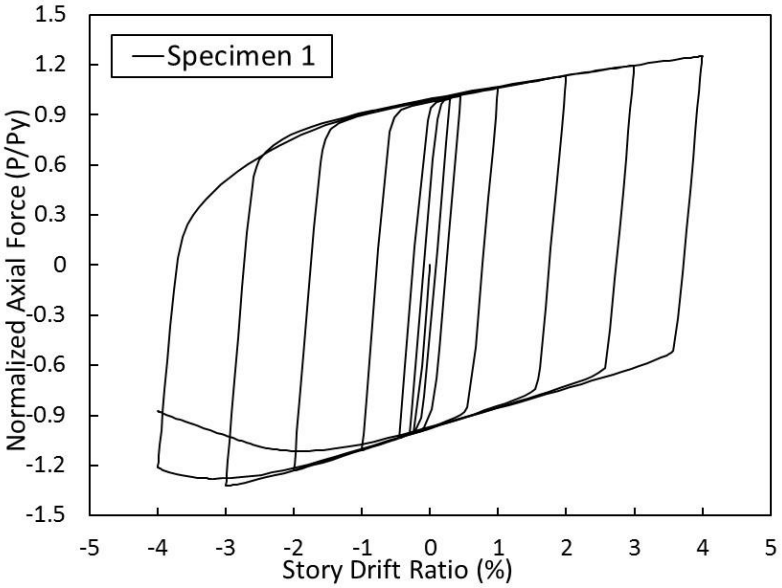

(a) Hysteresis

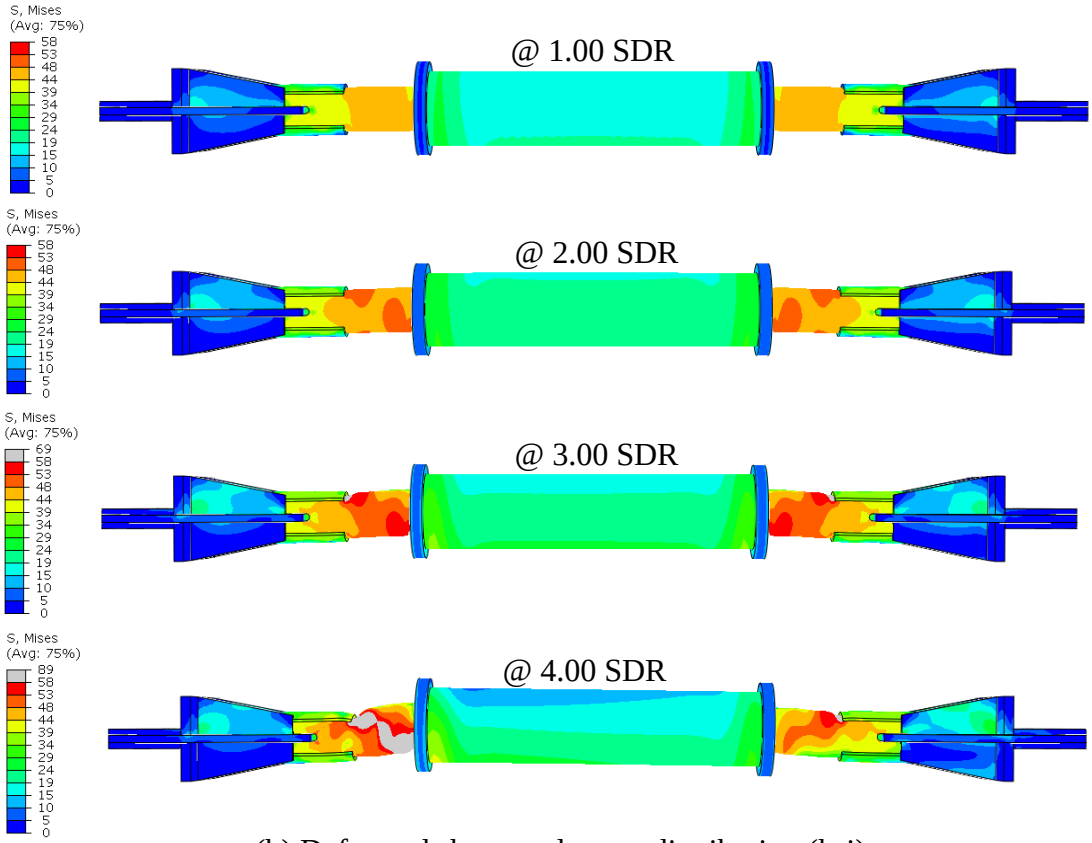

(b) Deformed shape and stress distribution (ksi)

Figure 4.14. Hysteretic response, deformed shape and stress distribution (ksi) of Specimen#6

4. Experimental Study

A set of small-scale three-segment brace specimens with a variety of design parameters and connection types has been tested to examine the hysteretic behavior of the developed three-segment braces under reversed cyclic loading. Table 4.5 summarizes the edge and center tube sections, the design parameters and connection type of the test specimens. The edge tube sections were determined based on the previously presented numerical study as well as considering the available loading capacity of the test equipment. Note that Specimen#2 and Specimen#2 (CJP) were identical except for their welded connections. The fillet welds used to attach the edge tubes to the connector plates of Specimen#2 were replaced with groove welds with complete joint penetration for the fabrication of Specimen#2 (CJP) with the purpose of avoiding potential connection failures.

Table 4.5. Properties of three-segment brace specimens

Specimen	Edge Tube	Center Tube	λ_e/λ_{hd}	I_c/I_e	A_c/A_e	L_p/L	Connection*
Specimen #1	HSS1.9x0.200	HSS4x0.219	0.42	12.4	2.59	0.133	Fillet Welds
Specimen #2	HSS2.375x0.218	HSS4x0.313	0.45	7.12	2.44	0.129	Fillet Welds
Specimen#2 (CJP)	HSS2.375x0.218	HSS4x0.313	0.45	7.12	2.44	0.129	Groove Welds

* The connections between the edge tube and the connector plate.

4.1. Fabrication of the three-segment brace specimens

Specimen 1 is composed of a three-segment brace, two gusset plates, two round connector plates, eight gusset plate stiffeners, four net section reinforcing plates, four horizontal supporting plates and four vertical supporting plates, which represent column/beam flange of a CBF. The three-segment brace consisted of two 11” long HSS1.90x0.200 sections (edge segment) and one 18.75” long HSS4.0x0.219 (center

segment), which were fillet welded to two five-inch diameter, 5/8" thick round plates. Drawing of Specimen 1 is given in Fig. 4.15.

The edge segment (HSS1.90x0.188) and the center segment (HSS4.0x0.220) of the three-segment brace were connected to the circular connector plate with 3/8" and 1/4" all-around fillet welds, respectively. The 5" inch slotted portion of the edge segment (Fig. 4.16a) was fillet welded to the 3/8" thick gusset plates. There was a 0.5" distance between the brace end and the vertical supporting plate. The 4.5" long net section reinforcing plates were connected to the edge tube with ¼" thick, 4.5" long fillet welds. The detailed description of the fabrication process of the gusset assemblies shown in Fig. 4.15(c) and (d) can be found in Chapter II.

Drawing of Specimen#2 is shown in Fig. 4.16. Similar to Specimen#1, Specimen#2 consisted of a three-segment brace, two gusset plates, two round connector plates, eight gusset plate stiffeners, four net section reinforcing plates, four horizontal supporting plates and four vertical supporting plates. The three-segment brace comprised two 11.5" long HSS2.375x0.218 sections (edge segments) and one 17.75" long HSS4.0x0.313 (center segment), which were fillet welded to two five-inch diameter, 5/8" thick round plates. The gusset assemblies and stiffeners of Specimen#2 were fabricated similar to the Specimen#1, even though the dimensions of the gusset assembly of Specimen#2 were slightly larger than those of Specimen#1.

As mentioned earlier, the design of Specimen#2 and Specimen#2 (CJP) were identical except that complete-joint-penetration (CJP) groove welds were utilized for the welded connections between the edge tube and circular connector plate of Specimen#2 (CJP). Therefore, Fig. 4.16 represents the design of both Specimen#2 and Specimen#2 (CJP).

The edge tubes were connected to the connector plates with shop-made CJP groove welds. Welding details of Specimen#2 (CJP) were determined based on the requirements of American Welding Society (AWS, 2000). The CJP welds were designed to have a bevel angle of 45 degrees, and root opening and root face of 1/8" and 0.100", respectively, as shown in Fig. 4.17. It should be noted that complete-joint-penetration groove welds were utilized only for the edge tube to connector plate connections, which were considered to be the demand critical connections. The other parts of the assembly were fillet welded to each other.

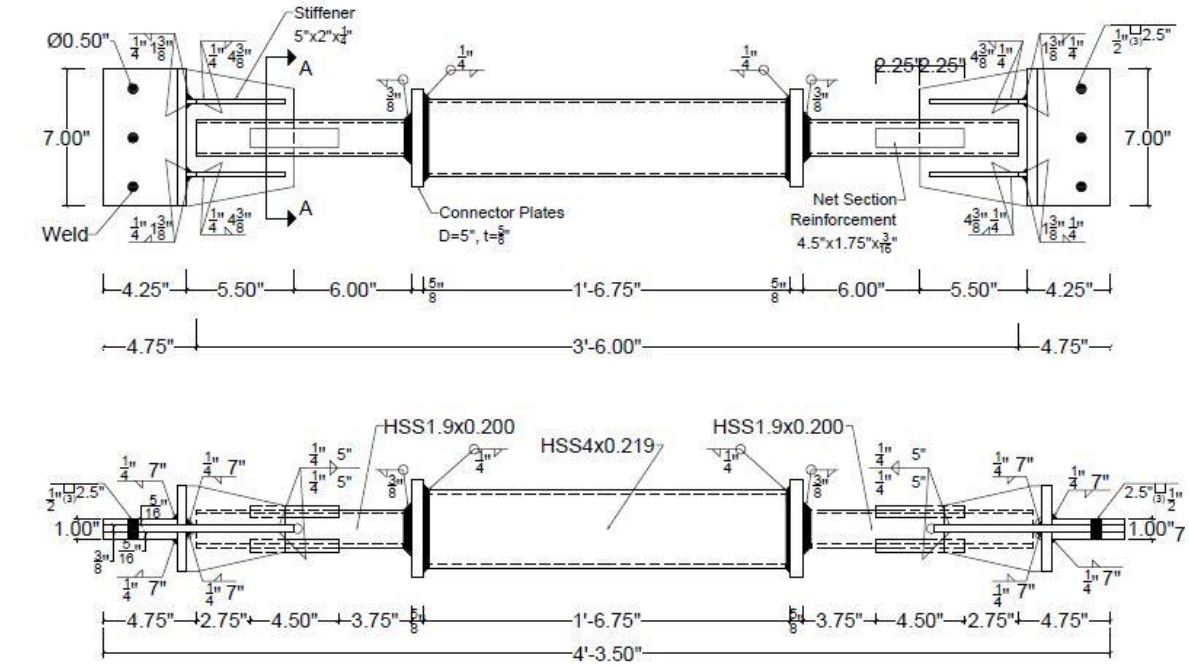

(a) Side view of Specimen 1

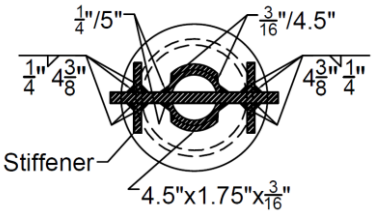

(b) Section A-A

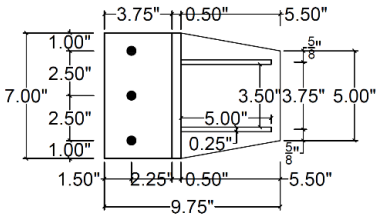

(c) Gusset assembly

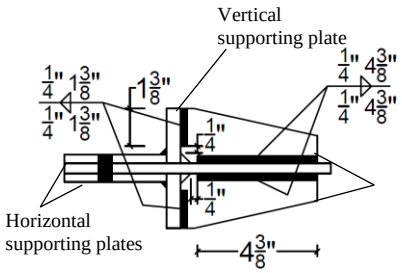

(d) Welding details of the stiffeners

Figure 4.15. Drawings of Specimen 1

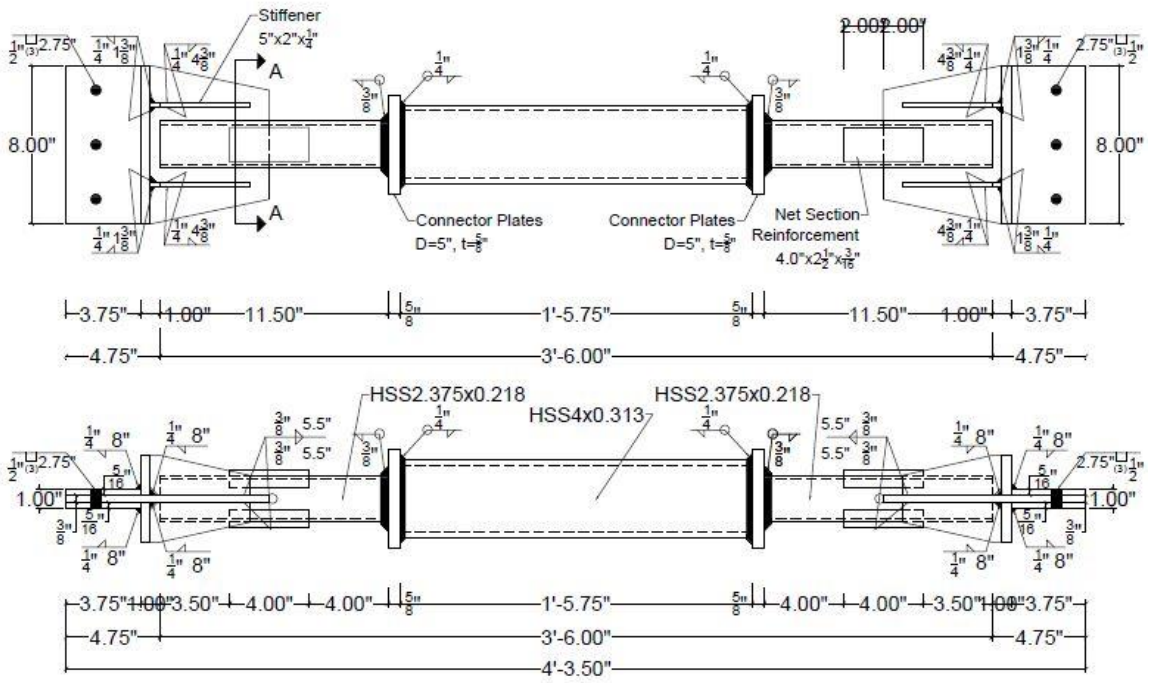

Figure 4.16. Drawings of Specimen 2

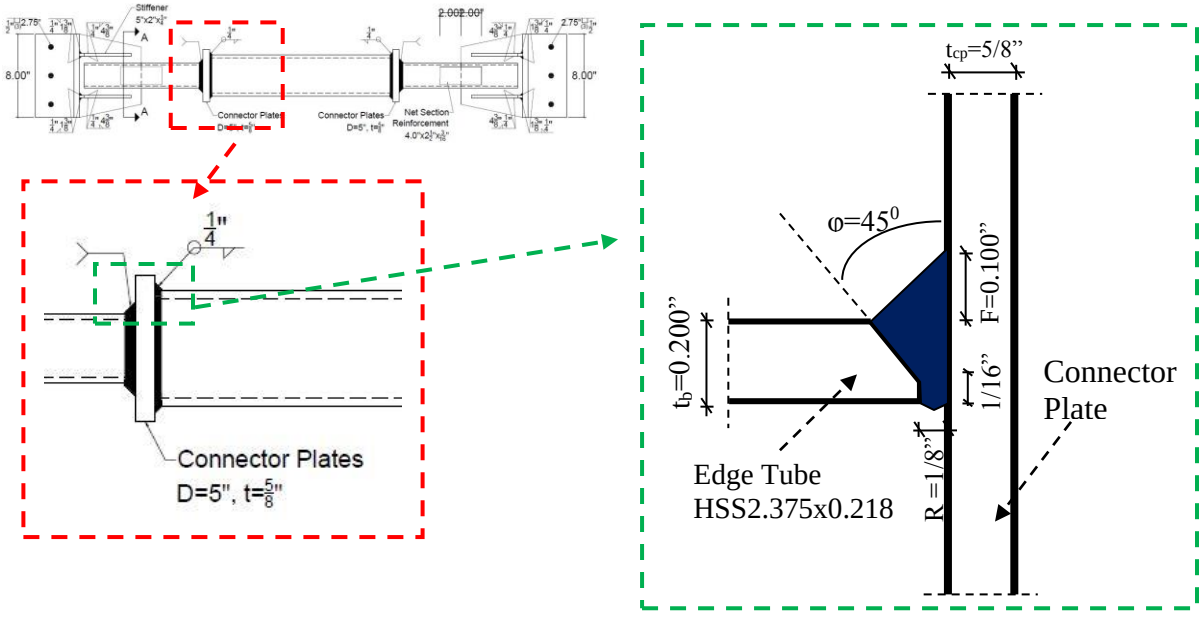

Figure 4.17. Welding detail of Specimen#2 (CJP) based on AWS D1.1 (2000)

The edge and center tubes of the specimens were made of ASTM A500 Gr.B type of steel with nominal yield stress of 42 ksi. Gusset plates, net section reinforcing plates and the stiffeners to reinforce the gusset plates were cut from ASTM A36 type of steel plates. Coupon tests were carried out to determine the actual material properties of the edge tubes, which are expected to undergo inelastic deformations. The actual material properties and the expected material strength factors, R_y and R_t for all specimens are given in Table 4.6.

Table 4.6. Coupon test results for the edge tubes of three-segment brace specimens

Specimen Name	Coupon #	$F_{y,\,meas}$ (ksi)*	$F_{u,meas}$ (ksi)	Max. Elongation,% (in/in)	R_y	R_t
Specimen#1	1	65	68.7	25.5	1.55	1.18
	2	63.5	66.9	28.5	1.51	1.15
Specimen#2	1	64.5	69.9	23.4	1.54	1.21
Specimen#2 (CJP)	1	65	72.1	21.2	1.55	1.24
	2	64	70.4	22.9	1.52	1.21

* Based on 0.2% offset rule.

4.2. Test setup, instrumentation and loading protocol

All three-segment brace specimens have been tested at the structural laboratory of Iowa State University. Side view of the test setup and the gusset plates attached to the top and the bottom grips are shown in Fig. 4.18.

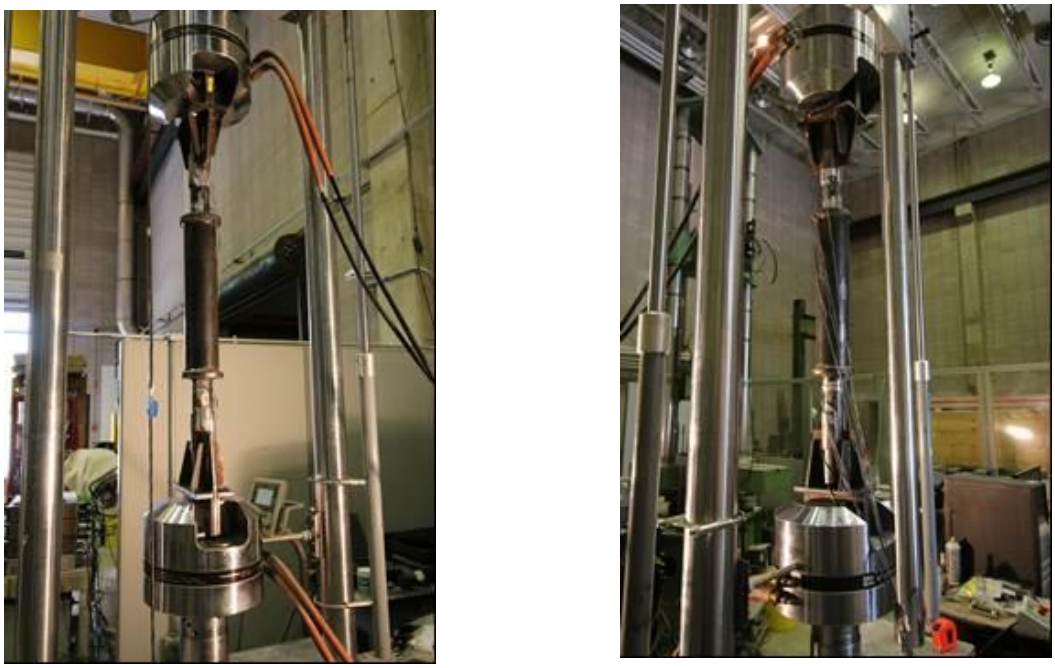

(a) Side views

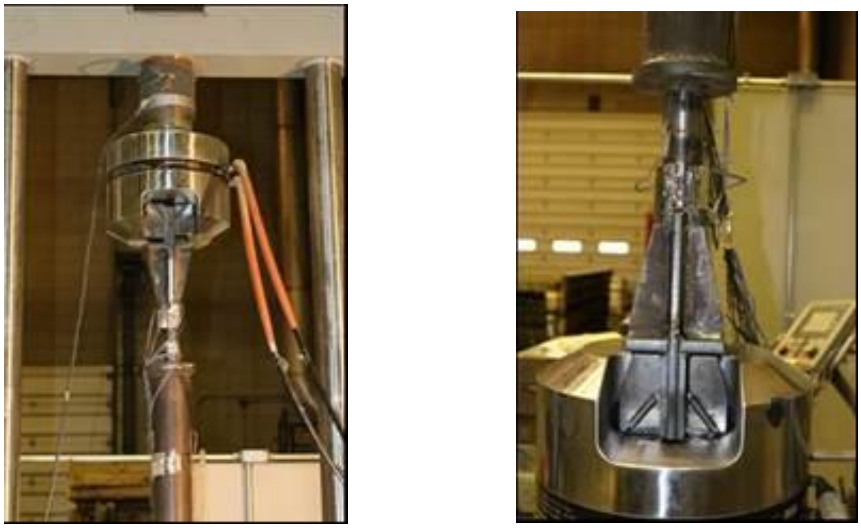

(b) Top grip (Loading end) (c) Lower grip (Fixed end)

Figure 4.18. Test setup and data acquisition system

4.2.1 Instrumentation

Instrumentation was installed for each test to measure strains, applied loads and displacements. A total of sixteen, eighteen and eight post-yield strain gauges have been mounted on Specimen#1, Specimen#2 and Specimen#2(CJP), respectively, to monitor strains in both axial and radial directions.

Location of each strain gauge installed to the first specimen is given in Fig. 4.19. The arrows next to the strain gauges show the direction of the strain measured. Strain gauge numbers, the part that the strain gauges are mounted on and the direction of the readings are given in Table 4.7. Based on the finite-element simulations conducted prior to the test program (Section 3), it is anticipated that the amplitude of the strains in radial direction of the edge tube would be as substantial as the expected strain amplitudes in axial direction. Therefore, equal number of strain gauges was placed in the axial and radial directions. As can be seen from Fig. 4.19, the locations of the strain gauges installed on the edge segments (i.e. strain gauge# 9 and 11 of the lower edge tube) were slightly different with the purpose of measuring the local deformations from alternative locations. Since the top edge tube was expected to experience more substantial plastic deformations, a total of four pairs of strain gauges were installed on the edge tube at the loading end (edge tube to the top). Some strain gauges located at the top edge tube are shown in Fig. 4.20(a). Two strain gauges were installed for each direction of the lower edge tube and the center tube (Figs. 4.20b and c). Note that the center tube was expected to remain elastic, but nevertheless two strain gauges were placed in both directions for the first test. The strain data was recorded with a sensitivity of 1 με.

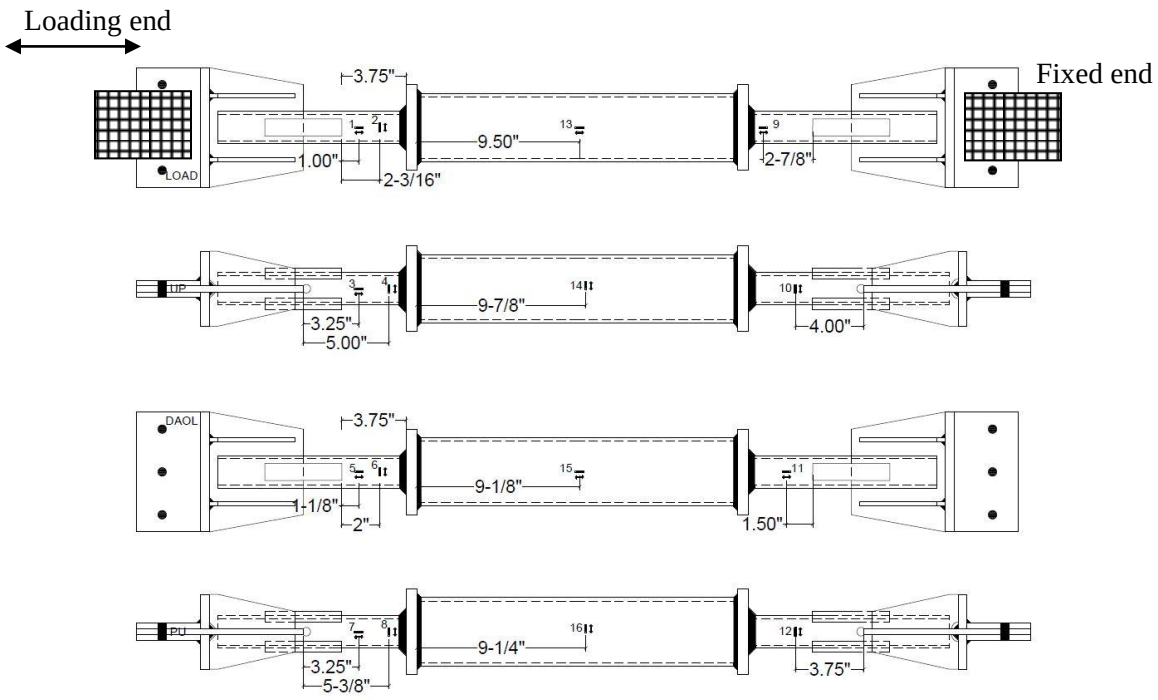

Figure 4.19. Strain Gauge Locations (Specimen#1)

Table 4.7. Strain gauge numbering of Specimen#1

Part	Direction	Strain Gauge #
Edge Tube to the Loading End	Axial	1
		3
		5
		7
	Radial	2
		4
		6
		8
Edge Tube to the Fixed End	Axial	9
		11
	Radial	10
		12
Center Tube	Axial	13
		15
	Radial	14
		16

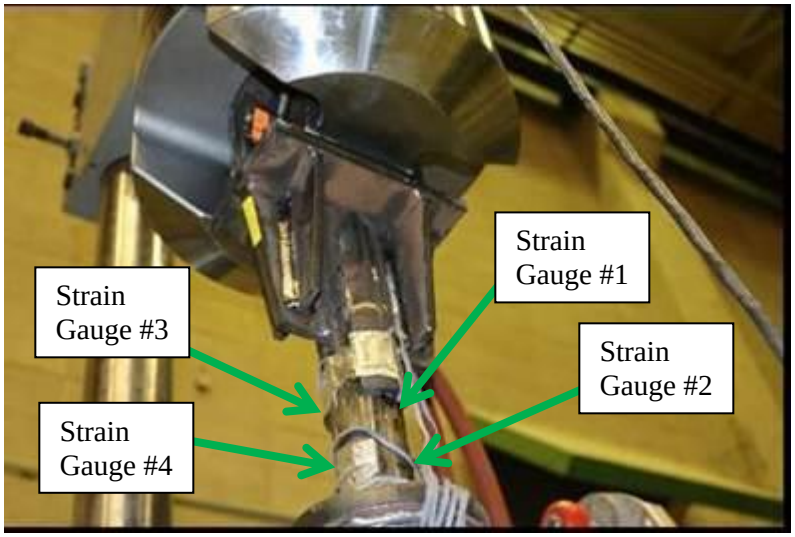

(a) Strain gauges 1 through 4 (Edge tube to the loading end)

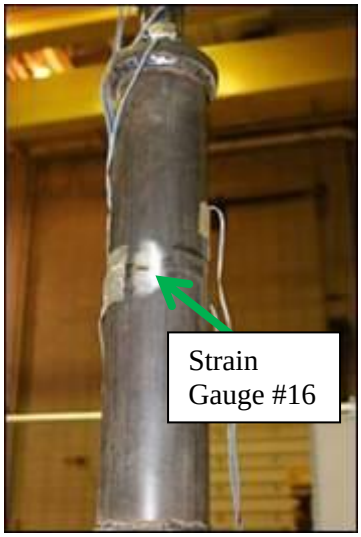

(b) Strain gauge#16 (Center Tube)

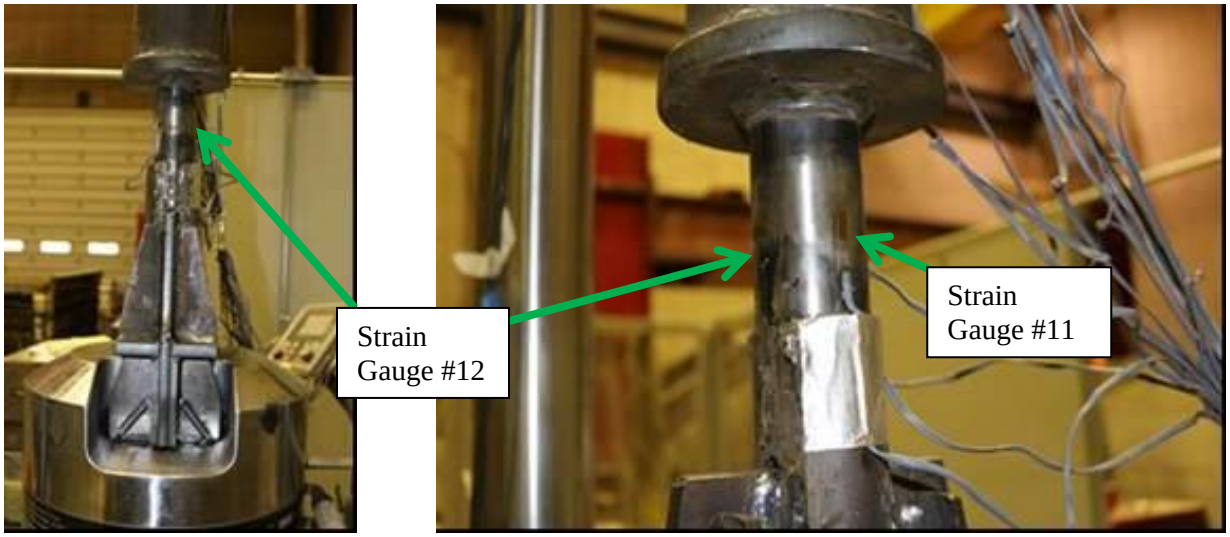

(c) Strain gauges 11 and 12 (Edge tube to the fixed end)

Figure 4.20. Strain gauges of Specimen#1

A total of eighteen post-yield strain gauges have been installed on the second specimen (Specimen#2) to monitor strains in both longitudinal and radial direction. Location of each strain gauge installed is given in Fig. 4.21. Strain gauge numbering of Specimen#2, the part that the strain gauges are mounted on and the direction of strain readings are given in

Table 4.8. Eight strain gauges were installed to each tube to the edge. Similar to Specimen#1, equal number of strain gauges were mounted in axial and radial directions. Although buckling or yielding of the center tube was not observed in the FE simulations, two strain gauges were installed to the center tube, which were located in the mid-length of the specimen, as given in Fig. 4.21. Fig. 4.22 demonstrates some of the strain gauges located at the edge tube to the fixed end (lower end). Owing to the unexpected problem with recording the strain data during the first test, the strain data was recorded with a sensitivity of 10 με in the second test.

Table 4.8. Strain gauge numbering of Specimen#2

Part	Direction	Strain Gauge #	Part	Direction	Strain Gauge #	Part	Direction	Strain Gauge #
Edge Tube to the Loading End	Axial	1	Edge Tube to the Fixed End	Axial	9	Center Tube	Axial	17
		3			11			
		5			13			
		7			15			
	Radial	2		Radial	10		Radial	18
		4			12			
		6			14			
		8			16			

The number strain gauges installed to Specimen#2 (CJP) were reduced compared to Specimen#2 on account of the redundant strain readings obtained from the same parts of Specimen#2. Additionally, the two strain gauges mounted on the center segment of Specimen#2 were eliminated for testing of Specimen#2 (CJP) due to the observed elastic behavior of the center segment during the second test. As seen in Fig. 4.23 and Table 4.9, a total of eight strain gauges were installed to Secimen#2 (CJP). Equal number of strain gauges was mounted in axial and radial directions and the strain data was recorded with a sensitivity of 10 με in the third test.

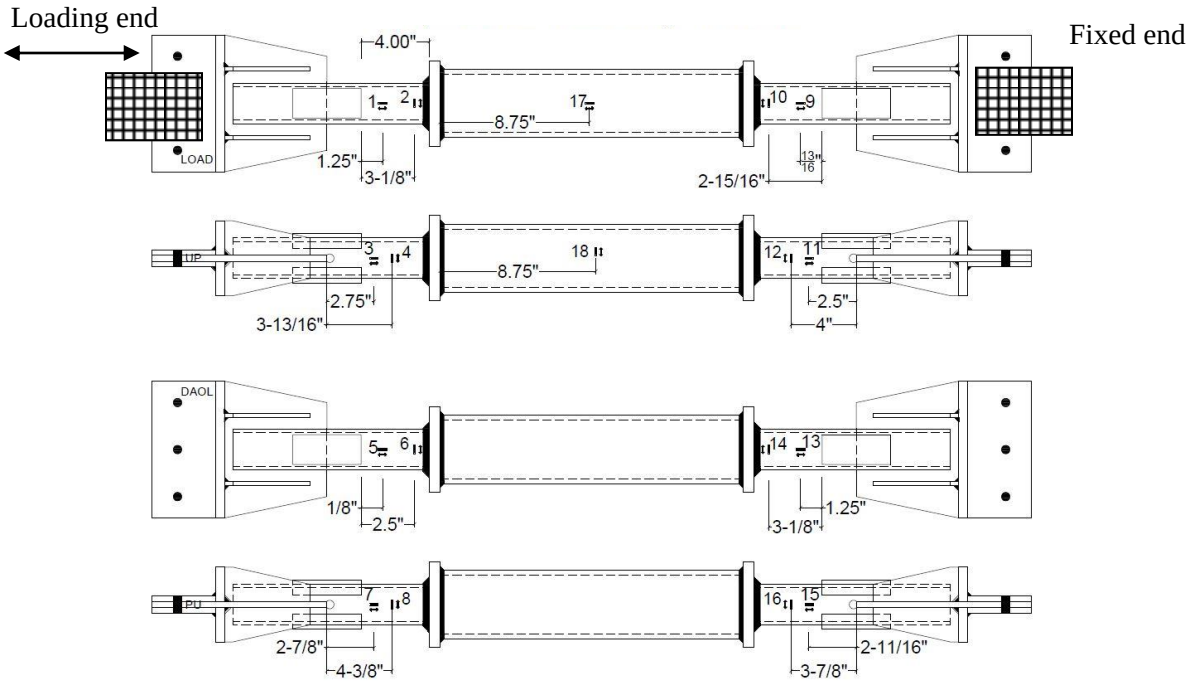

Figure 4.21. Strain gauge locations of Specimen#2

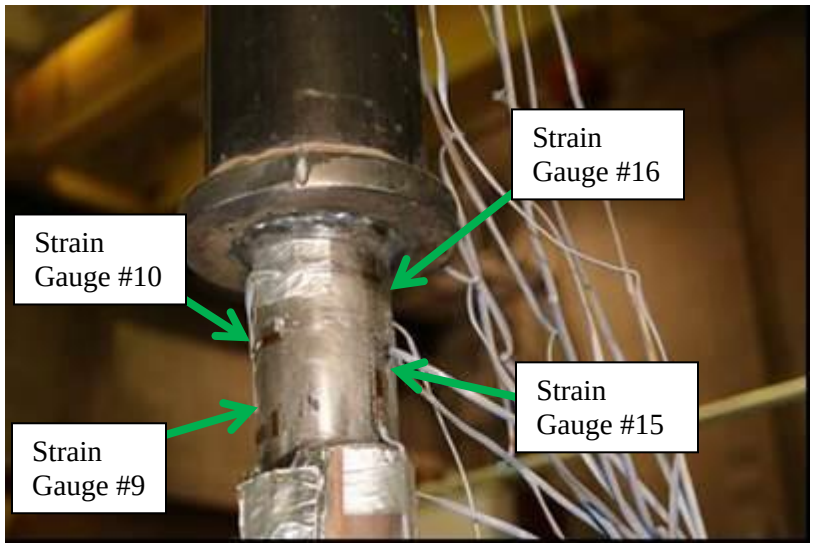

Figure 4.22. Strain gauges of Specimen#2 (# 9-10-15-16)

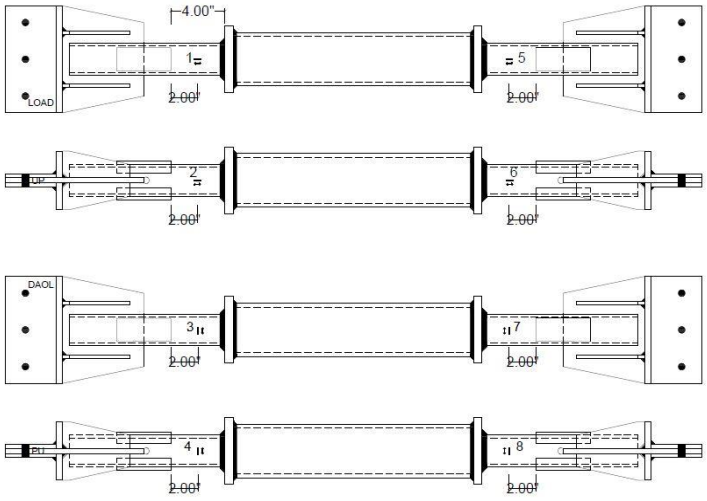

Figure 4.23. Strain gauge locations of Specimen#2 (CJP)

Table 4.9. Strain gauge numbering

Part	Direction	Strain Gauge#
Edge tube to the loading end	Axial	1
		2
	Radial	3
		4
Edge tube to the fixed end	Axial	5
		6
	Radial	7
		8

4.2.2. Loading protocol

A modified version of the loading protocol stipulated in AISC Seismic Provisions (2010) for qualification of BRB specimens was adopted for testing of Specimen#1. The loading sequence used in the first test and the applied axial displacement at each cycle are given in Figure 4.24 and Table 4.10, respectively. The axial displacements were converted to story drift ratio (%) by assuming an inclination angle of a 45 degree with respect to beam centerline (Story Drift Ratio=$2\delta/L_b$ where δ is the axial displacement and L_b is the brace length). The design story drift was assumed to be 2% of story height for the testing program. The dashed lines in Fig. 4.24 represent the cycles that were not completed due to the fracture of the edge tube. Note that the displacements were applied with a rate of 0.001 in/s for all specimens. Table 4.10 presents number of cycles at each deformation level, the relative axial displacements and the equivalent story drift ratio corresponding to each axial displacement.

Table 4.10. Loading protocol (Specimen#1)

# of Cycles	SDR%*	Axial Displacement (in)
3	0.05	0.010
3	0.07	0.015
2	0.20	0.040
2	0.25	0.053
2	0.28	0.059
2	0.30	0.063
2	0.32	0.067
2	0.35	0.074
2	0.40	0.084
2	0.45	0.095
2	0.60	0.126
2	1.00	0.210
2	2.00	0.420
2	3.00	0.630
2	4.00	0.840

*Equivalent story drift ratio.

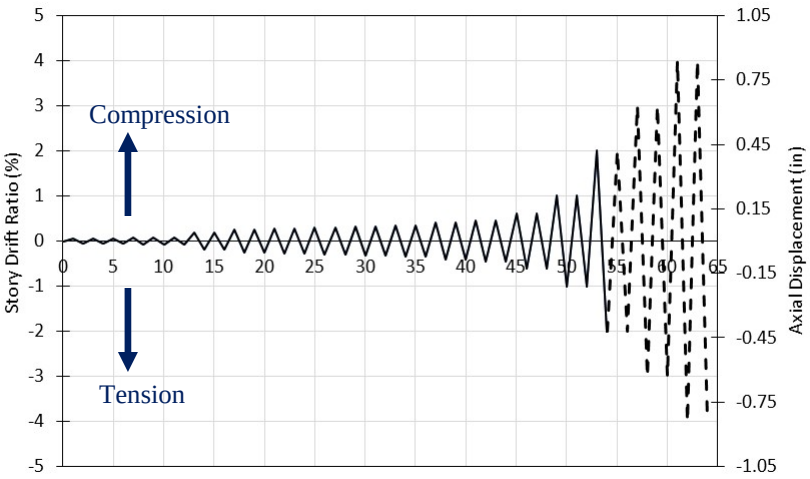

Figure 4.24. Loading protocol used in the first test.

The loading protocol adopted for the second test was similar to the one implemented for the first test. However, the number of the elastic cycles reduced in the second test. The loading sequence used in the test and the applied axial displacement at each cycle are given in Figure 4.25 and Table 4.11, respectively. In addition to the cycles required for qualification of BRB specimens, a number of elastic and inelastic cycles added to the protocol. Table 4.11 presents the details of the loading history. The axial displacements were converted to equivalent story drift ratios with the same assumption used for the first test. The dashed lines in Fig. 4.25 represent the incomplete cycles.

The second test began with three cycles at 0.10% story drift ratio with the purpose of detecting the possibility of a malfunctioning in the test setup prior to the inelastic cycles. Then, similar to the loading sequence used in the first test, the amplitude of the axial displacement for each cycle increased gradually with a small increment size in order to

capture actual yielding. Note that one cycle employed for each deformation level until yielding. Once yielding of the specimen observed, two cycles applied at each deformation level, as given in Table 4.11.

Table 4.11. Loading protocol (Specimen#2)

# of Cycles	SDR%*	Axial Displacement (in)
3	0.10	0.020
1	0.20	0.040
1	0.25	0.053
1	0.30	0.063
1	0.35	0.074
1	0.40	0.084
1	0.45	0.095
2	0.50	0.105
2	1.00	0.210
2	2.00	0.420
2	3.00	0.630
2	4.00	0.840

*Equivalent story drift ratio.

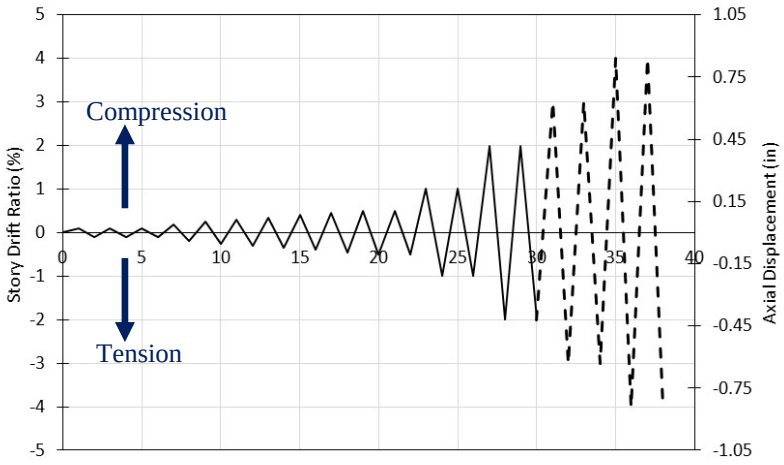

Figure 4.25. Loading protocol used in the second test.

The loading protocol adopted for testing of Specimen#2 (CJP) differed from the first two loading protocols in terms of number of cycles, as well as the deformation quantities at each cycle. Table 4.12 and Figure 4.26 present the number of cycles and axial displacements at each deformation level. As seen in Table 4.12, following the initial cycle at 0.20% story drift ratio, one cycle applied at 0.45% and 0.675% story drift ratios, which were corresponding to yielding (Δ_{by}) and 1.5 times the yielding ($1.5\Delta_{by}$) deformations, respectively. Then, the amplitude of the applied axial displacements were increased every cycle gradually to 1.00% SDR ($0.5\Delta_{bm}$), 1.50% SDR ($0.75\Delta_{bm}$), 2.00% SDR (Δ_{bm}) and 2.50% SDR ($1.25\Delta_{bm}$). The test was terminated soon after fracture initiation. The dashed lines in Fig. 4.26 account for the incomplete cycles.

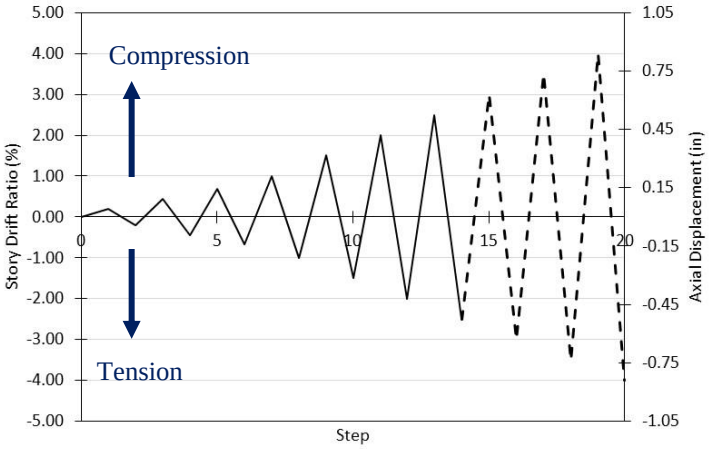

Figure 4.26. Loading protocol used in the third test.

Table 4.12. Loading protocol (Specimen#2 (CJP)).

# of Cycles	SDR%	Axial Displacement (in)
1	0.2000	0.042
1	0.4500	0.095
1	0.6750	0.142
1	1.0000	0.210
1	1.5000	0.315
1	2.0000	0.420
1	2.5000	0.525
1	3.0000	0.630
1	3.5000	0.735
1	4.0000	0.840

4.3. Test Results

4.3.1. Specimen#1

The cyclic behavior of Specimen#1 is shown in Fig. 4.27 in terms of story drift ratio, % (converted from relative displacement in axial direction) and the applied axial load. The specimen developed a peak axial load capacity of 69 and 66 kips in compression and tension, respectively. Yielding of the edge tube was observed at a story drift ratio of around 0.40% when the applied load was around 58 kips in tension. The initial elastic cycles, as well as the cycles at yielding (Δ_{by}) and 1.5 times the yielding deformations ($1.5\Delta_{by}$) did not develop any visible deformations during the test. Subsequent to the cycles at 0.60% SDR ($1.5\Delta_{by}$), the brace was subjected to an axial deformation corresponding to a story drift ratio of 1%. During the cycles at 1% story drift ratio, neither local nor global buckling of the brace was observed. Buckling of the specimen initiated at a story drift ratio of about 1.5% during the first compression cycle at 2% story drift ratio. As can be seen from Figs. 4.28(a) and (b), the transition zone between the edge tubes and center tube acted as a pin and a higher order out-of-plane and in-plane buckling took place simultaneously at around 1.50% story drift ratio.

Fig. 4.28(c) and (d) show out-of-plane rotations of the edge tubes to the loading and fixed ends, respectively. Bulging (necking) of the edge tubes due to compressive deformation was also observed close to the fillet welds during the cycle at 2.00% SDR.

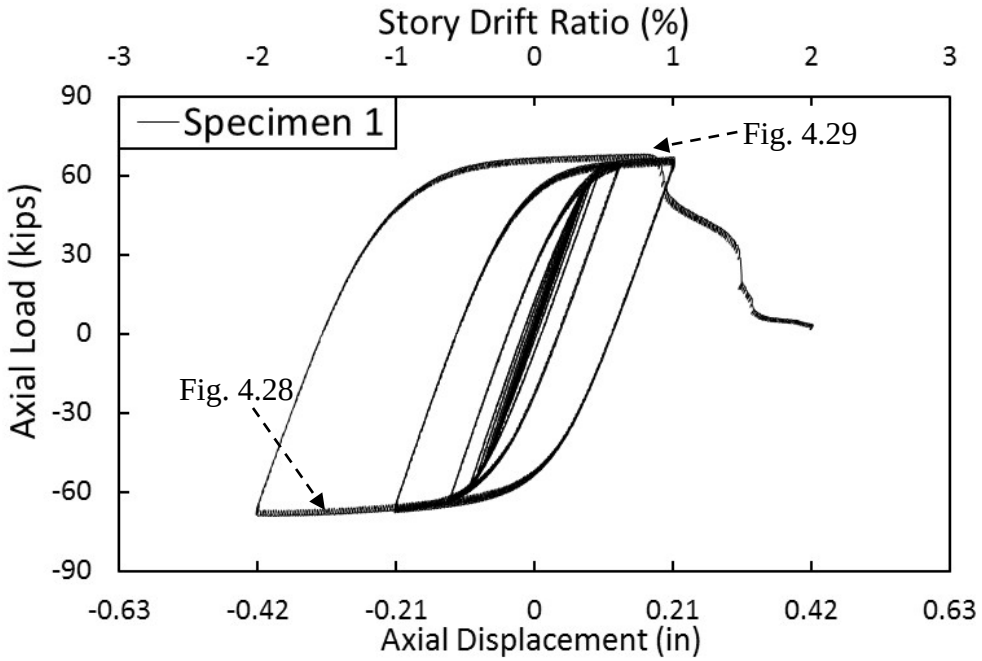

Figure 4.27. Hysteretic response of Specimen#1

Soon after initiation of global buckling (Fig. 4.28) during the compression cycle to 2.00% SDR, fracture initiation triggered at a story drift ratio of about 0.90% during the reversed tension cycle at 2.00% story drift ratio. Fig. 4.29 presents development of fracture of the edge tube to the loading end. Fracture initiation began in the vicinity of the heat affected zone (HAZ) of steel material, and gradually propagated through the all-around fillet welds that connect the edge tube to the connector plate in a ductile manner. Following the propagation of the fracture, a rapid drop in tension strength was observed (Fig. 4.27) and the test was terminated due to tearing out of the cross section.

(a) Out-of-Plane Buckling

(b) In-Plane Buckling

(c) Rotation of the top edge tube (Loading end)

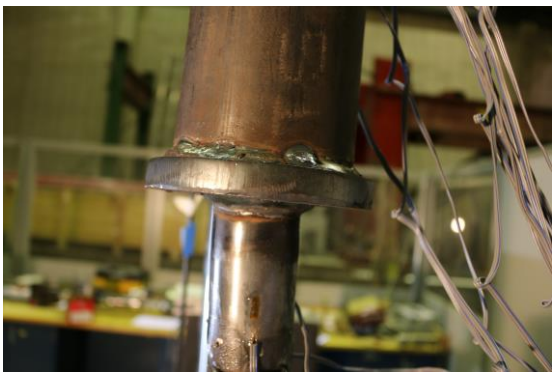

(d) Rotation of the lower edge tube (Fixed end)

Figure 4.28. Deformed shape of Specimen#1 at 1.50% SDR during the cycle to 2.00%

The strain readings obtained from the strain gauges installed to the center tube showed that the center tube remained elastic during the test, as expected. Fig. 4.30 shows the elastic cycles of the center tube. Note that the data acquisition system did not record strains larger than 1.6% during the first test due to an unexpected problem. Therefore, the peak

strain values obtained from the edge segment were not available for the edge tubes of the first specimen.

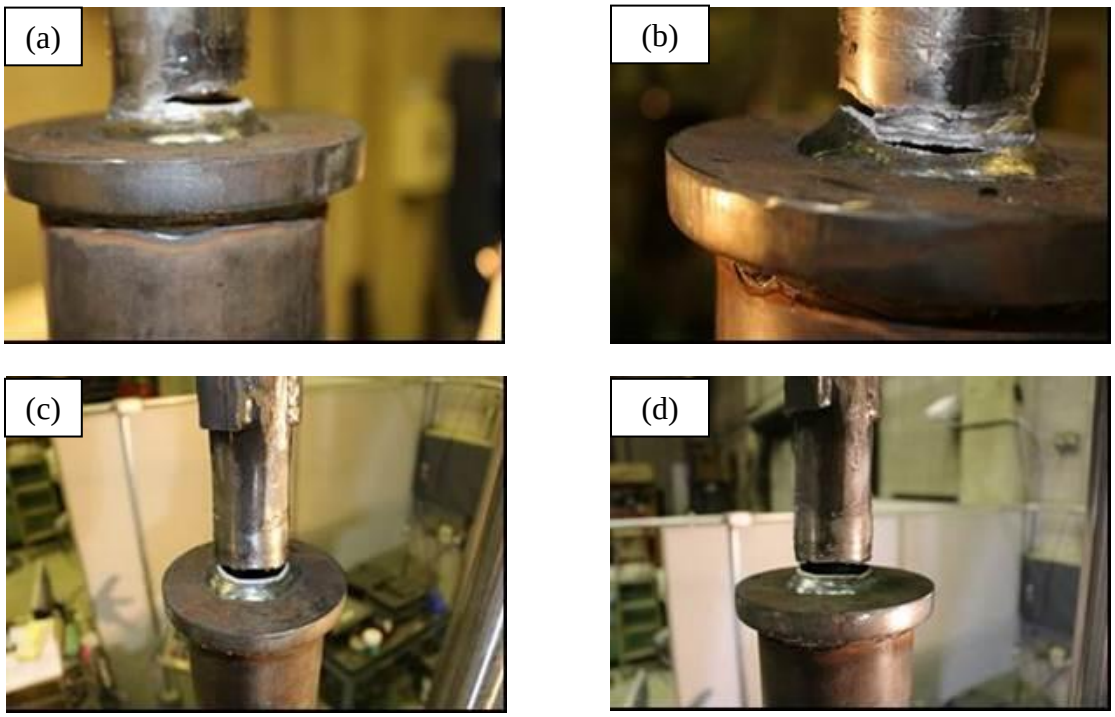

Figure 4.29. Fracture of the edge tube to the loading end

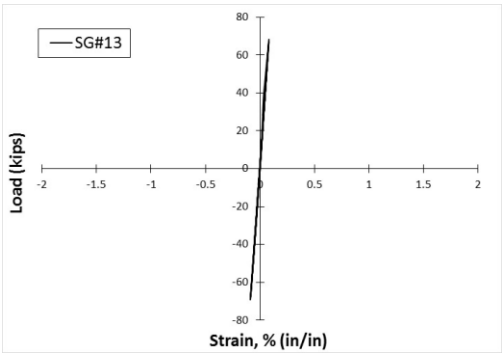

(a) Strain Gauge#13

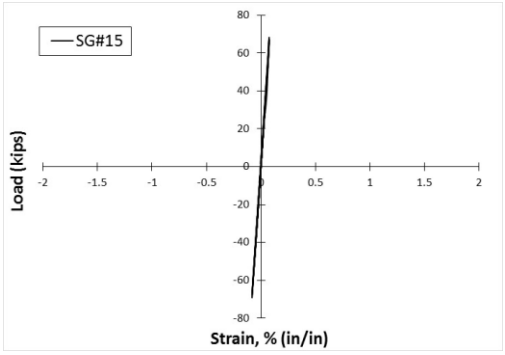

(b) Strain Gauge#15

Figure 4.30. Strain data obtained from the center tube in axial direction

Figure 4.31 shows the deformed shape of the specimen after the test. The residual local deformations of the plastic zones of the edge tubes were quite visible after the test (Fig.

4.31a and Fig. 4.31b). Bulging of the edge tube due to compressive yielding was significant in the cross-section close to the fractured section (Figs. 4.31c and d). It can be also observed that owing to the propagation of the cracking from steel material to the all-around fillet welds, a small portion of the fillet welds was also separated from the circular connector plate along with the fractured cross-section of the edge tube (Figs. 4.31e and f).

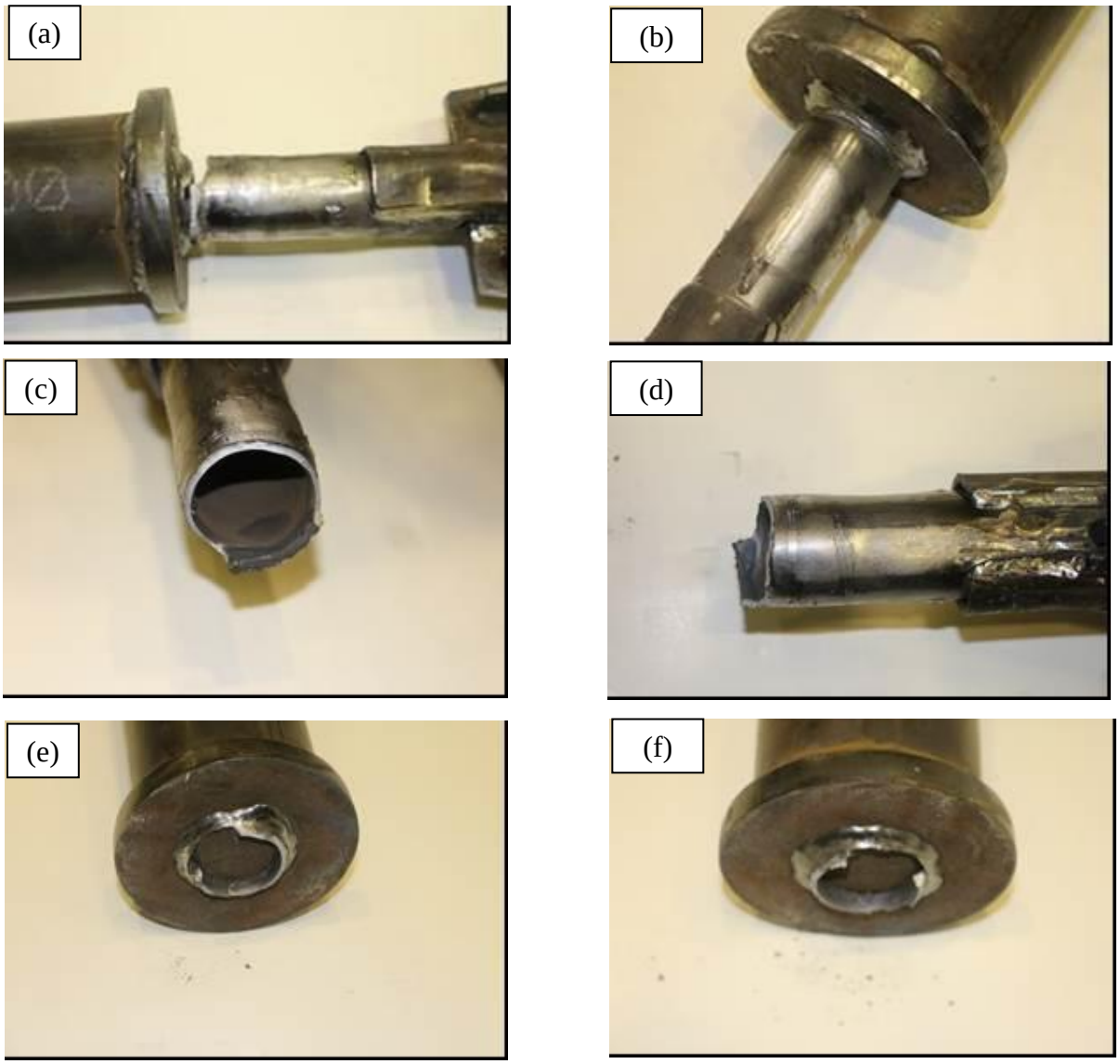

Figure 4.31. Photos after the first test (Specimen#1)

4.3.2 Specimen#2

The hysteretic behavior of Specimen#2 is presented in Fig. 4.32 in terms of story drift ratio (or axial displacement) and the applied axial load. The specimen developed a peak axial load capacity of 99 and 94 kips in compression and tension, respectively. The yielding of the edge tube became visible at a story drift ratio of about 0.50% when the applied load was around 78 kips in tension (Fig. 4.32). The initial elastic cycles, as well as the cycles at yielding deformation did not develop any visible deformations. After the cycles at Δ_{by}, the brace was subjected to the cycles at a story drift ratio of 1% and 2%, respectively. Buckling of the second specimen occurred at a story drift ratio of about 1.3% during the second compression cycle to 2% story drift ratio. The stiffness of the specimen slightly reduced after buckling. As can be seen from Fig. 4.33(a) and (c), similar to the observed deformation of Specimen#1, a higher order out-of-plane and in-plane buckling took place simultaneously. Fig. 4.33(b) and (d) show in-plane and out-of-plane rotation of the edge tubes, respectively.

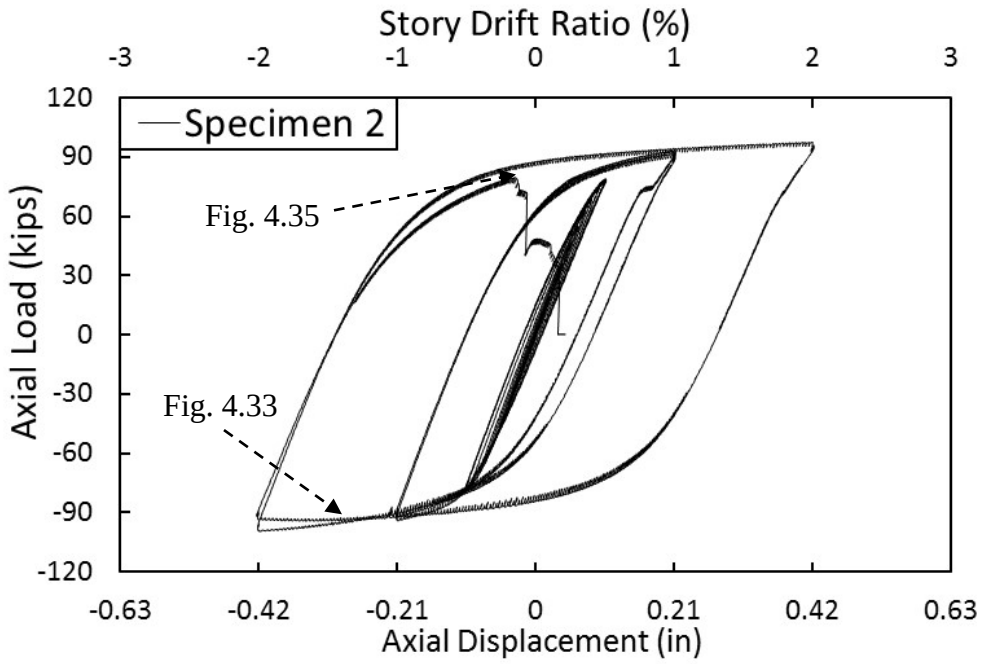

Figure 4.32. Hysteretic response of Specimen#2

(a) In-plane buckling shape

(b) In-plane rotation of the lower tube

(c) Out-of-plane buckling shape

(d) Out-of-plane rotation of the bottom tube

Figure 4.33. Buckling of the brace at a SDR of around 1.3% during the cycle at 2.00% SDR

Bulging of the edge tubes was also observed during the cycle at 2.00% SDR. Fig. 4.34 presents deformed shape of the specimen at 2% story drift ratio in compression. At this

stage buckling of the specimen, as well as bulging of the edge tubes became more substantial.

Figure 4.34. Bulging (necking) of the edge tube to the fixed end at 2.00% SDR in compression

Fracture initiation occurred at 0.13% story drift ratio in compression in the second tension cycle to 2% story drift ratio. Unlike the first test specimen, fracture occurred in the fillet welds that connect the lower edge tube to the connector plate. As shown in Fig. 4.35, the fracture propagated through the shear plane of the all-around fillet weld. It is evident from the coupon test results given in Table 4.6, the actual tension capacity of the edge tube was larger than the expected tension capacity of the edge tube determined based on the R_y factor specified for ASTM 500 Gr. B type of steel (AISC, 2010b).

The data obtained from the strain gauges installed to the center tube showed that the center tube remained elastic throughout the testing. Fig. 4.36 shows the elastic cycles of the center tube. Fig. 4.37(a) and (b) display the strain data obtained from the edge tubes to the loading and fixed ends, respectively. The peak strain amplitudes in axial direction obtained from strain gauge#7 and strain gauge#11. As shown in Fig. 5.39, the maximum axial strain reading obtained from the edge tubes was around 5.0%. The cycles obtained from the two

strain gauges (SG#7 and SG#11) were almost identical, which might have been due to the symmetry in higher order in-plane buckling.

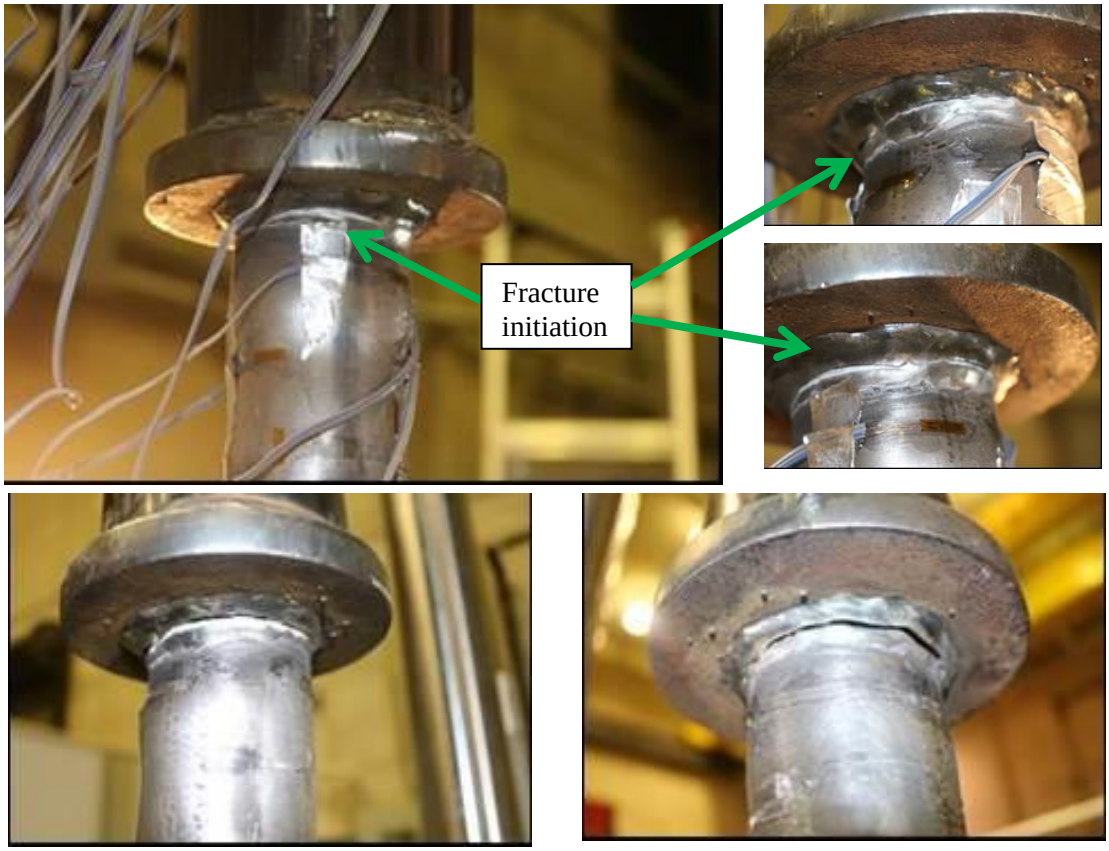

Figure 4.35. Fracture of the fillet welds of the edge tube to the fixed end

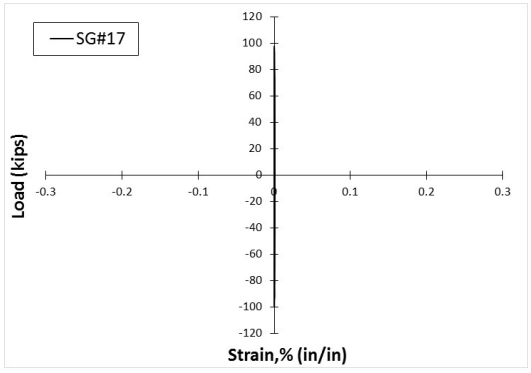

(a) Axial direction (SG#17)

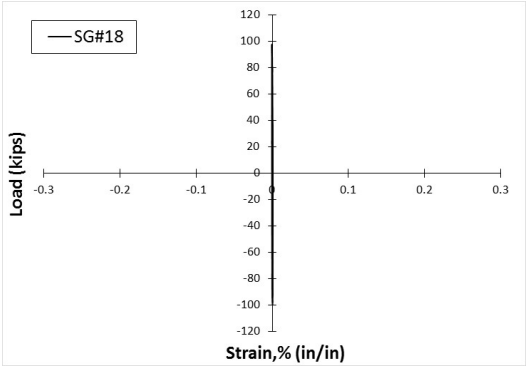

(b) Radial direction (SG#18)

Figure 4.36. Strain readings obtained from the center tube

Comparing Figs. 4.37(b) and 4.38(b) indicates that owing to the excessive bulging of the edge tube to the fixed end, the peak strain obtained from the edge tube to the fixed end in radial direction was around 40% larger than that in axial direction. As shown in Fig. 4.38(b), the peak radial strain obtained from the edge tube to the fixed end was slightly larger than 7%. On the other hand, the peak radial strain of the edge tube to the loading end was about 2.5% (Fig. 4.38a) while the peak axial strain amplitude of the edge tube to the loading end was almost two times the maximum radial strain obtained from the same segment (Fig. 4.37a).

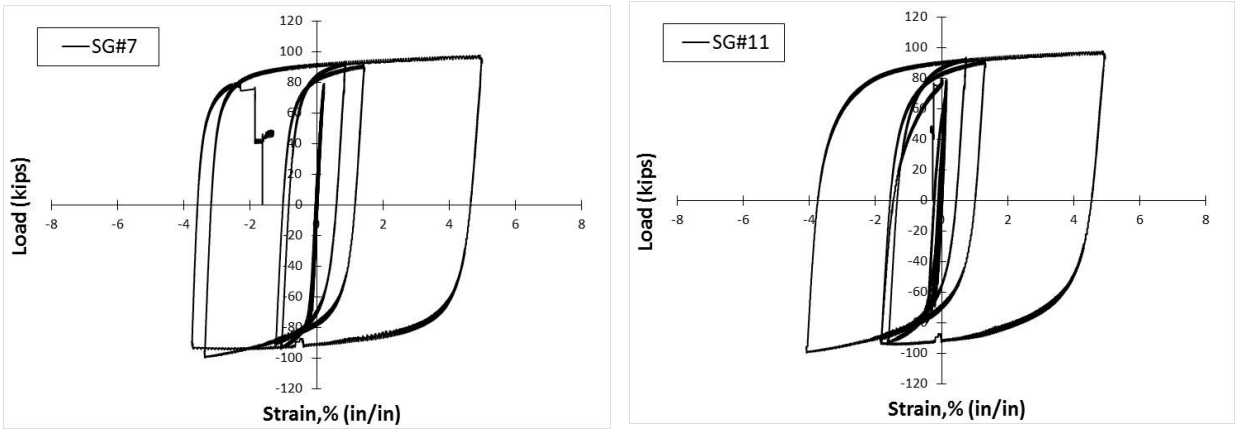

(a) Edge tube to the loading end (SG#7) (b) Edge tube to the fixed end (SG#11)

Figure 4.37. Strain readings obtained from the edge tubes in axial direction

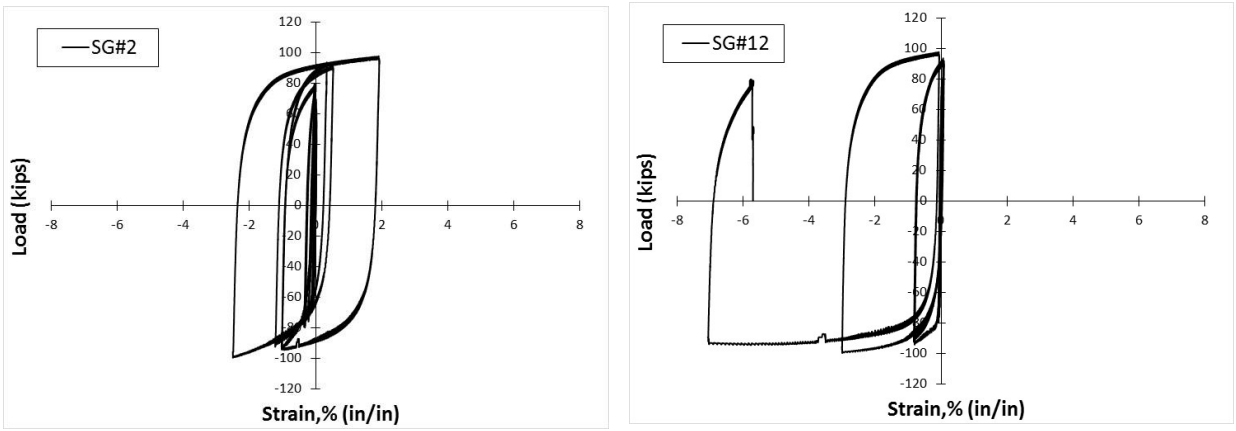

(a) Edge tube to the loading end (SG#2) (b) Edge tube to the fixed end (SG#12)

Figure 4.38. Strain readings obtained from the edge tubes in radial direction

Fig. 4.39 shows the deformed shape of the edge tube and the connector plate after the test. Necking of the yielding zone of the edge tube is given in Fig. 4.39(b). As indicated in Fig. 4.39(a), the fillet welds that connect the edge tube to the circular connector plate completely fractured from their shear plane with an almost 45 degree with respect to the connector plate surface.

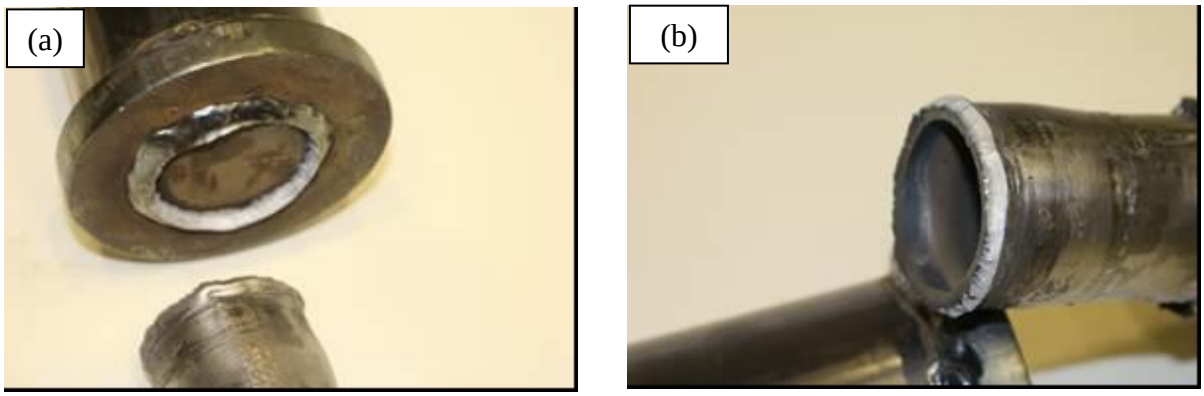

Figure 4.39. Photos after the second test (Specimen#2)

4.3.3. Specimen#2 (CJP)

The hysteretic behavior of Specimen#2 (CJP) is presented in Fig. 4.40. As mentioned previously, Specimen#2 (CJP) and Specimen#2 were identical except for their welded connections between the edge tubes and the connector plates. The specimen developed a peak axial load capacity of 97.9 and 97.2 kips in compression and tension, respectively. The first significant yielding of the brace was observed at a story drift ratio of around 0.45% when the applied load was around 71 kips in tension (Fig. 4.40). The brace specimen attained a peak axial deformation quantity that corresponds to an equivalent story drift ratio of 2.50%. The deformations during the cycles prior to the cycle to 2.50% story drift ratio were not observable.

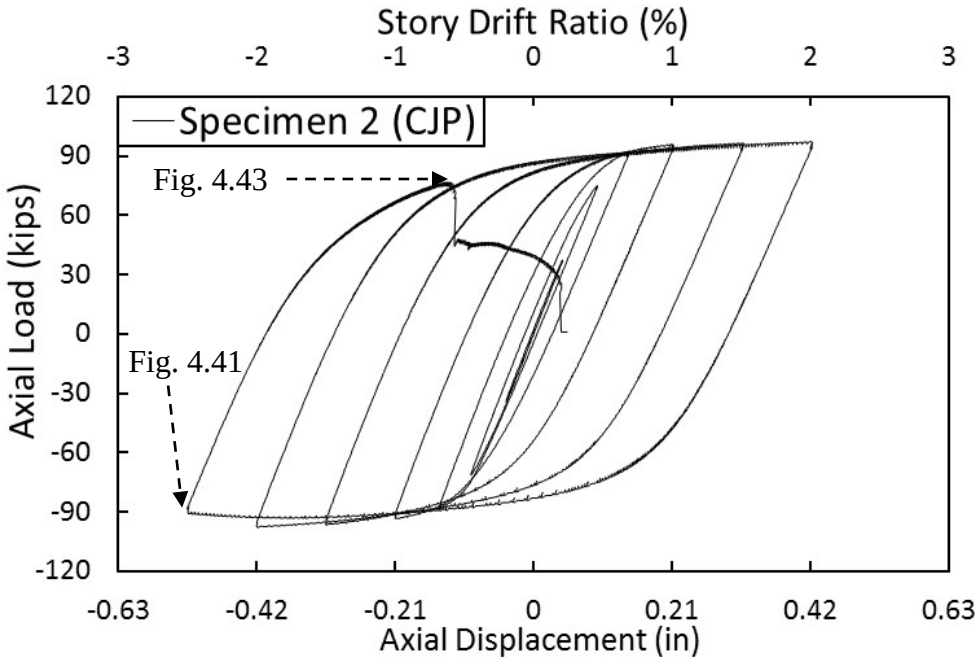

Figure 4.40. Hysteretic response of Specimen#2 (CJP)

As seen in Fig. 4.41, global buckling of the brace became noticeable at 2.50% story drift ratio in compression, even though there was a slight drop in the stiffness (Fig. 4.40) prior to reaching 2.50% SDR during the cycle to 2.5% SDR. Similar to the first two specimens, both in-plane and out-of-plane buckling of the specimen occurred simultaneously. The necking of the edge tube to the fixed end was substantial soon after buckling during the cycle at 2.50% story drift ratio, as given in Fig. 4.42. Subsequent to the in-plane and out-of-plane buckling, fracture initiation triggered in a cross-section close to the groove welds at a story drift ratio of around 0.80% during the reversed tension cycle to 2.50% story drift ratio. Figure 4.43(a) through (f) present the propagation of the fracture through the section.

(a) Out-of-plane (b) In-plane

Figure 4.41. Global buckling at 2.5% SDR

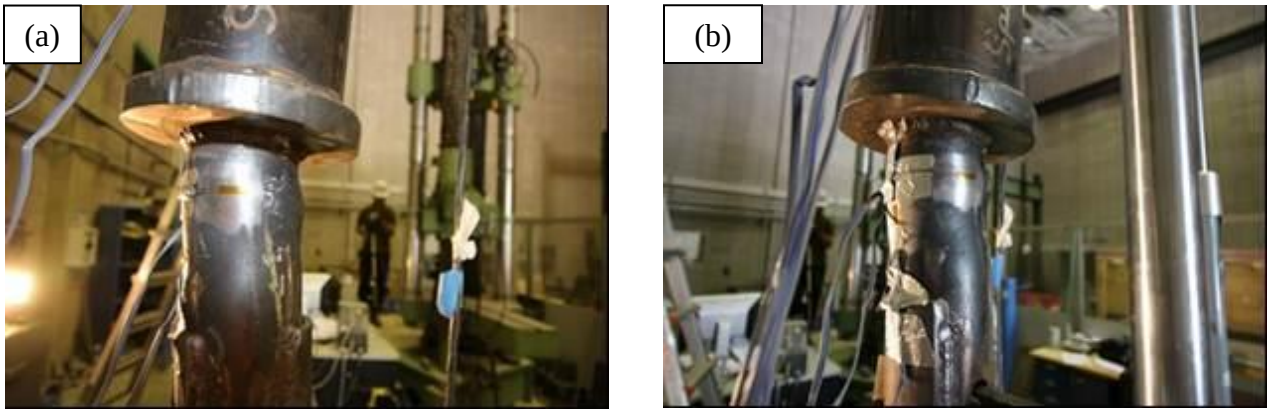

Figure 4.42. Out-of-plane rotation of the lower connector plate and necking of the edge tube to the fixed end at 2.5% SDR.

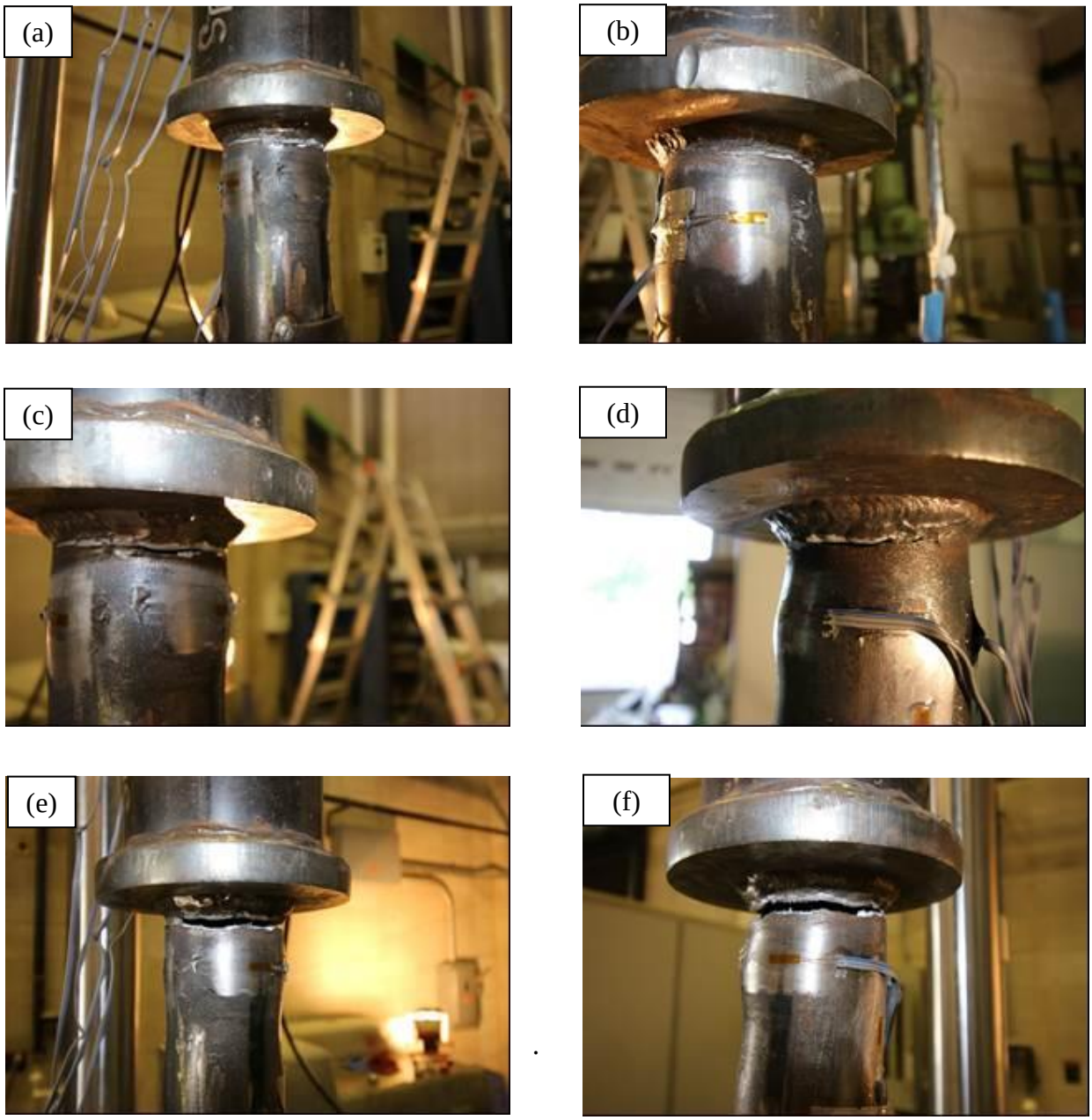

Figure 4.43. Fracture of the edge tube to the fixed end

Axial strain readings obtained from the edge tubes are presented in Fig. 4.44. The axial strain readings obtained from the strain gauges located at the edge tube to the loading end were consistent with each other (Fig 4.44a). The strain readings obtained from the edge tube to the fixed end, on the other hand, did not exhibit similar responses while their peak

axial strain amplitudes were on the same order, as indicated in Fig. 4.44(b). The peak axial strains of the top and bottom edge tubes were about 8.00% and 7.00%, respectively (Fig. 4.44a and b).

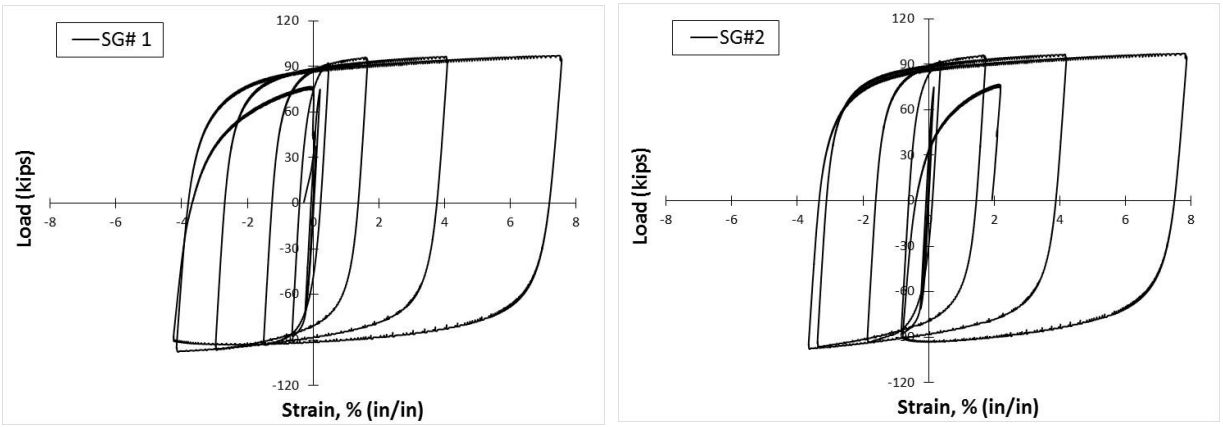

(a) Edge tube to the loading end

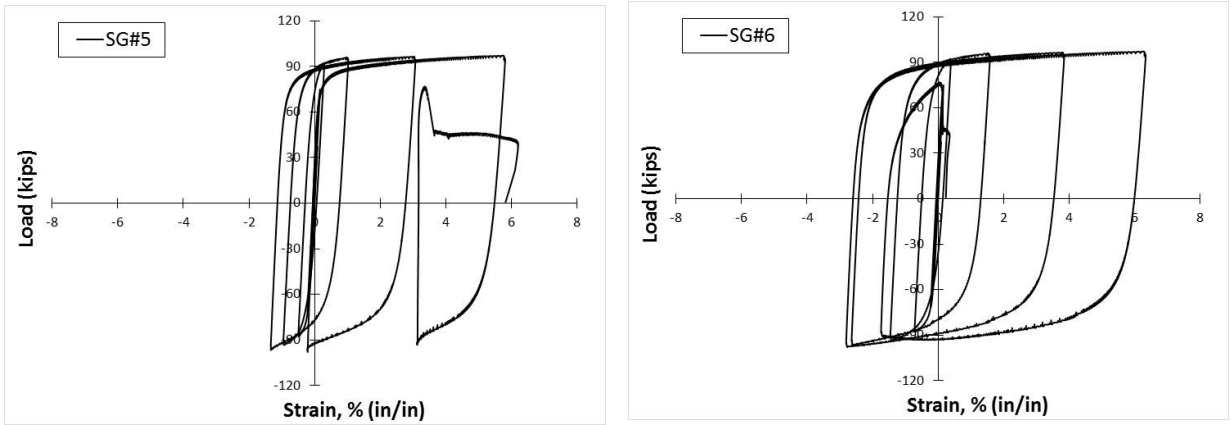

(b) Edge tube to the fixed end

Figure 4.44. Axial strain readings of Specimen#2 (CJP)

Comparing Figs. 4.45(a) and 4.45(b) clearly indicates that the strain data in radial direction of the two edge tubes substantially differ from each other in terms of the peak strain amplitudes. The maximum radial strain amplitudes obtained from the edge tubes to the loading and fixed ends were on the order of 1.50% and 13%, respectively. However, prior to

the last cycle, in which the fracture of the edge tube occurred, the ratio of the axial strain over the radial strain was about 40%. It is also noteworthy that the peak radial strain was about 85% larger than the peak axial strain for the edge tube to the fixed end, in which the fracture occurred. In other words, the growth in the radial strain was more significant than that in the axial strain due to severe bulging in the yielding segment of the edge tube.

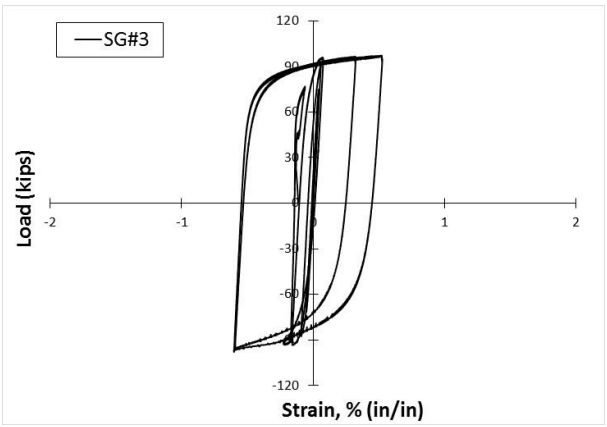

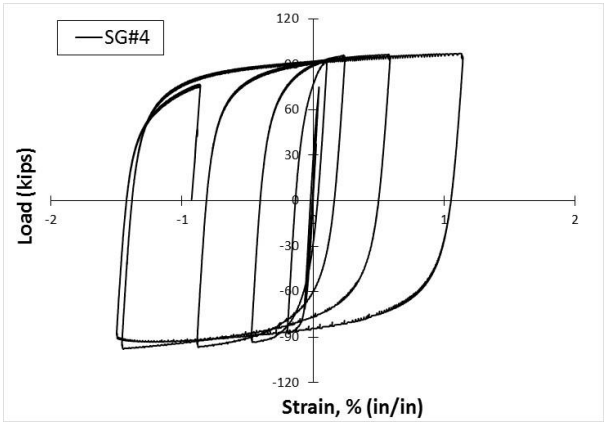

(a) Edge tube to the loading end

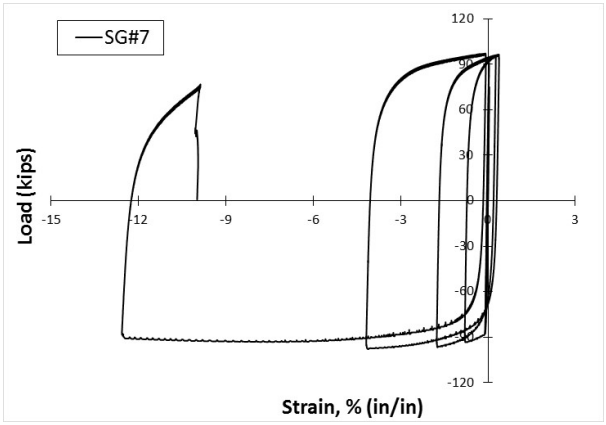

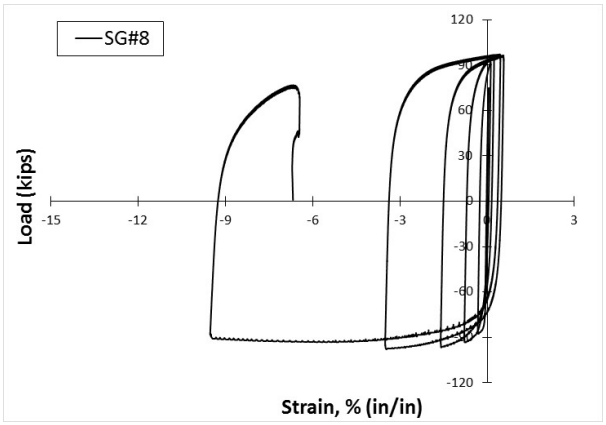

(b) Edge tube to the fixed end

Figure 4.45. Radial strain readings of Specimen#2 (CJP)

5. Summary and Conclusions

An innovative three-segment steel brace model have been developed and investigated by means of analytical, experimental and numerical studies. The concept was to develop a brace member that provides significant inelastic deformation capacity primarily through its yielding in tension and compression. For this purpose, first, the critical design parameters are identified through analytical solution to the elastic buckling problem, and examined by means of an initial FEM-based parametric study. Then, an ensemble of FE simulations were conducted on three-segment braces utilizing circular hollow sections for both edge and center segments of the brace in order to evaluate the cyclic response of the specimen options for testing. Subsequent to the investigation of the cyclic behavior of the three-segment brace specimen options through FE simulations, two specimens have been found to be promising for testing. In addition to the two specimens tested, a third specimen is added to the test program to reveal the effect of the type of welded connection.

Based on the numerical and experimental researches performed, the following conclusions can be drawn:

(1) The analytical investigation of the three-segment braces showed that the ratio of moment of inertia of center tube over that of edge tube (I_c/I_e) and the length ratio (L_c/L or L_e/L) were the most influential parameters on the elastic buckling load of the brace.

(2) The findings of the numerical investigation of the braces can be summarized as follows:

- The moment of inertia ratio (I_c/I_e) did not affect the inelastic deformation capability The elastic buckling strength of the three-segment braces, on the other hand, substantially affected by the moment of inertia ratio.

- Variations in the edge length ratio (L_e/L) did not affect the results when the length of the yielding segment (L_p) was constant.
- The length of the plastic zone (yielding segment) over the total length (L_p/L) is the most influential parameter in determining the stable inelastic response of the three-segment braces.

(3) Inelastic cyclic response of the simulated three-segment braces indicated that:

- The ratio of gross area of center tube over gross area of edge tube (A_c/A_e) has a substantial influence on the inelastic brace behavior, as well as hysteretic response when the area of the center tube was not large enough to remain elastic during the cycles. Ideally, the center tube section can be selected to possess a cross-sectional area of at least 50% larger than that of the edge tube. The brace behavior would be governed by global buckling of the center segment rather than yielding of the edge segment, otherwise.
- Similar to conventional buckling braces, regardless of the impact of the other design parameters, formation of the local plastic deformations was consistently postponed as the normalized D/t ratio of the edge tube decreases.
- Employing a center length over plastic zone length ratio (L_c/L_p) of around 5.50 was sufficient to obtain stable and symmetrical cyclic response.
- The compression overstrength with respect to the tension strength was less than 5% at any deformation level throughout the simulation of the specimens.

(4) Inelastic cyclic response of the tested three-segment braces indicated that:

- The tested three-segment braces specimens were capable of exhibiting stable and symmetrical hysteretic response, as well as dissipating a greater amount of energy compared to the conventional braces.
- A higher order out-of-plane and in-plane buckling initiated simultaneously for all specimens.
- The limit states of Specimen#1 and Specimen#2 (CJP) were edge tube fracture. Specimen#2, on the other hand, experienced weld fracture. The fracture initiated in the all-around fillet welds that connects the round connector plate to the edge tube to the fixed end, due to the fact that the actual tensile capacity of the edge tube was larger than the expected tension capacity of the edge tube determined based on the R_y factor specified for ASTM 500 Gr. B type of steel (AISC 2010).
- Utilizing CJP welds for edge tube-to-connector plate connections improved the fracture life of Specimen#2.
- Cracking of the edge tubes (or fillet welds) is triggered by the additional flexural demand imposed by the global buckling of the brace. Furthermore, fracture of the edge tubes, regardless of the welding procedure, initiated in a cross-section that is in the vicinity of the HAZ close to the welded connections between the edge tube and the connector plates soon after the global buckling.

(5) The strain reading obtained from the three specimens tested pointed out that:

- The center segments of all specimens remained elastic during the cycles.
- Owing to the excessive necking of the edge tubes under compressive loads, the peak strain readings in radial direction of the edge tubes were larger than those in axial direction for the fractured tubes. In other words, the growth in the radial strain was

more significant than that in the axial strain due to severe bulging in the yielding segment of the edge tube.

(6) Overall, the three-segment braces offer economy, as well as stable and symmetrical hysteretic behavior. Even though gradual accumulation of the plastic deformations in the edge segments has an adverse effect on the fracture life of the braces, the ductility provided by the three-segment braces might be sufficient to meet the expected ductility demand on braces in buckling-controlled braced frames. Thus, further study needed to evaluate the seismic demands on the CBFs that incorporate the developed three-segment braces.

CHAPTER V

CONCLUSIONS AND RECOMMENDATIONS

1. General Remarks

To enhance the performance of the concentrically braced frames, three innovative steel brace models are developed for seismic design of steel braced frames. Due to the fact that providing a restrain that completely prevents a brace from buckling (globally and locally) is not realistic, the concept of buckling-restrained braces redefined as buckling-controlled braces. The design of the developed buckling-controlled brace models primarily aimed at offering simplicity to the industry along with the energy dissipation capacity much greater than that of conventional buckling braces.

Extensive numerical simulations are supported with testing of a few small-scale specimens in order to evaluate inelastic cyclic behavior and fracture life of the braces properly. Experimental portion of the study helped establish numerical models that emulate the actual force-deformation relationships and the critical deformation patterns obtained from the experiments, as well as to examine fracture life of the developed braces. Numerical modeling, without exception, began with calibration of the material model and the other FE modeling parameters (e.g. mesh size) throughout the FEM-based parametric studies conducted in this study. The physical test results and the observed deformations given in the published experimental data are also collected and compared with the results obtained from the FE simulations to verify the reliability of the simulation results.

The FEM-based parametric study carried out on the inelastic cyclic behavior of tube-in-tube buckling-controlled braces pointed out the significance of discussing the impact of

each parameter considering the interaction between the key parameters. Even though tube-in-tube buckling-controlled braces are innovative in terms of practicality, the idea of providing a continuous lateral constraint along the load-bearing system is the common characteristic of all BRB models developed to date. Hence, the conclusions drawn in the parametric study can be considered to be valid for any type of BRB, covering concrete-encased and all-steel BRBs, which would allow this study to provide a solid foundation and understanding for the provisions to be established in the future for design of BRBs.

In addition to challenging the difficult task of quantifying the interrelation between the essential design parameters for the first time, this research also initiated an attempt to numerically evaluate the strain demands on the braces with and without buckling controllers. The hysteretic response, local deformations and strain demands are well-predicted by the FE models until fracture initiation. It should be noted that ductile fracture of steel members can be imitated by introducing a fracture criterion to the FE models but nevertheless, as soon as the loading and boundary conditions are altered, fracture of the exact same material cannot be predicted using the FE model that is previously calibrated for specific loading conditions and stress states. Therefore, the effect of buckling control on fracture life of tubular bracings is discussed in terms of the strain demands until the first visible cracking observed during the experiments, which clearly demonstrated the level of enhancement achieved by introducing the developed buckling-controllers.

Further, a three-segment steel brace model, which conceptually differs from any buckling-controlled brace model proposed to date, has been investigated to reveal the influential parameters on the buckling load and inelastic cyclic behavior of the developed braces. Likewise, several FEM-based parametric studies are carried out on the three-segment

brace model following the analytical solution, so as to identify and elaborate on the significance of each parameter. By doing that we were able to carefully design the test specimens, and to observe the actual behavior of the braces without going through an extensive test program that consists of a large number of specimens. Furthermore, the strain readings obtained from the experiments set forth the actual strain demands on the developed bracings in both axial and radial directions. On the whole, the developed three-segment braces are found to be promising in terms of hysteretic stability, accelerating the construction process and allowing inspection in the aftermath of a severe ground shaking.

2. Conclusions

Based on the previously presented numerical and experimental studies on the brace models, the following can be highlighted:

(1) TinT-BCBs were capable of exhibiting stable hysteretic response, controlling global and local buckling, as well as dissipating greater amount of energy compared to the conventional braces. TinT-BCBs are capable of sustaining large plastic deformations on the order of 3.5 to 4.0% equivalent story drift ratio when optimal design parameters are employed along with proper connection design.

(2) Numerical investigation of TinT-BCB models showed that the interaction among the key parameters is not straightforward, since there is a case-dependent interrelationship between the identified parameters. The impact of the gap amplitude, relative outer tube stiffness and coefficient of friction is heavily depending on each other. Therefore, any conclusions drawn on the impact of a parameter without considering the state of the other two parameters cannot be valid in general.

(3) TinT-BCB specimens would undergo larger inelastic deformations and possess longer fracture life when the gap between the two tubes is small and the thickness of the outer tube is sufficient to resist the lateral thrust imposed by the global or local deformation of the inside tube. Symmetry of the hysteretic response, on the other hand, is governed by the friction coefficient when optimal gap amplitude and outer tube stiffness is employed.

(4) Evaluation of the comparative efficiency of the developed TinT and channel-encased buckling-controlled braces in terms of local strain demands strongly indicated that besides their symmetrical and stable inelastic cyclic response, the developed TinT and channel-encased buckling-controlled braces, are capable of mitigating the strain demands substantially on the order of at least 7 times the obtained strain demands on the conventional braces, regardless of the slenderness ratio of the main brace or the test setup.

(5) A cost-effective application of the channel-encased BCBs with a satisfactory performance can be achieved with uneven stitch spacing distribution along the brace length. Since formation of the local deformations take place at brace ends, an optimal performance can be attained when the channels are connected with longer stitches (e.g. one fifth of the total length) at brace ends with the ratio of the total intermittent weld length over the total buckling-controller length equal to or larger than 0.60. This type of attachment, with much lower cost, would provide a local strain demand reduction that is virtually identical to the level of alleviation achieved with the continuously welded connectors.

(6) Our experimental study on the three-segment braces indicated that when the connection failure is prevented, the peak inelastic deformation that can be attained by a three-segment brace can be as large as the peak deformations obtained from tested concrete-encased BRB specimens.

(7) FEM-based numerical simulations of the three-segment braces pointed out that the ratio of center tube length over the plastic zone length and the ratio of gross area of the center tube over gross area of the edge tube are the controlling parameters to obtain stable and symmetrical hysteretic response. To obtain a stable inelastic cyclic response, the gross area and the length of the center tube can be adjusted to 1.50 and 5.50 times those of the edge tube, respectively.

3. Future Study

Major conclusions of the numerical and experimental studies are summarized in the previous section. Although the present study identified the fundamental design parameters and helped gain an understanding on their effects on the cyclic behavior, our efforts are not sufficient to fully understand the behavior and to propose well-established design recommendations for concentrically braced frames that incorporate the developed buckling-controlled braces. Recommendations for the potential future studies can be highlighted as follows:

- The research presented herein includes a number of small-scale isolated brace specimens due to the limitations on the available test setup. Even though the test results are encouraging, there remains a need for an extensive experimental study on full-scale isolated buckling-controlled braces to examine the inelastic cyclic behavior and fracture life of the developed braces in order to confirm the validity of the conclusions drawn based on the small-scale test results. Furthermore, the impact of the width-to-thickness (D/t or b/t) and effective slenderness ratio (KL/r) of the load-bearing tube of TinT-BCBs on the fracture life was not within the scope of the

present study. It is, however, evident from previously performed experimental studies that the width-to-thickness and effective slenderness ratio are the most influential parameters that affect the cyclic behavior and the fracture life of the buckling braces. Although effective slenderness ratio is a parameter that is meaningful when global buckling is of concern, it might have an impact on the wave length, as well as the order of the buckling tendency of the inside tube. It is, therefore, important to elaborate on the effect of the two parameters, which remains unstudied.

- Inelastic dynamic behavior of braced frames is highly-dependent on the hysteretic behavior of their braces. Thus, buckling control would play an important role on the inelastic dynamic behavior of the structure. The present study examined the capacity aspect of the developed buckling-controlled braces solely. Therefore, a comprehensive research is needed to evaluate the dynamic response of the structural systems that incorporates BCBs. Based on the expected seismic demand on the developed braces, the design of the braces can be subjected to alterations.
- The cyclic behavior of the developed buckling-controlled braces, as well as the connection design needs to be carefully investigated by means of large-scale frame tests. A few large-scale experimental programs on concrete-encased and all-steel buckling-restrained braces frames indicated that the failure limit states of the conventional buckling-restrained braces can substantially differ from those observed from the isolated brace specimens. The potential issues arise from incorporating buckling-controlled braces, such as the demands on the beam-column-gusset connections and the panel zones, in particular, should be systematically investigated, since the gusset assemblies, which are designed to be extra strong to avoid the end

rotations, are expected to impose significant demands on the beam and column flanges locally.

- Channel-encased BCBs are developed to mitigate likelihood of premature brace fracture, as well as to enhance the seismic performance of new and existing ductile braced frames. The possible applications of the channel-encased BCBs to the older non-ductile braced frames need to be studied.
- A further research direction for the potential future studies can be ductile fracture prediction of structural steel members utilizing FEM. In lieu of performing costly experimental studies, a general method can be developed for predicting fracture by means of an extensive numerical investigation of a number of carefully designed small scale test specimens.

REFERENCES

AISC (1997), "Seismic Provisions for Structural Steel Buildings." American Institute of Steel Construction, Chicago, Illinois 60601.

AISC (2010a), Prequalified Connections for Special and Intermediate Steel Moment Frames for Seismic Applications, ANSI/AISC 358-10, American Institute of Steel Construction, IL.

AISC (2010b), Seismic Provisions for Structural Steel Buildings, ANSI/AISC 341-10, American Institute of Steel Construction, IL.

AISC (2011), American Institute of Steel Construction, Manual of Steel Construction, 14th Edition. Chicago, IL.

Archambault, M. -H., Tremblay, R., and Filiatrault, A. (1995), "Étude du comportment séismique des contreventements ductiles en x avec profiles tubulaires en acier." Rep. No. EPM/GCS-1995-09, Dept. de Génie Civil Section Structures, École Polytechnique, Montréal (in French).

Aslani, F. and Goel, S.C. (1991), "Stitch Spacing and Local Buckling in Seismic Resistant Double Angle Bracing Members," Journal of Structural Engineering, ASCE, Vol. 177, No. 8, August.

Astaneh-Asl, A., Goel, S. C., and Hanson, R. D. (1982), "Cycle behavior of double angle bracing members with end gusset plates." Rep. No. UMEE 82R7, August, Dept. of Civil Engineering, The Univ. of Michigan, Ann Arbor, Mich.

A. Astaneh-Asl, S.C. Goel, Robert D. Hanson. (1985). "Cyclic out-of-plane buckling of double-angle bracing." J. Struct. Eng.; 111(5): 1135-1153.

Astaneh-Asl, A., (1986a), "A report on the behavior of steel structures during September 19, 1985 earthquake of Mexico", Proceedings, Annual Technical Session, Structural Stability research Council, Lehigh University, April.

Astaneh-Asl, A., Goel, S.C., and Hanson, R.D. (1986b), "Earthquake-resistant Design of Double Angle Bracing," Engineering Journal, AISC, Vol. 23, No. 4, 4th Quarter, Chicago, IL.

Astaneh-Asl, A., Bolt, B., McMullin, K., Donikian, R. R., Modjtahedi, D. and Cho, S.W. (1994). "Seismic performance of steel bridges during the 1994 Northridge Earthquake." Report No. UCB/CEESteel-94/01, Department of Civil Engineering, University of California, Berkeley, April.

Astaneh-Asl, A., and Kanada, M. (1995). "Performance of steel bridges during the 1995 Hanshin Earthquake." Proceedings, Struct. Steel Design Seminar-2, University of California, Berkeley.

Astaneh-Asl, A. (1998). "Seismic behavior and design of gusset plates. Steel TIPS 42."

ASTM E8 (2015). Standard Test Methods for Tension Testing of Metallic Materials, ASTM International, West Conshohocken, PA, 2015.

American Welding Society (2000). Structural Welding Code—Steel: AWS D1.1:2000, 17th ed., Miami, FL.

Black, R.G., W.A. Wenger, E.P. Popov. (1980). "Inelastic buckling of steel struts under cyclic load reversals." UCB/EERC-80/40, Earthquake Engineering Research Center, University of California, Berkeley.

Black, C. J., Makris, N., and Aiken, I. D. (2002). "Component testing, stability analysis and characterization of buckling restrained 'unbonded' braces." Technical Rep. No. PEER 2002/08, Pacific Earthquake Engineering Research Center, Univ. of California at Berkeley, Berkeley, Calif.

Broderick, B.M., J.M. Goggins, A.Y. Elghazouli. (2005). "Cyclic performance of steel and composite bracing members." Journal of Constructional Steel Research; 61(4): 493-514.

Chou, C., and Chen, S.Y. (2010). "Subassemblage tests and finite element analyses of sandwiched buckling-restrained braces." Engineering Structures, 32(8):2108–2121.

Clark, P., Aiken, I., Kasai, K., Ko, E., Kimura, I. (1999). "Design Procedures for Buildings Incorporating Hysteretic Damping Devices." Proceedings, 68th Annual Convention, Santa Barbara, California Structural Engineers Association of California.

Corte, G. D., D'Aniello, M., and Landolfo, R. (2014). "Field Testing of All-Steel Buckling-Restrained Braces Applied to a Damaged Reinforced Concrete Building." J. Struct. Eng.

Di Sarno, L., and Elnashai, A.S. (2009). "Bracing Systems for Seismic Retrofitting of Steel Frames." Journal of Constructional Steel Research, 65:452–465.

Di Sarno, L. and Manfredi, G. (2010). "Seismic retrofitting with buckling restrained braces: Application to an existing non-ductile RC framed building." Soil Dynamics and Earthquake Engineering, 30:1279–1297.

Dusicka, P., and Tinker, J. (2013). "Global Restraint in Ultra-Lightweight Buckling-Restrained Braces." J. Compos. Constr. 17:139-150.

El-Baheya, S., and Bruneau, M. (2011). “Buckling restrained braces as structural fuses for the seismic retrofit of reinforced concrete bridge bents.” Engineering Structures, 33(3):1052–1061.

Elchalakani, M., X.L. Zhao, and R. Grzebieta. (2003). “Tests of cold-formed circular tubular braces under cyclic axial loading.” J. Struct. Eng.; 129(4): 507-514.

Eryasar, M. E., and Topkaya, C. (2010). “An Experimental Study on Steel-Encased Buckling-Restrained Brace Hysteretic Dampers.” Earthquake Engng Struct. Dyn., 39:561–581.

FEMA. (2000a). “FEMA 350: Recommended Seismic Design Criteria for New Steel Moment-Frame Buildings” Federal Emergency Management Agency, Washington, DC.

FEMA. (2000b). “FEMA 355C: State of the Art Report on Systems Performance of Steel Moment Frames Subject to Earthquake Ground Motion Shaking.” H. Krawinkler, ed., Federal Emergency Management Agency, Washington, D.C.

FEMA. (2000c). “FEMA 355F: State of the Art Report on Performance Prediction and Evaluation of Steel Moment-Frame Buildings.” D. A. Foutch, ed., Federal Emergency Management Agency, Washington, D.C.

Fell, B., Kanvinde, A., Deierlein, G., Myers, A., Fu. X. (2006). “Buckling and Fracture of Concentric Braces under Inelastic Loading.” Steel TIPS 94.

Fell BV, Kanvinde AM, Deierlein GG, Myers AT. (2009). “Experimental investigation of inelastic cyclic buckling and fracture of steel braces.” J. Struct. Eng.; 135:19–32.

Genna F. and Gelfi P. (2012). “Analysis of the lateral thrust in bolted steel buckling restrained braces. I: experimental and numerical results.” J. Struct. Eng., 138:1231–43.

Goggins, J.M., B.M. Broderick, A.Y. Elghazouli, A.S. Lucas. (2006). “Behavior of tubular steel members under cyclic axial loading.” Journal of Constructional Steel Research; 62(1-2): 121- 131.

Gugerli, H. (1982). "Inelastic Cyclic Behavior of Steel Bracing Members", Ph.D. Thesis, Dept. of Civ. Eng., Univ. of Michigan, Ann Arbor, MI.

Haddad M. (2015). “Concentric tubular steel braces subjected to seismic loading: Finite element modeling.” Journal of Constructional Steel Research 104: 155–166.

Han, S.W.; Wook Tae Kim; and Douglas A. Foutch. (2007). “Seismic Behavior of HSS Bracing Members according to Width–Thickness Ratio under Symmetric Cyclic Loading.” J. Struct. Eng. 133:264-273.

Hibbit, Karlsson, Sorenson. (2012). ABAQUS Analysis User's Manual, Version 6.12. ABAQUS Inc.

Hoveidae, N., and Rafezy, B. (2012). "Overall Buckling Behavior of All-Steel Buckling Restrained Braces." Journal of Constructional Steel Research, 79:151–158.

Jain, A.K., R.D. Hanson, S.C. Goel. (1978). "Inelastic response of restrained steel tubes." Journal of the Structural Division; 104(6): 897-910.

Ju, Y. K., Kim, M. H., Kim, J., and Kim, S. D. (2009). "Component Tests of Buckling-Restrained Braces with Unconstrained Length." Engineering Structures, 31: 507–516.

Kanvinde AM and Deierlein G. (2007) "Cyclic Void Growth Model to Assess Ductile Fracture Initiation in Structural Steels due to Ultra Low Cycle Fatigue." J. Eng. Mech.; 133(6): 701-712.

Khoo, H.H., Tsai, K. C., Tsai, C.Y., Tsai C.Y., and Wang, K.J. (2016). "Bidirectional substructure pseudo-dynamic tests and analysis of a full-scale two-story buckling-restrained braced frame." Earthquake Engng Struct. Dyn.; DOI: 10.1002/eqe.2696.

Korzekwa, A., and Tremblay, R.. (2009). "Numerical Simulation of the Cyclic Inelastic Behavior of Buckling Restrained Braces.", Taylor & Francis, London, UK.

Krawinkler, H., Bertero, V.V., and Popov, E.P. (1971). "Inelastic Behavior of Steel Beam-to-Column Subassemblages." EERC Report No. 71-7, University of California, Berkeley, CA.

Lehman, D.E., C.W. Roeder, D. Herman, S. Johnson, B. Kotulka. (2008). "Improved seismic performance of gusset plate connections." J. Struct. Eng.; 134(6): 890-901.

Lee, S. and Goel, S.C. "Seismic Behavior of Hollow and Concrete-Filled Square Tubular bracing Members", Research Report UMCE 87-11, Dept. of Civ. Eng., Univ. of Michigan, Ann Arbor, MI, 1987.

Lemaitre, J., and J.-L. Chaboche. (1990). Mechanics of Solid Materials, Cambridge University Press.

Leowardi, L. S., and Walpole, W. R. (1996), "Performance of steel brace members." Dept. of Civil Engineering, Univ. of Canterbury, Christchurch, New Zealand.

Ma, N., Wu, B., Li, H., Ou, J., and Yang, W. (2009). "Full scale tests of all-steel buckling restrained braces." Proceedings of SPIE, Vol. 7288 728825-2.

Ma, N., Ou, J.P., and Li, H. (2012a). "Experimental Study of Low-yield Strength Steel Buckling Restrained Brace." Proceedings of 15 WCEE, Lisbon, Portugal.

Ma, N., Wu, B., and Ou, J. (2012b). "Finite Element Analysis on Critical Constraint Ratio of All-steel Buckling Restrained Brace." Advanced Materials Research, Vols. 374-377:2126-2129.

Martinez-Saucedo, G., Tremblay, R., Packer, J.A. (2009). "Seismic response of circular hollow section braces with slotted end connections" In Shen, Chen & Zhao (eds), Proc. 12th international symposium on tubular structures: 227–233.

McCormick, J., DesRoches, R., Fugazza, D., and Auricchio, F. (2007). "Seismic assessment of concentrically braced steel frames with shape memory alloy braces." J. Struct. Eng., 133(6), 862–870.

Merritt, S., Uang, C. M., and Benzoni, G. (2003). "Subassemblage testing of Star Seismic buckling-restrained braces." Structural Systems Research Project, Rep. No. TR-2003/04, Univ. of California at San Diego, San Diego.

Nakashima, M., Inoue, K., and Tada, M. (1998). ''Classification of damage to steel buildings observed in the 1995 Hyogoken-Nanbu earthquake.'' J. Engrg. Struct., 20(4–6), 271–281.

Nakashima, M., Roeder, C.,W., and Yoshiomi, M. (2000). "Steel Moment Frames For Earthquakes in the United States And Japan" J. Struct. Eng., 2000, 126(8): 861-868.

Nip KH, Gardner L, Elghazouli AY. (2000). "Cyclic testing and numerical modeling of carbon steel and stainless steel tubular bracing members." Eng Struct.; 32:424–41.

Palmer, K.D., Christopulos, A. S., Lehman, D. E., Roeder, C.W. (2014). "Experimental evaluation of cyclically loaded, large-scale, planar and 3-d buckling-restrained braced frames." Journal of Constructional Steel Research 101:415–425.

Palmer, K.D., Roeder, C.W., Lehman, D. E. (2016). "Connection Design Recommendations for Improved BRBF Performance." Engineering Journal, First Quarter, 29:59.

Park, Y. S., Park, S.J., Iwai, S., Kan, S.H. (2004). "Failure and damage of steel thin-plate elements and angle members due to very-low-cycle loading." Engineering Structures 26:1623–1632.

Popov, E. P. and Pinkney, R. B. (1968). "Behavior of steel building connections subjected to inelastic strain reversals." Center for Cold-Formed Steel Structures Library. Paper 111.

Popov EP, Stephen RM. (1972). "Cyclic loading of full-size steel connections." American Iron and Steel Institute, Bulletin No. 21.

Popov EP, Bertero VV. (1973a). "Cyclic loading of steel beams and connections." Journal of the Structural Division, ASCE 99(ST6).

Popov EP, Bertero VV, Krawinkler H. (1973b). "Moment-resisting steel subassemblages under seismic loadings." Proceedings of the Fifth World Conference on Earthquake Engineering, Rome, Italy, vol. 2, pp. 1481–1490.

Popov EP, Bertero VV, Chandramouli S. (1975). "Hysteretic behavior of steel columns." Report No. EERC 75-11, Earthquake Engineering Research Center, University of California at Berkeley.

Popov, E.P., R.G. Black. (1981). "Steel struts under severe cyclic loadings." Journal of the Structural Division; 107(9):1857-1881.

Roeder, C. W., Eric J. Lumpkin, Dawn E. Lehman. (2011). "A balanced design procedure for special concentrically braced frame connections." Journal of Constructional Steel Research; 67(11): 1760-1772.

Sabelli, R., Mahin, S., & Chang, C. (2003). "Seismic demands on steel braced frame buildings with buckling-restrained braces." Engineering Structures, 25(5), 655–666.

Sabelli R, et al. (2001). "Investigation of the nonlinear seismic response of special concentric and buckling restrained braced frames and implications for design." Report to EERI, FEMA/EERI Professional Fellowship Report.

Shaback, B., and Brown, T. (2003). "Behavior of square hollow structural steel braces with end connections under reversed cyclic axial loading." Canadian Journal of Civil Engineering 30, 745-753.

Shen, J., Wen, R., Akbas, B., Doran, B., Uckan, E. (2014). "Seismic demand on brace-intersected beams in two-story X-braced frames." Engineering Structures 76:295–312.

Shen, J., Wen, R., Akbas, B. (2015). "Mechanisms in two-story X-braced frames." Journal of Constructional Steel Research 106:258–277.

Shibata, M., T. Nakamura, N. Yoshida, S. Morino, T. Nonaka, M. Wakabayashi. (1973). "Elastic-plastic behavior of steel braces under repeated axial loading." 5th World Conf. on Earthq. Engng, Vol. 1, Rome.

Sutcu, F., Takeuchi, T., and Matsui, R. (2014). "Seismic retrofit design method for RC buildings using buckling-restrained braces and steel frames." Journal of Constructional Steel Research, 101:304–313.

Xie, Q. (2005). "State of the art of buckling-restrained braces in Asia." Journal of Constructional Steel Research, 61:727–748.

Tabatabaei, S. A. R., Mirghaderi, S. R., and Hosseini, A. (2014). "Experimental and numerical developing of reduced length buckling-restrained braces." Engineering Structures, 77:143–160.

Tang, X., and Goel S. C. (1989). "Brace Fractures and Analysis of Phase I Structures." Journal of Structural Engineering 115 (8), 1960-1976.

Timoshenko, S.P. and Gere, J.M. (1961). Theory of Elastic Stability, 2nd Edition, McGraw-Hill, New York.

Tirca, L. and Chen, L. (2014). "Numerical Simulation of Inelastic Cyclic Response of HSS Braces Upon Fracture." Advanced Steel Construction Vol. 10, No. 4, pp. 442-462.

Tremblay, R. (2002). "Inelastic Seismic Response of Steel Bracing Members." Journal of Constructional Steel Research, Vol. 58, No. 5-8, pp. 665-701.

Tremblay, R., Bolduc, P., Neville, R., and DeVall, R. (2006). "Seismic Testing and Performance of Buckling-Restrained Bracing Systems." Canadian Journal of Civil Engineering, 33:183–198.

Tremblay, R. (2008). "Influence of Brace Slenderness on the Fracture Life of Rectangular Tubular Steel Bracing Members Subjected to Seismic Inelastic Loading." Proceedings of ASCE Structures Congress, Vancouver.

Tremblay, R. and others. (2008). "Inelastic Cyclic Testing of Large Size Steel Bracing Members." The 14th World Conference on Earthquake Engineering, October 12-17, Beijing, China.

Uang, C. M., Nakashima, M., and Tsai, K.C. (2004)." Research and Application of Buckling-Restrained Braced Frames." Steel Structures, 4:301-313.

Usami, T., Wang, C., and Funayama, J. (2011). "Low-Cycle Fatigue Tests of a Type of Buckling Restrained Braces." Procedia Engineering, 14:956–964.

Uriz, P. (2005). "Towards earthquake resistant design of concentrically braced steel structures." Ph.D. thesis, Univ. of California, Berkeley, Calif.

Uriz, P. and Mahin, S.A. (2008). "Towards earthquake-resistant design of concentrically braced steel-frame structures." PEER Report 2008/08, Pacific Earthquake Engineering Research Center, College of Engineering, University of California, Berkeley.

Walpole, W.R. (1996). "Behavior of cold-formed steel RHS members under cyclic loading." Research Report 96-4. Christchurch, New Zealand: Department of Civil Engineering, University of Canterbury.

Watanabe, A., Hitomoi, Y., Saeki, E., Wada, A., and Fujimoto, M. (1988). "Properties of braced encased in buckling restrained concrete and steel tube." Proceedings of Ninth World Conference on Earthquake Engineering, Tokyo-Kyoto, Japan, Vol. 4, pp.719-724.

Yoo, J. H. Dawn E. Lehman, Charles W. Roeder. (2008). "Influence of connection design parameters on the seismic performance of braced frames." Journal of Constructional Steel Research; 64(6): 607-623.

Zayas, V. A., Popov, E. P., and Mahin, S. A. (1980), "Cyclic inelastic buckling of tubular steel braces." Rep. No. UCB/EERC-80/16, Earthquake Engineering Research Center, Univ. of California, Berkeley, Calif.

Zhao, J., Wu, B., and Ou, J. (2011). "A novel type of angle steel buckling-restrained brace: Cyclic behavior and failure mechanism." Earthquake Engng. Struct. Dyn., 40:1083–1102.

Zhao, J., Wu, B., and Ou, J. (2012). "Effect of brace end rotation on the global buckling behavior of pin-connected buckling-restrained braces with end collars." Engineering Structures, 40:240–253.

Zhao, J., Wu, B., Li, W., and Ou, J. (2014). "Local buckling behavior of steel angle core members in buckling-restrained braces: Cyclic tests, theoretical analysis, and design recommendations." Engineering Structures, 66:129–145.

APPENDIX

TUBE-IN-TUBE BUCKLING CONTROLLED BRACES

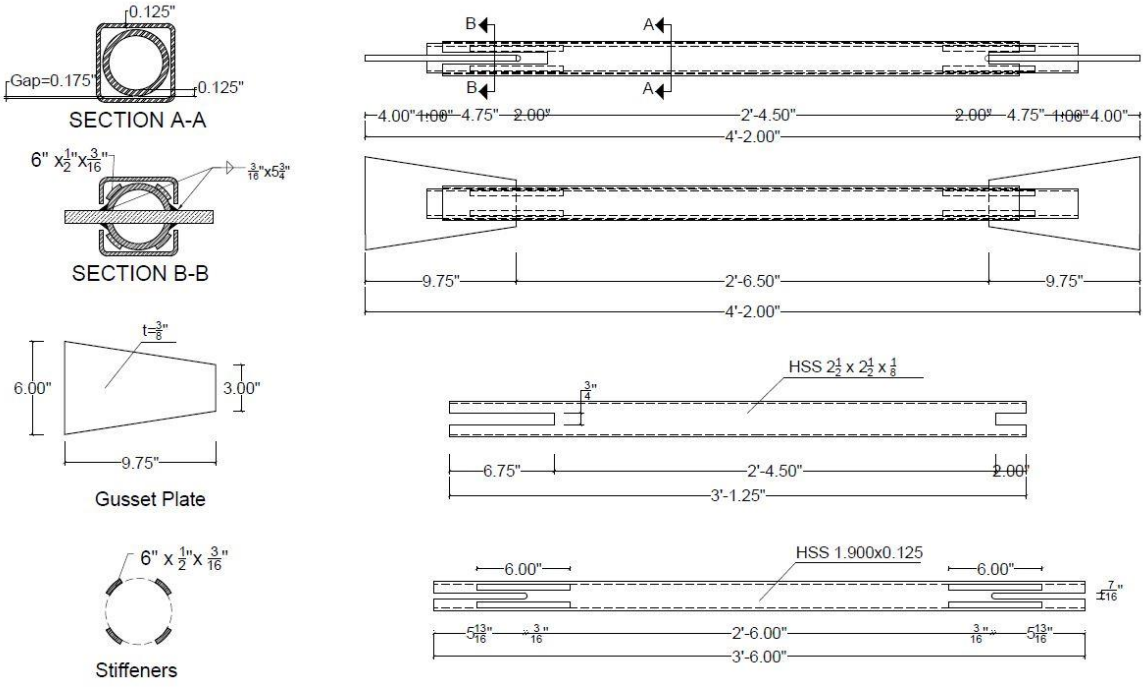

(a) TinT#1

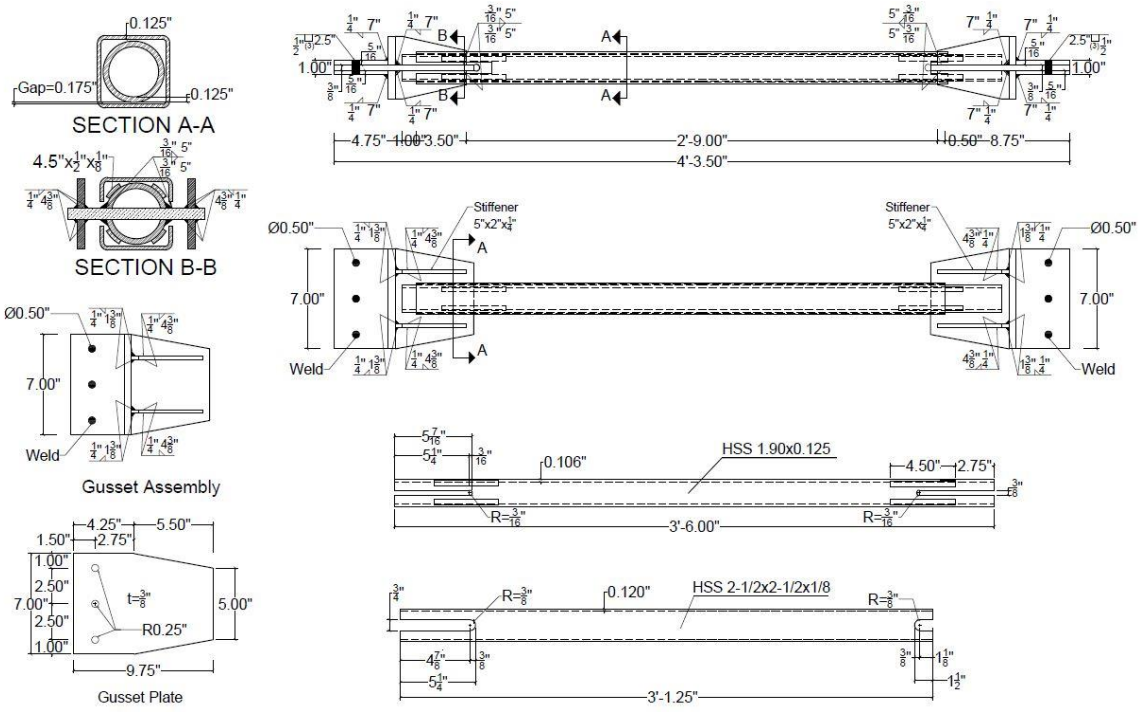

(b) TinT#2

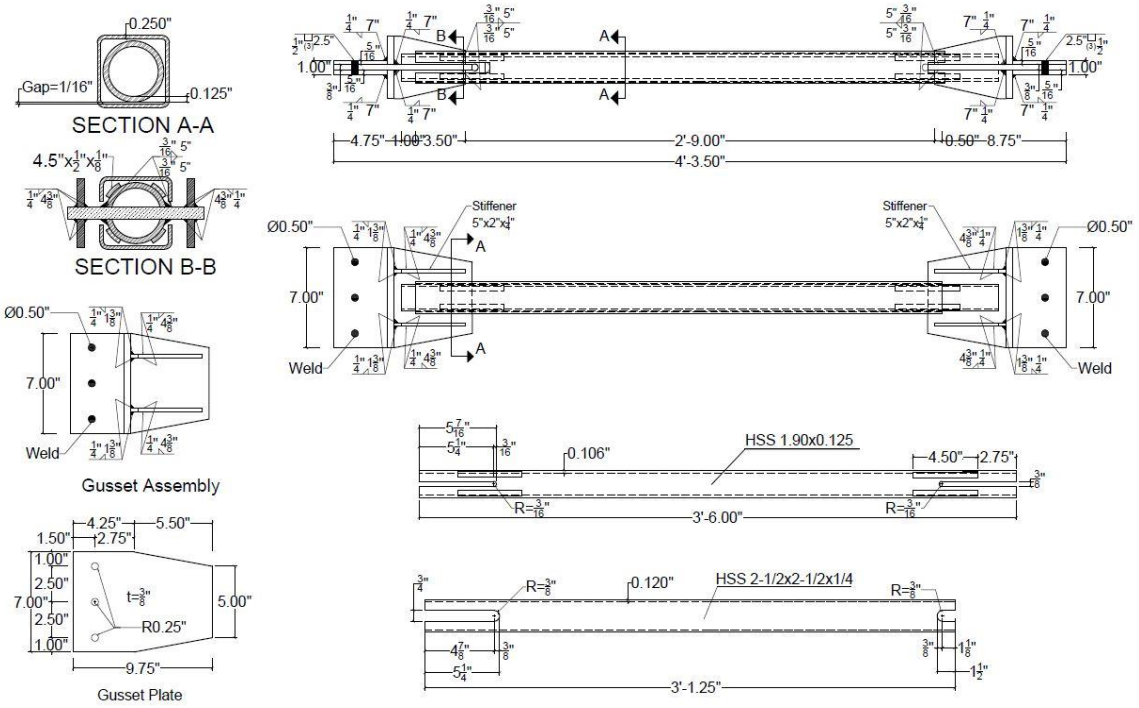

(c) TinT#3

Figure A.1. Detailed shop drawings of TinT specimens

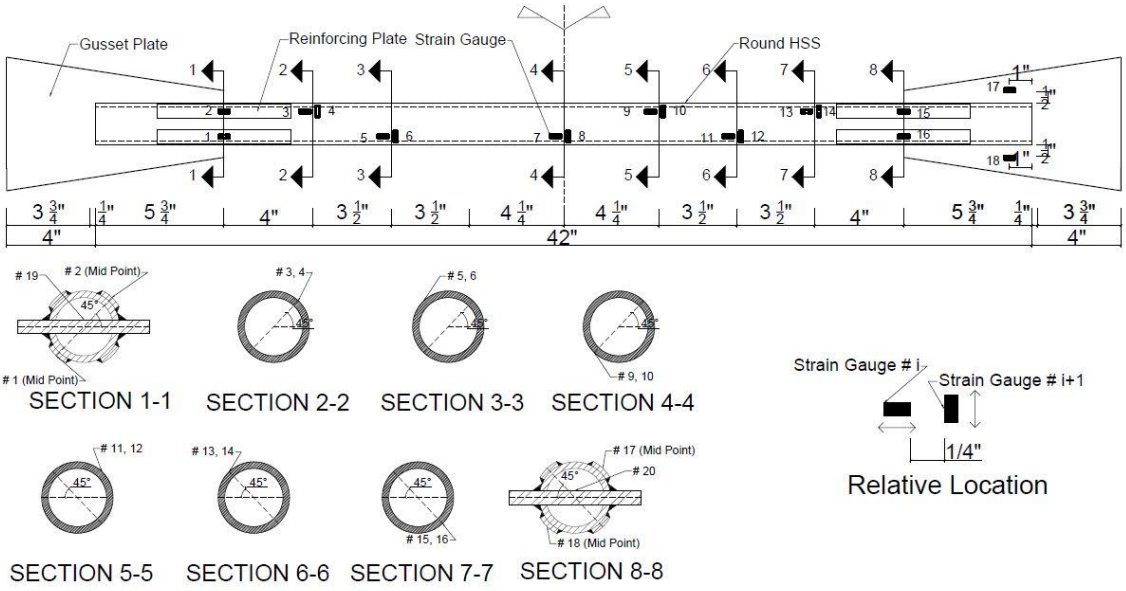

(a) TinT#1

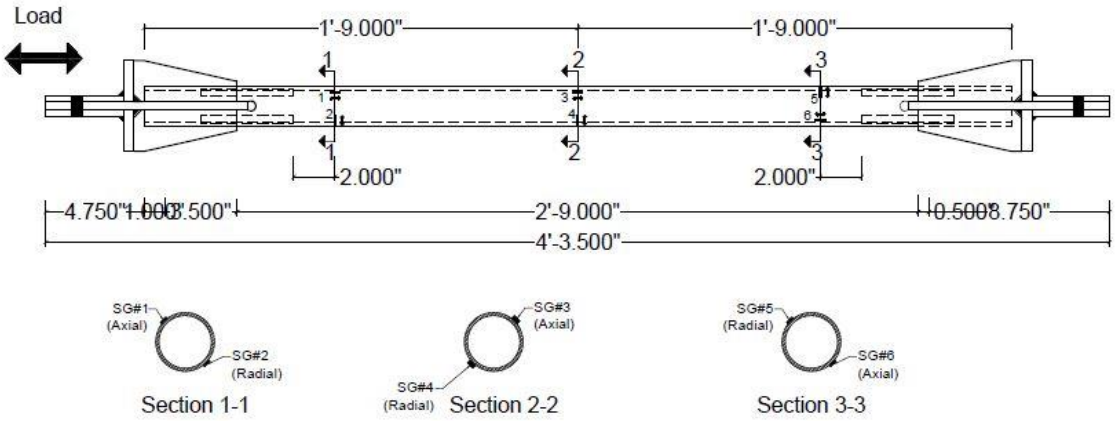

(b) TinT#2

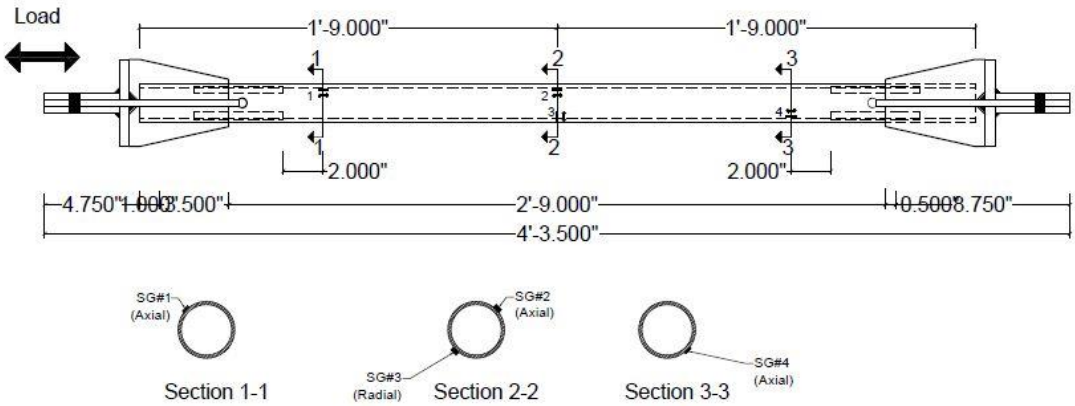

(c) TinT#3

Figure A.2. Strain gauge locations for TinT Specimens

Figure A.3. Coupon specimens prior to the test

Figure A.4. MTS and data acquisition system used for the coupon tests

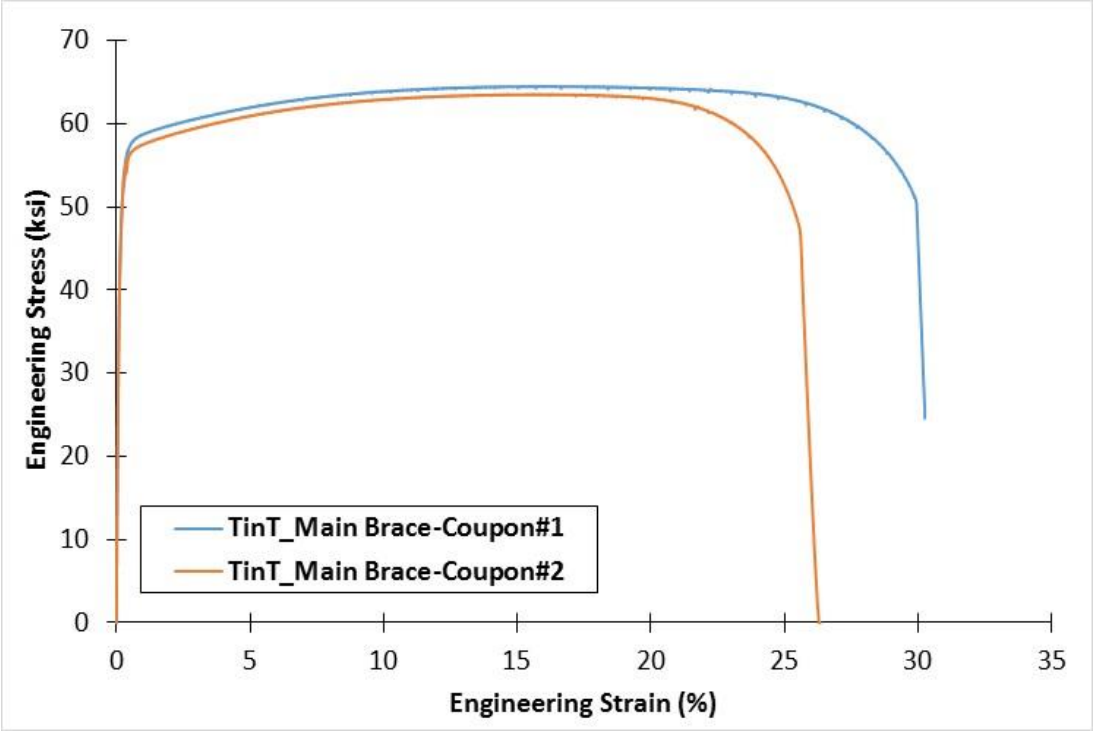

Figure A.5. Coupon test results of TinT#2 and TinT#3 specimens

(a) Loading end

(b) Fixed end

(c) Fractured slotted end of the outer tube

Figure A.6. Photos after TinT#1 test

Figure A.7. Photos after TinT#2 test